12-10-2019 2:00 PM

High Strain Dynamic Test on Helical Piles: Analytical and Numerical Investigations

Mohammed Fahad Alwalan, *The University of Western Ontario*

Supervisor: Dr. M. Hesham El Naggar, *The University of Western Ontario*

A thesis submitted in partial fulfillment of the requirements for the Master of Engineering Science degree in Civil and Environmental Engineering

ABSTRACT

Helical piles are currently considered a preferred foundation option in a wide range of engineering projects to provide high compressive and uplift resistance to static and dynamic loads. In view of the large capacity of large diameter helical piles, there is a need to determine their capacity using accurate and economically feasible testing techniques. The capacity of piles is usually determined by conducting a Static Load Test (SLT). However, the SLT can be costly and time consuming, especially for large capacity piles. The High Strain Dynamic Load Test (HSDT) evaluates the pile capacity using dynamic measurements generated through subjecting the pile to an axial compressive impact force by means of dropping a hammer at its head. The objective of this study is to investigate the performance and effectiveness of HSDT of helical piles using mathematical and numerical methods. Several case studies were examined to validate the mathematical model. The calculated pile responses were compared with the observed behavior during the actual HSDT. The mathematical model was then modified to investigate the impact response generated at the head of helical piles with different geometries. A method to approximate the pile impedance of helical piles with single and double helices were developed using added soil mass model. Furthermore, two-dimensional (axi-symmetrical) nonlinear dynamic finite element analyses were conducted using Plaxis 2D to investigate the response of helical piles during HSDT. The finite element models were verified against two case histories. The verified models were used to perform a comprehensive parametric study to better understand the aspects of the soil-pile-hammer system on the dynamic response of helical piles during axial impact loads. Finally, the results of mathematical and numerical investigations were used to formulate guidelines for the design of effective HSDT on helical piles as well as on driven piles.

Keywords: Helical piles, Static, Dynamic, Impedance, Axial impact, Numerical modelling, Analytical modelling, Plaxis 2D, High Strain Dynamic Test, Driven piles, Design.

SUMMARY FOR LAY AUDIENCE

Helical piles are composed of circular or square shafts fitted with one or more helical plates attached near the bottom of the shaft. They are used to transfer structural loads at the surface to stiffer and stronger soil. Helical piles are installed using a rotary hydraulic head that generates a torque and vertical force capable of pushing the pile into the ground. In order to determine their load carrying capacity, a Static Load Test (SLT) is conducted, The SLT involves applying loads increasingly at the pile head and measuring the movement at the pile head. However, SLTs is relatively expensive and time-consuming, thus limiting the number of helical piles that can be tested. As an alternative, the High Strain Dynamic Test (HSDT), which involves applying an impact load at the pile head through a falling mass, has been recently applied to determine the capacity of helical piles. This thesis investigates the performance of helical piles during the HSDT and provides guidelines for proper design using HSDT for helical piles.

CO-AUTHORSHIP STATEMENT

This thesis is prepared in accordance with the regulation for Integrated-Article format thesis stipulated by the school of graduate and post graduate studies at Western University, London, Ontario, Canada. Data analysis, mathematical and numerical modelling, and results interpretation were performed by the candidate himself under the supervision of his research advisor, Dr. Hesham El Naggar. The supervisor also reviewed the draft and the final thesis. In addition, two journal manuscripts will be prepared based on the material presented in Chapters 3 and 4 by the author which will be co-authored with Dr. El Naggar for possible publication in the near future.

Chapter 3: Analytical Modelling of Impact Force-Time Response Generated from High Strain Dynamic Load Test on Driven and Helical Piles.

A part of chapter 3 will be submitted to the Journal of Geotechnical and Geoenvironmental Engineering, ASCE.

Chapter 4: Finite Element Analysis of Helical Piles Subjected to Axial Impact Loading.

A part of chapter 3 will be submitted to Géotechnique – ICE Journal.

Dedicated

*To my **mother** and **father***

To my sisters and brother

ACKNOWLEDGMENTS

I gratefully acknowledge the help and support of Dr. Hesham El Naggar throughout the previous two years. Without whom, the completion of this thesis would not be possible. His feedback, guidance, and patience during the writing of this thesis are deeply appreciated.

I am also gratefully indebted to the University of King Saud, Saudi Arabia, for their financial support during my study in order to provide this learning opportunity for me.

Special thanks to my colleagues; Abdalla El Tawati, Jamal Assaf, Osama Drbe, Meshel Alkahtani, Safwat Ramadan, AbdelRahman Fayez, Abdalla Alhashmi, Daniel Mroz, Yazeed Alsharedah, Maged Abdlrahem, Ali Fallah, Mohamed Mansour, and Kareem Embaby for their suggestions and encouragements throughout the research period. May God bless them all.

I would like to extend my thanks to the staff within the Department of Civil and Environmental Engineering at the University of Western Ontario, Canada, for their support and for making a wide range of resources available to me.

Finally, thanks to all my family for their love and encouragement. You have always been there for me.

TABLE OF CONTENTS

ABSTRACT i
SUMMARY FOR LAY AUDIENCE ii
CO-AUTHORSHIP STATEMENT iii
ACKNOWLEDGMENTS v
LIST OF TABLES x
LIST OF FIGURES xi
LIST OF ABBREVIATIONS AND SYMBOLS xvi
CHAPTER 1: INTRODUCTION 1
1.1. Overview 1
1.2. Scope of the Thesis 3
1.3. Thesis Structure 4
1.4. Original Contribution of the Thesis 5
1.5. References 6
CHAPTER 2: BACKGROUND AND LITERATURE REVIEW 8
2. Introduction 8
2.1. Longitudinal Elastic Waves in A Bar 10
2.2. Elastic Waves in a Pile and Static Capacity 12
2.3. Soil Parameters Used in Wave Equation Analysis 14
2.3.1. Soil Ultimate Resistant (Ru) 14
2.3.2. Soil Quake (Q) and Soli Damping (J) 14
2.4. Axial Load Testing of Piles 16
2.4.1. Static Load Test (SLT) 16
2.4.2. Dynamic Testing of Piles Via Impact Loading 18
2.4.3. Types of Dynamic Testing 20
2.4.3.1. Quasi-Static testing method 20
2.4.3.2. High Strain Dynamic Test (HSDT) 20
2.4.3.3. Rapid Load Test (STATNAMIC) 21
2.4.4. Characteristics of Pile Load Tests 22
2.4.5. Reliability of Dynamic Load Tests 23
2.4.6. Pile Movement Versus Developed Capacity 23

2.4.7. Static Capacity of Axially Loaded Piles Based on Dynamic Measurements . 24
2.4.7.1. Pile Driving Formulas (Dynamic Formulas) 24
2.4.7.2. Pile Driving Analyzer (PDA) 26
2.4.7.3. The Case Method 27
2.4.7.4. Case Pile Wave Analysis Program (CAPWAP) 28
2.5. Numerical Modelling of Dynamic Pile Load Tests 28
2.5.1. Finite Element Modelling (FEM) of Pile Load Tests 28
2.5.2. Comparison of Signal Matching Analysis and FEM 29
2.5.3. Analysis of Piles Subjected to STATNAMIC Test 30
2.6. Axial Load Testing on Helical Piles 31
2.6.1. Overview 31
2.6.2. Helical Piles Response to Impact Loading 34
2.6.3. Shortcomings of Preceding Studies 36
2.7. References 37
CHAPTER 3: ANALYTICAL MODELLING OF IMPACT FORCE-TIME RESPONSE GENERATED FROM HIGH STRAIN DYNAMIC LOAD TEST ON DRIVEN AND HELICAL PILES 43
3. Introduction 43
3.1. Basic Definitions 45
3.2. Impact Load-Deformation Characteristic of Cushioning Block 46
3.3. Idealized Hammer-Cushion-Pile Model 48
3.4. Formulation of the Analytical D-R Model 49
3.4.1. Pile Head Force-Time Response 54
3.4.2. The Influence of Impedance Ratio 55
3.4.3. Pile Peak Force 56
3.4.4. Velocity at Impact 57
3.5. Validation of the D-R Model for HSDT 57
3.5.1. Underdamped Systems 60
3.5.1.1. Bemardes et al. (2000): Taubate, Sao Paulo 60
3.5.1.2. Sakr (2013): Alberta, Canada 63
3.5.2. Overdamped Systems 66
3.5.2.1. GEOTECHNOLOGY, INC (2013): Livingston County, Missouri. 66
3.5.2.2. Ta el al. (2013): Thi Vai International Port. 69

3.5.3. Comparison of Peak Force Coefficient 70
3.5.4. Estimated Vs. Calculated Damping 72
3.5.5. Effect of Drop Height and Impact Velocity 73
3.6. Helical Piles 77
3.6.1. Single-Helix Pile 84
3.6.2. Double-helix Pile 86
3.7. Mobilized Soil Resistance 87
3.8. Conclusion 90
3.9. References 92
CHAPTER 4: FINITE ELEMENT ANALYSIS OF HELICAL PILES SUBJECTED TO AXIAL IMPACT LOADING 95
4. Introduction 95
4.1. Case Histories of HSDT on Helical Piles 97
4.2. Soil Material Model 101
4.3. Soil Behaviour 102
4.4. Parameter Determination of The Hardening Soil Model 103
4.4.1. Strength Parameters 103
4.4.2. Stiffness Parameters 104
4.4.3. Stress-Level Dependent Stiffness 106
4.4.4. Groundwater Modelling 107
4.4.5. Dynamic Properties 107
4.4.6. Interface Modeling 108
4.4.7. Initial Stress State 109
4.5. Helical Pile Model 110
4.6. Mesh Generation 111
4.7. Final Model Geometry and Input Parameters 112
4.8. Simulation of Static Load Test 115
4.8.1. Failure Mechanism 117
4.9. Simulation of High Stain Dynamic Test 118
4.9.1. Dynamic Time Discretization 119
4.9.2. Dynamic Calculation Phases 119
4.9.3. Derived load-displacement curve: Case 1. 123
4.9.3.1 Employing CAPWAP (CAse Pile Wave Analysis Program) 123

4.9.3.2 The Modified Unloading Point Method (MUP) 124
4.9.3.3 G-C Method 124
4.9.4. Derived Load-Displacement Curve: Case 2 125
4.9.4.1 CAPWAP (CAse Pile Wave Analysis Program) 125
4.9.4.2 The Unloading Point Method (UP) 126
4.9.4.3 G-C Method 127
4.10. Validation of Dynamic Model 128
4.11. Parametric Study 129
4.11.1. Effect of Number of Helices 129
4.11.2. Effect of Spacing Between Helices 131
4.11.3. Effect of Hammer Drop Height 133
4.11.4. Effect of Hammer Weight 137
4.11.5. Effect of Cushion Stiffness 141
4.12. Validation of Mathematical Model 145
4.13. Relationship of Hammer Potential Energy and Mobilized Resistance at a Required Displacement 146
4.13.1. For Clay 147
4.13.2. For Sand 148
4.13.3. Design Procedure 149
4.13.4. Limitations of Design Procedure 150
4.14. Conclusion 153
4.15. References 155
CHAPTER 5: CONCLUSIONS AND RECOMMENDATIONS 159
5.1. Overview 159
5.2. Conclusions 159
5.3. Recommendations for Future Research 162
APPENDIX A: METHOD OF ANALYZING AXIAL PILE RESPONSE UNDER DYNAMIC LOADING 163
APPENDIX B: GEOTECHNICAL CORRELATIONS FOR THE DETERMINATION OF SOIL PROPERTIES 167
VITA 175

LIST OF TABLES

Table 2- 1: Allocation of soil resistance to the shaft and the base of a pile in wave equation analysis as proposed by Forehand and Reese (1964). 14
Table 2- 2: Soil damping and quake characteristics after Lowery (1993). 15
Table 2- 3: CASE damping values for different types of soil after Halder (2016). 15
Table 2- 4: Characteristic of pile load tests after Holscher & Van (2008). 22
Table 2- 5: List of dynamic formulas. 25
Table 3- 1: Case histories used in this study……..58
Table 3- 2: Pile and Test Equipment Data. 67
Table 3- 3: Information for the Tested Piles 78
Table 3- 4: Comparison between the estimated impedance from signal matching and the calculated impedance from equation 3.50. 86
Table 3- 5: Comparison between the estimated impedance from signal matching and the calculated impedance from equation 3.51. 87
Table 4- 1: Basic parameters in the HS model…….102
Table 4- 2: Soil strength parameters for the HS models. 104
Table 4- 3: Selected stiffness parameters for Case 1 sand model in Plaxis 2D. 106
Table 4- 4: Typical values for m in cohesionless and cohesive soils. 107
Table 4- 5: Interface parameter $Rinter$ for Case 1 – Sandy soils. 108
Table 4- 6: Interface parameter $Rinter$ for Case 2 – Clayey soil..... 109
Table 4- 7: Initial stress state parameters. 110
Table 4- 8: Optimization of soil meshing. 112
Table 4- 9: Summary of soil layers properties for Case 1 in Plaxis 2D..... 113
Table 4- 10: Summary of soil layers properties for Case 2 in Plaxis 2D..... 113
Table 4- 11 Helical piles configuration considered in analysis to study effect of number of helices. 129
Table 4- 12: Helical pile geometries considered to study the effect of helix spacing. ... 131
Table 4- 13: Limitations of Design Procedure. 152

LIST OF FIGURES

Figure 2- 1: Problem idealization of pile-soil system for wave equation analysis after smith (1962). 10
Figure 2- 2: Wave mechanics at (A) free end bar and (B) fix end bar. 11
Figure 2- 3: The influence of soil resistance on the force and velocity records measured at the pile top..... 13
Figure 2- 4: Classification of pile load test methods after Holeyman (1992). 16
Figure 2- 5: Schematic view of the Static load test after ASTM (2013). 18
Figure 2- 6: Schematic diagram for dynamic mentoring of deep foundations after ASTM (2013). 19
Figure 2- 7: Comparison between different types of pile load testing. 20
Figure 2- 8: Rapid Load Test (TN) component and setup after Briaud et al. (2000). 21
Figure 2- 9: Relative pile movement in relation to soil after Brom (1978). 24
Figure 2- 10: Basic helical pile component after Perko (2009). 32
Figure 2- 11, Failure mechanism of helical piles; (A) individual plate bearing method, and (B) cylindrical shear method. 33
Figure 3- 1: Cushion deformation properties during impact..... 48
Figure 3- 2: Physical (A), and analytical (B) representation of pile hammer model. 49
Figure 3- 3: (A) system model; (B) pile element under analysis; (C) free body diagram. 50
Figure 3- 4: Force coefficient, Fc, after Parola (1970). 56
Figure 3- 5: Flowchart of the validation process. 60
Figure 3- 6: Comparison between measured and calculated force time response at the pile head for piles: (a) D230; (b) D260; and (c) D330. 62
Figure 3- 7: Comparison between measured and calculated force time response at the pile head for piles: (a) D1; and (b) D2. 65
Figure 3- 8: Peak force versus Pile impedance for a given hammer and cushion set up.. 66
Figure 3- 9: Comparison of measured and calculated force-time response. 67
Figure 3- 10: graphical representation of the effect of increasing cushion stiffness for overdamped system. 69
Figure 3- 11: Force-time response at the head of pile TSP1..... 70

Figure 3- 12: Peak pile force coefficient, Fc, versus impedance ratio, I, for all case histories. 71
Figure 3- 13: Peak force coefficient vs damping ratio. 72
Figure 3- 14: Calculated damping versus estimated damping. 73
Figure 3- 15: Peak force results at various drop height. 74
Figure 3- 16: Load-settlement curves from different blows performed on two piles with the same geometry and soil profile. 76
Figure 3- 17: Flow Chart for Helical Pile impedance determination adopted in this study. 80
Figure 3- 18: Comparison of peak force coefficient and impedance ratio between a driven pile and a helical pile with the same shaft size and embedment length. 81
Figure 3- 19: Results of peak force coefficient and impedance ratio for helical piles; (a) peak force coefficient vs. impedance ratio assuming uniform shaft, (b) peak force coefficient vs. adjusted impedance ratio, (c) increase in pile impedance caused by single helix, and (d) increase in pile impedance caused by double helices. 84
Figure 3- 20: Single-helix pile model: a) physical, and b) idealized. 85
Figure 3- 21: Double-helix pile model: (a) physical, and (b) idealized. 86
Figure 3- 22: Mobilized soil resistance at various pile impedance: (a) for the top measured displacement at the pile head (b) for cohesive soil. 89
Figure 4- 1: Stratification of soil layers from the surface exploration tests and groundwater level for case 2 after Elkasabgy & El Naggar (2018). 99
Figure 4- 2: General outline of the 3D model (left) and 2D axisymmetric (right). 100
Figure 4- 3: Model geometry size and boundary conditions for FEM. 101
Figure 4- 4: Profile for the initial stiffness, Ei, and secant modulus, Es, for Case 2. 105
Figure 4- 5: (a) Geometry of tested helical piles; and (b) helical piles geometry in the axisymmetric numerical model. 110
Figure 4- 6: Zones of localized mesh refinement. 111
Figure 4- 7: Case 1 model (a) helical pile and soil-pile interface, (b) model geometry, and (c) Generated mesh. 114
Figure 4- 8: Case 2 model: (a) helical pile and soil-pile interface, (b) model geometry, and (c) Generated mesh. 114

Figure 4- 9: Calculated and measured load-displacement curves for Case 2 helical pile. 116
Figure 4- 10: Calculated and measured load-displacement curves for Case 1 helical pile. 116
Figure 4- 11: Displacement contours for: a) single helix pile; b) 2-helix pile with cylindrical failure mechanism. 117
Figure 4- 12: Force functions used to simulate hammer impact in numerical models. .. 118
Figure 4- 13: Helical pile displacement time history, (a) Case 1 and (b) Case 2. 120
Figure 4- 14: Dynamic response of the helical pile installed in sand (Case 1). 121
Figure 4- 15: Dynamic response of the helical pile installed in clay (Case 2). 122
Figure 4- 16: Load-displacement curves from numerical model and CAPWAP – Case 1. 123
Figure 4- 17: Load-displacement curve numerical model and MUP method – Case 1.. 124
Figure 4- 18: Load-displacement curves from numerical model and G-C method – Case 1..... 125
Figure 4- 19: Load-displacement curves from numerical model and CAPWAP – Case 2. 126
Figure 4- 20: Load-displacement curves from numerical model and the UP method - Case 2..... 127
Figure 4- 21: Load-displacement curves from numerical model and G-C method – Case 2..... 128
Figure 4- 22: Derived static load-displacement curves obtained from dynamic and static simulations for helical piles installed in sand: a) single helix pile; b) double-helix pile.130
Figure 4- 23: Derived static load-displacement curves obtained from dynamic and static simulations for helical piles installed in clay: a) single helix pile; b) double-helix pile. 131
Figure 4- 24: Load-displacement curves obtained from G-C method and static simulations at different spacing ratio for the helical piles installed in sand: (a) $S/DH = 1.5$ and (b) $S/DH = 3$. 132
Figure 4- 25: Load-displacement curves obtained from dynamic and static simulations at different spacing ratio for the helical piles installed in clay: (a) $S/DH = 1.5$ and (b) $S/DH = 3$. 132

Figure 4- 26: Shape of force pulses generated at different heights: (a) for single-helix pile installed in sand, and (b) for the double-helix pile installed in clay. 133
Figure 4- 27: Load-displacement curves obtained from dynamic and static simulations for different hammer drop heights for piles installed in sand: (a) 0.9 m; (b) 1.5 m; (c) 2 m. 134
Figure 4- 28: Load-displacement curves obtained from dynamic and static simulations for different drop heights for piles in clay: (a) 0.9 m; (b) 1.5 m; (c) 2 m. 135
Figure 4- 29: (a) Maximum force at helical pile head; and (b) maximum compression stress generated at the helical pile due to changing in hammer drop height. 136
Figure 4- 30: Load-displacement curves from dynamic and static analyses for different hammer weights for helical piles installed in sand: (a) 20 kN; (b) 30 kN; (c) 50 kN; and (d) 80 kN. 138
Figure 4- 31: Load-displacement curves from dynamic and static analyses at different hammer weights for helical piles installed in clay: (a) 20 kN; (b) 30 kN; (c) 50 kN; and (d) 80 kN. 139
Figure 4- 32: Displacement contours obtained for the helical pile installed in sand at a different hammer weight: (a) 20 kN; (b) 30 kN; (c) 50 kN; and (d) 80 kN. 140
Figure 4- 33: Displacement contours obtained for helical pile installed in clay for different hammer weight: (a) 20 kN; (b) 30 kN; (c) 50 kN; and (d) 80 kN. 141
Figure 4- 34: Force pulse generated at pile head for different cushion stiffness: (a) for Case 1; and (b) Case 2. 142
Figure 4- 35: Responses of the helical pile to different values of Ks for Case 1: (a) 8E06 N/m, (b) 8E07 N/m. 143
Figure 4- 36: Responses of piles at different values of Ks for Case 2: (a) 3E08 N/m, (b) 3E09 N/m. 143
Figure 4- 37: Variations of contours of displacements with different cushion stiffness for helical pile installed in sand Case 1: (a) 8E06 N/m, (b) 8E07 N/m. 144
Figure 4- 38: Variations of contours of displacements with different cushion stiffness for helical pile installed in clay Case 2: (a) 3E08 N/m, (b) 3E09 N/m. 144
Figure 4- 39: Relationship between mobilized static soil resistance and impedance ratio obtained from numerical analysis and mathematical model results. 146

Figure 4- 40: A 3D plot of the Variation of potential energy with mobilized static resistance ratio (static / dynamic) at a maximum measured top displacement for cohesive soils. 148
Figure 4- 41: A 3D plot of the variation of potential energy with mobilized static resistance ratio (static / dynamic) at a maximum measured top displacement for cohesionless soils. 149

LIST OF ABBREVIATIONS AND SYMBOLS

Abbreviations

American Petroleum Institute	API
American Piledriving Equipment, Inc.	APE
American Society for Testing and Materials	ASTM
Automatic signal Matching Technique	AMT
Beginning of restrike	BOR
Capacity to Torque Correlation	CTC
CAse Pile Wave Analysis Program	CAPWAP
End of drive	EOD
Finite Element Model	FEM
Hardening soil model	HS
High Strain Dynamic Test	HSDT
Match quality	MQ
Modified Unloading Point method	MUP
Over consolidation ratio	OCR
Pile Driving Analyzer	PDA
Plasticity index	PI

Symbols

α – method coefficient	α
A constant representing initial conditions	B
Acceleration at the maximum displacement	$a(t_{max})$
Acceleration of the hammer	$\ddot{v}_1$
Amplitude of the dynamic load	$\hat{F}$
Angular frequency of the applied load	w
Area of the outside shaft diameter	A_{OD}
Average dynamic modulus of elasticity	$E_{dynamic}$
Average static modulus of elasticity	E_{static}
β-method coefficient	β
Characteristic load	F_w
Coefficient of lateral earth pressure at rest	K_o
Compression wave velocity	V_P
Cone tip-resistant	q_t
Cross-section area	A
Cushioning stiffness	k_s
Cushioning unloading stiffness	k_u
Damping coefficient	J

Damping of the hammer-cushion-pile model	D
Damping ratio	ξ
Dashpot coefficient	c
Deformation	v
Depth below ground	z
Diameter of the helix	d_{helix}, D_h
Diameter of the shaft	d, d_s
Dilatancy angle	ψ
Displacement at the pile head	S
Displacement of the pile at time t of the applied load	$u(t)$
Displacement position of the hammer and the pile top, respectively.	v_1, v_2
Drop height	h
Dynamic time interval	Δt
Effective angle of internal friction	$\emptyset'$
Effective overburden pressure	σ'_{v_o}
Elapsed time	t
Elastic modulus	E
Elastic unloading-reloading stiffness	E_u^{ref}, E_{ur}
Element length of the pile	Δx
Exponent control the nonlinearity	N
Fitting parameters	f, g
Force coefficient	F_c
Force generated at the pile head	F
Friction angle	$\emptyset$
Gravitational acceleration	g
Hammer speed	$\dot{v}_1$
Helical pile impedance	Z_H
Hydrostatic pore water pressure	u_o
Impact load duration	T
Impedance ratio	I
Initial stiffness	k_i
Initial stress state	$K_{0,x}$
Initial tangent undrained modulus of elasticity	E_{ui}, E_i
Inter-helix spacing	S
Kinetic energy	E_k
Lateral earth pressure coefficient in compression	K_s
Length of the pile	L
Mass of the added soil	M_s
Mass of the hammer	m_r

Mass of the pile	M_p
Max. velocity	V_{max}
Maximum measured force at the pile head	F_{d_max}
Maximum potential energy	$(E_p)_{60\%}$
Measured acceleration at the pile head at a time t	$a(t)$
Measured force at the pile head at time t	$F_d(t)$
Measured velocity at the pile head at a time t	$V(t)$
Mobilized stress relative to ultimate stress	$\frac{\mathrm{q}}{\mathrm{q_{ult}}}$
Mobilized static resistance ratio (i.e. static/dynamic)	R_m
Motion direction	x
Overall impedance of a helical pile	Z_H
Particles velocity	V
Particles velocity at the impact zone	$\dot{v}_2$
Peak force at the pile head	F_p
Pile impedance	Z
Pile's unit mass	ρ, ρ_{pile}
Pore-water pressure	u_2
Potential energy	E_p
Power for stress-level dependency of stiffness	m
Reduction empirical factor to account for the rate effect	η
Required top pile head displacement	S_{max}
Robert Miner Dynamic Testing corporation	RMDT
Secant modulus of elasticity	E_s
Secant stiffness at 50% of the failure load	E_{50}
Secant triaxial loading stiffness	E_{50}^{ref}
Seismic cone penetration test	SCPT
Shear modulus	G
Shear modulus at small strain	G_{max}
Shear wave velocity	V_s
Skin friction angle	δ
Sleeve friction	f_s
Soil layer thickness	H
Soil static resistance at time t	$P_s(t)$
Soil's unit mass	ρ_{soil}
Specific gravity	G_s
Spring coefficient	k
Standard Penetration Test	SPT
SPT-N value	N

SPT-N value corrected for field procedures	N_{60}
SPT-N value corrected for field procedures and overburden pressure	$(N_1)_{60}$
Static Load Test	SLT
Static soil response at time t of the applied load	$F_{static}(t)$
Static strength of the soil	P_s
STATNAMIC load test	STN
Strain	ϵ
Strength reduction factor	R_{inter}
Stress	σ
Surface area of the helix	A_{helix}
Tangent oedometer loading modulus	E_{oed}^{ref}, E_{oed}
Targeted frequencies	f_1 , f_2
Tension cut-off and tensile strength	σ_t
The frequency of the hammer-cushion-pile model	ω
The static soil response at the maximum displacement	$F(t_{max})$
The time at zero velocity, i.e. Maximum displacement	t_{max}
Theoretical or empirical cone factor	N_k
Thickness	t_i
Time of impact at which negative force is developed	t_0
Total dynamic strength of the soil	P_d
Traveled wave distance	Δl
Undrained shear strength	S_u, C_u
Unified soil classification system	USCS
Unit weight	γ
Unit weight above phreatic line	γ_{unsat}
Unit weight below phreatic line	γ_{sat}
Unloading Point method	UP
Velocity at impact	$\dot{v}_o$
Vertical or mean in situ stress	σ_o
Void ratio	e
Water content	W
Wave speed	C
Wavenumber parameter	N_w

CHAPTER ONE

INTRODUCTION

1.1 Overview

Accurate determination of static load carrying capacity of individual piles is necessary for reliable design of piled foundations. Quantitative determination of the static pile capacity is traditionally accomplished through the conventional Static Load Test (SLT), which is considered to be the most accurate test to determine pile capacity. However, the SLT is relatively expensive and time consuming, thus limiting the number of piles that can be tested. These inherent limitations are acute for large capacity piles because large test setups are required. It is therefore highly desirable to seek an alternative test that could determine the static capacity quickly and with less cost compared to SLT.

In the recent past, the High Strain Dynamic Test (HSDT) has been introduced as an efficient means for evaluating the bearing capacity through the concept of "dynamic soil resistance". The High Strain Dynamic Test is characterized by its short duration of loading, which results in high velocity and acceleration of the test pile compared with the Static Load Test. In the HSDT, the pile top is subjected to a hammer impact dropped from a height. The hammer can be simply released to fall mechanically under gravity, hydraulically operated weight, or a hammer with a diesel engine combustion. The strain and acceleration signals measured at the top of the pile are converted by the Pile Driving Analyzer (PDA) into force and velocity records plotted against time. These records are post-processed using special software called The CAse Pile Wave Analysis Program (CAPWAP). The software can isolate the dynamic resistance from the total resistance to provide insight into the static response of the pile under consideration. Typically, one blow is selected for analysis. However, different results may be obtained from different blows within the same soil layer. Thus, a representative blow should be selected with care for the analysis to determine the pile capacity. Several studies have been performed using the

CAPWAP for the analysis of HSDT indicated a good correlation with the SLT results (Likins & Rausche, 2004; Green & Kightley, 2005; Vaidya, 2006; Long et al., 2009; Basarkar et al., 2011; and Rajagopal et al., 2012).

There are two main approaches used for the analysis of pile response to axial impact loading: the Winkler based model and the finite element analysis. The Winkler based model has been commonly used, and its ability to predict load-deflection behavior of the pile-soil model has been proven (Smith, 1960; Nogami & Konagai 1987; El Naggar & Novak, 1992, 1994; Long et al., 2009). Similarly, several studies are available concerning modelling pile dynamic load tests and its associated computation using the finite and boundary element analysis in the literature. Several attempts have been made to simulate real dynamic pile load test conditions (Nath, 1990; Mabsout & Tassoulas, 1994; Mahutka et al., 2006; Feizee, 2008; and Fakharian et al., 2014). Nevertheless, a more precise analysis is required to account for various test variables (Krasiński & Wiszniewski, 2017).

Helical piles are non-displacement steel piles comprised of one or more helical bearing plates affixed to a circular or square shaft. They could be installed at various depths to derive the required capacity considering the soil condition at the planned location (Elsherbiny & El Naggar, 2013). Helical piles offer unique advantages, including quick installation using relatively small driving machinery, which enables installation in limited access areas and minimum disturbance to the site with low noise and vibration. In addition, helical piles offer instant load carrying capacity (Perko, 2009). Recently, there has been an increase in the use of high capacity helical piles to support large compressive loads. Therefore, dynamic load tests by an impact hammer have become an alternative system to the conventional static pile load tests due to the difficulties associated with transporting kentledges that are required to fully mobilized the bearing capacity of large helical piles.

Significant efforts have been dedicated to study the response of helical piles subjected to axial static loading (Zhang, 1999; Perko, 2000; Tappenden, 2007; Sakr, 2009; El Elsherbiny and El Naggar, 2013; Gavin et al., 2014; Elkasabgy and El Naggar, 2015). However, the performance of helical piles under axial impact loads has received much less attention since dynamic load tests are commonly associated with driven piles mainly because the hammer used for the pile installation is used for the test. There is a limited

number of studies available in the literature that investigated the performance of helical piles subjected to the HSDT (Cannon, 2000; Beim & Luna, 2012; Benjamin White, n.d.; and Sakr, 2013). The derived static pile capacity obtained in previous studies was in satisfactory agreement with the static load carrying capacity.

All previous studies (Cannon, 2000; Beim & Luna, 2012; Benjamin White, n.d.; and Sakr, 2013) demonstrated that HSDT is suitable for evaluating the static capacity of helical piles based on full-field tests. However, this conclusion was largely based on a limited number of test data using semi-empirical methods that were developed for driven and drilled piles. In addition, none of the previous studies examined the load transfer mechanism for helical piles during the HSDT nor studied the influence of dynamic load tests on helical piles that comprise multiple helices or helices of different diameter. For instance, the effect of increasing the number of helices on the application of HSDT to helical piles has never been investigated. Furthermore, most previous researches focused on helical piles installed in cohesive soils, while HSDT of helical piles installed in cohesionless soils has not been addressed appropriately. Most importantly, there is no available method to determine how much energy is required to sufficiently displace the helical pile to fully mobilize its capacity. Beim & Luna (2012) reported that the derived static capacity of helical piles evaluated from the HSDT was overly conservative when compared to static load results, because the chosen hammer weight and drop height were not sufficient to fully mobilize the end-bearing capacity of helical piles.

1.2 Scope of the Thesis

The purpose of the current study is to investigate mathematically and numerically the dynamic behaviour of helical piles under axial impact loads. The main objectives of the thesis are to improve the accuracy of predicting the helical pile's capacity using dynamic measurements; and to aid in establishing a reliable and practical test setup for the dynamic loading on helical piles. A mathematical model is employed to derive analytical solutions for the force-time response generated at the pile head for both driven and helical piles. Subsequently, the various parameters controlling the force-time response are studied. Furthermore, the finite element software Plaxis 2D (Bentley Systems, 2019) is utilized to perform the numerical analyses, whereby the dynamic behaviour of helical piles subjected

to the HSDT is studied. Finally, an attempt is made to correlate the results of static and dynamic load tests with the characteristic of the equipment used in the HSDT.

1.3 Thesis Structure

The thesis is comprised of five chapters, and they are orderly organized as follow:

Chapter 1 introduces the motivation behind this work and its scope, and describes the thesis structure.

Chapter 2 presents a comprehensive background and literature review relevant to the thesis topic. It discusses the concept of propagation of compression wave in piles and its applications and the axial load testing on piles. In addition, it briefly discusses the finite element modelling of dynamic load tests of piles and introduces the available methods for estimating the pile's load-settlement response based on pile-dynamic data. Furthermore, the behaviour of helical piles subjected to both axial static and dynamic loading is discussed. Finally, Chapter 2 summarizes the published studies regarding full-field load tests conducted on helical piles with an emphasis on the axial dynamic load tests and discusses where the literature has reached regarding the evaluation of helical piles response to axial impact loading.

Chapter 3 describes the theoretical study of the dynamics of impact loads at the top of piles by means of wave propagation theory. A relatively simple mathematical model consisting of a hammer, a cushion, and a pile was utilized to accomplish this task. The validation and the calibration of the analytical solutions for the hammer-cushion-pile model based on field data obtained from various case studies found in the literature are also discussed. Finally, the chapter explores the characteristics of hammer impact on driven and helical piles with particular attention in estimating the impedance increases caused by the helices of the helical pile.

Chapter 4 discusses in depth the process of modelling the SLT and the HSDT on helical piles installed in cohesionless and cohesive soils in a 2D domain by employing the Plaxis 2D software package. The discussion includes model geometry, soil-pile interaction, boundary conditions, modelling of impact loads, time-domain effect, and analysis

procedures and data interpretation of dynamic measurements (i.e. force, acceleration, and velocity measurements). Chapter 4 also describes a simple approach to derive the load-displacement curve form the dynamic measurements obtained during the HSDT. The finite element models were validated against the results of two full-scale field tests. Lastly, a parametric study was performed to investigate the influence of various geometric aspects on the axial dynamic response of helical piles and the results are presented and discussed.

Chapter 5 provides conclusions of the study and offers recommendations for further research.

1.4 Original Contribution of the Thesis

The principal contributions of this thesis are to:

1. Introduce a set of equations to estimate the overall impedance of helical piles.
2. Propose an empirical correlation that relates the potential energy of the hammer with the mobilized resistance and displacement for helical and driven piles.
3. Understand the response of helical piles to axial impact loading through numerical methods.
4. Establish guidelines for the design of effective HSDT on helical piles.

1.5 References

Basarkar, S. S., Kumar, M., & Vaidya, R. (2011). High strain dynamic pile testing practices in India-favourable situations and correlation studies. In Proceedings of Indian Geotechnical Conference Kochi. (Paper No. Q-303).

Beim, J., & Luna, S. C. (2012). Results of dynamic and static load tests on helical piles in the varved clay of Massachusetts. DFI Journal, the Journal of the Deep Foundations Institute, 6(1): 58-67.

Bentley Systems. (2019). PLAXIS 2D Geotechnical finite element analysis software. Bentley Systems: Advancing Infrastructure. Delft, Netherlands.

Benjamin W, P. E., & Engineers, G. R. L. (n.d.) High strain dynamic load testing on helical piles – Case Study.

Cannon, J. G. (2000). The application of high strain dynamic pile testing to screwed steel piles. In Sixth International Conference on the Application of Stress-Wave Theory to Piles. pp. 11-13.

Elkasabgy, M. and El Naggar, M.H. (2015). Axial compressive response of large-capacity helical and driven steel piles in cohesive soil. Canadian Geotechnical Journal, 52(2): 224-243.

El Naggar, M. E., & Novák, M. (1992). Analytical model for an innovative pile test. Canadian geotechnical journal, 29(4): 569-579.

Elsherbiny, Z. H., & El Naggar, M. H. (2013). Axial compressive capacity of helical piles from field tests and numerical study. Canadian Geotechnical Journal, 50(12): 1191-1203.

Fakharian, K., Masouleh, S. F., & Mohammadlou, A. S. (2014). Comparison of end-of-drive and restrike signal matching analysis for a real case using continuum numerical modelling. Soils and Foundations, 54(2): 155-167.

Feizee, S. (2008). Evaluation of design parameters of pile using dynamic testing and analyses. [Ph.D. Thesis]. Amir Kabir University of Technology; Tehran, Iran.

Gavin, K., Doherty, P., & Tolooiyan, A. (2014). Field investigation of the axial resistance of helical piles in dense sand. Canadian Geotechnical Journal, 51(11): 1343-1354.

Green, T. A. L., & Kightley, M. L. (2005). CAPWAP testing-theory and application. In Proceedings of the International Conference on Soil Mechanics and Geotechnical Engineering. AA BALKEMA publishers, 16(4): 2115-2118.

Krasiński, A., & Wiszniewski, M. (2017). Static load test on instrumented pile – field data and numerical simulations. Studia Geotechnica et Mechanica, 39(3): 17-25.

Likins, G., & Rausche, F. (2004). Correlation of CAPWAP with static load tests. Proceedings of the Seventh International Conference on the Application of Stress wave Theory to Piles. Petaling Jaya, Selangor, Malaysia. pp. 153-165.

Long, J. H., Hendrix, J., & Jaromin, D. (2009). Comparison of five different methods for determining pile bearing capacities (No. WisDOT 0092-07-04). Wisconsin Highway Research Program.

Mabsout, M. E., & Tassoulas, J. L. (1994). A finite element model for the simulation of pile driving. International Journal for numerical methods in Engineering, 37(2): 257-278.

Mahutka, K. P., König, F., & Grabe, J. (2006). Numerical modelling of pile jacking, driving and vibratory driving. In Proceedings of International Conference on Numerical Simulation of Construction Processes in Geotechnical Engineering for Urban Environment (NSC06), Bochum, ed. T. Triantafyllidis, Balkema, Rotterdam. pp. 235-246.

Nath, B. (1990). A continuum method of pile driving analysis: comparison with the wave equation method. Computers and Geotechnics, 10(4): 265-285.

Nogami, T. and Konagai, K. (1987). Dynamic response of vertically loaded nonlinear pile foundations. Journal of Geotechnical Engineering, ASCE, Vol. 113: 147-160.

Perko, H. A. (2009). Helical piles: a practical guide to design and installation. John Wiley & Sons.

Perko, H. A. (2000). Energy method for predicting installation torque of helical foundations and anchors. In New technological and design developments in deep foundations. pp. 342-352.

Rajagopal, C., Solanki, C. H., & Tandel, Y. K. (2012). Comparison of static and dynamic load test of pile. Electronic Journal of Geotechnical Engineering, Vol. 17: 1905-1914.

Sakr, M. (2009). Performance of helical piles in oil sand. Canadian Geotechnical Journal, 46(9): 1046-1061.

Sakr, M. (2013). Comparison between high strain dynamic and static load tests of helical piles in cohesive soils. Soil Dynamics and Earthquake Engineering, Vol. 54: 20-30.

Smith, E. A. (1962). Pile-driving analysis by the wave equation. American Society of Civil Engineers Transactions.

Vaidya, R. (2004). Low strain integrity and high strain dynamic testing of piles-an Indian overview. In the Seventh International Conference on the Applications of Stress Wave Theory to Piles, Malaysia. pp. 193-197.

Zhang, D. J. Y. (1999). Predicting Capacity of Helical Screw Piles in Alberta Soils. [Master thesis]. ProQuest Dissertations Publishing.

CHAPTER TWO

BACKGROUND AND LITERATURE REVIEW

This chapter reviews and provides background information on the propagation of compression waves in a pile subjected to an axial impact load at its head, including the one-dimensional wave equation and its applications. It also reviews axial load testing techniques of piles, including Dynamic Load Tests (DLT) via impact loads, such as the High Strain Dynamic Test, the Quasi-Static Test and the Rapid Load Test, as well as the Static Load Test (SLT). Correspondingly, the estimation of a pile's load-settlement response based on pile-dynamic data is described; including Pile Driving Analyzer (PDA), Case Pile Wave Analysis Program (CAPWAP), and Pile driving formulas (i.e. dynamic formulas).

The application of the finite element method to the analysis of piles response to DLTs, including rapid load testing, is summarized and the assumptions and findings of previous studies that addressed this topic are discussed. Finally, the published studies regarding full-field load tests conducted on helical piles are summarized, with a special focus on axial dynamic load testing. This includes a discussion of the findings with regard to evaluation of helical piles response to axial impact loading.

Chapter 2 : Introduction

The wave equation analysis generally utilizes a mathematical model of a system consisting of a hammer, pile and soil. It relates the pile penetration to driving stresses in order to estimate pile capacity and driving resistance (Bostwick, 2014). The Dynamic Load Test provides two sets of measured data: force and acceleration distribution over time. In the analysis process, one of those sets of data is used, and the other is considered as supernumerary information; typically, the acceleration records are considered to provide information on pile capacity (Rausch et al., 1972). The measured force and acceleration records are used in the wave equation analysis.

Pochhammer (1876) derived the formulation of the wave equation for analyzing an infinitely long cylindrical bar with a circular cross-section using stress wave propagation (Valsamos et al., 2013). Subsequently, Cheer (1889), Love (1944), Kolsky (1963), and Graff (1975) investigated the wave propagation in a rod. However, the concept of implementing the wave equation to piles was introduced by Isaacs (1931). The basic form of the stress wave propagation is the classical one-dimensional wave equation illustrated in equation 2.1.

$$E \frac{\partial^2 \omega}{\partial x^2} = \rho \frac{\partial^2 \omega}{\partial t^2} \tag{2.1}$$

In which, ρ is the mass density of the material, E is Young's modulus, ω is displacement, x is axial direction, and t represents the time.

This equation was derived by considering the developed internal forces and motions in a segment of a bar that is subjected to an impact load at one end. In the case of piles, the surrounding soil resistance must be incorporated into equation 2.1 (Bowles, 1996). The wave equation can be solved analytically or numerically. Analytical methods include: separation of variables method, Laplace transform method, or method of characteristics. Numerical approaches have been pioneered by Smith (1960), Bear and Verruijt (1987), Bowles (1996), and Das and Ramana (2011), who provide extensive review of applications of numerical approached to the wave equation analysis.

Isaacs (1931) proposed the adaptation of the one-dimensional wave equation to analyze pile-hammer impact instead of pile-driving formulas to investigate pile driving resistance. An exact solution for Isaacs formulation was proposed by Fox (1932), but was quite complicated, and involved significant assumptions to facilitate the calculations. Smith (1962) proposed a more simplified solution to analyze stresses and displacements for a pile under impact by dividing the pile into a series of lumped masses, typically one meter each, in which the elastic and the inertial properties of each discretized lumped are represented by springs and masses. Figure 2-1 depicts the spring-mass model suggested by Smith; in which, W, K, and K' represent the lumped weight, internal spring (static resistance), external spring or dashpot (dynamic resistance), respectively. Smith modelled the static resistance by using the elastic-plastic spring and the dynamic resistance by a linear viscous

dashpot. In general, the computation process of the stresses at each lumped mass starts by assuming an ultimate capacity and define the characteristics and distribution of the springs and the dashpots along the pile shaft and toe. The velocities and the displacements due to the hammer struck at the top of the pile are then determined. The process is repeated for successive time intervals until all lumped masses converge to their maximum downward movement or the pile tip starts to rebound. Finally, a variety of ultimate capacities are examined by the wave equation until achieving the best-fitted bearing graph that relates the measured forces to the calculated forces. According to Reese et al. (2006), the wave equation analysis provides reliable and rational results of pile capacity.

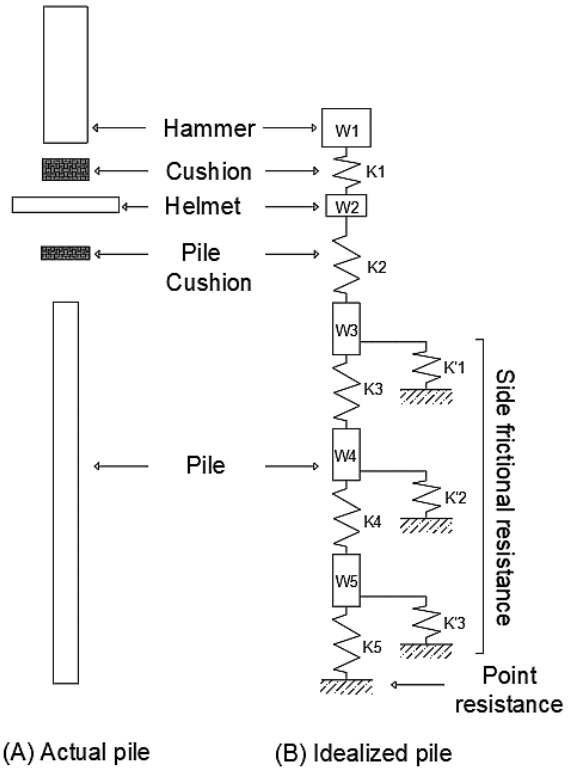

Figure 2- 1: Problem idealization of pile-soil system for wave equation analysis after smith (1962).

2.1. Longitudinal Elastic Waves in A Bar

To illustrate the basic wave mechanics concept, consider an elastic bar with a uniform section and properties that are identical throughout the bar, which is suddenly struck with a load, F. The impact generates a compression wave that travels to adjacent parts of the rod toward the end with a constant speed, C. If there is no outside resistance, the

compression wave that has been induced at the top is reflected with the same magnitude and shape as a tension wave at the end of the bar. The developed stresses at the section where the compression and the tension waves cross each other are therefore zero, and the magnitude of particles velocity is doubled. This is true only if the bar is free to move at the end. In the instance of a fixed end bar, two opposite and equal compression waves are developed at the end; hence, the stress magnitude at the section of interference will be doubled and the velocity of the particles will be zero. Figure 2-2 illustrates these wave mechanics. The reason for this phenomenon is that the compression wave and the velocity of the particles are in the same direction, while the tension wave and the velocity of the particles are in the opposite direction (Das, & Ramana 2011). However, the frictional resistance of the soil will interfere; therefore, it must be taken into consideration. Typically, the soil resistance is incorporated into the system using springs and dashpots, as mentioned earlier.

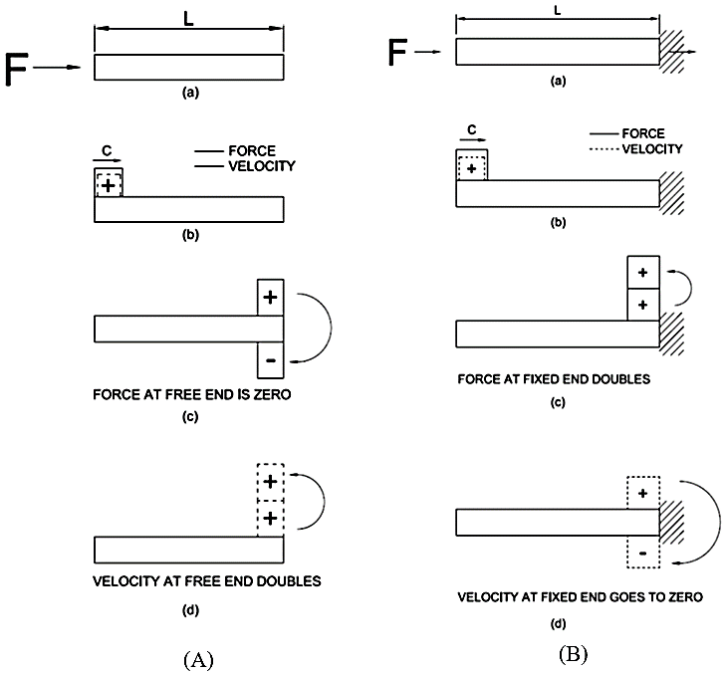

Figure 2- 2: Wave mechanics at (A) free end bar and (B) fix end bar.

It is important to distinguish between the velocity of the propagated wave and the velocity of the particles in the stressed section of the bar. The wave propagation velocity depends exclusively on the material properties; whereas the particle velocity depends on the intensity of the applied stress (Das, & Ramana 2011). In case of compression stresses, both

velocities act in the same direction. On the other hand, if tensile stresses are developed, the two velocities act on opposite directions. Also, at any point along a uniform elastic bar, the wave speed remains constant, and the velocity of the particles is proportional to the force developed at the same point (Green & Kightley, 2005).

2.2. Elastic Waves in a Pile and Static Capacity

The estimation of pile load-carrying capacity historically relied on judgment established from empirical driving formulas or by conducting a SLT. The emergence of computer programs that utilize the wave equation method has permitted a more reasonable estimation of axial pile capacity at a faster rate. The input parameters for the wave equation analysis are usually straightforward, as it only requires the properties of the pile and soil as well as the characteristics of the driving system. The basis of applying this to pile response during impact load is described below.

When a pile is instantaneously subjected to an axial transient load at its head, the impact induces deformation that spreads progressively with time throughout the pile via stress waves (Das, & Ramana 2011). The propagated waves travel to successive zones of the pile at a constant speed. When the wave reaches the toe, its amplitude reduces due to the soil resistance along the pile shaft (i.e. static and dynamic forces) and based on the soil resistance at the toe, the generated reflected waves could be either tensile or compression waves. Initially, the hammer impact generates compression waves, and if the pile toe is located in a relatively soft soil, the reflected waves change its condition from compression to tension waves. On the other hand, if the pile toe is driven into a stiff soil or rock stratum, compression waves will be doubled at the reflected point (Bear & Verruijt, 1987; and Hertlein & Davis, 2009). Those reflected waves are recorded and used in the estimation of the total resistances, consisting of static resistance and dynamic resistance, of the soil experienced by the pile shaft and toe (Green & Kightley, 2005).

To further understand the influence of soil resistance on the force and velocity records, consider a pile with embedment length, L, placed in a soil that offers a minor resistance at depth 1 and a major resistance at depth 2, and no resistance between depth 1 and 2 or beyond. When this pile is subjected to an axial impact load, F, the measured force and velocity waves (in force unit) will be similar to the one shown in Figure 2-3. The first

portion of the two curves is proportional until the wave reaches to depth 1. At this instant, the force and velocity curves deviate from each other due to the soil resistances, i.e., an increase in the force record and a decline in the velocity record. It can be observed that the separation is not significant; thus, it is considered to be a minor effect. Again, from depth 1 and 2, there is no significant resistance from the soil; hence, force and velocity records remain parallel over time. At depth 2, a substantial increase in the force record and a decrease in the velocity can be observed, which indicates a significant soil-resistant is encountered. Finally, at the time where the waves arrived at the pile toe, the velocity records increase, and a reduction of the force will take place. This implies that the pile toe does not provide any resistance, in other words the pile capacity is only derived from skin friction.

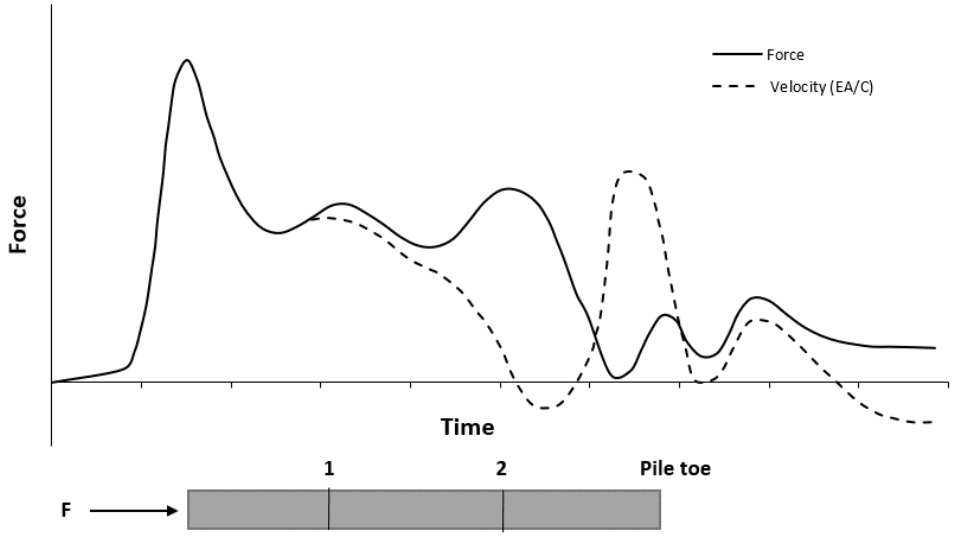

Figure 2- 3: The influence of soil resistance on the force and velocity records measured at the pile top.

The soil resistance measured by the method discussed above is the total resistance of the soil along the pile shaft and toe that consists of both static and dynamic resistances. Further analysis is needed to isolate the dynamic response from total resistance (Green & Kightley, 2005). The CAse Pile Wave Analysis Program (CAPWAP) performs such separation and provides an insight into the characteristics of the load-displacement behavior of the pile (Rausche et al., 2000).

2.3. Soil Parameters Used in Wave Equation Analysis

Three sets of soil-data are required to initiate the analysis by the wave equation: soil ultimate resistant (R_u), quake (Q), and soil damping (J).

2.3.1. Soil Ultimate Resistant (R_u)

It is necessary to determine the ultimate resistance of the soil along the pile shaft and at its toe either by assumption or from the soil strength parameters if known. A typical procedure to solve this issue is to estimate the static shaft capacity and base resistance from the given soil properties or assigning presumed values such as those suggested by Forehand and Reese (1964) that are based on soil type and shaft to base resistance ratio (Poulos & Davis, 1980).

Table 2- 1: Allocation of soil resistance to the shaft and the base of a pile in wave equation analysis as proposed by Forehand and Reese (1964).

Soil type	Side resistant (as a % of R_u)	Note
Coarse sand	35	
Mix of sand and gravel	75 to 100	
Fine sand	100	
Send and clay	25	50% or more pf the pile is penetrated in sand
Silt and fine sand	40	Hard stratum exists at the pile toe
Sand and gravel	25	Hard stratum exists at the pile toe

2.3.2. Soil Quake (Q) and Soli Damping (J)

The movement of the pile toe during the elastic behavior of the soil is denoted a soil "quake" (Smith, 1962). It represents the maximum elastic deformation of a soil at the maximum elastic force. Samson (1963) suggested the quake value ranges from 1.27 mm to 3.81 mm, while Chellis (1951) suggested a value of 2.54 mm. To accurately estimate the quake value for any soil, a full-scale pile test should be conducted. Moreover, the soil resistance along the pile shaft, in reality, will change gradually with depth, increasing to a

maximum value at the pile end compared to the recommended empirical data by Chellis (1951), which is assumed to have constant resistance over the whole pile length.

The soil damping parameter is used to describe the dynamic behavior and represents the additional forces developed within the soil, which is proportional to the loading velocity. Smith considered two values for soil damping: one for the pile tip, and the other for the side friction of the pile. Due to the remolding effect, the damping constant (J) is predominantly concentrated around the pile toe; therefore, it is determined based on the soil type at the pile toe (Goble et al., 1975). For saturated Ottawa sand, the damping value ranges between 0.05 to 0.2 compared to dry sand, which approaches zero (Smith, 1962; Forehand and Reese, 1963; Samson, 1963). Forehand and Reese indicated that the damping constant could be between 0.4 to 1 for cohesive soil.

Lowery (1993) suggested the values presented in Table 2-2 for soil damping and quake. However, these values should be used with care and only when more accurate data is not available. These values are assumed initially, then iteratively modified through the implementation of the CAse Pile Wave Analysis Program (CAPWAP). Soil damping values will commonly follow the guidelines mentioned in Rausche et al. (1985) or in the PDA (1996) manual and are correlated well with dynamic load tests (Vaidya, 2004).

Table 2- 2: Soil damping and quake characteristics after Lowery (1993).

Soil type	Side damping (friction) [sec/ft]	Point Damping (bearing) [sec/ft]	Quake [in.]
Sand	0.05	0.15	0.1
Silt	0.1	0.15	0.1
Clay	0.2	0.01	0.1

Table 2- 3: CASE damping values for different types of soil after Halder (2016).

Soil type	Soil damping constant	
	(PDI, 1996)	*(Rausche et al, 1985)*
Clay	0.7 or higher	0.6 to 1.1
Silty Clay	0.4 to 0.7	0.4 to 0.7
Silts	0.25 to 0.4	0.2 to 0.45
Silty Sand	0.15 to 0.25	0.15 to 0.3
Sand	0.1 to 0.15	0.05 to 0.2

2.4. Axial Load Testing of Piles

Pile load testing to confirm design capacity is an integral part of a proper design process (Poulos, 1998). It can be accomplished by static or dynamic methods. The classification of testing methods is determined based on three factors; the imposed longitudinal wave velocity, pile length, and the impact force duration (Holeyman, 1992). These factors are used to compute wave number, relative wavelength, or relative duration to determine the type of loading for the pile load test method (Holeyman, 1992; Middendorp et al., 1995; Karkee et al., 1997), as can be seen in Figure 2-4.

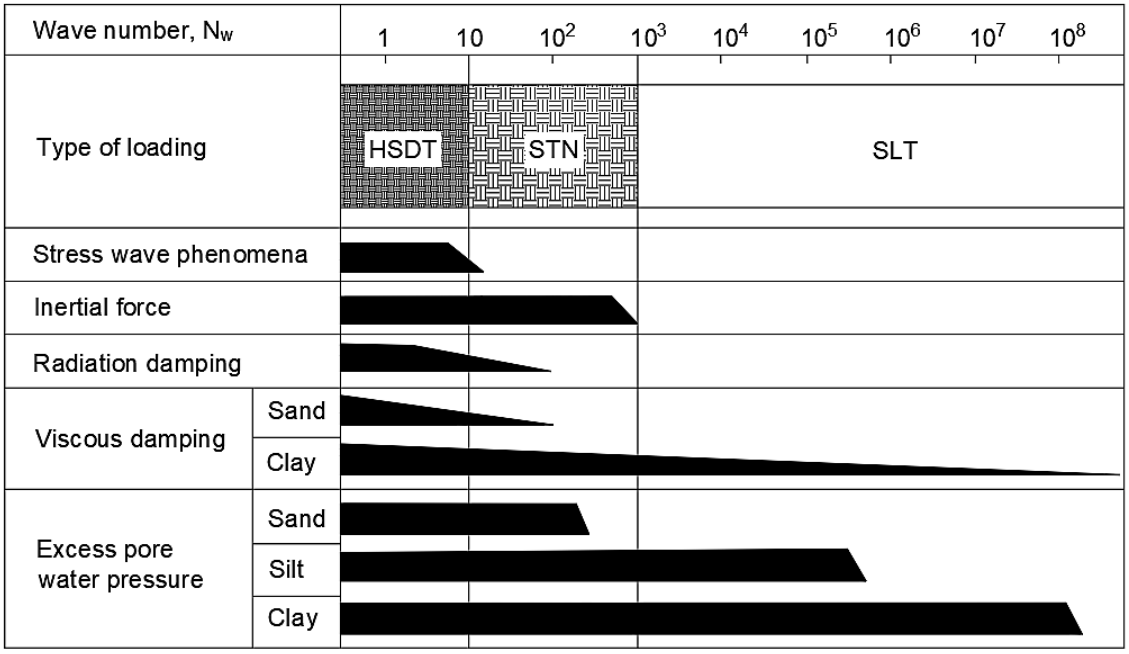

Figure 2- 4: Classification of pile load test methods after Holeyman (1992).

A review of pile load tests is presented below and organized with the following aspects:

1. General definitions and testing procedures;
2. Load application methods;
3. Data acquisition and interpretation methods.

2.4.1. Static Load Test (SLT)

The Static Load Test is the most common technique to accurately determine pile capacity. The objective of the SLT is to investigate the load-deformation behavior of a pile in order

to confirm that the pile can sustain the expected forces. The test standard procedures and guidelines are specified by the standard ASTM D1143 (ASTM, 2013) which allows for several SLT procedures to be conducted on piles. These procedures are the Quick Test, the Maintained Test, the Loading in Excess of Maintained Test, the Constant Time Interval Test, the Constant Rate of Penetration Test, the Constant Movement Increment Test, and the Cyclic Loading Test. The major difference among these procedures is the manner in which the load is applied and the time of application.

Generally, several piles are installed around the tested pile to act as reaction piles. A rigid beam is mounted crosswise on the tested pile and securely connected to the reaction piles. The applied loads are then transmitted to the pile through a large-capacity jack placed between the rigid beam and the tested pile. The loads are recorded using a load cell, and the corresponding vertical displacements are measured by dial gauges. Figure 2-5 depicts a schematic set-up for the SLT. A plot of vertical pile loads against vertical pile head displacements is generated, which is then used to determine the ultimate load capacity of the tested pile using a suitable criterion. Commonly, the ultimate load capacity is taken as the point where the settlement increases significantly with a small increase of applied load (plunging failure). Alternatively, it may be taken as the load corresponding to a prescribed settlement value, for instance, 25 mm. Some building codes specify a required procedure to follow in the estimation of the ultimate pile capacity from pile load tests. The most widely adopted method in North America is the Davisson Offset Limit (Davisson, 1972), and it is commonly used in practice (Das, 2010).

The SLT is a reliable and feasible for piles with low or moderate in capacity. However, for piles with high capacity, it is requires building a large reaction system to execute the test appropriately, which is very expensive. In this case, dynamic load tests are commonly employed with a minimum cost to estimate the pile capacities.

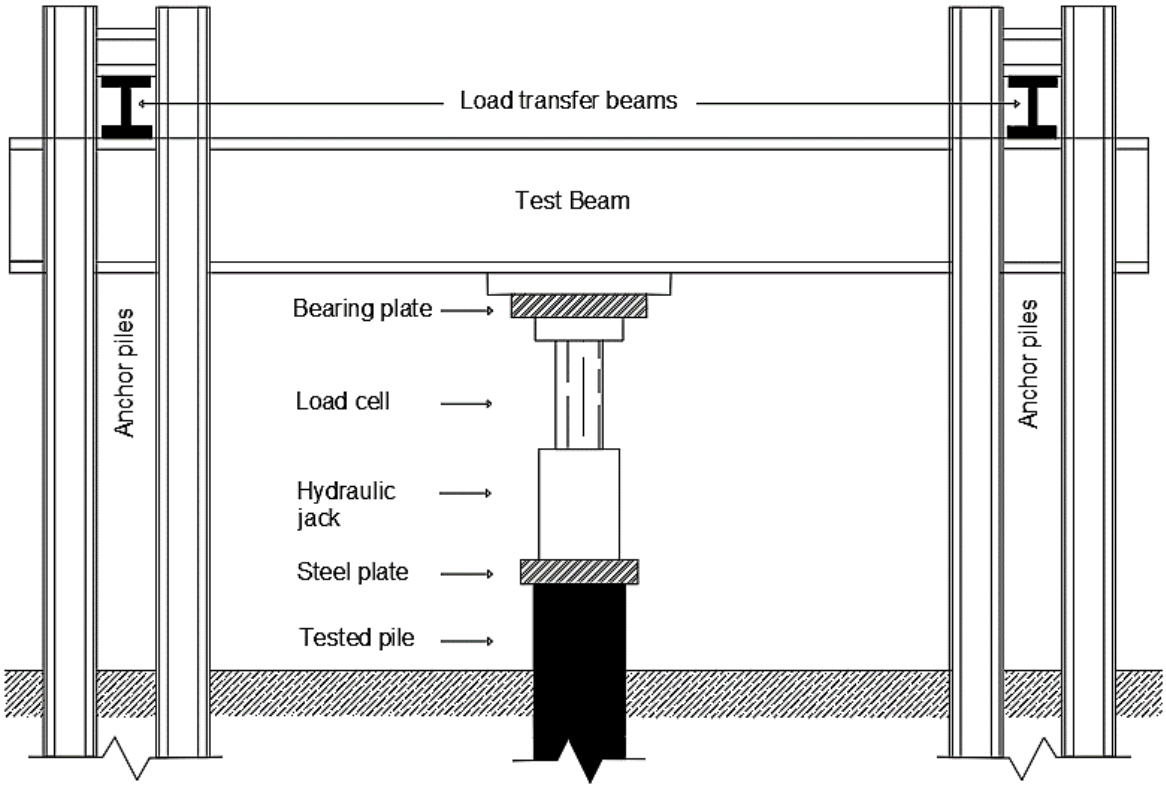

Figure 2- 5: Schematic view of the Static load test after ASTM (2013).

2.4.2. Dynamic Testing of Piles Via Impact Loading

The pile dynamic load test (DLT) via an impact load is an alternative to the SLT for predicting pile behavior. It requires comprehensive knowledge of wave propagation, soil mechanics, and understanding of input and output parameters to provide good predictions of pile capacity. When performing the DLT, a pile is subjected to a compressive force by means of dropping a hammer or a reaction mass. The subsequent strain and acceleration responses at the pile top could be measured by the Pile Driving Analyzer (PDA). A pair of strain gauges and accelerometers are affixed at the pile head. A schematic diagram of the test apparatus is shown in Figure 2-6. The test is specified under the standard designation ASTM D4945, which stipulates several procedures to perform the test. The applied impact load must have the ability to initiate a force capable of causing the pile to move sufficiently or can make the resistance of the pile to be fully mobilized. A verity of standard testing procedures and methods for interpretation of data have emerged. Dynamic testing of piles could be performed for a variety of reasons, including:

1. To determine the static pile capacity and to establish a load-settlement curve with relatively cheap cost and quick implementation. Several piles can be tested over a short period compared to the SLT.
2. To estimate the maximum kinetic energy delivered from a hammer and its rating for energy output.
3. To determine the maximum axial compression stresses for driving purposes.
4. To investigate pile integrity and structural defects.

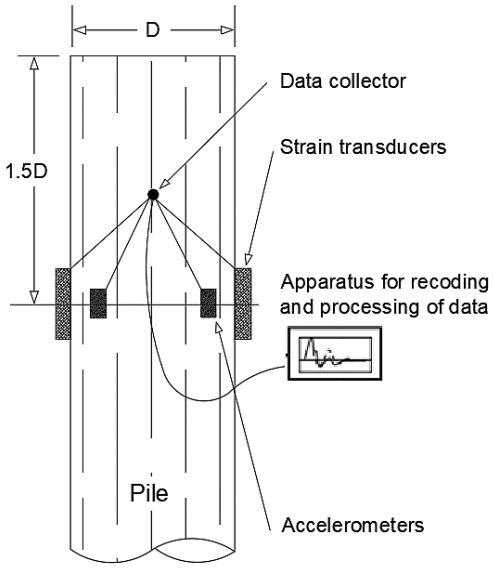

Figure 2- 6: Schematic diagram for dynamic mentoring of deep foundations after ASTM (2013).

Interpretation of the DLT results is accomplished either from using direct or indirect approaches. In the direct approach, the analysis is applied to the measured data obtained from a single load impact where a simple soil-pile model is considered to estimate pile capacity (Hertlein & Davis, 2006). The Case Method adapted by the PDA is an example of the direct approach. The indirect approach utilizes a signal matching software such as CAPWAP, TNOWAVE (TNO, 1996) and SIMBAT (Borgman et al., 1993) to perform the analysis on the measured data obtained from the impact of one or multiple blows. The Case method and the CAPWAP method are mostly applied to analyze dynamic measurements in practice, and both are developed based on one-dimensional wave propagation theory (Halder, 2016).

2.4.3. Types of Dynamic Testing

In general, there are three types of testing available: Quasi-Static test, High Strain Dynamic Test (HSDT), and Rapid load test.

2.4.3.1. Quasi-Static testing method

In this test, the impact force is applied for a relatively long period by dropping a weight or a heavy hammer, generally last for about 100 to 250 milliseconds (Lewis, 1999). According to Middendorp et al. (1992), the falling mass should have a weight between 5% to 10% of the expected capacity of the tested pile. The Quasi-Static testing method is also known as the Pseudo-Static pile load test (Gonin et al., 1984; & Schellingerhout et al., 1996). The STATNAMIC (Janes et al., 1991) test uses a reaction mass instead of a falling mass.

2.4.3.2. High Strain Dynamic Test (HSDT)

If the impact load duration is between 5 and 20 milliseconds, the test is no longer considered as a Quasi-Static test; instead, it is considered a High Strain Dynamic Test (HSDT). For decades, HSDT has been utilized in the field to investigate the bearing capacity of deep foundations in both onshore and offshore industries. It is accomplished by a dropping weight of about 1% to 2% of the ultimate pile capacity (Holeyman, 1992). After conducting the test, the resultant measurements per blow is analyzed using a pile dynamic formula to evaluate the pile capacity. However, this solution has a low dependability, and its results vary by a significant margin (Hannigan et al., 1996). There are two possible ways to conduct the test, either at the End Of Driving (EOD) or at the Beginning Of Re-Strike (BOR). Because of soil set-up and relaxation phenomena, the latter is usually implemented for accuracy in the installed pile after an adequate time has been passed.

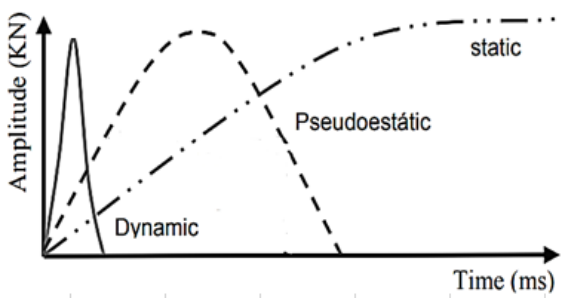

Figure 2- 7: Comparison between different types of pile load testing.

2.4.3.3. Rapid Load Test (STATNAMIC)

This method is derived based on Newton's second and third laws of motion. The test has been standardized by ASTM, under the designation D7383 – 10. According to ASTM, there are two procedures to execute the test: Procedure (A) utilizes a combustion gas pressure gear to initiate a force pulse; and Procedure (B) where a dropped mass with a soft cushion is used to replace the gas apparatus. Figure 2-8 shows the typical components and setup of this testing method. The STATNAMIC has been categorized as a test that is longer than the HSDT and faster than the SLT in terms of loading duration. The analysis of the test results can be simplified by combining the analysis of static and dynamic tests with relatively lower cost but at similar efficiency (Hannigan et al. 2006).

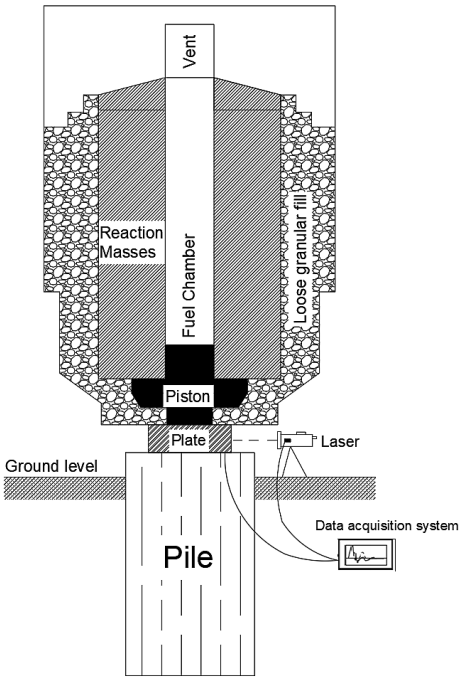

Figure 2- 8: Rapid Load Test (TN) component and setup after Briaud et al. (2000).

Since the rapid load test generates an acceleration of the complete pile mass, Middendorp et al. (1992), Kato et al. (1998,) and Deeks and Randolph (1993) proposed the use of a concentrated mass model to analyze the measured data. Later, Nishimura et al. (1995), Ochiai et al. (1997), Van Foeken et al. (2000) confirmed the eligibility of the wave propagation analysis in interpreting the result of the rapid load test. El Naggar and Baldinelli (2000) interpreted the STATNAMIC load test data by adopting an automatic signal matching technique (AMT). In this method, the pile-soil model parameters are

adjusted within specified ranges until an acceptable agreement is achieved between the measured and the computed response. El Naggar & Baldinelli (2000) demonstrated the applicability of the approach by analyzing STATNAMIC tests on six piles to determine their capacity and static load-displacement relationship.

2.4.4. Characteristics of Pile Load Tests

The purpose of pile load tests is to determine the performance of a pile when subjected to a working load. SLT provides the most reliable and accurate result, but it is time consuming could be costly. On the other hand, DLT is faster and cheaper than the SLT, and it gives a reasonable estimate of the pile capacity. Thus, the testing technique should be selected with due consideration of the size of the project, the number of piles to be tested, available time, cost, and regulations. Table 2-4 summarizes the major characteristics of different pile load tests (Holscher & Van, 2008).

Table 2- 4: Characteristic of pile load tests after Holscher & Van (2008).

Characteristic	**Type of test**		
	Dynamic	*Rapid*	*Static*
Load duration	7 milliseconds	100 milliseconds	16 hours
Tested piles per set	8	2	1
Dropped weight or reaction mass size (as a % of the pile ultimate capacity)	1% to 2%	5% to 10%	100% to 200%
Time for the interpretation of data	4 hours	10 minutes	Directly
Piles exhibit tension stresses	Probable	No	No
Testing Prefabricated piles and screw piles	Yes	Yes	Yes
Stress experienced by the soil	Static and Dynamic	Static and Dynamic	Only dynamic
Pore-water pressure in sand	Occurs	Occurs	Absent
Reliability	Reasonable	Yet, unclear	Most reliable

2.4.5. Reliability of Dynamic Load Tests

The reliability of HSDT as a pile load testing method and as a means of estimating static pile capacity has been rigorously investigated through comparisons between static and dynamic tests (Likins, 2004). Many researchers reported good agreement between pile ultimate axial capacity obtained from the SLT and DLT (Likins & Rausche, 2004: Vaidya, 2006; Long et al., 2009; Basarkar et al., 2011; and Rajagopal et al., 2012). The reliability of the test lies mainly on the input parameters and engineer's experience. Inappropriate pile-soil model results in inaccurate results and cannot represent the actual soil response. Therefore, a proper procedure of data inspection and software application is required to check the outcomes before a final judgment is made.

2.4.6. Pile Movement Versus Developed Capacity

The load required to sufficiently move the pile and mobilize the soil resistance is essential in dynamic load tests. Das (2008) indicates that the pile shaft resistance is fully mobilized when the pile moves 5 to 10 mm irrespective of its size or length, while the tip capacity will be mobilized when the pile has displaced approximately 10 to 25% of its diameter. Figure 2-9 elaborates on this mechanism graphically. Generally, a penetration equal to the elastic deflection is considered sufficient enough to mobilize the shaft resistance in contrast to the tip resistance which needs a considerably higher downward movement (Crowther, 1988). Brom (1978) stated that soil type and pile diameter influence the full development of shaft and toe resistance. He noted that small diameter piles reached its maximum tip resistance at a lower pile movement compared to large diameter piles; and piles installed in clay exhibit reduced shearing resistance compared to sand after reaching the maximum value. The Federal Highway Administration (FHWA) stipulates that the failure load for drilled piles corresponds to a total settlement equal to 5% of the diameter (Neill & Reese, 1999). Livneh and El Naggar (2008) had defined that the failure load for helical piles occurred when the movement of the pile exceeded the elastic deformation plus 8% of the largest helix diameter if more than one is affixed to the central shaft.

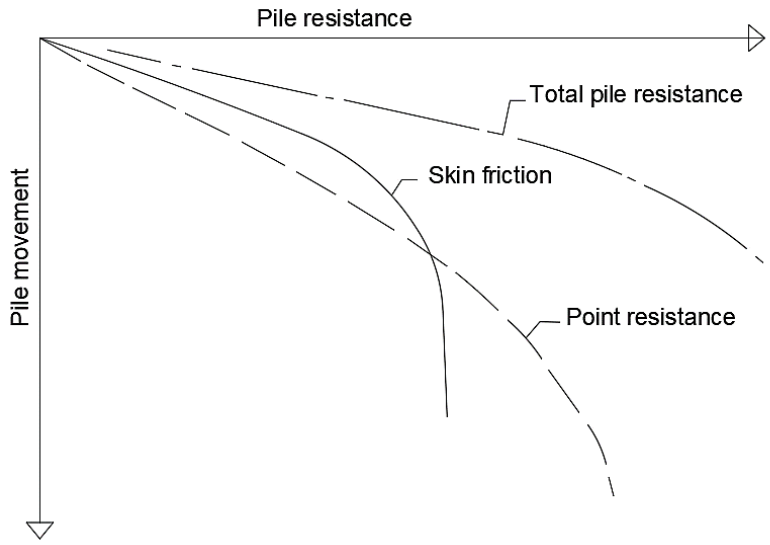

Figure 2- 9: Relative pile movement in relation to soil after Brom (1978).

2.4.7. Static Capacity of Axially Loaded Piles Based on Dynamic Measurements

Two basic methods are available to estimate the static capacity of piles based on dynamic measurements: pile driving formulas and the wave equation. The former methods are formulated based on the work done during pile driving installation, while the latter is based on the propagation of compression stress wave throughout the pile. A brief coverage of those methods is presented herein.

2.4.7.1. Pile Driving Formulas (Dynamic Formulas)

Dynamic formulas are used to predict pile capacity during driving and are commonly adopted since the early 1900s (Likins et al. 2012). The formulas were developed based on penetration per hammer blow and potential energy equilibrium. They relate the energy transformed from the collision of a hammer at the pile head to a specific displacement of the soil (Long et al. 2009). In addition, these formulas can correlate the results obtained from an impact of a hammer to the pile's static capacity by assuming that the load capacity under normal static loads is equivalent to the driving resistance (Salgado, 2017). A set of equations formulated either empirically or theoretically through the years with a varying degree of reliability are available in the literature, some of which are presented in Table 2-5. Bowles (1996) and Long et al. (2009) provide detailed discussion of these equations.

The reliability of pile driving formulas varies significantly; nevertheless, engineers in practice implement those formulas because of their simplicity and fast application in pile design. In some cases, the factor of safety in pile design employing pile driving formulas are far from the accepted values or may lead to excessive settlement beyond the tolerable values. Extreme caution and practical experience are required to overcome such defects. Long et al. (1999) conducted a study to compare the predicted capacity by dynamic formulas and measured capacity by SLT. They concluded that relatively old methods were less accurate with a considerable discrepancy compared to the more sophisticated modern methods, in consistence with Terzaghi (1943).

Table 2- 5: List of dynamic formulas.

Name of the formula	Equation	Remarks
Modified Engineering News Formula (EN)	$Q_u = \frac{e_h E_h}{s + c} \frac{W + n^2 w}{W + w}$	c is 1.0 for drop hammers or 0.1 for steam hammers.
The Gates Formula	$Q_u = \left(\frac{6}{7}\right) \sqrt{e_h E_r} \log(10 N_b)$	e_h is considered as 75% for drop hammers and 85% for all others.
The FHWA Gates formula	$Q_u = 1.75 \sqrt{E_d} \log(10 N_b) - 100$	Reduced the tendency to underestimate capacity
Janbu	$Q_u = \frac{e_h E_h}{K_u s}$ $C_d = 0.25 + 0.15 \frac{w}{W}$ $K_u = C_d \left(1 + \sqrt{1 + \frac{\lambda}{C_d}}\right)$ $\lambda = \frac{e_h E_h L}{A E s^2}$	

Symbols in formula equations: Q_u = predicted pile capacity. e_h = hammer efficiency; E_h, E_d, and E_r = manufacturer's hammer energy, developed hammer energy, and theoretical delivered energy, respectively. s = observed pile set. W = weight of the ram (in kN). w = weight of the pile (in kN). L = pile length. A = pile's cross-sectional area. E = Young's modulus of the pile material. N_b = number of blows per one unit of pile penetration.

The limitations of pile driving formulas are:

1. Soil and pile types are not considered in the existing equations, and their reliability in predicting pile capacity is questionable (Salgado, 2017).

2. They do not address the hammer-soil model accurately due to neglecting test accessories such as pile cap, and cushion. The equations do not actually account for soil parameters in the calculation (Long et al. 2009).
3. The pile is assumed to be rigid, overlooking the axial stiffness of the pile during driving (Hannigan et al. 1998).
4. They do not accurately reflect the true dynamic response of piles and do not have the capability of predicting stresses generated in piles (Lowery, 1993).
5. They are empirical and their accuracy varies considerably (El Naggar & Novak, 1992).
6. They do not compute compressive and tensile stresses and have a lower representation of the hammer-pile-soil system (Edde, 1991).

To overcome these limitations, the pile capacity is estimated from dynamic test methods by accommodating the wave equation concept in which the compression stress wave in a pile is examined rather than the potential energy equilibrium and pile penetration concept.

2.4.7.2. Pile Driving Analyzer (PDA)

The Pile Driving Analyzer (PDA) is used with the High Strain Dynamic Test. It comprises a computer-based program for data acquisition and analysis at the field utilizing a simple procedure defined following the Case method (Goble et al., 1970). It has been developed and implemented in design and monitoring of piles by Globes (1964). This system has been extensively employed along with the HSDT and pile integrity tests. The PDA can evaluate the bearing capacity of piles, assess pile integrity, calculate driving stresses, and determine hammer performance. It also offers a real-time display of measured signals, calculation of results, and provides more options that can be viewed instantaneously.

The analog strain and acceleration signals are converted by the PDA into force and velocity records plotted against time. Then, a fundamental dynamic model (e.g. Case model) is used to estimate static pile capacity. Alternative versions of Case methods were developed but yield different pile static capacity values for the same pile (Long et al., 2009). Nevertheless, this procedure is considered as preliminary field results and further analysis is required to

determine the static capacity of the test pile. The signal matching program (CAPWAP) is applied for such an analysis to correlate the dynamic to static capacity result.

The minimum number of sensors required by the PDA are four; two strain gauges and two accelerometers. The two accelerometers data are typically compared with each other in order to verify the eligibility of the measured data. The PDA gives the data in curve formats, and if the velocity curves obtained from the two accelerometers are in close proximity to each other or coincide, the data is reliable and can be accepted. Also, the force curves should not be significantly reduced below the x-axis at the end of the recording period nor significantly higher than the x-axis as this could indicate either sensors are mounted wrongly or due to damage of pile head (Likins et al., 2000; and Vaidya 2004). Likins et al. (2000) further explained the proportionality of the resultant curves between force and velocity. They indicated that the first portion of the two curves should approximately coincide. No proportionality may reveal that pile material is of poor quality, particularly for concrete piles, or sensor location is not appropriately selected. In addition, the non-uniformity of the pile section will cause the two curves to be diverted; consequently, a non-perfectly match will be observed (Likins et al., 2000).

2.4.7.3. The Case Method

The Case method employs a closed-form solution to assess the pile capacity based on the travelling wave (Hertlein & Davis, 2007). It is implemented widely with HSDT because it offers simple calculation formula. The pile is assumed to be uniform and deform elastically, and the soil is considered to behave as a perfectly plastic medium (Paikowsky, 2002). The resistance is divided into two components static and dynamic. The dynamic resistance is derived from the pile bottom velocity and a damping coefficient, which must be subtracted from the total resistance to obtain the pile static axial capacity (Yan et al., 2011). Three main factors need to be investigated prior to making a final judgment regarding the predicted resistance of the pile-soil model: the soil resistance and sensitivity and the damping coefficient (Paikowsky, 2002). An appropriate value of damping coefficient is selected based on the soil type at the pile toe. It is suggested to conduct a site-specific test to confirm the selected values or to appropriately determine new values.

2.4.7.4. Case Pile Wave Analysis Program (CAPWAP)

The CAPWAP is a computer program developed in 1970. It executes the analysis based on the concept of stress wave propagation with signal matching techniques to find a reasonable solution that includes both total and static soil resistance, damping coefficients, and soil stiffnesses. The unknown variables are iteratively calculated by tracing either the measured travelling wave or force and velocity measurement. Several data are needed to correctly initiate the calculation process and reasonably predict pile capacity. These data are the pile-soil model (similar to Smith' model) and the strain and acceleration obtained from the PDA. Other dynamic properties, for instance, soil quack, damping coefficient, and soil resistance, are calculated within the program once the analysis is in progress. Several studies have indicated that CAPWAP analysis results are in a good agreement with SLT (Likins & Rausche, 2004; and Green & Kightley, 2005).

2.5. Numerical Modelling of Dynamic Pile Load Tests

There are two main numerical methods for the analysis of pile response to impact loading: the continuum approach or the Winkler based model. In the Winkler model, the pile is discretized into segments while the soil is treated as a series of springs and dashpots to simulate its static and dynamic response. The Winkler approach has been widely used, and its suitability to predict load-deflection behavior of the pile-soil model has been proven (Smith, 1960; Nogami & Konagai 1987; El Naggar & Novak, 1992, 1994; Long et al., 2009). No further discussion will be made relating to this method since it is well documented in the literature. Instead, a concentration toward the finite element analysis method will be considered in the succeeding sections.

2.5.1. Finite Element Modelling (FEM) of Pile Load Tests

The pile-soil model in finite element analysis is discretized into several elements connected by nodes with given properties. The interface between the pile and the soil, energy dissipation, nonlinear behavior of the soil, and boundaries can be easily considered in FEM. The numerical analysis is usually performed along with real filed data to understand the pile-soil behavior and to improve the interpretation of the results through modifications or correlations. The FEM has provided a reasonable solution to many complicated situations

in simulating pile load tests; nevertheless, more precise analysis is required to account for various test variables (Krasiński & Wiszniewski, 2017). Moreover, limited information is available concerning modelling pile dynamic load tests and its associated computation in the literature.

2.5.2. Comparison of Signal Matching Analysis and FEM

Several studies investigated the dynamic response of piles subjected to an axial impulse load and simulated soil conditions accurately by adopting continuum analysis (Nath, 1990; Mabsout and Tassoulas, 1994). Similarly, Liao and Rosset (1997) and Mahutka et al. (2006) used one-dimensional (1D) wave equation model (based on Smith's (1960)) and a three-dimensional (3D) FEM to investigate the dynamic response of piles exposed to an axial impulse load. All have reported generally good agreement between results obtained from the 1D wave equation and 3D FEM analyses. However, these studies have not compared their finding with actual load tests, and mostly focused on damping issues in numerical modelling. Feizee (2008) conducted FEM for an actual pile driven in sandy deposits. He adjusted the soil parameters in order to match the recorded data provided by the PDA. Initially, the measured and the computed forces at the pile toe differed. He then adjusted the elastic modulus of the soil layer at the toe and achieved a good match.

Fakharian et al. (2014) carried out a comparative study between the results obtained from CAPWAP signal matching analysis on two conditions, EOD and BOR, and the results from finite difference and finite element analyses. Eight concrete piles were driven and dynamically tested by using the PDA. The numerical analyses were performed by FLAC-2D and Plaxis 2D. Non-linear axisymmetric condition was adopted in all analyses, and the soil was modeled as an elastic perfectly plastic material with Mohr-Coulomb criterion. Undrained and drained soil parameters were considered for EOD and BOR, respectively. The results of their study regarding the BOR condition were successful. The predicted load-deformation behavior of the piles using continuum models were close enough to the SLT, and it can be accomplished using conventional soil parameters, unlike the Winkler based models. Moreover, Fakharian et al. confirmed the work of Feizee (2008) concerning the increase of the elastic modulus at the base layer to enable a good correlation between measured and computed force waves.

Naveen et al. (2014) performed FEM simulation using Plaxis 2D to establish the load-deflection curve for piles in residual soil and compared it against the load-deflection curve derived from the CAPWAP. The soil medium consisted of two clay layers, underlain by a soft-weathered rock. The top layer behaved was simulated by Mohr-Coulomb criterion while the bottom layer was modelled using the soil hardening model. An axisymmetric model with 15-nodes triangular elements was established. The pile-soil interface was modelled as an elastic-plastic condition. The bottom boundary was fixed while the side boundaries were modeled as a roller, permitting only vertical movements. Their results showed good agreement between the load-displacement curves obtained from the CAPWAP and Plaxis 2D. They recommended further study to investigate different aspects of the dynamic load tests used for predicting the ultimate pile capacity.

2.5.3. Analysis of Piles Subjected to STATNAMIC Test

Matsumoto (1998) utilized a finite element model to explain the characteristic of soil deformation and the behavior of an open-ended steel pile during a STATNAMIC load test. The calculated responses were comparable to the observed behavior during the actual test. Horikoshi et al. (1998) also modelled the STATNAMIC test using finite element considering the soil to be linearly elastic, and the pile-soil interaction is modelled using joint elements to represent the slip failure mechanism. They established a reduction factor that allowed the soil to undergo very high strain. Their analysis involved the following steps: determining soil properties through field and laboratory testing; evaluating shear modulus from pre-existing P-S wave log or a seismic cone penetration test; applying a reduction factor to reduce the pre-used shear modulus and repeat the analysis until an agreement between the measured and the calculated pile response is achieved. Bakker et al. (2000), Huy (2010) and Bak (2013) investigated the suitability of 2D and 3D modelling of pile load tests and they concluded their suitability.

Van & Boonyatee (2014) suggested that FEM is more suitable the analysis of STATNAMIC load test on driven piles than the unloading point method (UPM) suggested by Middendorp et al. (1992). However, they cautioned that damping constant should be similar to the value estimated from the UPM, velocity and acceleration measurement should be reduced to 80% if the peak of the rapid load was less than the calculated

maximum static capacity of the pile, and an additional soil mass should also be considered in the UPM to account for the soil movement around the pile (Van & Boonyatee, 2014). They considered damping values of 0.65 and 0.50 form shaft and toe, and soil quake was presumed to be 2.54 mm.

2.6. Axial Load Testing on Helical Piles

Helical piles are used for rehabilitation of existing structures and supporting new ones. With the advent of powerful drive heads, helical piles of large diameter have become a viable option for supporting heavy axial loads in many geotechnical applications. This requires ascertaining their load carrying capacity. This section discusses axial load tests performed on helical piles including both static and dynamic with the focus on the latter, and identifies the gap in the literature concerning evaluating the response of helical piles to dynamic load tests.

2.6.1. Overview

A helical pile is made of one or more helical bearing plates affixed to a circular or squared shaft as shown in Figure 2-10. Helical piles are installed using a rotary hydraulic head that generates a torque force capable of pushing the pile into the ground. They could be installed at various depths and angles with proper design of the pile section and using a suitable drive head (Elsherbiny & El Naggar, 2013). Helical piles industry has been growing exponentially in the last decades due the fast installation process and efficient use of material to maximize the pile capacity (Perko, 2009).

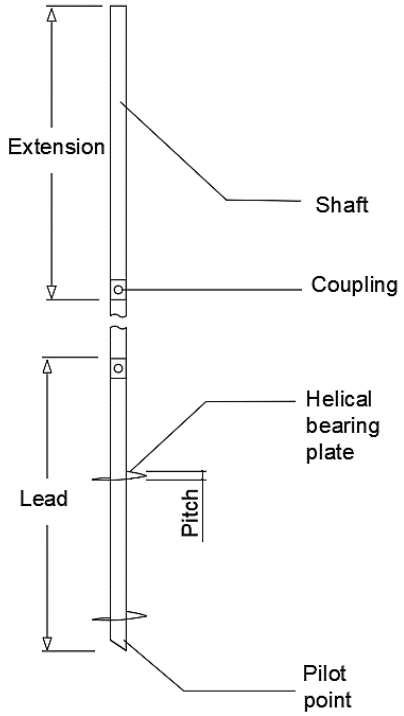

Figure 2- 10: Basic helical pile component after Perko (2009).

The axial static capacity of helical piles has been the subject of several investigations (Zhang, 1999; Perko, 2000; Tappenden, 2007; Sakr, 2009; Elsherbiny and El Naggar, 2013; Gavin et al., 2014). The static capacity is determined by considering two recognized methods: the cylindrical shear method or the individual plate bearing method. The application of either method depends on the spacing to helix diameter ratio. For instance, the helix acts independently if the spacing between them compared to their diameter is large, and vice versa. Figure 2-11 illustrates the failure mechanisms considered in these methods.

The axial capacity based on cylindrical shear method is derived from the bearing resistance offered by the bottom helix and friction resistance along the cylinder formed in-between the helixes, plus shaft friction above the top helix. For the individual plate bearing method, the static resistance is established based on shear stresses along the shaft and the pressure developed on the underside of each helix, which is assumed to be uniform. A detailed formulation and design process for the cylindrical shear method and the individual plate

bearing method for both piles installed in sand and clay is discussed by Elsherbiny and El Naggar (2013).

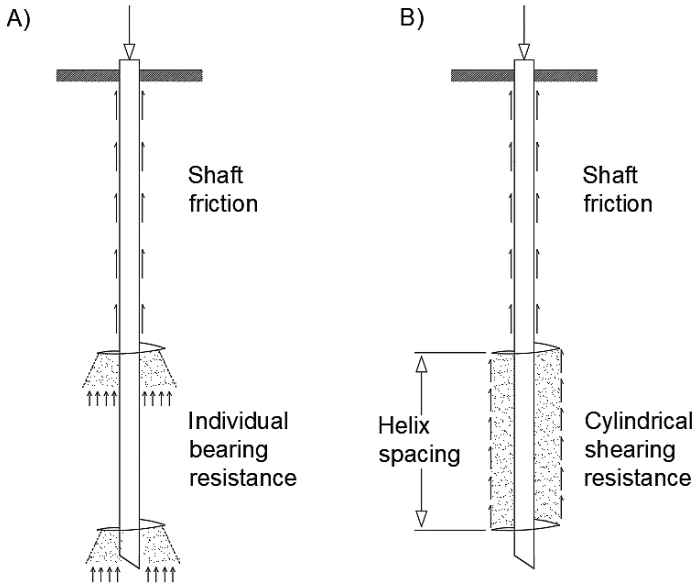

Figure 2- 11, Failure mechanism of helical piles; (A) individual plate bearing method, and (B) cylindrical shear method.

The axial compression capacity of helical piles is commonly estimated using empirical correlations referred to as Capacity to Torque Correlations (CTC). The approach relies mainly on measuring the applied torque during installation to verify the helical pile static capacity employing the CTC. This approach allows prediction of pile capacity immediately during installation and provides a means for quality control of pile installation (Livneh and El Naggar, 2008). However, the accuracy of CTC in predicting pile capacity is affected by the number and spacing of helices, the existence of hard stratum, and pore water pressure generation during installation (Perko, 2009).

The standard SLT and loading procedures for helical piles are same as other piles, and it is usually performed in accordance with ASTM D1143 / D1143M. Results of full-scale loading test conducted on helical piles installed in both sand and clay are widely reported in the literature (e.g. Zhang, 1999; El Naggar, 2004; Livneh & El Naggar, 2008; Beim & Luna, 2012, Harnish & El Naggar, 2017).

2.6.2. Helical Piles Response to Impact Loading

SLT for large diameter helical piles could requires significant time, and in some cases, would be prohibitively expensive. Thus, dynamic load testing is growing in popularity for large capacity helical piles. The available information regarding dynamic load testing of helical piles is limited to date compared to driven piles. The application of dynamic load tests on helical piles was first investigated by Cannon (2000), who reported several projects where the pile capacity is evaluated from the HSDT along with PDA and CAPWAP analysis. HSDT were successfully applied on a range of helical pile size and depth installed in various ground conditions. He reported that for small shaft diameter, the test is limited by the shaft stresses or the yield strength of the steel instead of the geotechnical pile capacity. In these situations, the test has been terminated due to the high dynamic stresses developed in the shaft prior to reaching the ultimate pile capacity. Additionally, the geotechnical resistance could not be mobilized even with large permanent sets. Cannon suggested that the helix should not be modelled in the CAPWAP analysis because the stress waves at the location of the helix undergoes a quick rise on the shaft impedance over a small segment for a short instant. However, the point resistance offered by the helix must be modelled with a low stiffness (Cannon, 2000).

Beim & Luna (2012) conducted HSDT on helical piles with three helices installed in clay using a dropping hammer. The load was applied with few blows using 1.34 kN hammer released from a height of 0.9 m. The PDA with the Case method was utilized to collect force and acceleration data and to perform the analysis. They also used the CAPWAP based only on the highest energy delivered by the blows. The soil static and dynamic parameters were established based on the analysis results. In order to obtain a good match between the load-displacement curve originated from SLT and the curve computed from the CAPWAP, a radiation damping model was adopted as suggested by Likins et al. (1996). They reported that the pile capacity interpreted by the Davisson criterion from SLT results agreed well with the results obtained from HSDT. Nevertheless, the HSDT results were overly conservative owing to the insufficiency of the applied set per blow, i.e. applied energy was not enough to fully mobilize the capacity. Accordingly, failure loads determined from SLT were much higher than the values derived from the HSDT using the CAPWAP analysis.

Consequently, Beim & Luna recommended a minimum set per blow of 2.5 mm or more should be achieved. However, they modelled the pile as a uniform rod and ignored the increase in the impedance induced by the helices. Moreover, they used a reduction damping model for the shaft resistance and slacks at the joint between segments in the modelling process in order to obtain results that match the static load results. These assumptions may work for the soil at the studied site but certainly not for all soils. Therefore, more investigations are needed to establish at least a broader solution to accumulate various types of soil conditions.

Benjamin White (GLE engineering, Inc.) performed HSDT on a helical pile with double helices installed in sand underlain by stiff to hard clay. He derived load-deflection curves for the measured velocity and force data resulting from several hammer impacts. The overall curve was established based on tracing the corresponding set of each curve generated from multiple impacts, unlike Beim & Luna (2012) study where the helical pile capacity was considered to be mostly from shaft resistance, and only the highest energy impact was analyzed. The main findings from this study were;

1. The load-settlement curves derived from HSDT corresponded well with the anticipated results based on the theoretical calculations.
2. All principles and limitations of dynamic load test applied to driven or drilled piles are applicable to helical piles.
3. If the impact produces a small permanent set (less than 2.5 mm), it is possible that the resistance of the soil was not fully mobilized; therefore, the estimated capacity should be considered as a lower bound.
4. Duration of impact may have a significant effect on the results. Its effect can be observed only if two tests are conducted with two impact durations.

Sakr (2013) conducted a comparison study between the axial load-bearing behavior of helical piles in cohesive soil obtained using both HSDT and SLT. The HSDT was performed on helical piles with a single and double helix. In the measured HSDT data, the force and the velocity impedance coincided at the beginning and then diverged similarly to the commonly noticed behavior in driven piles. However, a significant deviation has been observed between velocity records and force-time history around the toe, with an evident second peak on the velocity records. He attributed this behavior to the reflected waves

caused by the helix. Sakr (2013) reported that the load-displacement curves obtained from CAPWAP analysis agreed well with those originated from the SLT. Finally, he reported that the calculated soil quakes for the shaft were similar to the values provided by the CAPWAP same as proposed for driven piles. For the base quake, however, the calculated values were significantly higher than the computed values using CAPWAP analyses compared to driven piles. This was attributed to the large end-bearing of the helical pile not being fully mobilized.

2.6.3. Shortcomings of Preceding Studies

All previous studies demonstrated that HSDT is a suitable tool for evaluating the static capacity of helical piles. However, this observation was based on a limited number of test data. Consequently, a more comprehensive examination of a larger database is required to strongly confirm and support this observation and to establish a set of parameters (i.e. soil quake, shaft and toe damping factors, and CAPWAP pile-soil model) explicitly specified for helical piles. In addition, none of the previous studies examined the response of helical piles to an impact load using FEM, nor studied the influence of dynamic load tests on helical piles that consist of different helix sizes and number in the same soil conditions. For instance, the effect of the number of helices on the application of HSDT to helical piles needs to be investigated. Also, most reported researches investigated helical piles installed in cohesive soils, not cohesionless soils. Furthermore, the influence of the helices on the measured dynamic data needs to be carefully evaluated.

Most importantly, there is a need to accurately evaluate how much energy is required to sufficiently displace the helical pile to a position where its capacity has been fully mobilized. Beim & Luna (2012) reported that some helical piles had shown conservative dynamic load test results when compared to static load results because the chosen hammer weight and drop height were not enough to fully mobilize the end-bearing capacity of helical piles. This underscores the need for a methodology for selecting the proper hammer weight and falling height to fully mobilize the pile capacity with compromising its structural integrity.

2.7. References

ASTM. (2013). Standard test method for piles under static axial compressive load.

Bak, E. (2013). Numerical modeling of pile load tests. Pollack Periodica, 8(2): 131-140.

Bakker, K. J., Hoefsloot, F. J. M., & de Jong, E. (2010). Dynamic analysis of large diameter piles Statnamic load test. In Numerical Methods in Geotechnical Engineering. CRC Press. pp. 629-634.

Baldinelli, M. J. (1999). Analysis of the axial response of flexible piles to rapid-loading. [Doctoral thesis]. The University of Western Ontario, London, Canada.

Basarkar, S. S., Kumar, M., & Vaidya, R. (2011). High strain dynamic pile testing practices in india-favourable situations and correlation studies. In Proceedings of Indian Geotechnical Conference Kochi. Paper No. Q-303.

Bear, J., & Verruijt, A. (1987). Theory and applications of transport in porous media. Modeling of Groundwater Flow and Pollution, Dordrecht, Reidel.

Beim, J., & Luna, S. C. (2012). Results of dynamic and static load tests on helical piles in the varved clay of Massachusetts. DFI Journal - the Journal of the Deep Foundations Institute, 6(1): 58-67.

Benjamin W, P. E., & Engineers, G. R. L. (n.d.). High strain dynamic load testing on helical piles–Case Study.

Borgman, L. E., Bartel, W. A., & Shields, D. R. (1993). SIMBAT theoretical manual (No.

NCEL-TR-941). NAVAL CIVIL ENGINEERING LAB PORT HUENEME CA.

Bostwick, D. A. (2014). Calibration of resistance factors for driven piles using static and dynamic tests. [Master thesis]. University of Arkansas, Fayetteville, Arkansas, USA.

Bowles, E. J. (1996). Foundation analysis and design. 5th edition. McGraw-Hill, Inc. New York, USA.

Briaud, J. L., Ballouz, M., & Nasr, G. (2000). Static capacity prediction by dynamic methods for three bored piles. Journal of Geotechnical and Geoenvironmental Engineering, 126(7): 640-649.

Broms, B. (1978). Precast concrete piles. Balken Piling System and Royal Institute of Technology. Sweden.

Cannon, J. G. (2000). The application of high strain dynamic pile testing to screwed steel piles. In Sixth International Conference on the Application of Stress-Wave Theory to Piles. pp. 11-13.

Chellis, R. (1951). Pile foundations: theory, design, practice. McGraw-Hill, Inc. New York.

Crowther, C. (1988). Load testing of deep foundations: the planning, design, and conduct of pile load tests. Wiley, Inc. Hoboken, New Jersey, USA.

Das, B. M. (2010). Principles of foundation engineering. Cengage Learning, Inc. Boston, Massachusetts, USA.

Das, B., Ramana, G.V. (2010). Principles of soil dynamics. Cengage Learning, Inc. Boston, Massachusetts, USA. ISBN: 0495411345.

Edde, R. D. (1991). Case pile wave equation analysis: CAPWAPC evaluation of driven piles. [Master thesis]. University of Ottawa, Ottawa, Canada.

EL Naggar M.H., (2004). Evaluation of SSI75 helical screw foundation system. Technical Report, University of Western Ontario, London, Canada.

El Naggar, M. E., & Novák, M. (1992). Analytical model for an innovative pile test. Canadian Geotechnical Journal, 29(4): 569-579.

El Naggar, M. H., & Baldinelli, M. J. (2000). Interpretation of axial Statnamic load test using an automatic signal matching technique. Canadian Geotechnical Journal, 37(5): 927-942.

Elsherbiny, Z. H., & El Naggar, M. H. (2013). Axial compressive capacity of helical piles from field tests and numerical study. Canadian Geotechnical Journal, 50(12): 1191-1203.

Fakharian, K., Masouleh, S. F., & Mohammadlou, A. S. (2014). Comparison of end-of-drive and restrike signal matching analysis for a real case using continuum numerical modelling. Soils and Foundations, 54(2): 155-167.

Feizee, S. (2008). Evaluation of design parameters of pile using dynamic testing and analyses. [Doctoral thesis]. Amir Kabir University of Technology, Tehran, Iran.

Fellenius, B. H., & Tech, P. (2001). What capacity value to choose from the results a static loading test. The Newsletter of the Deep Foundations Institute, Ottawa, Canada.

Forehand, P. W., & Reese, J. L. (1963). Pile driving analysis using the wave equation. [Doctoral thesis]. Princeton University, Princeton, USA.

Forehand, P. W., & Reese, J. L. (1964). Prediction of pile capacity by the wave equation. Journal of the Soil Mechanics and Foundations Division, ASCE, 90(2): 1-26.

Gavin, K., Doherty, P., & Tolooiyan, A. (2014). Field investigation of the axial resistance of helical piles in dense sand. Canadian Geotechnical Journal, 51(11): 1343-1354.

Goble, G. G., Likens, G. and Rausche, F. (1975). Bearing capacity of piles from dynamic Measurements - final report DOT-05-75. Ohio Department of Transportation. Ohio, USA.

Goble, G. G., Likens, G., and Rausche, F. (1970). Dynamic studies on the bearing capacity of piles - phase iii, report no. 48. Division of Solid Mechanics, Structures, and Mechanical Design. Case Western Reserve University. Cleveland, USA.

Gonin, H., Coelus, G. & Leonard, M. (1984). Theory and performance of a new dynamic. Method of Pile Testing, Proceeding 2nd International Conference: Application of Stress-Wave Theory to Piles. Stockholm, Balkema Rotterdam, NL. pp. 403-410.

Green, T. A. L., & Kightley, M. L. (2005). CAPWAP testing-theory and application. In Proceedings of the International Conference on Soil Mechanics and Geotechnical Engineering. AA BALKEMA Publishers, 16(4): pp. 2115-2118.

Halder, A. K. (2016). Pile load capacity using static and dynamic load test. [Master thesis]. Bangladesh University of Engineering and Technology, Dhaka, Bangladesh.

Hannigan, P. J. (1990). Dynamic monitoring and analysis of pile foundation installations. Deep Foundations Institute Short Course. pp. 69-75.

Hannigan, P. J., Goble, G. G., Thendean, G., Likins, G. E., & Rausche, F. (1997). Design and construction of driven pile foundations. Department of Transportation, Federal Highway Administration, USA. Vol. 1 and 2.

Hannigan, P. J., Goble, G. G., Thendean, G., Likins, G. E., and Rausche, F. (1998). Design and construction of driven pile foundations: workshop manual. Department of Transportation, Federal Highway Administration, USA. Vol. 2.

Hannigan, P.J., (1990). Dynamic monitoring and analysis of pile foundation installations. Deep Foundation Institute, 99 1-69.

Harnish, J. & El Naggar, M.H. 2017. Large- diameter helical pile capacity torque correlations. Canadian Geotechnical Journal, Vol. 54, No. 7, pp. 968-986.

Hertlein, B., & Davis, A. (2007). Nondestructive testing of deep foundations. John Wiley & Sons. Wiley, Inc. Hoboken, New Jersey, USA.

Holeyman, A.E. (1992). Keynote lecture: technology of pile dynamic testing. Proceeding 4th International Conference: Application of Stress-Wave Theory to Piles. The Hague. pp. 195-216.

Holscher, P., & Van Tol, F. A. (2008). Rapid load testing on piles. CRC Press. Boca Raton, Florida, USA.

Horikoshi, K., Kato, K., & Matsumoto, T. (1998). Finite element analysis of Statnamic loading test of pile. In Proceeding 2nd International Statnamic Seminar. pp. 295-302.

Huy, N. Q. (2010). Literature review Quasi-static and Dynamic pile load tests: primarily report on non-static pile load tests. TU Delft Publications.

Janes, M. C., Horvath, R. C., & Bermingham, P. D. (1991). An innovative dynamic test method for piles. International Conferences on Recent Advances in Geotechnical Earthquake Engineering and Soil Dynamics. pp. 253-261.

Krasiński, A., & Wiszniewski, M. (2017). Static load test on instrumented pile–field data and numerical simulations. Studia Geotechnica et Mechanica, 39(3): 17-25.

Liao, S. T., & Roesset, J. M. (1997). Dynamic response of intact piles to impulse loads. International Journal for Numerical and Analytical Methods in Geomechanics, 21(4): 255-275.

Likins, G, Rausche, F. (2004). Correlation of CAPWAP with Static Load Tests. Proceedings of the Seventh International Conference on the Application of Stress wave Theory to Piles. Petaling Jaya, Selangor, Malaysia. pp. 153-165.

Likins, G. E., & Rausche, F. (2004). Correlation of CAPWAP with static load tests. Proceedings of the Seventh International Conference on the Application of Stress-wave Theory to Piles. pp. 153-165.

Likins, G. E., Fellenius, B. H., & Holtz, R. D. (2012). Pile driving formulas: past and present. In Full-Scale Testing and Foundation Design: Honoring Bengt H. Fellenius. pp. 737-753.

Likins, G. E., Rausche, F., & Goble, G. G. (2000). High strain dynamic pile testing, equipment and practice. Proceedings of the Sixth International Conference on the Application of Stress-wave Theory to Piles. pp. 327-333.

Livneh, B., & El Naggar, M. H. (2008). Axial testing and numerical modeling of square shaft helical piles under compressive and tensile loading. Canadian Geotechnical Journal, 45(8): 1142-1155.

Long, J. H., Hendrix, J., & Jaromin, D. (2009). Comparison of five different methods for determining pile bearing capacities - report No. WisDOT 0092-07-04. Wisconsin Highway Research Program. Wisconsin, USA.

Long, J., Bozkurt, D., Kerrigan, J., & Wysockey, M. (1999). Value of methods for predicting axial pile capacity. Transportation Research Record: Journal of the Transportation Research Board. pp. 57-63.

Lowery, L. (1993). Pile driving analysis by the wave equation. Wild West Software. Bryan, Texas, USA.

Mabsout, M. E., & Tassoulas, J. L. (1994). A finite element model for the simulation of pile driving. International Journal for Numerical Methods in Engineering, 37(2): 257-278.

Mahutka, K. P., König, F., & Grabe, J. (2006). Numerical modelling of pile jacking, driving and vibratory driving. In Proceedings of International Conference on Numerical Simulation of Construction Processes in Geotechnical Engineering for Urban Environment. Bochum, Balkema, Rotterdam. pp. 235-246.

Matsumoto, T. (1998). TEM analysis of Statnamic test on open-ended steel pipe pile. 2nd International Statnamic Conference. Tokyo, Japan.

McVay, M. C., Birgisson, B., Zhang, L., Perez, A., & Putcha, S. (2000). Load and resistance factor design (LRFD) for driven piles using dynamic methods - A Florida perspective. Geotechnical Testing Journal, 23(1): 55-66.

Middendorp, P., Bermingham, P.D. & Kuiper, B. (1992). STATNAMIC load testing of foundation piles. Processes 4th International Conference: Application of stress-wave theory to piles. The Hague. pp. 581-588.

Nath, B. (1990). A continuum method of pile driving analysis: comparison with the wave equation method. Computers and Geotechnics, 10(4): 265-285.

Naveen, B. P., Parthasarathy, C. R., & Sitharam, T. G. (2014). Numerical modeling of pile load test. Conference: 4th China International Piling and Deep Foundations Summit. Vo. 1. Shanghai, China.

Nogami, T. and Konagai, K. (1987). Dynamic response of vertically loaded nonlinear pile foundations. Journal of Geotechnical Engineering, ASCE. Vol. 113: 147-160.

O'Neil, M. W., & Reese, L. C. (1999). Drilled shafts: construction procedures and design methods. Department of Transportation, Federal Highway Administration. USA.

Paikowsky, S. (2018). Drop weight dynamic testing of drilled deep foundations.

Paikowsky, S. G. (2002). Load and Resistance Factor Design (LRFD) for dynamic analysis of deep foundations. In Proceedings of the International Conference on Soil Mechanics and Geotechnical Engineering. AA BALKEMA Publishers, Vol. 2: 981-984.

PDA Manual. (1996). Pile Dynamics, Inc., model PAK. Cleveland, Ohio, USA.

Perko, H. A. (2000). Energy method for predicting installation torque of helical foundations and anchors. In New Technological and Design Developments in Deep Foundations. pp. 342-352.

Perko, H. A. (2009). Helical piles: a practical guide to design and installation. John Wiley & Sons, Inc. Hoboken, New Jersey, USA.

Poulos, H. G., & Davis, E. H. (1980). Pile foundation analysis and design.

Poulos, H.G. (1998). Keynote lecture: pile testing-from the designer's viewpoint. In Proceedings 2nd International STATNAMIC Seminar. Tokyo, Japan. pp. 3-21.

Rajagopal, C., Solanki, C. H., & Tandel, Y. K. (2012). Comparison of static and dynamic load test of pile. Electronic Journal of Geotechnical Engineering. Vol. 17: 1905-1914.

Rausch, F., Moses, F., & Goble, G. G. (1972). Soil resistance predictions from pile dynamics. Journal of the Soil Mechanics and Foundations Division, 98(9): 917-937.

Rausche, F., Goble, G.G. &Likins, G.E. (1985). Dynamic determination of pile capacity. Journal of Geotechnical Engineering, ASCE. Vol. 111: 367-383.

Reese, L. C., Isenhower, W. M., & Wang, S. T. (2006). Analysis and design of shallow and deep foundations. Wiley, Inc. Hoboken, New Jersey, USA.

Rinaldi, V. A., & Viguera, R. (2013). Pseudo-static pile load test: experience on pre-bored and large diameter piles. Proceedings of the 18th International Conference on Soil Mechanics and Geotechnical Engineering. Paris, France. pp. 2847-2850.

Sakr, M. (2009). Performance of helical piles in oil sand. Canadian Geotechnical Journal, 46(9): 1046-1061.

Sakr, M. (2013). Comparison between high strain dynamic and static load tests of helical piles in cohesive soils. Soil Dynamics and Earthquake Engineering, 54: 20-30.

Salgado, R., Zhang, Y., Abou-Jaoude, G., Loukidis, D., & Bisht, V. (2017). Pile driving formulas based on pile wave equation analyses. Computers and Geotechnics, Vol. 81: 307-321.

Samson, C. H., Hirsch, T. J., & Lowery, L. L. (1963). Computer study of dynamic behavior of piling. Journal of The Structural Division, ASCE, 89(4): 413-450.

Schellingerhout, A.J.G. & Revoort, E. (1996). Pseudo static pile load tester, Proceedings 5th International Conference: Application of Stress-Wave Theory to Piles. Florida, USA.

Smith, E. A. (1962). Pile-driving analysis by the wave equation. American Society of Civil Engineers Transactions.

Tappenden, K. M. (2007). Predicting the axial capacity of screw piles installed in western Canadian soils. [Doctoral thesis]. University of Alberta, Edmonton, Canada.

TNO report. (1996). TNO-DLT Dynamic Load Testing Signal Matching, User's Manual.

Vaidya, R. (2004). Low strain integrity and high strain dynamic testing of piles an Indian overview. Proceedings of the 7th International Conference on the Application of Stress Wave Theory to Piles. Kuala Lumpur, Malaysia.

Vaidya, R. (2006). Introduction to high strain dynamic pile testing and reliability studies in southern India. In Proceedings of Indian Geotechnical Conference. Chennai, India. pp. 901-904.

Valsamosa, G., Casadeia, F., and Solomos, G. (2013). A numerical study of wave dispersion curves in cylindrical rods with circular cross-section. Applied and Computational Mechanics. Vol. 7: 99-114.

Van, D. L., & Boonyatee, T. (2014). Finite element analysis of rapid load testing on a driven pile. Conference paper: The Twenty-Seventh KKHTCNN Symposium on Civil Engineering. Shanghai, China. pp. 9-12.

Yan, Q., Song, F., & Wang, Y. (2011). CASE method to ascertain the accurate evaluation of the ultimate bearing capacity of pile. In 2011 International Conference on Electric Technology and Civil Engineering. pp. 6487-6492.

Yu, Y. W. (2009). Pile driving analysis via dynamic loading test. pp. 1-173.

Zhang, D. J. Y. (1999). Predicting capacity of helical screw piles in Alberta soils. [Master thesis]. ProQuest Dissertations Publishing.

CHAPTER THREE

ANALYTICAL MODELLING OF IMPACT FORCE-TIME RESPONSE GENERATED FROM HIGH STRAIN DYNAMIC LOAD TEST ON DRIVEN AND HELICAL PILES

Chapter 3 : Introduction

Pile load testing is used to determine pile capacity and provides quality control of installation (Poulos, 1998). It can be accomplished by static or dynamic loading methods. The Static Load Test (SLT) is the most common technique to accurately determine the pile capacity, but it is time consuming, and for large capacity piles, could be prohibitively expensive. Alternatively, the pile could be tested dynamically via an impact load at its head, which offers faster implementation and potentially reduced cost. In general, there are three types of testing available: High Strain Dynamic Test (HSDT), Quasi-Static testing methods and Rapid load test.

In HSDT, a pile is subjected to an axial compressive force by means of dropping a hammer or a reaction mass. The subsequent strain and acceleration responses at the pile top are measured employing a pair of strain gauges and accelerometers affixed at the pile head. The HSDT is designated by American Society for Testing and Materials (ASTM) as D4945 (ASTM, 2013). This standard specifies several procedures to perform the test. In all procedures, the impact mass must have the ability to initiate a force capable of causing the pile to move sufficiently in order to mobilize the pile capacity fully. A verity of testing procedures and methods for interpretation of test data are used in practice.

Interpretation of the dynamic load test can be accomplished using either direct or indirect methods. In the direct approach, the measured data obtained from a single load impact is analyzed employing a simplified soil-pile model to estimate pile capacity (Hertlein & Davis, 2006). Case method (GRL Engineers, Inc., 1997) adopted by the Pile Driving

Analyzer is an example of the direct method. The indirect approach utilizes signal matching software such as CAPWAP (Pile Dynamics, Inc., n.d.), TNOWAVE (TNO, 1996), and SIMBAT (Borgman et al., 1993) to perform the analysis on the measured data due to the impact of one or multiple blows. The CAPWAP method is mostly applied to analyze displacement piles in practice and is developed based on the one-dimensional wave propagation theory (Halder, 2016).

The HSDT is widely used to investigate the load carrying capacity of piles. In this method, the impact force is maintained for a duration of about 5 to 20 milliseconds and is accomplished by a dropping weight of about 1% to 2% of the ultimate pile capacity (Holeyman, 1992). The test is conducted at the end of driving (EOD), or at beginning of re-strike (BOR). Because of soil set-up and relaxation phenomena, the latter is usually implemented for accuracy (Hussein, 1993). After conducting the test, the measured set per blow is substituted in a dynamic pile formula to calculate the pile capacity. However, this solution may not be reliable and the estimated pile capacity may vary by a significant margin (Hannigan et al., 1996).

Likins and Rausche (2004) summarized several studies that investigated the HSDT as a means for estimating static pile capacity and confirmed its reliability. In addition, several researchers reported a good agreement between the pile capacity values obtained from the SLT and HSDT (Vaidya, 2006; Long et al., 2009; Basarkar et al., 2011 and Rajagopal et al., 2012). However, the reliability of the interpretation of the test data relies mainly on the input parameters and engineer's experience. Therefore, a proper procedure for data inspection and software application is required to check the outcomes before a final judgment is made.

Typically, the SLT and torque-capacity correlations are adapted to determine the helical pile capacity. Nevertheless, the SLT is costly and time consuming, and torque-capacity correlations are empirical and approximate at best. Therefore, dynamic load testing on the helical pile is becoming a viable alternative to the SLT. However, the available information regarding the application of dynamic load test on helical piles is limited. A few studies have demonstrated that the dynamic load test could be a suitable tool to evaluate the static capacity of helical piles (Cannon, 2000; Beim & Luna, 2012; and Sakr, 2013). However,

this finding was derived based on a limited number of tests involving limited configurations of helical piles and using interpretation methods that were established for driven and drilled piles. Therefore, a more comprehensive examination is required to ascertain suitability of dynamic load testing to helical piles, and to explore the characteristics of hammer impact on helical piles, evaluate the effect of helices on the pile mechanical impedance and establish the necessary parameters for appropriate models to interpret HSDT on helical piles.

A mathematical model developed by Deeks and Randolph (1993), denoted here as the D-R model, is employed to analytically predict the force-time response at the head of a pile during the HSDT. The model considers a hammer, a cushion and a pile. The applicability of D-R model to HSDT is verified employing seven case studies involving driven and bored piles subjected to dynamic load tests using the PDA. The model is employed to explore the characteristics of hammer impact on helical piles and is modified to account for the increase in pile impedance caused by the helices.

3.1. Basic Definitions

When a falling mass strikes a pile, a compression wave is induced at the pile head. This compression wave propagates through the pile with a constant wave speed, C, which depends on the pile material properties and can be calculated by:

$$C = \sqrt{\frac{E}{\rho}} \tag{3.1}$$

In which, E and ρ are the elastic modulus density of pile material.

As the wave travels, the pile is compressed causing a downward movement of the particles along the pile length with particles velocity, V. The particle motion causes pile compression, v, over a time interval, Δt, and a distance, Δl; resulting in strain, ϵ, in the pile compressed segment, i.e.

$$V = \frac{v}{\Delta t} \tag{3.2}$$

and

$$\epsilon = \frac{v}{\Delta l} \tag{3.3}$$

Substituting equation 3.1 and 3.2 into equation 3.3 and multiplying both sides by E and pile cross-sectional area, A, produces the basic expression of stress wave measurement, i.e.,

$$F = \frac{EA}{C}\, V \tag{3.4}$$

Where, $\frac{EA}{C}$ is the pile mechanical impedance (Kolsky, 1963). Equation 3.4 can be written as:

$$F = \rho C A\, V \tag{3.5}$$

Where, F = Force in the pile and ρCA = pile impedance, referred to as Z.

The pile impedance, Z, is used in analysis of HSDT data to convert the measured velocity records into equivalent forces in order to compare with the measured forces on the same scale. Therefore, it is essential to determine the pile impedance before conducting the HSDT. Considering equation 3.5, the force and the velocity records would coincide as long as the initiated stress wave travels in one direction, which is the case of initial hammer impact. However, the direct proportionality between the force and the velocity does not hold when an upward wave is generated and travels back to the pile head. This occurs when either the pile is embedded into the ground due to soil resistance or when there is a change in the cross-section of the pile.

In addition, available analytical solutions of the hammer-pile system that are used to derive force-time response at the pile head simulate the pile as a dashpot equal to pile's impedance, Z. This is acceptable for a pile with uniform cross-section along its length, which is not valid for helical piles. Thus, it is necessary to investigate the influence of the helices on the pile impedance and measured dynamic data.

3.2. Impact Load-Deformation Characteristic of Cushioning Block

A cushion is frequently placed between the helmet and the pile head when conducting the High Strain Dynamic Test. The pile cushion is used to uniformly distribute the impact load

over the surface of the pile head and to attenuate the impact load such that the introduced stresses do not exceed the specified yield stress of the pile material. The pile cushion is typically softer than the hammer cushion, which will reduce the induced peak force by spreading it over a greater duration. Hence, it is essential to incorporate the effect of cushion in mathematical models that describe impact force time history.

When a hammer collides with a cushion, the load-deformation of cushioning block has a characteristic hysteresis loop as depicted in Figure 3-1. This curve demonstrates energy dissipation within the cushion (in the form of heat). The amount of energy dissipated can be estimated using the coefficient of restitution, e, which is defined as the ratio of the velocity of the hammer after impact to the velocity of the hammer before impact (Hirsch & Hirsch, 1966). To simplify the analysis, the cushion is assumed to have elastic behavior with stiffness, k_s, and its impact load-deformation behavior follows the model proposed by Lowery (1967), i.e., the curve is composed of two straight lines instead of curved lines as shown in Figure 3-1.

For composite cushioning materials, an equivalent stiffness is used. The equivalent stiffness is estimated based on elastic properties of composite cushions using the method proposed by Svinkin (2000). The stiffness of any layer in a composite hammer cushion may be written as;

$$K_{s_i} = \frac{E_i A_i}{t_i} \tag{3.6}$$

Where: E_i, A_i and t_i are the layer elastic modulus, cross-sectional area and thickness, respectively. Thus, for a hammer cushion consisting of stiff and soft layers arranged in a series, the stiffness of the composite hammer cushion, k_s, can be expressed as:

$$k_s = \frac{1}{\frac{t_{stiff}}{E_{stiff}A_{stiff}} + \frac{t_{soft}}{E_{soft}A_{soft}}} \tag{3.7}$$

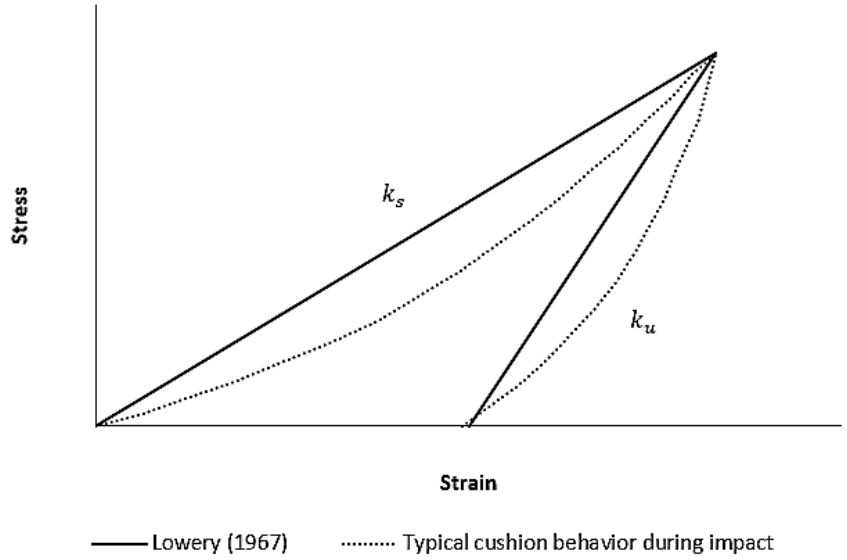

Figure 3- 1: Cushion deformation properties during impact.

3.3. Idealized Hammer-Cushion-Pile Model

The model consists of an infinitely long elastic pile with an elastic cushion and a free-falling hammer, as shown in Figure 3-2. The pile is represented by a dashpot equivalent to its impedance, Z, with a uniform cross-sectional area to capture its response to the impacting mass. Hammer and pile cushions are replaced by an equivalent spring with coefficient k_s. No reflection of the force wave from the pile tip is considered. Thus, the model can be used to determine approximate force-time impact history and peak force generated at the pile head. Furthermore, the cushion is assumed to be under compression and cannot transfer any tension to the pile. Deek and Randolph (1993) stated that if tension stresses are developed in the cushion, the hammer will separate from the pile; hence, the force exerted on the pile at the instant negative force is generated will be set to zero. Solving the differential equation of stress wave in an elastic medium considering the boundary conditions introduced by the continuity of the cushion compression and compatibility of pile head displacements, the equation for the force generated at the pile head can be developed.

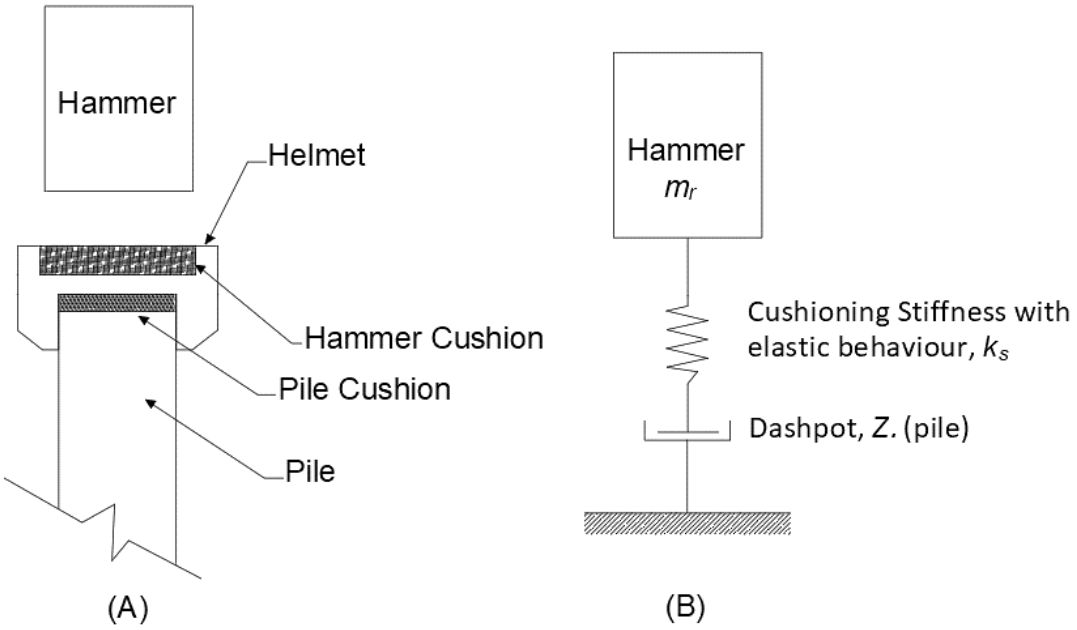

Figure 3- 2: Physical (A), and analytical (B) representation of pile hammer model.

3.4. Formulation of the Analytical D-R Model

The force generated at the hammer-cushion and at pile head-cushion interfaces can be determined considering the diagram shown in Figure 3-3a. Two coordinates, namely v_1 and v_2 , define the displacement position of the hammer and the pile top. The equilibrium of a pile element of length, Δx, is considered as shown in Figure 3-3b and the forces acting at the interfaces between the hammer and cushion as well as the cushion and pile head are given in terms the cushion stiffness, k_s, as shown in the free body diagram presented in Figure 3-3c.

Considering the pile as an infinitely long rod, the compression stress wave generated from the impact will propagate throughout the pile without developing tension waves (i.e. no reflection). The maximum transmitted force will be attained when the kinetic energy of the falling hammer has been fully transmitted to the pile head.

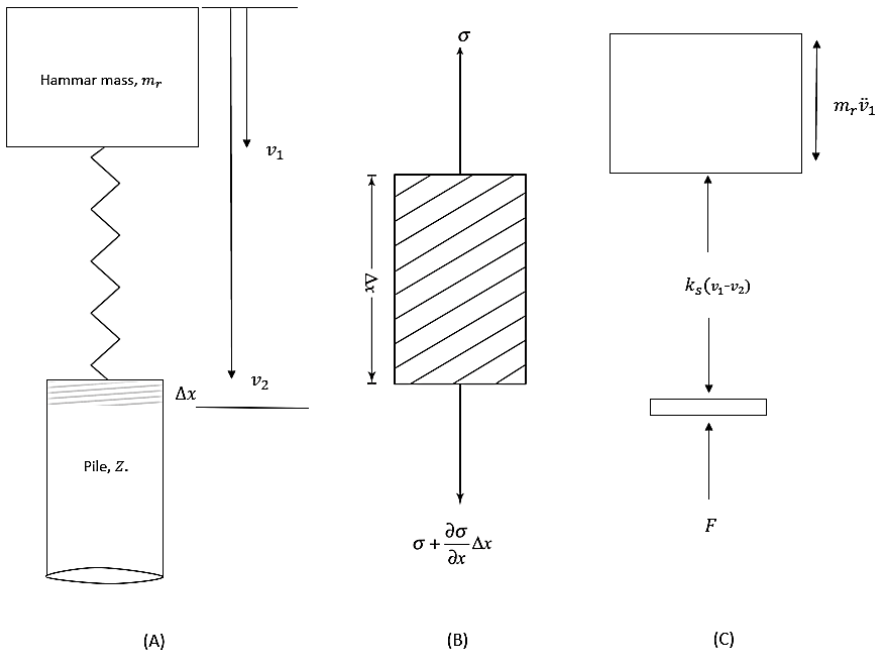

Figure 3- 3: (A) system model; (B) pile element under analysis; (C) free body diagram.

Initially, the dropped weight continues its motion downward after impact to a maximum displacement of the cushion before it either rebounds or remains at its location. If the dropped weight rebounds, the transmitted energy to the pile head would be less than the delivered impact energy due to the loss in the initial kinetic energy. If the dropped weight motion remains downward to a maximum displacement without rebounding, the impact energy will transmit fully to the pile and the maximum force is generated at the pile head. Thus, the pile can be replaced by a dashpot since the radiation energy exerted from the impact is dissipated from the stressed zone – cushion – by the pile. The equation of motion when the hammer strikes the head of the pile is;

$$m_r\ddot{v}_1 + k_s(v_1 - v_2) = 0 \tag{3.8}$$

$$F - k_s(v_1 - v_2) = 0 \tag{3.9}$$

Where, m_r is the mass of the hammer, v_1 the position of the hammer at impact, v_2 is the displacement of the small portion Δx at the pile head, and F is the force generated at the pile head.

The response of hammer-cushion-pile depends on the stiffness of the cushioning material (Deeks and Randolph, 1993). Softer cushion tends to elongate the time of impact and

reduces the peak force transmitted to the pile head compared to a stiffer cushion which tends to shorten the time impact and increases the force at the pile head. Herein, the behavior is assumed to be linearly elastic following the load-displacement curve suggested by Lowery (1967). The idealized dynamic stress-strain curve for any cushion can be easily represented by two stiffnesses; k_s for loading and k_u for unloading, which can be determined experimentally. The former is measured based on a typical secant modulus method whilst the latter is defined based on displacement and the cushion coefficient of restitution. Considering the equilibrium of the upper pile segment of length, Δx, and uniform cross-sectional area of A in the v direction gives:

$$\Sigma F = ma \tag{3.10}$$

$$\left(\sigma + \frac{\partial \sigma}{\partial x}\Delta x\right) A - \sigma A = (\rho A \Delta x).(\frac{\partial^2 v}{\partial t^2})$$

$$\frac{\partial \sigma}{\partial x} = \rho \frac{\partial^2 v}{\partial t^2} \tag{3.11}$$

In which, v is displacement, x is motion direction of the longitudinal elastic wave, and t represents the elapsed time. Since only a compression wave will develop and the pile is behaving elastically, Hooke's law can be applied. Thus, the stress required to compress the segment, Δx, is

$$\sigma = \varepsilon E \tag{3.12}$$

$$\sigma = \frac{\partial v}{\partial x} E \tag{3.13}$$

Differentiate Eq. 3.13 with respect to x:

$$\frac{\partial \sigma}{\partial x} = \frac{\partial^2 v}{\partial x^2} E \tag{3.14}$$

Substituting Eq. 3.14 in Eq. 3.11, yields:

$$\frac{\partial^2 v}{\partial x^2} E = \rho \frac{\partial^2 v}{\partial t^2} \tag{3.15}$$

Equation 3.15 is the one-dimensional wave equation, which is used to calculate internal forces and motions on a segment of a pile to an impact load at one end. The surrounding soil resistance around the pile is neglected since the analysis is made just at the impact;

otherwise, the surrounding soil resistance must be incorporated. The one-dimensional wave equation can be expressed as:

$$\frac{\partial^2 v}{\partial t^2} = \frac{\partial^2 v}{\partial x^2} C^2 \tag{3.16}$$

At an instant time t, the stress wave has moved a distance equal to $(x - Ct)$; therefore, the solution of equation 3.16 is given by some function as follows:

$$v = F\big(g(x)\big) \tag{3.17}$$

$$v = F(x - Ct) \tag{3.18}$$

Applying the chain rule to differentiate the above equations in order to calculate $\frac{\partial v}{\partial t}$.

$$\frac{\partial v}{\partial t} = \frac{\partial v}{\partial x} . \frac{\partial x}{\partial t} \tag{3.19}$$

$$\frac{\partial v}{\partial t} = \frac{\partial v}{\partial x} . (-C) \tag{3.20}$$

Rearranging equation 3.20;

$$\frac{\partial v}{\partial x} = \frac{-1}{C} \frac{\partial v}{\partial t} \tag{3.21}$$

The force generated at the pile head is obtained by substituting equation 3.21 in equation 3.13; so,

$$\frac{F}{A} = E \frac{-1}{C} \frac{\partial v}{\partial t}$$

$$F = -\frac{AE}{C} \frac{\partial v}{\partial t} \tag{3.22}$$

The term $\frac{AE}{C}$ or ρAC is known as the mechanical impedance of the pile (Kolsky, 1963). So, equation 3.22 becomes;

$$F = Z \dot{v}_2 \tag{3.23}$$

In which $\dot{v}_2$is particles velocity at the impact zone (i.e. segment Δx). The velocity of the particles is proportional to the force developed at the same point (Green & Kightley, 2005). Replacing F in equation 3.9 gives;

$$-\rho AC \ \dot{v}_2 + k_s(v_1 - v_2) = 0 \tag{3.24}$$

The first term represents the viscous damping force, and the second term is the static force generated at the pile head. Equating equation 3.24 with equation 3.8;

$$m_r \ddot{v}_1 = -\rho A C \, \dot{v}_2 \tag{3.25}$$

Integrating this equation is given by;

$$m_r \dot{v}_1 = -\rho A C \, v_2 + B \tag{3.26}$$

B is a constant which can be determined by applying the initial conditions. At the moment of impact $\dot{v}_1$ is equal to $\dot{v}_o$ – velocity at impact and v_2 is equal to zero since the pile has not yet been displaced.

$$B = m_r \dot{v}_o \tag{3.27}$$

From Figure 3-3, v_1 and v_2 represent movement of the hammer and the pile head, hence, $\dot{v}_1$ is nothing but the velocity at impact. So, equation 3.26 becomes,

$$m_r \dot{v}_1 = -\rho A C \, v_2 + m_r \dot{v}_o \tag{3.28}$$

Solving for v_2,

$$v_2 = \frac{m_r}{\rho A C} \, \dot{v}_o - \frac{m_r}{\rho A C} \dot{v}_1 \tag{3.29}$$

Finally, the equation of the motion for the hammer-cushion-pile system is given by,

$$m_r \ddot{v}_1 + k_s \left(v_1 - \frac{m_r}{\rho A C} \, \dot{v}_o + \frac{m_r}{\rho A C} \dot{v}_1 \right) = 0$$

$$m_r \ddot{v}_1 + k_s v_1 + \frac{k_s m_r}{\rho A C} \dot{v}_1 = \frac{k_s m_r}{\rho A C} \, \dot{v}_o \tag{3.30}$$

Define the following terms,

$$D = \frac{\sqrt{k_s m_r}}{2 \rho A C} \; and \; w = \sqrt{\frac{k_s}{m_r}} \tag{3.31}$$

Where, the term $\sqrt{k_s m_r}$ is known to be as hammer impedance. Hence,

$$m_r \ddot{v}_1 + k_s v_1 + \frac{k_s m_r}{\sqrt{k_s m_r}} . 2D \, \dot{v}_1 = \frac{k_s m_r}{\sqrt{k_s m_r}} . 2D \, \dot{v}_o$$

$$w^2 v_1 + 2Dw \, \dot{v}_1 + \ddot{v}_1 = 2Dw \, \dot{v}_o \tag{3.32}$$

Equation 3.32 is the equation governing of the hammer-cushion-pile system. The damping, D, represents energy dissipation by the pile. The solution of this equation will provide the dynamic characteristic of the system such as frequency of the loading, natural frequency, damping coefficient, peak force, and force-time distribution at the pile head.

3.4.1. Pile Head Force-Time Response

From equation 3.23 and 3.24, the force at the pile head considering the head pile displacement is;

$$F = -\rho AC\ \dot{v}_2 = m_r \dot{v}_1 \tag{3.33}$$

Substituting in equation 3.32 gives;

$$w^2 v_1 + 2Dw\ \dot{v}_1 + \frac{F}{m_r} = 2Dw\ \dot{v}_o \tag{3.34}$$

Solve for v_1;

$$v_1 = \frac{2D\ \dot{v}_o}{w} - \frac{F}{m_r w^2} - \frac{2D\ \dot{v}_1}{w} \tag{3.35}$$

And;

$$v_2 = \frac{m_r}{\rho AC}\ \dot{v}_o - \frac{m_r}{\rho AC}\dot{v}_1 \tag{3.36}$$

These expressions are substituted in equation 3.9 to determine the pile head force-time response. The solution of this problem is obtained by applying Laplace transformation. The details of solution can be found in (Deeks and Randolph, 1993). The force at the pile head can then be given by:

For D < 1,

$$\mathrm{F(t)} = \frac{\mathrm{k_s \dot{v}_o}}{\mathrm{w}\sqrt{1-\mathrm{D}^2}}\ \mathrm{e}^{-\mathrm{Dwt}} \sin(\mathrm{tw}\sqrt{1-\mathrm{D}^2}) \tag{3.37}$$

For D > 1,

$$\mathrm{F(t)} = \frac{\mathrm{k_s \dot{v}_o}}{\mathrm{w}\sqrt{\mathrm{D}^2-1}}\ \mathrm{e}^{-\mathrm{Dwt}} \sinh(\mathrm{tw}\sqrt{\mathrm{D}^2-1}) \tag{3.38}$$

For D = 1,

$$\mathrm{F(t)} = \mathrm{k_s \dot{v}_o t}\ \mathrm{e}^{-\mathrm{wt}} \tag{3.39}$$

Equations 3.37 to 3.39 provide the force distribution in the cushion, which is equal to the force applied on the pile. Equation 3.37 will provide negative force when the impact time is greater than time t_0. Negative values mean the cushion separates from the pile resulting in hammer rebound.

$$t_0 = \frac{\pi}{w\sqrt{1 - D^2}} \tag{3.40}$$

In addition, equation 3.38 does not yield any negative forces if D > 1, which means no rebound of the hammer would occur. Also, the maximum force occurs at a time, t, equal to the reciprocal of the frequency, ω, of the hammer-cushion-pile system.

3.4.2. The Influence of Impedance Ratio

For optimum hammer-pile performance, Parola (1970) specifies that maximum force is transmitted to the pile when the pile impedance is about 0.6 to 1.1 of the hammer impedance. The impedance ratio can be estimated from the following expression;

$$I = \frac{\rho AC}{\sqrt{k_s m_r}} \tag{3.41}$$

For a pile with high impedance compared to a given hammer and cushion (i.e. impedance ratio > 1), the pile-cushion-hammer system experiences energy loss due to hammer rebound. The hammer will continue moving at a fast rate to a maximum displacement before it rebounds; therefore, the energy transmitted to the pile head is much lower than the energy expected to be delivered from optimized hammer and cushion. For a pile with low impedance, the energy is transmitted gradually to the pile head at a low rate before it is fully transmitted to the pile head. In this case, the pile may be damaged due to the significant impact created by the falling mass. Thus, the pile peak force is inversely proportional to impedance ratio, i.e., high impedance ratio will produce lower peak force at the pile compared to low impedance ratio for a given pile and hammer impact velocity (Parola, 1970; and Van Kotten, 1977). Therefore, for a helical pile, equation 3.23 should be modified to reflect the effect of the helices on the pile impedance.

3.4.3. Pile Peak Force

The maximum pile head force is expressed in terms of force coefficient, F_c, and pile and hammer characteristics as proposed by (Parola, 1970; Van Kotten, 1977; and Holeyman, 1992), i.e.

$$F_{max} = Z\dot{v}_2 = F_c \frac{\rho AC}{I} \dot{v}_o \tag{3.42}$$

Force coefficient, F_c, can be estimated from Figure 3-4. Considering equation 3.41, equation 3.42 can be rewritten as:

$$F_{max} = F_c \sqrt{k_s m_r}\, \dot{v}_o \tag{3.43}$$

Where, k_s is cushion stiffness and m_r is hammer mass. In general, equation 3.43 indicates that the maximum force at the pile head increases as hammer weight, velocity of impact, or cushion stiffness increase.

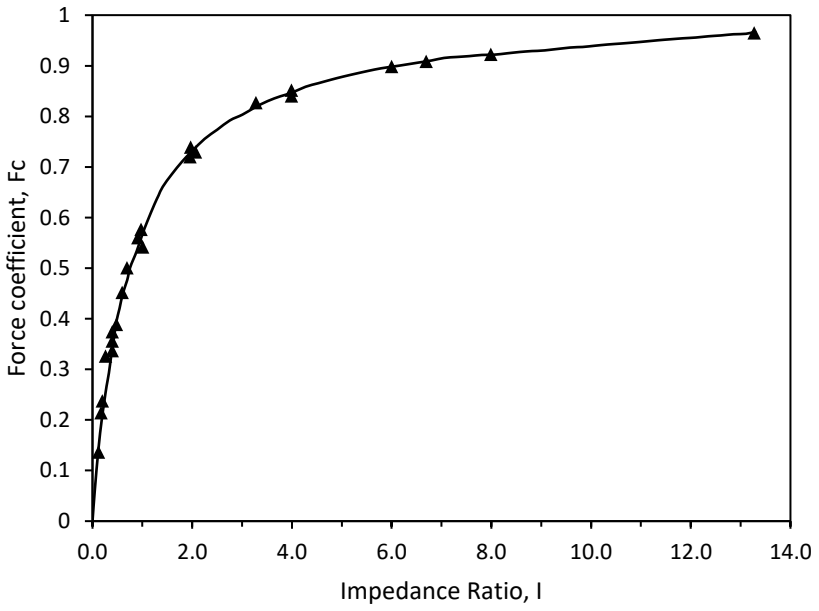

Figure 3- 4: Force coefficient, F_c, after Parola (1970).

Figure 3-4 shows the relationship between force coefficient and impedance ratio, which can be used to estimate the maximum force for a particular pile impedance. At low impedance ratio, below 0.6, the force coefficient decreases at a faster rate as hammer

weight and cushion stiffness increase to a point after which the peak force increase is limited; hence, damage to the pile may exist. For impedance ratio between 0.6 and 1.1, the optimum hammer-cushion-pile system has been achieved. For higher impedance ratio, the pile force coefficient increases slightly with increase of impedance ratio, and hammer rebound would occur.

3.4.4. Velocity at Impact

For a heavy mass, m_r, being held up at height, h, above some reference point, the gravitational potential energy due to its position is given as;

$$E_p = m_r g h \tag{3.44}$$

Where g is the gravitational acceleration of 9.81 m/s^2. As soon as the weight dropped, the "stored" potential energy is converted to kinetic energy, and it is defined as;

$$E_k = \frac{1}{2}.m.\dot{v}_o{}^2 \tag{3.45}$$

At the impact zone, assuming ideal situation, all stored energy is converted to kinetic energy and the velocity at impact can be obtained as

$$\dot{v}_o = \sqrt{2.g.h} \tag{3.46}$$

3.5. Validation of the D-R Model for HSDT

The above formulations of the D-R model for the response of the hammer-cushion-pile system are validated against several published HSDT performed on driven and bored piles embedded in cohesive soils. The equation predictions are compared with the measured results. It is crucial to assess test sites where detailed measurements are reported using both the HSDT and conventional load test in which the failure of the pile is achieved.

Seven cases were selected for validation. Each case contains two dynamically tested piles of different material and geometry, except for one case where three piles had the same material but with different diameters. Table 3-1 lists the case studies considered. For the sake of brevity, only four cases are comprehensively discussed herein while the others are used along with the four cases to develop charts and guidelines. These cases are chosen for

two reasons: a comprehensive description of their testing program is provided, and the force-time responses at the pile head were given. The HSDT was conducted based on re-strike condition and after the SLT.

Table 3- 1: Case histories used in this study.

Case	Pile label	Pile Type	Test Type	Soil Type	Mobilized Soil Resistance Ratio (Static/Dynamic)
Bemardes et al. (2000)	D=230 mm	Concrete piles	HSDT and SLT	Cohesive soil	0.65
	D=260 mm				0.66
	D=330 mm				0.65
Niyama et al. (2000)	Pile 1	Bored pile	HSDT and SLT	Sandy silt and clayey silt	0.35
GEOTECHNOLOGY (2013)	Pile 1	Driven steel pile	HSDT	Cohesive soil	---
Ta et al. (2013)	TSC1	Driven prestressed concrete pile with circular hollow section	HSDT and SLT	Soft clay, Clayey sand, and Silt clay	1.2
	TSP1	Driven steel pipe pile			1.19
Sakr (2013)	D1	Driven steel pile	HSDT and SLT	Cohesive soil	1.05
	D2				0.96
Ding et al. (2013)	Pile 1	Drilled concrete pile	HSDT and SLT	Silty-fine sand	0.79
Halder (2016)	TP1	Precast driven pile	HSDT and SLT	Silt and Silty sand	0.82
	TP2				0.60

Note:
HSDT = High Strain Dynamic Pile Test.
SLT = Static Load Test.
"---" = Not provided.

The D-R model assumes a free-falling hammer with no energy loss, which is generally not true. The hammer speed decreases during its descent due to: friction formed between the hammer and the guide, inefficient combustion of fuel in diesel hammers, misalignment between the hammer and pile top or between the hammer and the cushion, inappropriate connection at the interface surfaces, and hammer rebound. Ignoring such factors will inevitably leads to either the selection of inefficient hammer system or inaccurate interpolation of the HSDT; thus, it is necessary to consider those factors in the mathematical model.

For simplicity and to extend the applicably of this method, all factors have been lumped into one coefficient. This coefficient relates the expected peak force that would be generated from the nominated hammer system to the actual measured force at the pile head, which is equivalent to the force coefficient, F_C, shown in Figure 3-4. It is essential to acknowledge that the measured force or energy delivered to the pile head is not greater than the net force or energy that the hammer system could deliver, i.e., peak force reduction will take place between the hammer and the pile.

To validate equation 3.43, the measured force due to the hammer impact at the pile head is first plotted against time. Then, damping, cushion stiffness, and loading frequency of the hammer-cushion-pile system are evaluated and substituted into equations 3.37, 3.38, and 3.39 to calculate the force-time response at the pile head. However, in most considered cases, these parameters are not reported; therefore, these parameters are varied until a match is attained between the measured and calculated responses. After estimating damping, cushion stiffness, and loading frequency, the impedance ratio and the peak pile force for each case are calculated using equation 3.41 and 3.43, respectively. The results are then plotted in Figure 3-4 to compare the outcomes of this approach with available peak force data presented by Parola (1970). The flowchart presented in Figure 3-5 summarizes the process adopted to validate and calibrate the developed equations. It should be noted that the matching criteria were based on the peak force, the time at which the peak force occurs, and the duration of impact.

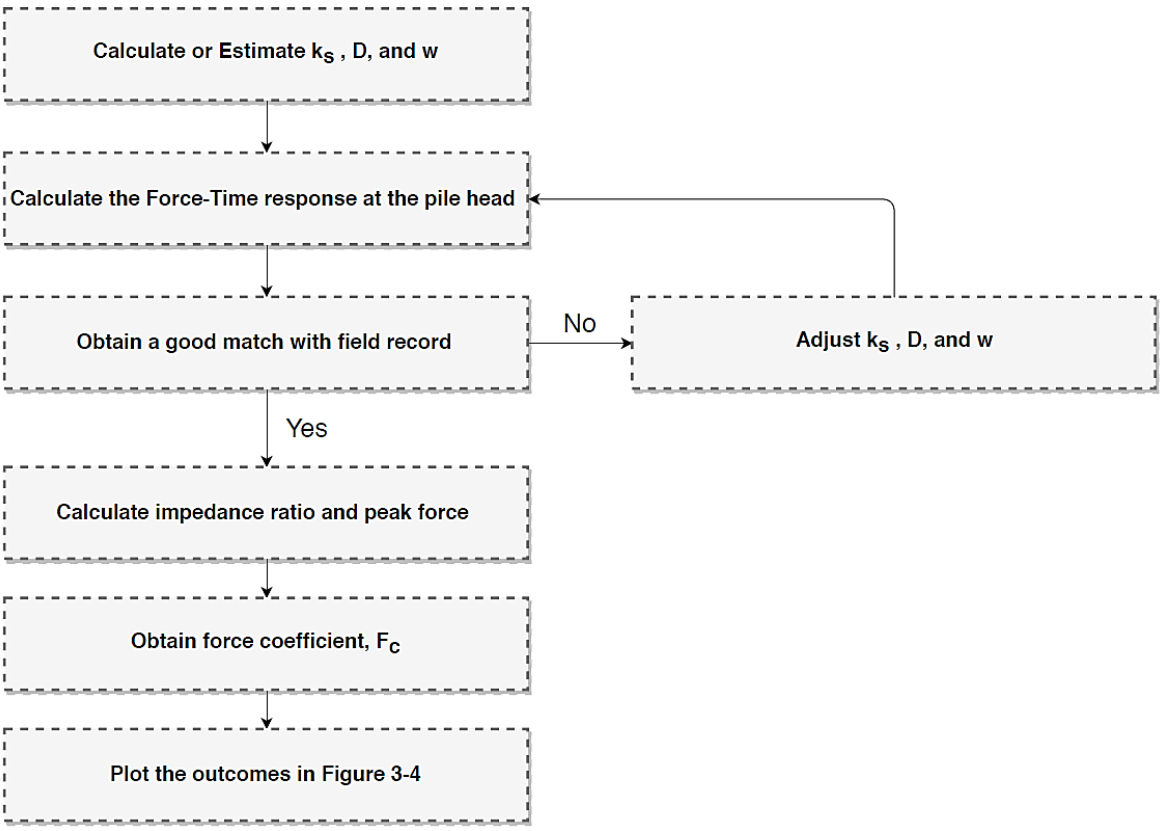

Figure 3- 5: Flowchart of the validation process.

Each case history is discussed in terms of hammer and pile configurations, test setup, and matched response between the measured and the calculated force against time. After critically evaluating all cases, modifications to the simple analytical model are proposed. Errors and overprediction of capacity in some of these cases are also discussed.

3.5.1. Underdamped Systems

3.5.1.1. Bemardes et al. (2000): Taubate, Sao Paulo

The HSDT was implemented in three precast concrete piles with different diameters in which the dynamic measurements are monitored using the PDA. The test was carried out 6 days after pile installation. All piles were driven 9 m into clayey soil, and had an elastic modulus of 30.15 MPa, and wave speed of 3510 m/s. For the 330 mm pile, the hammer weight was 2855.16 kg, and was dropped from a height of 1.4 m. For the 260 mm and 230 mm piles, the hammer weight was 2039.4 kg and was dropped from a height of 1.0 meter and 0.8 meters, respectively. A composite cushion system made of Hardwood and

Masonite fibre plate with steel helmet were used. Such a system is expected to have an efficiency of about 50%. The CAPWAP analyses were performed on the best-recorded signals and the calculated capacity was compared with the pile capacity estimated from the empirical method based on SPT-N value. Figure 3-6 shows the force-time response measured at the pile head against the calculated response from equation 3.37 for all piles.

The predicted force-time history for pile D230 reasonably agreed with measured response as can observed from Figure 3.6a. This was not the case for the other two piles as shown in Figures 3.6b and 3.6c. The agreement for the initial force records and peak forces are satisfactory, suggesting that the equivalent cushion, pile impedance, and damping for the system were successfully estimated. After the peak force, however, the predicted forces did not coincide with the filed data in which a sudden reduction of force occurred. This indicates that either the pile impedance was not uniform due to a change of the piles' cross-section or the pile head was damaged from the impact; hence, the damping of the system is no longer a constant value. Also, it could be due to uneven cushion behavior. Nonetheless, a match between the measured and the calculated forces occurs towards the end of the signal. Furthermore, the predicted time at which negative force would occur for all piles was approximately equal to the time observed in the filed data, with difference less than 10%. The calculated times were 32, 28, and 26 milliseconds whereas the measured time was approximately 35, 32, and 27 millisecond for piles D230, D260, and D330, respectively. It was also noted that the maximum force occurred at a time, t, equal to the reciprocal of the frequency, ω, of the hammer-cushion-pile system. The value of ω were 150, 140, and 200 rad/s for piles D230, D260, and D330, respectively. The reciprocal of these values will give the time at which maximum force appears as depicted in Figure 3-6.

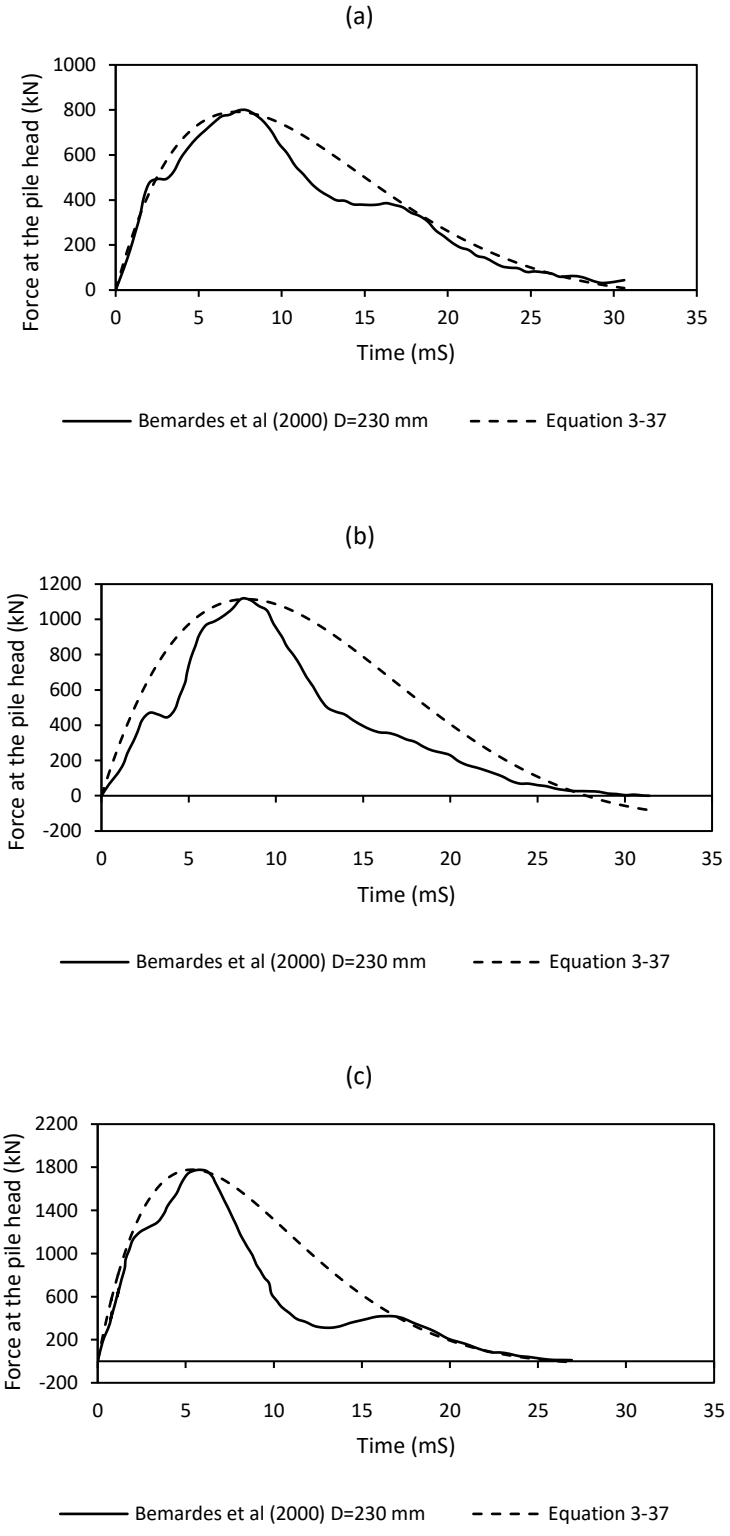

Figure 3- 6: Comparison between measured and calculated force time response at the pile head for piles: (a) D230; (b) D260; and (c) D330.

The damping ratio, D, is a function of hammer and pile impedances. The hammer impedance has been quantified as $\sqrt{k_s m_r}$ and depends on the hammer and the cushioning characteristics. This value is typically considered to be constant and does not change through the test. Hence, any change of the damping ought to change in the pile impedance for a given hammer and cushion materials. Reduction in pile impedance will cause the damping to increase. If there is a significant reduction in the pile impudence such as pile damage, the recorded force would decrease. Also, the pile impedance may change due to shaft friction (Viggiani et al., 2012), which is not accounted for in the model (i.e. external resistance is not considered). So, assuming a uniform pile impedance will only approximate the solution. The responses from equation 3.37 shown in Figure 3-6 would be enhanced if the damping variation was accounted for.

The equivalent cushion stiffness, k_s, is selected such that the calculated peak force is equal to the generated peak force at the field, i.e., it represents the loading stiffness only, which has been approximated by a straight line as indicated previously. This may be sufficient to estimate the generated peak force for a given hammer and cushion material but may not capture the real shape of the force-time response. The actual load-deformation curve for cushion behavior under impact loading should be accounted for in the analyses by dividing the curve into a series of straight lines with considering the unloading stiffness as proposed elsewhere (Lowery et al., 1967; Hirsch et al. 1966; and Parola, 1970). If the cushion loading stiffness is progressively increased in the loading stage and considering unloading stiffness in the unloading stage, the shape of force-time response in loading and unloading will be subjected to the same behavior. This would require more sophisticated input, which is not always readily available. Since equation 3.37 could provide the peak force and the time at which it occurred as well as the force pulse duration similar to the field measurement, it may be concluded that the D-R model can be used to represent a hammer impact on the top of a pile with reasonable accuracy.

3.5.1.2. Sakr (2013): Alberta, Canada

Two steel driven piles with a diameter of 324 mm and a wall thickness of 9.5 mm embedded in a cohesive soil were subjected to a SLT up to failure followed by an HSDT. The two piles were close-ended with a tip cut of 45 degrees. The soil profile consisted of three main

layers: a silt layer at the top, underlain by thick clay and silty clay layers, over silty clay layer interbedded with silt lenses. The SLT was carried out in accordance with the quick maintained load test method. Pile head settlement was recorded electronically at each load increments, which was kept for about 5 minutes. The maximum applied load for piles D1 and D2 was 810 kN and 840 kN with a corresponding settlement of 41.2 mm and 42.4 mm, respectively. For the HSDT, a drop hammer system with a weight of 19 kN dropped for a distance of 0.9 m was used. The impact was transferred first to a pile cushion before it reached the top of the pile. Sensors were attached near the pile head to measure force and vertical acceleration signals. Processing these signals were accomplished using a PDA device. Post-processing analyses using CAPWAP signal matching software was implemented for the measured pile head force and velocity to estimate static capacity. The predicated static capacity from the CAPWAP analyses were 1.05 and 0.96 of that obtained from the SLT for piles D1 and D2, respectively.

Figure 3-7 shows excellent agreement between the measured force-time responses at the pile head for both piles with the corresponding calculated force-time response form equation 3.37. Similar to the previous case history, the results show that for underdamped systems, the behavior of the hammer-cushion-pile system is governed by the hammer mass, the equivalent cushion stiffness, damping, and pile impedance. However, the damping ratio in this case was well below 1.0; therefore, the estimated force at the pile head for both piles shown in Figure 3-7 had the form of a damped half sine wave.

Comparing Figure 3-7 to Figure 3-6, it is observed that the oscillatory behavior of the measured decaying force was more pronounced because the pile impedance was relatively lower than hammer impedance, which resulted in multiple peaks. For higher impedance ratio (i.e. piles tested in Bemardes et al., 2000), the decaying force had the form of a damped sinusoidal wave. Also, the pile peak force increased as the impedance ratio increased (i.e. the estimated force coefficient increased), consistent with Parola (1970) observations presented in Figure 3-4.

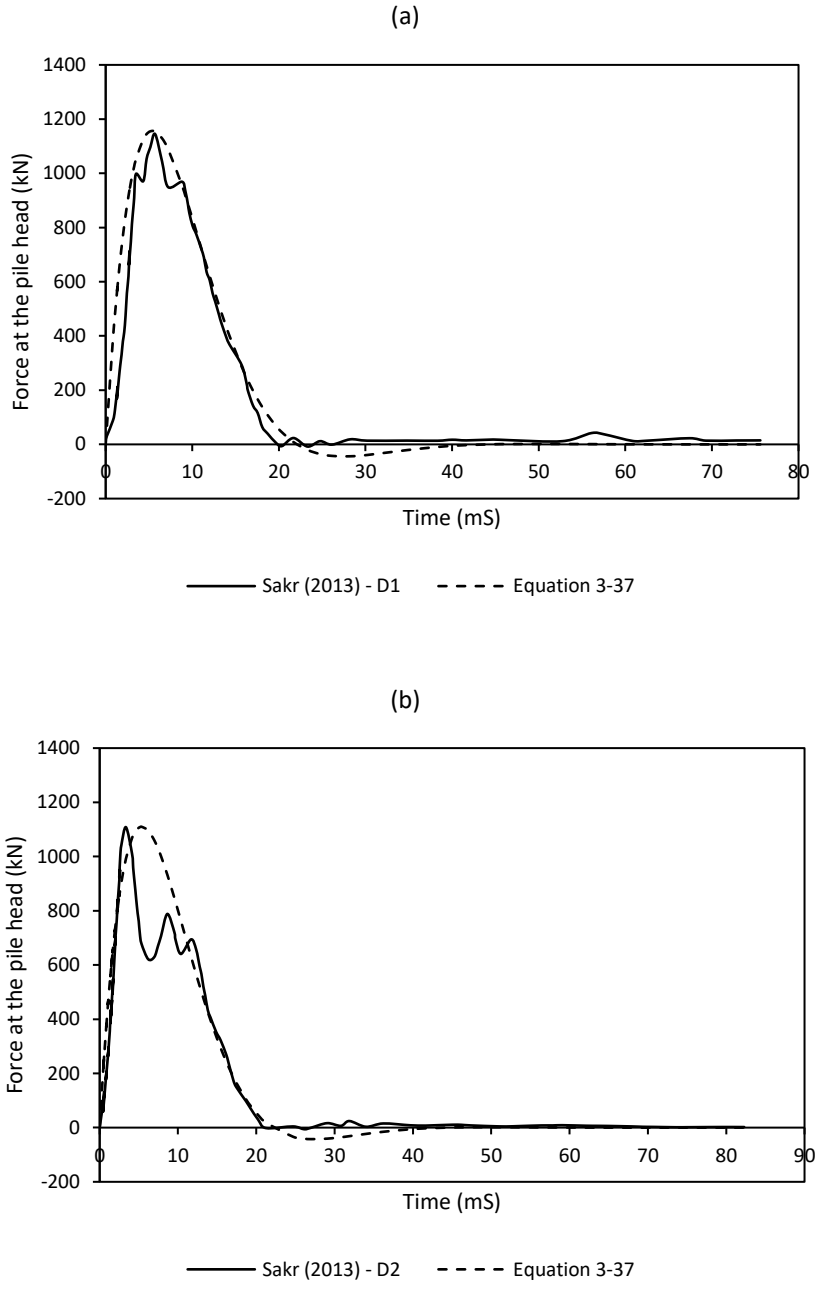

Figure 3- 7: Comparison between measured and calculated force time response at the pile head for piles: (a) D1; and (b) D2.

The influence of pile impedance on the generated peak force for the given hammer and cushion setup has been investigated. A linear proportional relationship exists between the peak force and pile impedance at a very low pile impedance. With the increase of pile impedance, the peak force increased at a much slower rate as presented in Figure 3-8. This

explains the small difference between the peak force in piles D1 and D2 even though the two pile had the same material properties and geometry. This is because pile impedance changed due to shaft friction.

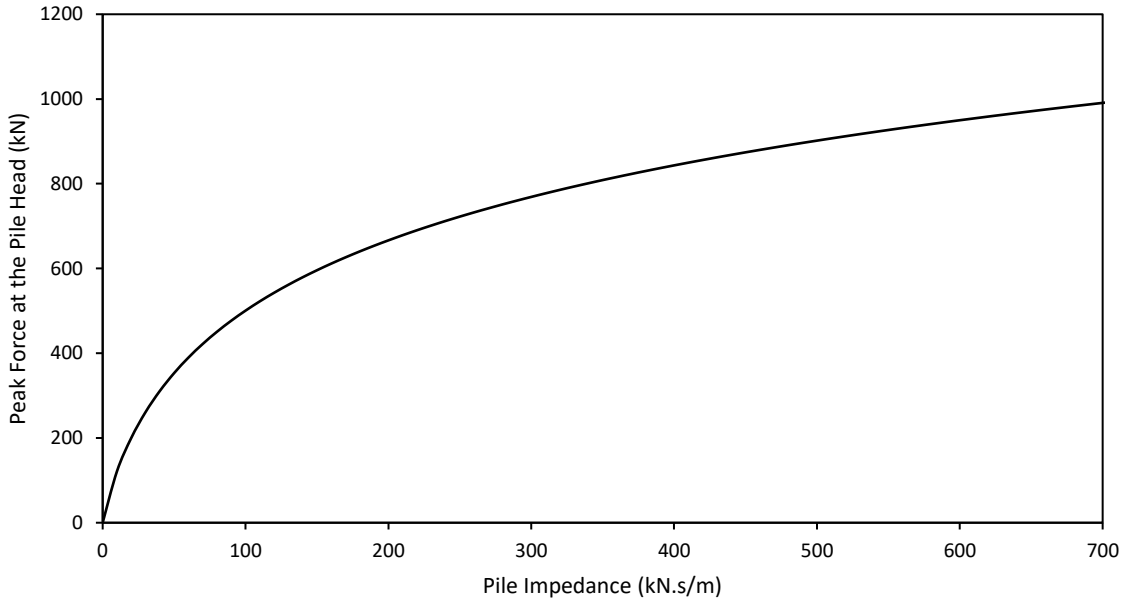

Figure 3- 8: Peak force versus Pile impedance for a given hammer and cushion set up.

3.5.2. Overdamped Systems

3.5.2.1. GEOTECHNOLOGY, INC (2013): Livingston County, Missouri.

A HSDT was carried out by GEOTECHNOLOGY, INC in Missouri. The testing program intended to evaluate the accuracy of HSDT in predicting the static load-displacement curve for a steel pile driven in cohesive soil. The tested pile was monitored using a PDA system which collected the strain and acceleration measurements from two strain gauges and two accelerometers attached to the pile head. The gauges and accelerometers were mounted 71 cm away from the pile top. The HSDT was performed seven days after the installation of the pile using open-ended diesel hammer (Delmag D19-42) with a hammer weight of 17.8 kN and an equivalently rated stroke of 3.3 m. A 5.1 cm thick hammer cushion made from aluminum/conbest with a coefficient of restitution of 0.8 and a helmet were used along with hammer pile system. Table 3-2 summarizes the pile and test equipment data.

Table 3- 2: Pile and Test Equipment Data.

Mass of the Hammer $(\boldsymbol{m_r})$	*1814.37*	$[kg]$	***Pile Length*** $(\boldsymbol{L})$	*15.2*	$[m]$	***Cushion Stiffness*** $(\boldsymbol{k_s})$	*4.45E+08*	$[N/m]$
Stroke Hight $(\boldsymbol{h})$	*3.3*	$[m]$	***Area*** $(\boldsymbol{A})$	*1.04E-02*	$[m^2]$	***Cushion Material***	*50% Aluminum and 50% Conbest*	
Maximum Force $(\boldsymbol{F})$	*2464*	$[kN]$	***Wave Speed*** $(\boldsymbol{C})$	*5139.24*	$[m/s]$	***Thickness***	*5.1*	$[cm]$
coefficient of restitution	*0.8*		***Pile Impedance*** $(\boldsymbol{Z})$	*423119.45*	$[N.s/m]$	***Cushion Modulus of Elasticity***	*3.65E+09*	$[N/m^2]$

The helmet was neglected in the analysis due to its small mass and to simplify the solution. It is reported that the helmet has a generally negligible effect on estimating the maximum peak force for a given hammer-pile system (Parola, 1970; and Deeks and Randolph, 1993).

The damping ratio was estimated as 1.46, which is higher than 1. Therefore, equation 3.38 is used to calculate the force generated at the pile head. Figure 3-9 shows excellent agreement between the calculated and measured force-time history, which confirms the ability of the D-R model to predict the force generated at the pile head during the HSDT.

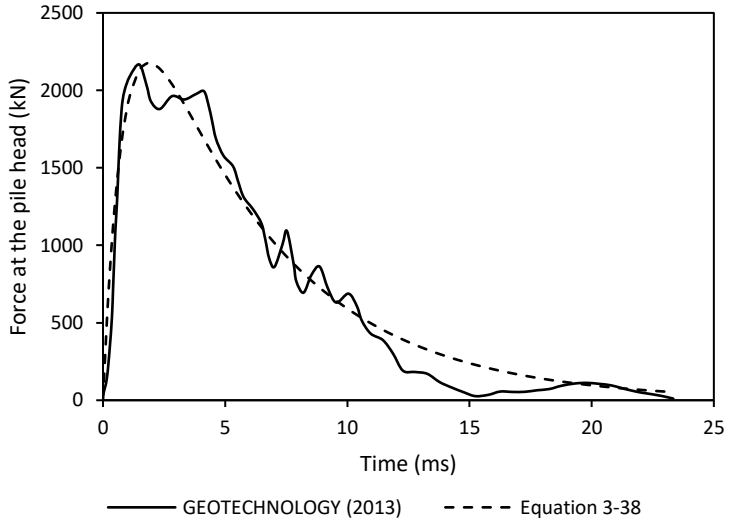

Figure 3- 9: Comparison of measured and calculated force-time response.

The maximum force occurred at a time, t, and its equal to 2 millisecond which is approximately equal the inverse of the natural frequency, ω, (460 rad/s) of the hammer-cushion-pile system similar to the underdamped system. However, the effect of natural frequency on the time of peak force for the overdamped system is significant compared to underdamped system. As natural frequency increases, the peak force occurs over a short time and becomes more pronounced than for the low-frequency system. For over-damped system, the force is transmitted gradually to the pile head in contrast to underdamped systems where the force is transmitted at a higher rate. Additionally, equation 3.38 does not produce negative force even for time beyond the time of the test, which means no hammer rebound would occur for over-damped system. The impedance ratio for these piles was estimated to be 0.47. This means the selected hammer and cushion material gave a hammer impedance that is approximately twice the pile impedance, resulting in observed oscillations more significant compared to the response presented in Figure 3-7 which is for an impedance ratio of 0.79.

The effect of varying cushion stiffness on the shape and duration of the force-time history was examined by analyzing the system presented in Table 3-2. As the cushion stiffness increase, the effect of the damping is almost negligible, and a sharper force pulse is achieved as depicted in Figure 3-10. At a very high stiffness, the impact of the hammer will exert an instantaneous peak force and then attenuates fast. Such systems must be avoided when conducting the HSDT. For softer cushion stiffness, the time of impact seems to increase as the cushion gets softer with a variation of about 10%, and the time for peak force is also elongated noticeably. This demonstrates the effect of cushion material and its resultant stiffness on the performance of equation 3.38.

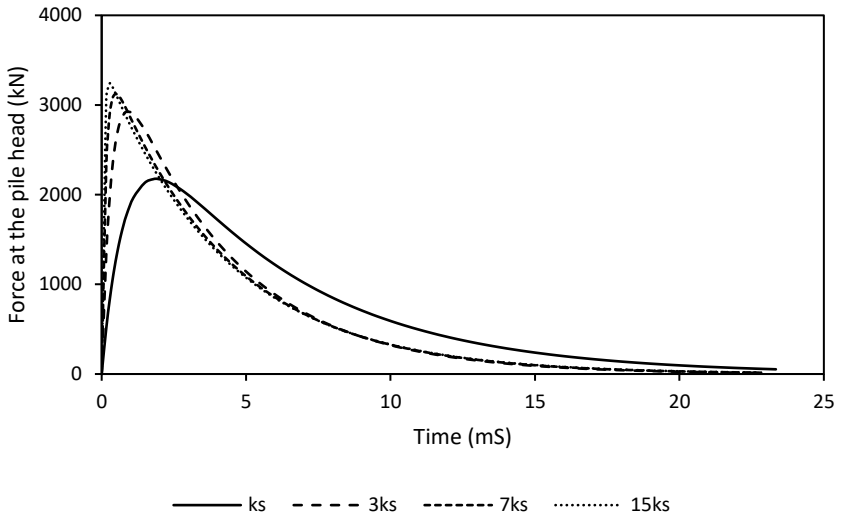

Figure 3- 10: graphical representation of the effect of increasing cushion stiffness for overdamped system.

3.5.2.2. Ta el al. (2013): Thi Vai International Port.

In this case study, one steel driven pile (TSP1) was subjected to both SLT and HSDT to compare the static load-deformation of the pile obtained from both tests. The pile was 1 m in diameter with wall thickness of 12 mm, and 60 m long. The pile was driven to the desired depth using a diesel hammer with a mass of 10 tons. The soil profile consisted of a soft clay layer, approximately 14 m deep, underlain by a 25 m thick clayey sand layer followed by the bearing stratum that was characterized as hard silty clay. The ground surface existed at 6 m below the mean sea level. The TSP1 was subjected to SLT up to large displacements (S = 72.0 mm) to ensure that both shaft and toe beating resistances have been fully mobilized. The HSDT was carried out in accordance with ASTM-D4945 standard and based on a re-striking period of 34 days using a diesel hammer, Delmag D100-13, with a hammer weight of 10 ton, dropped from a height of 2.8 m. The dynamic signals were measured using two strain gauges and two accelerometers that are mounted symmetrically to the pile at a distance of 3.5 m from the pile head. The dynamic measurements were analyzed to derive the static load-displacement curve, which compared favorably with the curve obtained from the SLT. Nevertheless, the mobilized capacity from the static test was higher than the mobilized capacity from the dynamic test by approximately 20%.

Figure 3-11 compares the calculated and measured force-time history at the pile head. The calculated peak force and time of impact were in good agreement with the measured response. It is also observed that there was a sudden increase in the force in a very short period followed by fast decay of the force. The drop in the force right after the peak is attributed to the high cushion stiffness (4.5 time higher than the cushion stiffness in the previous case). The fluctuation of the measured force was more significant because the impedance ratio was very small (0.34). Overall, the observations from this case were similar to that of GEOTECHNOLOGY (2013) owing to the high damping.

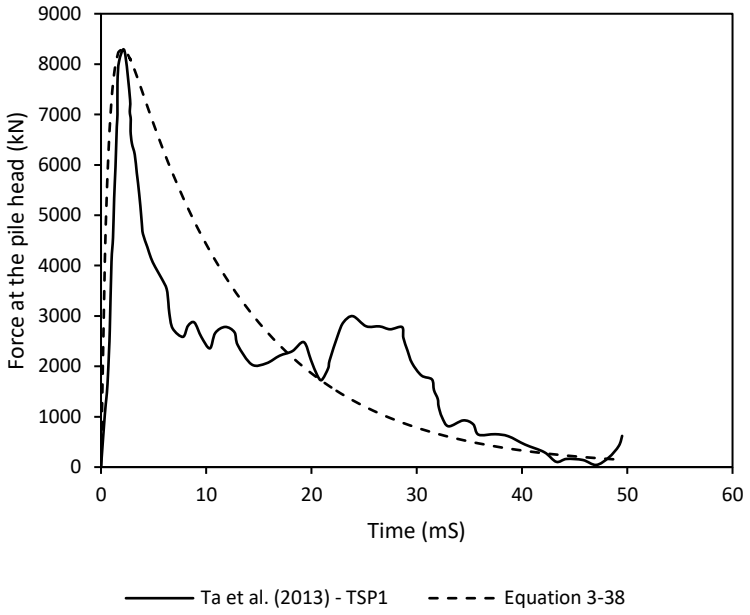

Figure 3- 11: Force-time response at the head of pile TSP1.

3.5.3. Comparison of Peak Force Coefficient

The pile peak force coefficient, F_c, and the impedance ratio, I, for the investigated case histories are plotted in Figure 3-12 along with the results proposed by Parola (1962) to compare the predictions of the D-R model with that adopted in Parola (1962). Generally, a satisfactory agreement between the two sets is observed.

For driven piles, the results compare favorably with the findings of Parola (1962) except for two piles where the estimated force coefficient and impedance ratio deviated from the average line by approximately 20%. This is attributed to the pile damage during installation. In both piles, there was a sudden increase in the velocity record and corresponding reduction in the force record occurred at a time before the time for stress wave reflection from the pile toe to arrive at the pile head, which indicated damage to the pile shaft. This implies the assumption of a uniform cross-section is no longer valid and the original expression of pile impedance, ρAC, should be modified.

Interpretation of the HSDT data for a non-uniform pile (e.g. drilled shaft) is more difficult and possibly less accurate. This issue is still undergoing research scrutiny in regard to acceptable dynamic instrumentation and interpolation of the results. It has been observed that the developed model could not adequately estimate neither the peak pile force coefficient, F_c, nor the impedance ratio, I, as can be seen in Figure 3-12.

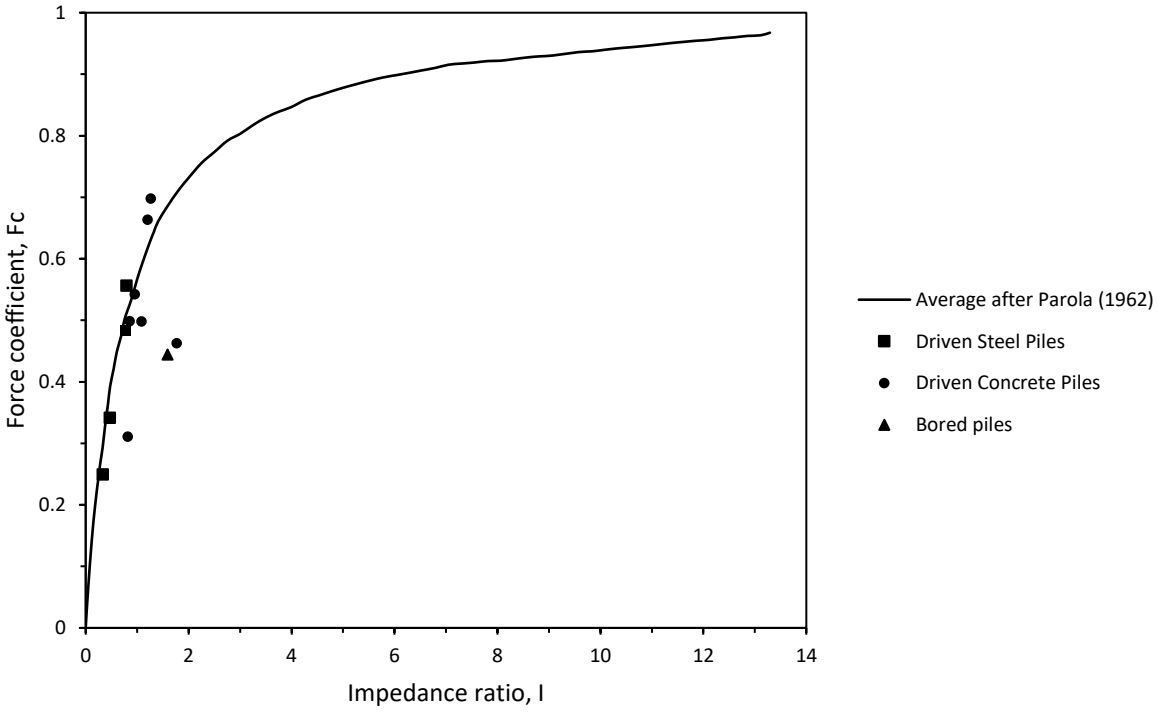

Figure 3- 12: Peak pile force coefficient, Fc, versus impedance ratio, I, for all case histories.

3.5.4. Estimated Vs. Calculated Damping

The damping ratio, D, considered herein manifests the influence of the cushion impedance relative to the pile's impedance on the generated force pulse and its time length. It is defined as the ratio of the hammer impedance to twice the pile impedance as presented previously. When $D \geq 1$, the force shape is expressed by an exponential and non-periodic function. The attenuation of the force slowly returns to equilibrium without the development of negative force. As the cushion stiffness increases for a given hammer and pile set up, a decidedly sharper and shorter duration of the force pulse will be generated, and the solution approaches the case of hammer-pile system only akin to a direct impact of steel over steel which is of limited interest when conducting the HSDT. On the other hand, when $D < 1$, the solution involves both exponential and goniometric functions and displays periodic behavior, especially if $D < 0.5$. Such systems possess a soft cushion causing the force shape to have a long rise time after which the force attenuate at a high rate. Furthermore, the peak force coefficient is inversely related to the damping, as shown in Figure 3-13.

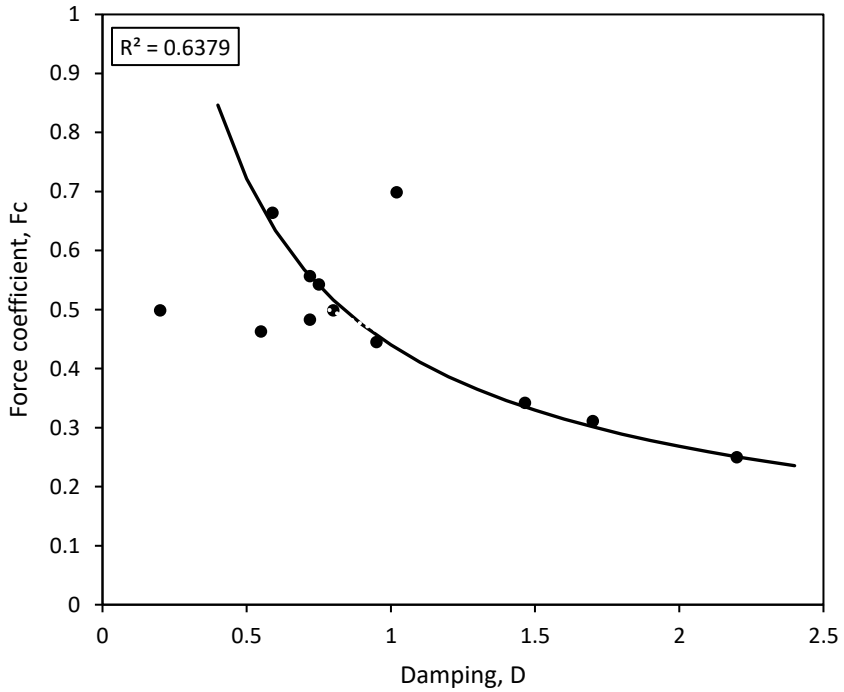

Figure 3- 13: Peak force coefficient vs damping ratio.

The estimated damping ratio obtained from matching the equations prediction of force-time response to the filed data was higher than the calculated damping using equation 3.31 (i.e. $\sqrt{k_s m_r}/2\rho CA$) for all case histories, see Figure 3-14. This is because the cushion load-deformation curve is assumed to be linear instead of a nonlinear. Therefore, the original equation should be modified to account for this effect. A proposed modification to the original damping equation is presented in equation 3.47 which represents the fitted regression line depicted in Figure 3-14. A linear regression model was found to be the best to describe the observed data compared to other regression models (e.g. exponential regression, power regression, and polynomial regression)

$$D = \frac{3\sqrt{k_s m_r}}{4\rho CA} \tag{3.47}$$

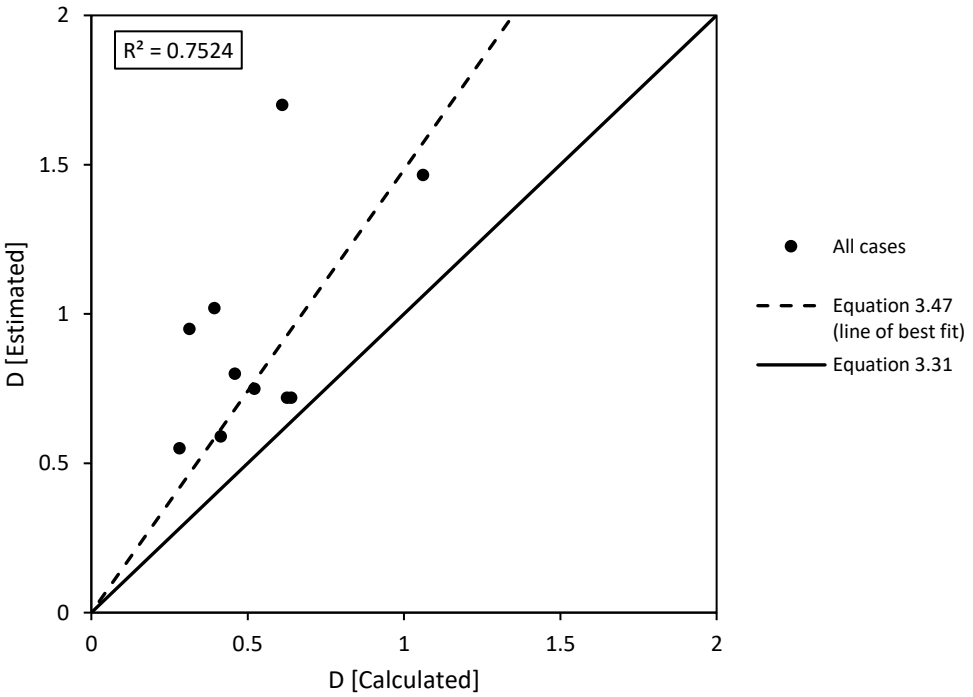

Figure 3- 14: Calculated damping versus estimated damping.

3.5.5. Effect of Drop Height and Impact Velocity

Underestimation or overestimation of pile's axial capacity obtained from dynamic measurements is a common concern. In fine-grained soils, excess positive pore water

pressures are usually generated during and at the end of pile installation. The shear strength of surrounding soil will decrease, and accordingly pile shaft and toe resistance will decrease. Hence, estimating axial pile capacity at the end of installation will underestimate the actual pile capacity. Thus, it is recommended to conduct HSDT and CAPWAP analysis based on a restrike condition (Edde, 1991). On the other hand, the pile capacity may be overestimated due to the excessive transfer of energy – drop height – to the pile head. Inadequate velocity variations occur at the pile head; thus, damping forces may be mistakenly included in the static resistance.

Energy and impact forces generated at the pile head during HSDT can be controlled by the drop height. Two case histories were selected to show the effect of varying drop height and the impact velocity on the measured peak force at the pile head. Figure 3-15 shows the relationship of the pile top force and drop height for overdamped and underdamped systems. The maximum force exhibits an exponential growth at a slow rate with an increase in the drop height. Even though high drop heights would permit maximum transmission of force and energy to the pile and more mobilization of soil static resistance, it may cause damage to the pile and compromise its integrity. A suitable height should be selected considering hammer system, fall mechanism, and soil stiffness to ensure maximum compressive and tensile stresses during testing remain within recommended limits.

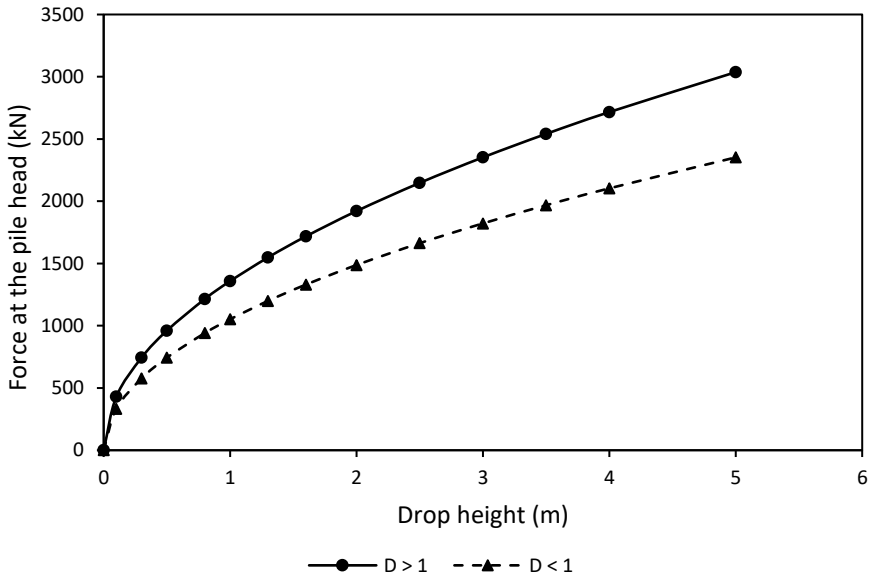

Figure 3- 15: Peak force results at various drop height.

Typically, a single representative blow of high energy is selected for the analysis of HSDT. The force and velocity at the pile head due to a single blow are measured by the PDA, and interpreted to separate the dynamic resistance from the static resistance using a signal matching software (e.g. CAPWAP). If a blow of a lower imparted energy is chosen for the analyses, the ultimate soil resistance at the pile toe would not be fully mobilized, and the pile capacity is underestimated. Conversely, a blow with excessive energy would add dynamic resistance to the static pile capacity, and pile capacity is overestimated. Alternatively, several blows can be chosen to derive the load-settlement curve of a pile. Figure 3-16 depicts the effect of drop height on the estimation of the load-settlement curve for the same pile obtained from; (a) from a representative blow, (b) for two blows dropped from a height of 33 cm and 64 cm, (c) for three consecutive blows dropped from a height of 30 cm, 40 cm, and 90 cm. Figure 3.16 shows that increasing the drop height produces a load-settlement curve with low elastic compression compared to one significant blow. Moreover, the plastic region occurred at lower load after which minimal increase in the load produces large settlement until plastic yielding is fully mobilized within the soil. Therefore, different drop height sets may not provide similar results when conducting the HSDT.

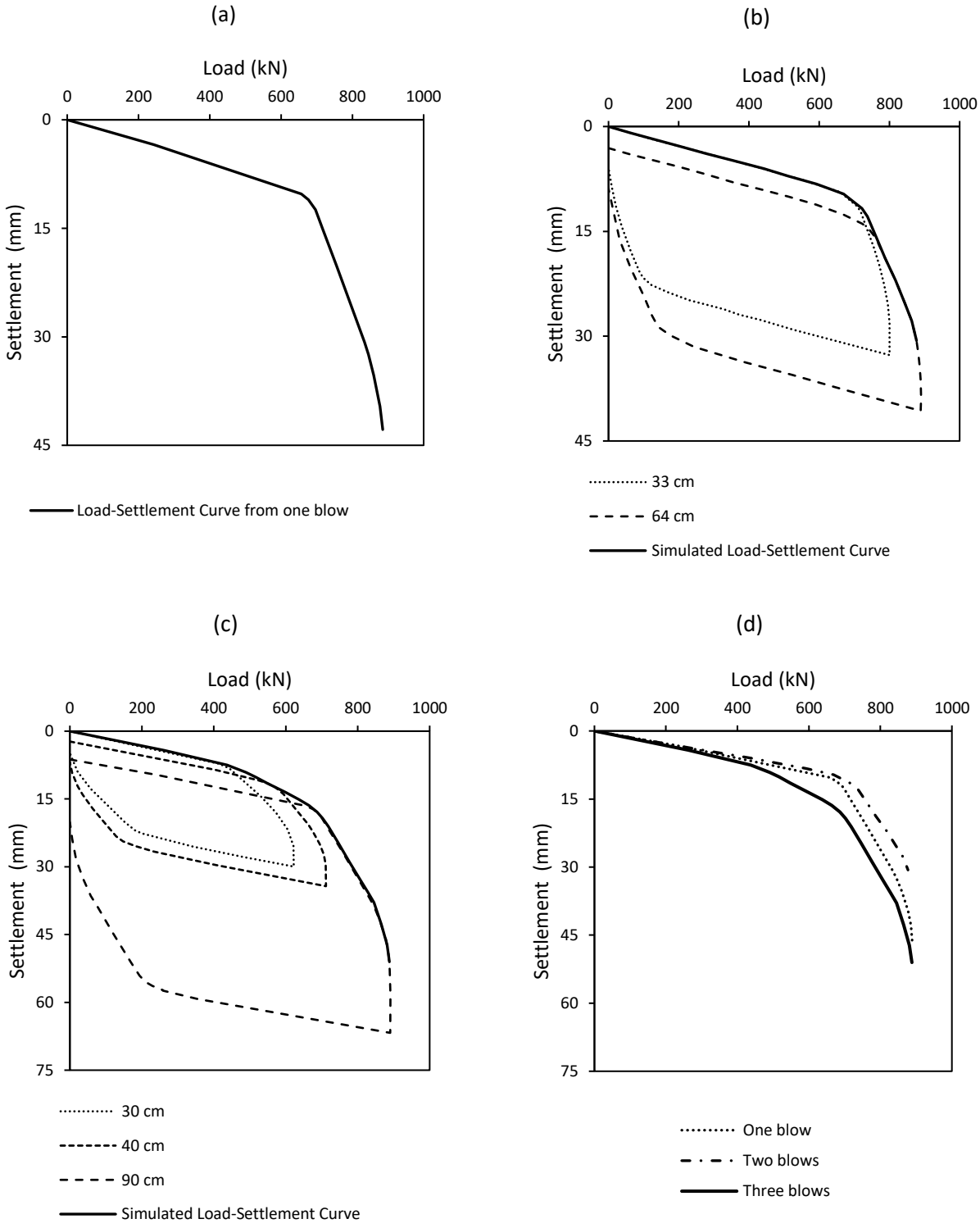

Figure 3- 16: Load-settlement curves from different blows performed on two piles with the same geometry and soil profile.

3.6. Helical Piles

This section investigates the results of cases studies of HSDT conducted on fourteen helical piles in North America. The data were gathered from multiple sources, including published literature and geotechnical load test reports. Four helical piles had single helix and 10 had double helices. The shaft diameter varied from 177 mm to 508 mm and the embedded depth ranged from 3.7 m to 14.1 m. The soil profiles have been categorized based on the predominant soil condition. The soils surrounding the shaft and most importantly around the helices in the collected test results were comprised of either clay, clay till, or silty clay layer as referred to in the geotechnical reports. Thus, the soil in all cases considered herein was cohesive soil. Some of the geotechnical reports noted some sand and sandy silt layers near the ground surface with a thickness of less than 4 m. These layers had minor effects on the piles responses since the response is mostly governed by the soil near and beneath the helices. More information regarding the collected helical piles data is summarized in Table 3-3, including, pile and site reference, shaft and helix diameter, pile length, and dynamic test configurations.

The helical piles were installed by applying both torque and axial compressive load to the pile head to advance the piles into the soil. Hydraulically powered rotary motors were used to apply the required torque. Based on the geotechnical reports, pile installation process and measurement of torque appeared to be of high quality and high efficiency. The tested helical piles were subjected to a dynamic impact load generated form a hydraulic hammer that is dropped from variable drop heights. The hammer weight ranged from 19 kN to 50 kN. A steel plate was welded to the pile head and served as impact plate. Blocks of plywood with variable thickness were placed on top of each test piles to provide impact cushioning. The instrumentation associated with the PDA in HSDT comprised two strain transducers and two accelerometers bolted externally and diametrically in opposed pairs near the pile head. This instrumentation was affixed to the pile such that they were above the ground surface by a distance between 0.3 m and 0.5 m in the other cases. A follower or external extension made for steel was added on the top of the all tested helical piles in order to facilitate testing, avoid damage of the instrumentation, and enhance data quality.

Table 3- 3: Information for the Tested Piles

Pile ref.	Site ref.	L [m]	d [mm]	d_H [mm]	No. of helices	S/d_H	h [cm]	W_r [kN]	L_E [m]	Hammer System
S3	*Ponoka, Alberta*	9	324	610	2	1.5	90	19	1.2	*N.A.*
S4	*Ponoka, Alberta*	9	324	610	1	N/A	90	19	1.2	*N.A.*
P4-31	*Fort St John, British Columbia*	3.7	178	356	1	N/A	31 46	31	0.6	*HPS drop hammer*
P5-09	*Fort St John, British Columbia*	4.4	220	406	2	3	15 31 46	31	0.6	*HPS drop hammer*
P5-19	*Fort St John, British Columbia*	4.2	220	406	1	N/A	15 31	31	0.6	*HPS drop hammer*
HP2	*Edmonton, Alberta*	8.3	220	914	2	3	38 90	40	N/A	*HHK4SL Hydraulic Hammer*
HP12S24	*Calgary, Alberta*	6.7	324	610	1	N/A	46	40	N/A	*HHK4SL Hydraulic Hammer*
HP12D36	*Calgary, Alberta*	8.5	324	914	2	3	61	40	N/A	*HHK4SL Hydraulic Hammer*
HP12D40	*Calgary, Alberta*	9.2	324	1000	2	N.A.	46	40	N/A	*HHK4SL Hydraulic Hammer*
HP20D40	*Calgary, Alberta*	9.2	508	1000	2	N.A.	61	40	N/A	*HHK4SL Hydraulic Hammer*
52-14	*Midland, Michigan*	13.7	245	508	2	3	15 25	40	0.61	*APPLE IV Drop Hammer*
52-18	*Midland, Michigan*	13.8	245	558	2	3	30 46	40	0.61	*APPLE IV Drop Hammer*
52-19	*Midland, Michigan*	14.1	245	508	2	3	30 46	40	0.61	*APPLE IV Drop Hammer*

62-02	*Midland, Michigan*	13.8	245	610	2	3	30 46	40	0.61	*APPLE IV Drop Hammer*

Where; L = length, d = shaft diameter, d_H = helix diameter, S/d_H = interhelix spacing to diameter ratio, h = dropping height, W_r = hammer weight, L_E = extension length, N.A. = not available, and N/A = not applicable.

Signals for strain and acceleration were converted by the PDA to force and velocity record and were saved for processing. Maximum stresses developed in the test piles due to the applied loads were below the permissible stress limits, typically 90% of the minimum yield strength of the steel. This was confirmed by inspecting the collected force and velocity records, which showed no signs of pile damage. The post-processing signal matching method on the acquired records has been performed using CAPWAP to evaluate the static resistance and to approximate the resistance distribution for each impact. None of the cases investigated, except for one, involved static load testing before or after the HSDT on the same helical pile; therefore, comparison of the derived static-displacement and mobilized static resistance ratio could not be made with SLT data. Nevertheless, the mobilized static resistance ratio was established for each case based on axial capacity theory methods, or from torque-capacity correlations. It should be noted that all performed HSDTs were based on a restrike condition.

The impact response at the pile head for all the collected cases of HSDT on helical piles were analyzed using the D-R model. The force-time responses were first obtained from the analytical model and were compared with the field measurements to evaluate the appropriate values for the increase in pile impedance (due to helices), cushion stiffness and damping ratio. Figure 3-17 presents the flowchart for the procedure to obtain these parameters from the analysis of the test data. The estimated damping ratio of the hammer-cushion-pile system is then used to evaluate the increase in pile impedance since it is a function of hammer system elements as well as pile impedance. However, inevitable uncertainties are expected in the adopted process. These uncertainties are associated with installation methods, used hammer system, and variability inherent in the soil layers.

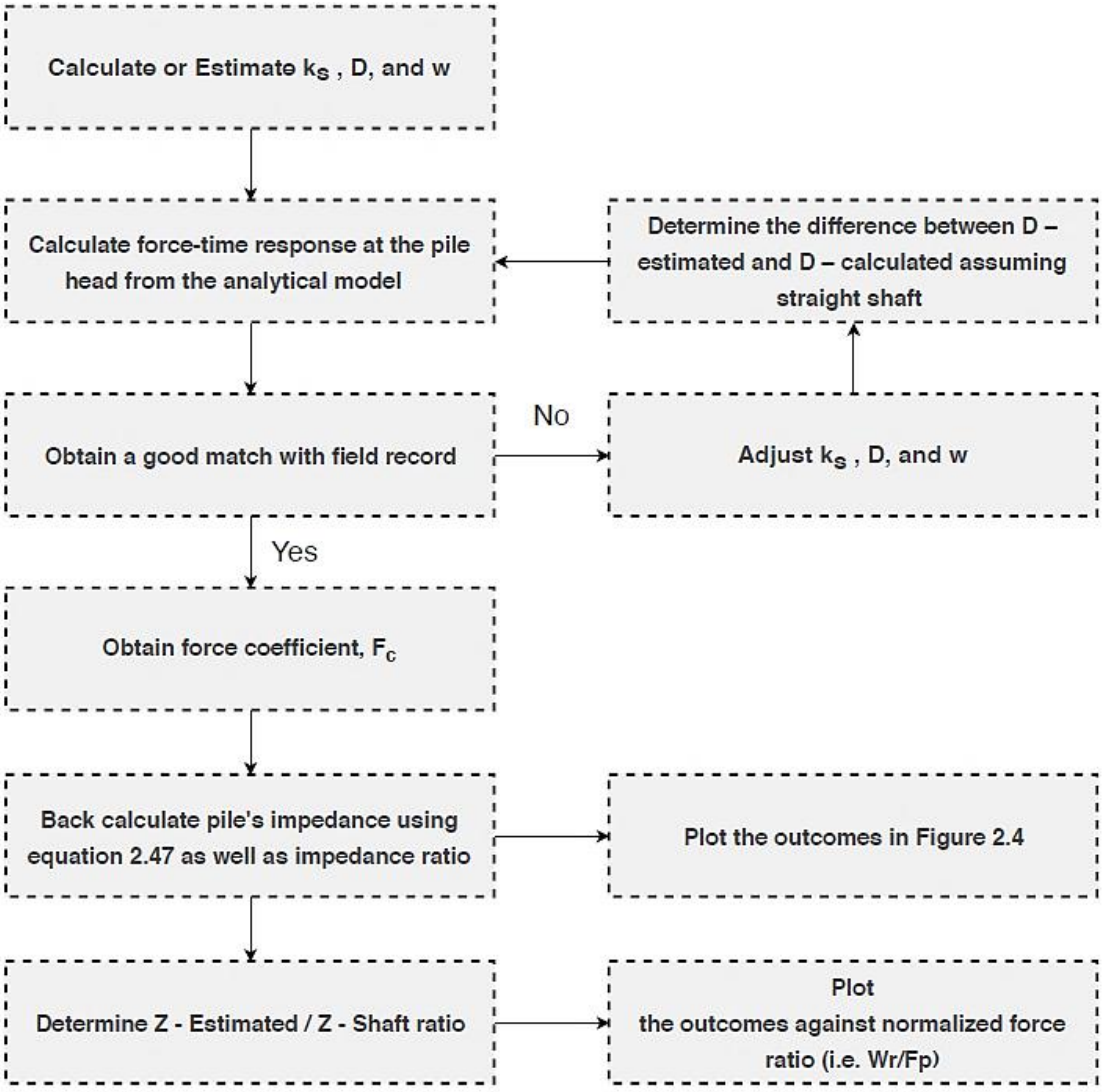

Figure 3- 17: Flow Chart for Helical Pile impedance determination adopted in this study.

To evaluate the significance of pile impedance on the performance of the HSDT on helical piles, the results of the D-R model are compared for a driven and a helical pile with double helices, namely D1 and S3, which have same shaft diameter and length, and dynamic test set-up. More pile details are provided in Sakr (2013) and Elkasabgy and El Naggar (2015). The pile impedance to hammer impedance ratio for pile D1 was estimated to be 0.780 and the corresponding peak force coefficient was 0.48. These estimates conform to the proposed behavior of impedance ratio versus peak force coefficient as depicted in Figure 3-18 and is in good agreement with Parola (1962). On the other hand, for the helical pile

S3, the matching between the calculated and measured force-time response assuming a uniform pile cross-section in the D-R model resulted in impedance ratio of 0.505 and peak force coefficient of 0.701, which do not conform with Parola (1962) as can be noted from Figure 3-18 even though the same dynamic test configurations were used. The estimated impedance ratio was lower than the expected value. This indicates that the ratio of pile impedance to the hammer impedance was higher than what was obtained from the matched impedance. Furthermore, the predicted load-displacement curve from dynamic measurements for D1 is in good agreement with axial compression load test results done by Elkasabgy (2011). For the helical pile, the predicted load-displacement curve is considerably lower than the estimated curve from axial compression load test results, which implies that the selected hammer system was not sufficient to fully mobilize the end-bearing provided by the helices (Sakr, 2013).

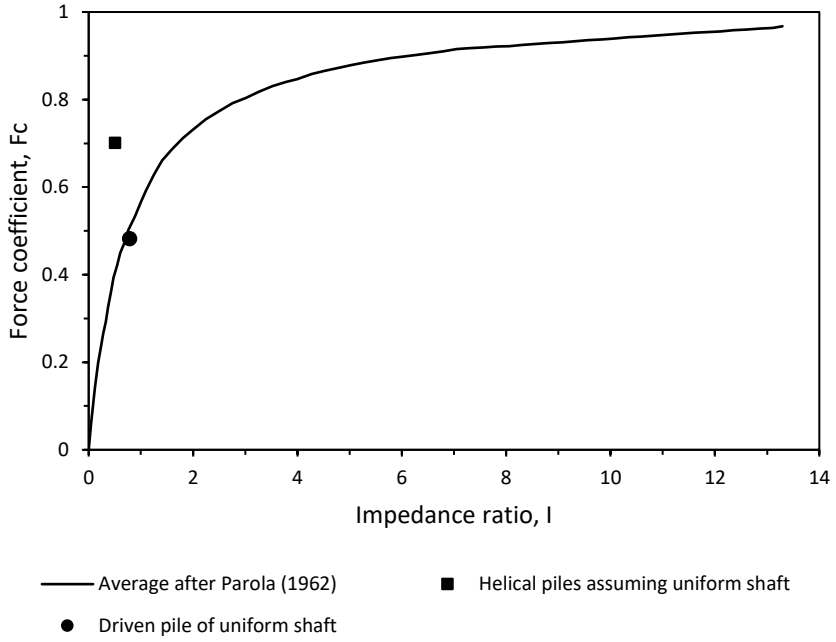

Figure 3- 18: Comparison of peak force coefficient and impedance ratio between a driven pile and a helical pile with the same shaft size and embedment length.

The shape of the force-time response for the helical pile approached a half-sine wave with minimal skewed behavior in the force near the time for peak force as expected for impedance ratio > 0.9 as discussed previously. This clearly demonstrates that the

impedance ratio of helical piles used in the D-R model should be adjusted to account for the increase in impedance due to the contribution of the helices.

The impedance ratio and peak force coefficient obtained before and after matching the measured and calculated force-time response for all helical piles are presented in Figure 3-19. Figure 3-19b shows the peak force coefficient plotted against the adjusted impedance ratio. It can be seen that the pile impedance ratio was ≥ 1. Hence, the pile impedance $Z = \rho CA$, considering a uniform cross-section in the D-R model is not valid for helical piles, and Z should be revised to account for impedance increase due the helices. This also indicates that the selected combination of hammer and cushion material are insufficient to produce enough energy to mobilize the end-bearing resistance of helical piles. Some of the energy will be lost due to the separation of the cushion for the top of the pile as the hammer rebounds.

The impedance increase caused by the helices is plotted against the normalized force ratio for both single and double helices in Figure 3-19b and Figure 3-19c. In these figures, $Z-$Helical pile is impedance of the helical pile obtained from its force-time response history and $Z-$Shaft = ρCA. It is clear that the helical pile impedance (with the effect of the helices) is much higher than the impedance considering the shaft only. In general, Z-Helical pile to Z-Shaft ratio ranged from 1 to 4.1 with an average value of 2.1. It is also noted that the ratio $Z-$ Helical pile to $Z-$ Shaft for the same helical pile is approximately the same despite the change in hammer drop height.

The increase in pile impedance due to the helices varied from pile to pile, even for piles of the same geometry, which is attributed to the influence of the soil stratum at the location of the helices. The soil mass near the helix or enclosed between the helices provides additional resistance, especially for piles with low shaft impedance. Therefore, it is necessary to incorporate a concentrated soil mass, m_s, in the D-R model in order to correctly predict the force-time response for helical piles. The concept of added soil mass is adopted here and its influence on the dynamic behavior of helical piles as a function of helix size and number will be evaluated.

(a)

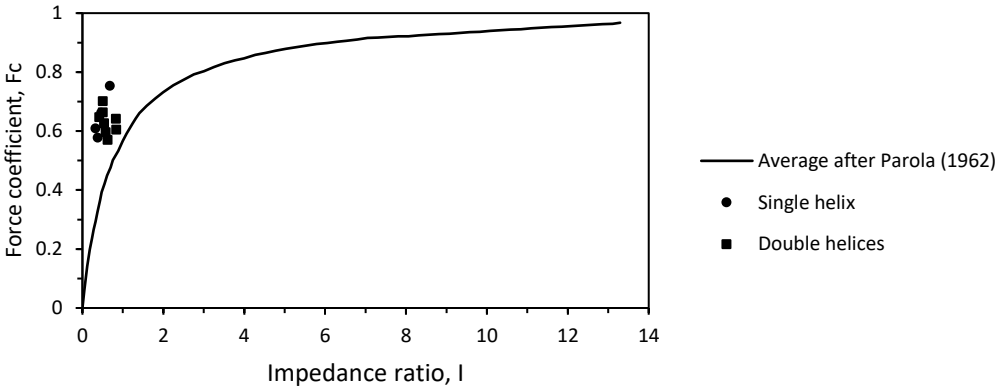
Force coefficient, Fc
Impedance ratio, I
Average after Parola (1962)
Single helix
Double helices

(b)

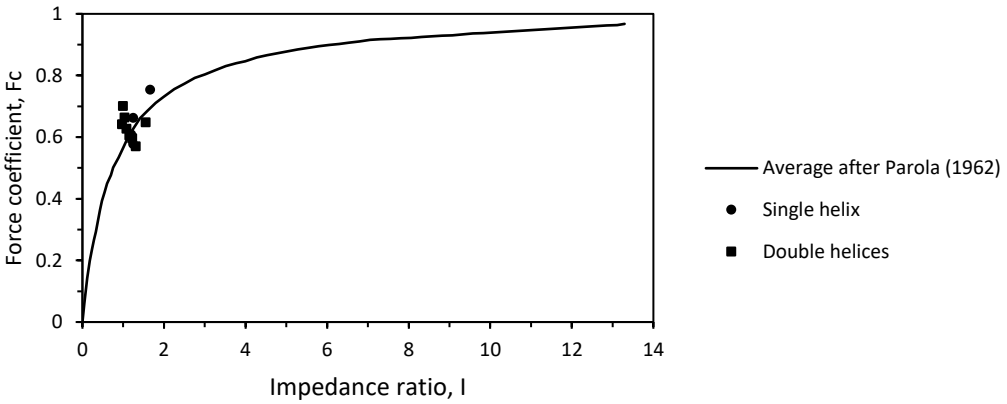
Force coefficient, Fc
Impedance ratio, I
Average after Parola (1962)
Single helix
Double helices

(c)

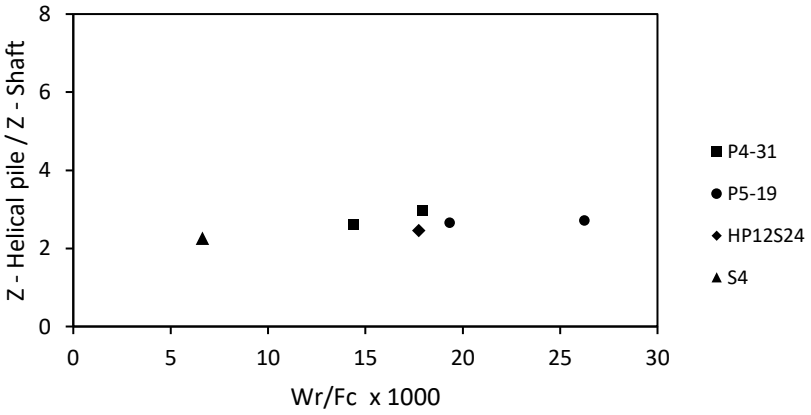
Z - Helical pile / Z - Shaft
Wr/Fc x 1000
P4-31
P5-19
HP12S24
S4

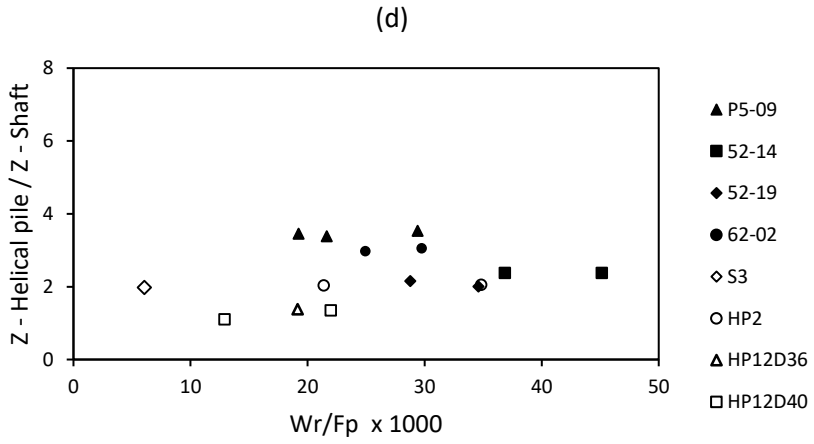

Figure 3- 19: Results of peak force coefficient and impedance ratio for helical piles; (a) peak force coefficient vs. impedance ratio assuming uniform shaft, (b) peak force coefficient vs. adjusted impedance ratio, (c) increase in pile impedance caused by single helix, and (d) increase in pile impedance caused by double helices.

3.6.1. Single-Helix Pile

The form of the D-R model and its associated parameters are kept the same, and only the dashpot Z is revised to account for the effect of the helix. The added soil mass model is adopted herein to account for the change in impedance caused by the helix. The influence of soil is incorporated in the helical pile model as a lumber mass, m_s. The soil is assumed to be fully attached to the bottom of the helix as shown in Figure 3-20. The added mass is obtained for a soil cylinder with a diameter and height equal to the helix diameter as shown in Figure 3-20. The shaft impedance can be rewritten as:

$$Z = \frac{M_p C}{L} \tag{3.48}$$

$$M_p = \rho_{pile} L A \tag{3.49}$$

The overall impedance of a helical pile with a single helix can be then given by:

$$Z_H = \frac{M_P C}{L} + \frac{M_s V_p}{d_{helix}} \tag{3.50}$$

Where: $M_s =$ Mass of the added soil $= \rho_{soil}\, d_{helix} A_{helix}$, $V_P =$ soil compression wave velocity and ρ_{pile} and ρ_{soil} are pile and soil unit weight. Finally, $A =$ shaft area and $A_{helix} =$ helix area.

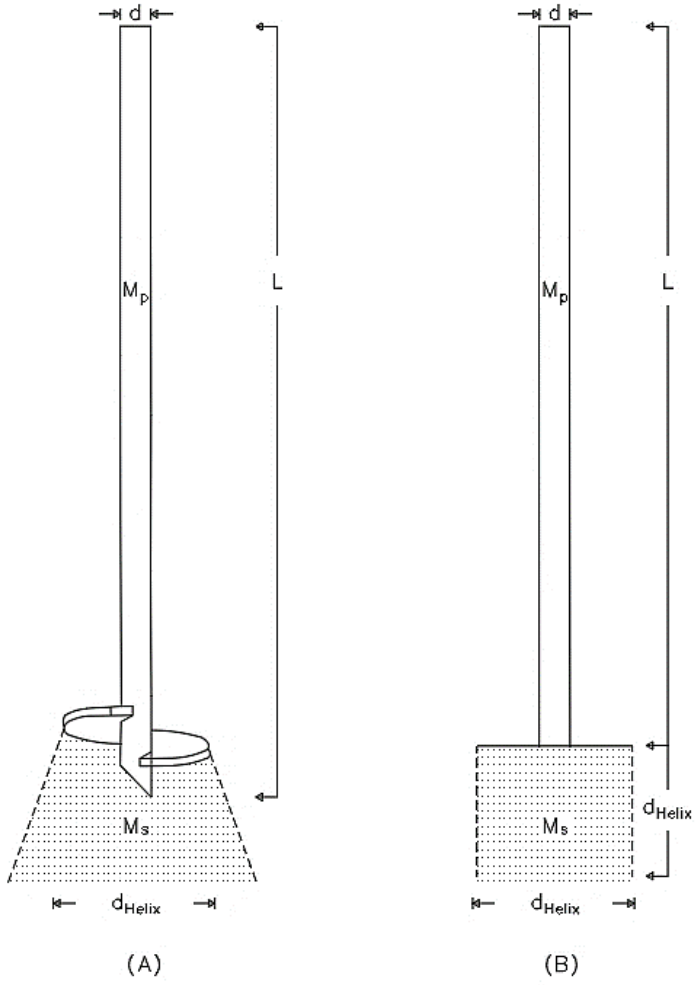

Figure 3- 20: Single-helix pile model: a) physical, and b) idealized.

Pile S4 is used here to compare the prediction of equation 3-50 for increase in helical pile impedance due to the helix with the estimated increase in impedance based on the matching process. Pile data is as follows: diameter, $d = 324\ mm$; wall thickness, $t = 9.5\ mm$; $d_{helix} = 610\ mm$; ; $L = 9\ m$; $\rho_{pile} = 7997\ kg/m^3$; and $C = 5124\ m/s$. Also, $\rho_{soil} = 1784\ kg/m^3$; and $V_p = 1500\ m/s$.

Thus; $M_P = 675.56\ kg$; $M_s = 318.02\ kg$; and $\frac{Z_H}{Z_{shaft}} \approx 3$.

This value is in reasonable agreement with that estimated from the signal matching process as depicted in Table 3-4, which also shows other examples.

Table 3- 4: Comparison between the estimated impedance from signal matching and the calculated impedance from equation 3.50.

Pile Name	Estimated [Z - $_{\text{Helical pile}}$ / Z - $_{\text{Shaft}}$]	Calculated [Z - $_{\text{Helical pile}}$ / Z - $_{\text{Shaft}}$]
S4	2.30	3.00
P5-31	2.59	2.62
P5-19	2.65	2.86
HP12S24	2.46	2.89

3.6.2. Double-helix Pile

For helical piles with two helices, the mass of soil within the inter-helix cylinder is taken as the added mass that moves with the vibrating pile, and is idealized as shown in Figure 3-21. This assumption is consistent with the cylindrical shear failure mechanism (Livneh and El Naggar, 2008; Aydin et al., 2011).

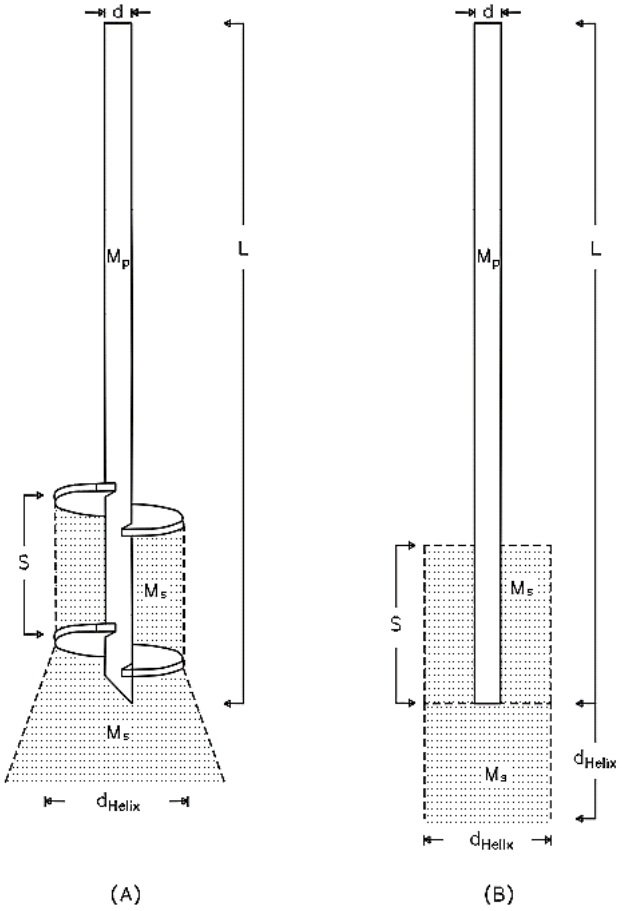

Figure 3- 21: Double-helix pile model: (a) physical, and (b) idealized.

Similar to the case of single-helix piles, the impedance for a double helix pile may be given by the following equation.

$$Z_H = \frac{M_P C}{L} + \frac{M_s V_p}{S + d_{helix}} \quad (3.51)$$

Where, M_s = Mass of added soil = ρ_{soil} $[S(A_{helix} - A_{OD}) + d_{helix}A_{helix}]$; A_{OD} = gross area of shaft; A_{helix} = helix and S = Inter-helix spacing.

The first part of Equation 3.51 represents the impedance of uniform pile and the second part accounts for the effect of added soil mass on pile motion. Table 3-5 compares the results obtained using equation 3.51 and those obtained from signal matching of tested double-helix piles. The good agreement between the two sets indicate the ability of equation 3.51 to predict the impedance of double-helix piles during HSDT.

Table 3- 5: Comparison between the estimated impedance from signal matching and the calculated impedance from equation 3.51.

Pile Name	Estimated [Z - Helical pile / Z - Shaft]	Calculated [Z - Helical pile / Z - Shaft]
S3	1.98	2.40
HP12D40	1.34	1.77
HP12D36	1.37	1.62
P5-09	3.45	3.05
52-18	2.96	2.48
62-02	2.95	2.82
HP2	2.04	2.51
52-19	2.15	2.17
52-14	2.37	2.18

3.7. Mobilized Soil Resistance

The reliability of the HSDT to predict long-term static capacity still has some uncertainties. Several studies attempted to correlate the capacity predictions from the HSDT with the SLT (Likins et al., 1996; Seidel et al., 1984; Duzceer et al., 2002; Long, 2009). These correlations have indicated that bearing capacity from dynamic measurements is generally conservative. Perhaps, this is because these studies did not assess the hammer-cushion-pile system that would lead to a good match between the predictions of pile capacity from SLT and HSDT (i.e. mobilized soil resistance ratio (Static/Dynamic) ≈ 1).

Figure 3-22a shows the variation of the ratio of the static pile capacity to the mobilized static capacity from HSDT with impedance ratio, whereas the variation of the measured displacement at the pile head with impedance ratio is depicted in Figure 3-22b. The impedance ratio was calculated using a pile impedance in accordance to $Z = \rho AC$ for driven pile and Z_H for helical pile (equation 3.50 and equation 3.51). The data is represented in terms of impedance ratio because it relates the hammer and cushion characteristics with the characteristic of the tested pile in one dimensionless value. Most of the observed data are spread within 1 standard deviation (σ) on each side of the mean (μ). The coefficients of variation for the data in Figures 3-22 a and b were 0.257 and 0.401, respectively. This means that the observed data are clustered around the mean.

The scatter observed in the data presented in Figure 3-22 is attributed to the variation of the hammer and cushion characteristic used during the HSDT. This highlights the need for guidelines described as a function of the hammer-cushion characteristics and pile displacement to better predict pile's capacity from dynamic measurement.

A set of guidelines are proposed to define the required characteristics of hammer weight and cushion stiffness to provide the input force at the pile head that is sufficient to mobilize the static capacity for piles in cohesive soil. These guidelines are derived based on observations from the analysis of the investigated case histories and from Figure 3-22.

1. HSDTs should be accompanied with at least one SLT for calibration.
2. Soil strength is expected to be higher when HSDT results are obtained based on Beginning Of Restrike (BOR) to determine pile capacity with a minimum restrike period of six days or at least based on a restrike condition.
3. The Impedance ratio, I, should be kept between 0.7 and 0.9 with corresponding damping, D, between 0.7 and 1.1.
4. The displacement at the pile head should generally be larger than 9 mm for driven piles and 13 mm for helical piles.
5. The drop height is a critical parameter in simulating load-displacement curve. Selecting one representative blow, with the highest energy, seems to overestimate the piles' response. The derive load-displacement curve would represent stiffer response and higher capacity compared to the load-displacement curve obtained

from several blows. It is recommended to carry out a multi blow test with increasing drop height. For each height, the load-displacement curve is obtained, and the mobilized static resistance of the soil is determined. The derived static load-displacement curve is then constructed by a best-fit curve that passes through the curves form each height.

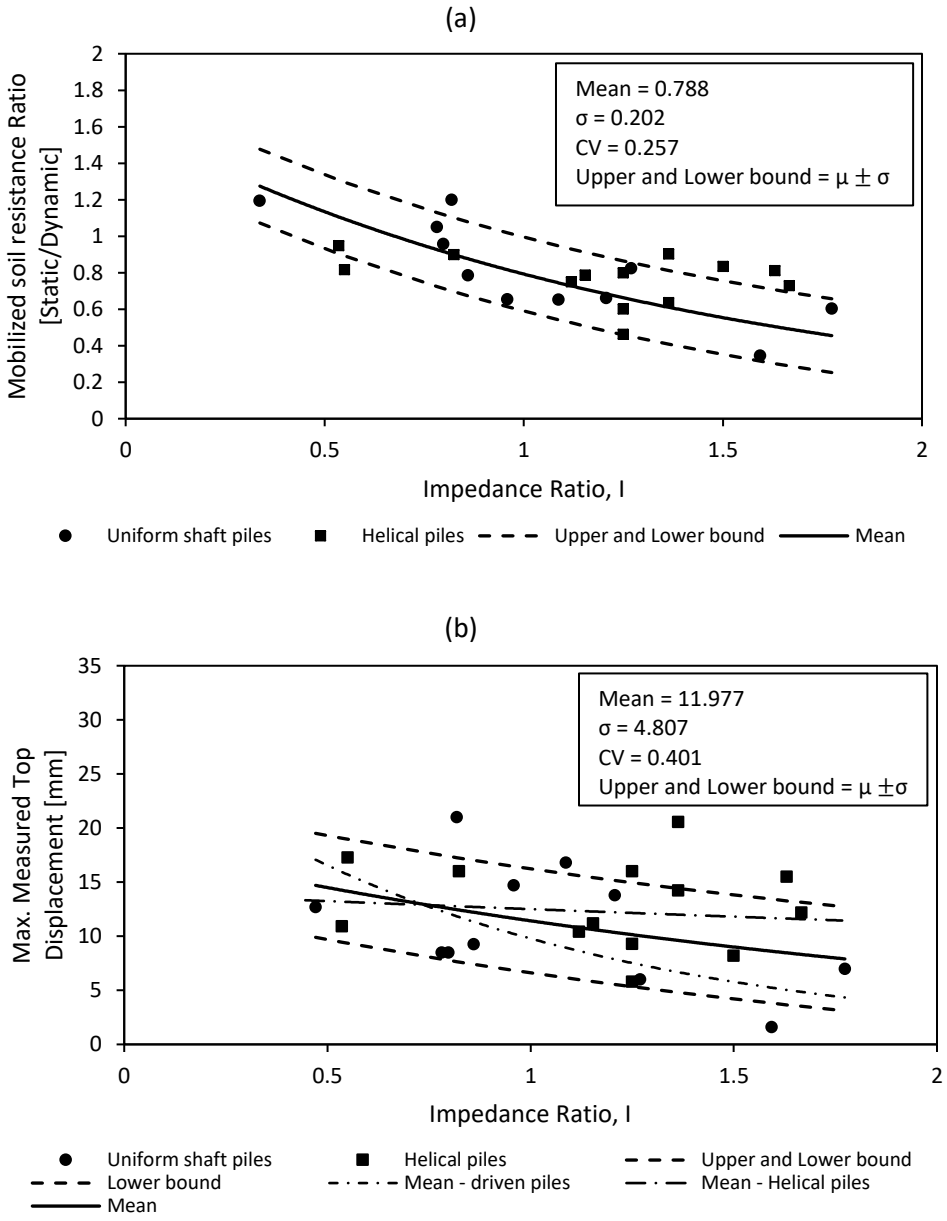

Figure 3- 22: Mobilized soil resistance at various pile impedance: (a) for the top measured displacement at the pile head (b) for cohesive soil.

3.8. Conclusion

A mathematical model to evaluate the force-time response generated at the top of a pile due to a hammer impact during High Strain Dynamic Test (HSDT) is presented and employed to analyze several cases studies. The model consists of a hammer, a cushion stiffness, and a pile. The model predictions agreed with measured field data such as peak force generated, shape of force time history, and total time response. The mathematical model was modified to investigate the force-time response generated at the head of helical piles with different geometries. The results of the modified model compared well with field data of 14 case histories. Based on the findings of analysis of 11 driven piles and 14 helical piles, the following conclusions are made:

1. The hammer-cushion-pile system response is governed mainly by the equivalent cushion stiffness, and pile impedance. For systems with an impedance ratio ≥ 1, the force pulse is approximately a half-sine wave. For impedance ratio < 1, a sharp peak is developed over a short time followed by an abrupt reduction in force. This behavior becomes more pronounced as the impedance ratio decreases.
2. The cushion stiffness used in HSDT has a significant effect on the generated pulse shape. Stiffer cushions produce short time impact and increase the peak force at the head of the pile, compared to a softer cushion which elongates the pulse time and reduces the peak force transmitted to the pile head.
3. The hammer-cushion-pile system damping, D, which represents energy dissipation by the pile, influences the impact force time history. When $D \geq 1$, the force time history can be expressed by an exponential and non-periodic function. The attenuation of the force slowly returns to equilibrium without the development of negative force. When $D < 1$, the force time history is both exponential and goniometric, thereby is periodic in shape.
4. The force at pile head becomes negative (i.e. hammer rebounds) when the impact time is greater than the time t_0. As D increases, hammer rebound is less likely to occur; hence, more kinetic energy is transferred to the head of the pile (i.e. higher force to mobilize pile capacity). Nevertheless, overdamped system could cause

excessive compressive and tensile stresses above the recommended limit stresses and damage the pile. Monitoring such a system is necessary.

5. The maximum force occurs at a time, t, equal to the inverse of the natural frequency, ω, of the hammer-cushion-pile system.
6. The force pulse shape and behavior at the pile head is significantly influenced by the impudence ratio of the selected system.
7. Increasing the pile impedance will case the damping to be reduced and vice versa.
8. When selecting cushion and hammer system for HSDT of piles installed in cohesive soil, it is recommended to have impedance ratio, I, between 0.7 and 0.9 with corresponding damping, D, between 0.7 and 1.1. This leads to a better derived static response from dynamic measurements.
9. It is necessary to account for increase of helical pile impedance due to its helices, especially for large helical piles. Modifying the helical pile impedance considering an added soil mass (equations 3.50 and 3.51) provide good estimate of helical piles impedance and should be used when designing HDST for helical piles (i.e. selection of a hammer and cushion material to produce enough energy to fully mobilize helical pile capacity).

Finally, it should be emphasized that more field tests are essential to support the outcomes of this work, especially for HSDT on helical piles.

3.9. References

Aydin, M., Bradka, T. D., & Kort, D. A. (2011). Osterberg cell load testing on helical piles. In Geo-Frontiers 2011: Advances in Geotechnical Engineering. pp. 66-74.

Basarkar, S. S., Kumar, M., & Vaidya, R. (2011). High strain dynamic pile testing practices in india-favorable situations and correlation studies. In Proceedings of Indian Geotechnical Conference, Kochi. Paper No. Q-303.

Beim, J., & Luna, S. C. (2012). Results of dynamic and static load tests on helical piles in the varved clay of Massachusetts. DFI Journal-The Journal of the Deep Foundations Institute, 6(1): 58-67.

Beim, J., & Niyama, S. (2000). Application of stress-wave theory to piles: quality assurance on land and offshoring piling. A.A. BALKEMA, Rotterdam, Netherlands. ISBN: 90 5809 150 3.

Benamar, A. (2000). The shaft dynamic response of a pile in clay: induced pore pressure. Proceedings of the International Conference on the Application of Stress-Wave Theory to Piles, Sao Paulo, Brazil. pp. 255-260.

Borgman, L. E., Bartel, W. A., & Shields, D. R. (1993). SIMBAT theoretical manual (No. NCEL-TR-941). NAVAL CIVIL ENGINEERING LAB PORT HUENEME CA.

Cannon, J. G. (2000). The application of high strain dynamic pile testing to screwed steel piles. In Sixth International Conference on the Application of Stress-Wave Theory to Piles. pp. 11-13.

Das, B., Ramana, G.V. (2010). Principles of soil dynamics. Cengage Learning, Inc. ISBN: 0495411345.

Deeks, A. J., & Randolph, M. F. (1993). Analytical modelling of hammer impact for pile driving. International Journal for Numerical and Analytical Methods in Geomechanics, 17(5): 279-302.

Edde, R. D. (1991). Case pile wave equation analysis: CAPWAPC evaluation of driven piles. [Master thesis]. University of Ottawa, Ottawa, Canada.

Elkasabgy M. (2011). Dynamic and static performance of large-capacity helical piles in cohesive soils. [Doctoral thesis]. University of Western Ontario, London, Ontario, Canada.

Elsherbiny, Z. H., & El Naggar, M. H. (2013). Axial compressive capacity of helical piles from field tests and numerical study. Canadian Geotechnical Journal, 50(12): 1191-1203.

Elkasabgy, M., & El Naggar, M. H. (2014). Axial compressive response of large-capacity helical and driven steel piles in cohesive soil. Canadian Geotechnical Journal, 52(2): 224-243.

Forehand, P. W., & Reese, J. L. (1964). Prediction of pile capacity by the wave equation. Journal of the Soil Mechanics and Foundations Division, 90(2): 1-26.

Geotechnology, Inc. (2013). High-Strain Dynamic Pile Testing Report. Livingston County, USA. Project No. J019907.01.

Green, T. A. L., & Kightley, M. L. (2005). CAPWAP testing-theory and application. Proceedings of the international conference on soil mechanics and geotechnical engineering, A.A. BALKEMA Publishers, 16(4): 2115-2118.

GRL Engineers, Inc. (1997). Case Pile Wave Analysis Program. GRL Engineers, Inc. Cleveland, OH, USA.

Halder, A. K. (2016). Pile load capacity using static and dynamic load test. [Master thesis]. University of Engineering and Technology, Dhaka, Bangladesh.

Hannigan, P. J., Goble, G. G., Thendean, G., Likins, G. E., & Rausche, F. (1997). Design and construction of driven pile foundations-volume and Volume II. National Highway Institute. Federal Highway Administration.

Hertlein, B., & Davis, A. (2007). Nondestructive testing of deep foundations. John Wiley & Sons, Inc.

Hirsch, T. J., & Edwards, T. C. (1966). Impact load-deformation properties of pile cushioning materials. Texas Transportation Institute.

Holeyman, A.E. (1992). Technology of Pile Dynamic Testing. Proceedings, Fourth International Conference on the Application of Stress-Wave Theory to Piles, F.B.J. Barends ed., The Hague. Balkema, Rotterdam, the Netherlands. pp.195-215.

Hussein, M. H., Likins, G. E., & Hannigan, P. J. (1993). Pile evaluation by dynamic testing during restrike. In Proceedings of the Eleventh South East Asian Geotechnical Conference, Singapore. pp. 535-539.

Likins, G. E., & Rausche, F. (2004). Correlation of CAPWAP with static load tests. In Proceedings of the Seventh International Conference on the Application of Stress wave Theory to Piles. pp. 153-165.

Likins, G. E., Rausche, F., & Goble, G. G. (2000). High strain dynamic pile testing, equipment and practice. In Proceedings of the Sixth International Conference on the Application of Stress-wave Theory to Piles. pp. 327-333.

Likins, G., Rausche, F., Thendean, G., & Svinkin, M. (1996). CAPWAP correlation studies. In Proceedings of the Fifth International Conference on the Application of Stress-Wave Theory to Piles, Orlando, FL. pp. 447-455.

Livneh, B., & El Naggar, M. H. (2008). Axial testing and numerical modeling of square shaft helical piles under compressive and tensile loading. Canadian Geotechnical Journal, 45(8): 1142-1155.

Long, J. H. (2009). Comparison of five different methods for determining pile bearing capacities. Wisconsin Highway Research Program.

Long, J. H., Hendrix, J., & Jaromin, D. (2009). Comparison of five different methods for determining pile bearing capacities. Wisconsin Highway Research Program. (No. WisDOT 0092-07-04).

Lowery, L. (1993). Pile driving analysis by the wave equation. Wild West Software: Bryan, Texas.

Lowery, L., Hirsch, T. J., & Samson, C. H. (1967). Pile driving analysis: simulation of hammers, cushions piles and soils. Texas Transportation Institute, Texas A & M University. Research Study No. 2-5-62-33.

Mabsout, M. E., & Tassoulas, J. L. (1994). A finite element model for the simulation of pile driving. International Journal for numerical methods in Engineering, 37(2): 257-278.

Pile Dynamics, Inc. (n.d.). CAPWAP software. Cleveland, OH, USA.

Poulos, H.G. 1998. Keynote lecture: Pile testing-From the designer's viewpoint, Proceedings 2nd International STATNAMIC seminar, Tokyo, Japan. pp. 3-21.

Rajagopal, C., Solanki, C. H., & Tandel, Y. K. (2012). Comparison of static and dynamic load test of pile. Electronic Journal of Geotechnical Engineering, Vol. 17.

Sakr, M. (2013). Comparison between high strain dynamic and static load tests of helical piles in cohesive soils. Soil Dynamics and Earthquake Engineering, Vol. 54; 20-30.

Seidel, J., & Rausche, F. (1984). Correlation of static and dynamic pile tests on large diameter drilled shafts. 2nd International Conference on the Application of Stress Wave Theory on Piles, Stockholm, Sweden.

Smith, E. A. (1962). Pile-driving analysis by the wave equation. American Society of Civil Engineers Transactions.

Svinkin, M. R. (2000). Modulus of elasticity and stiffness of composite hammer cushion. In Proceedings on the Sixth International Conference on the Application of Stress Wave Theory to Piles, Sao Paulo, Brazil. pp. 11-13.

TNO report. (1996). TNO-DLT Dynamic Load Testing Signal Matching, User's Manual.

Vaidya, R. (2006). Introduction to high strain dynamic pile testing and reliability studies in southern India. In Proceedings of Indian Geotechnical Conference, Chennai, India. pp. 901-904.

Viggiani, C., Mandolini, A., & Russo, G. (2012). Piles and pile foundations. New York, Spon Press, Inc.

Van Kotten, (1977). Dynamic Pile Testing. TNO for Building Materials and Building Structures, Report, the Netherlands.

CHAPTER FOUR

FINITE ELEMENT ANALYSIS OF HELICAL PILES SUBJECTED TO AXIAL IMPACT LOADING

Chapter 4 : Introduction

Helical piles are an efficient foundation option for a wide range of engineering projects that require high compressive and uplift resistance to static and dynamic loads. In view of the large capacity of large diameter helical piles, there is a need to determine their capacity using accurate and economically feasible testing techniques. Recently, the high strain dynamic test (HSDT) has been applied to large diameter helical piles (Cannon, 2000; Beim & Luna, 2012; Benjamin White, n.d.; and Sakr, 2013). The behavior and analysis of single vertical helical piles subjected to static loading is well investigated (e.g. Livneh and El Naggar, 2008; and Elsherbiny and El Naggar, 2013). However, a few studies investigated the dynamic behavior of single helical piles and the load transfer under axial dynamic loading (Bakker et al., 2010; Elkasabgy and El Naggar, 2013; Fakharian et al., 2014; and Keshavarz et al., 2016).

For axial static loading, the limit equilibrium method is usually employed to estimate the theoretical axial capacity of helical piles, i.e., the static equilibrium of the pile at the onset of failure of the soil around the pile. This requires identifying the failure surface and shape of failed soil mass. Accordingly, two possible failure mechanisms are considered for helical piles with multiple helices: individual bearing failure; or cylindrical shear failure. Analyses of helical piles subjected to axial compressive demonstrated that the governing failure mechanism depends on the inter-helix spacing and the type of soil within the inter-helix zone (Elsherbiny and El Naggar, 2013; and Elkasabgy and El Naggar, 2015). However, no similar characterization for the failure mechanism under axial impact loading. To correctly plan, execute and interpret HSDT to helical piles, there is a need to establish their failure mechanism under axial impact loading. Finite element analysis offers a

powerful tool for identifying the failure surface and shape of failed soil mass under static and dynamic loading.

An axisymmetric finite model enables simulating a three-dimensional geotechnical problem that is rotationally symmetric about an axis using 2-dimensional (2D) inputs. The analysis in this model is carried out as an asymmetric 3-dimensional (3D) problem. The axisymmetric model is suitable for uniform circular sections and loading schemes around the axis of symmetry. It assumes stresses and deformations in all directions to be equal. Several studies have been conducted and published on modelling piles under axial static and dynamic loads using axisymmetric models (Bakker et al., 2010; Khelifi et al., 2011; Fakharian et. al, 2014; Osula et al., 2016; Popa et al., 2018; Farshi & Hamidi, 2017; and Alnuaim et al., 2018). The results of these studies compared well with the measured results obtained from full-scale load tests or small-scale laboratory tests.

In order to accurately model the soil response during static and impact loads caused by the SLT and the HSDT, the model boundaries should be placed far enough from the test pile to minimize the boundary effects. Krasiński (2014) simulated static load tests on helical piles employing 2D axisymmetric models. He reported that the model with the vertical boundary placed at a distance equal to 12 times the diameter of the pile from the axis of symmetry and the bottom boundary placed at a distance equal to 1.4 times the pile length below the pile toe was sufficient to simulate the SLT well. Limas & Rahardjo (2015) simulated the static load test conducted on bored piles using 2D axisymmetric models, which is approximately equivalent to the pile length in the horizontal direction and 1.2 the pile length in the vertical direction. The generated load-displacement curve from the numerical model matched the curve obtained from field testing, confirming that the fixed boundary had no effect on the results. Lv et al. (2017) utilized a 3D finite element model to investigate the effect of drag-load on single piles with different geometry that are situated in consolidating ground. They used roller supports at the side boundaries and pinned support at the bottom boundary. The geometry of the numerical model extended laterally 15 times the pile diameter (also equal to pile length) from the centre of the pile and extended vertically 1.7 times the pile length below the ground surface. The calculated results compared well with the measured results from three centrifuge model tests. Hence,

the position of the structure in relation to the boundary distances of the model was sufficient to minimize the boundary effects.

Bakker et al. (2010) simulated a STATNAMIC load test for a large diameter piles using an axisymmetric model with roller support at the side boundary conditions and fixed boundary at the bottom. The model boundaries were extended vertically to a total length equal to 4 times the pile length and horizontally to a total radius of about 6 times the pile length. They used the large size model because no absorbing boundaries were used. Fakharian et al. (2014) utilized 2D non-linear axisymmetric model to simulate the HSDT on a driven pile considering both End-Of-Drive (EOD) and Beginning of Restrike (BOR). The model boundary extended laterally about 13 times the pile diameter and vertically 1.3 times the pile length. Viscous boundaries were adopted to prevent wave reflections. Similarly, Keshavarz et al. (2016) analyzed the response of floating piles under dynamic axial loading employing an axisymmetric 2D model with a geometry domain size twice the shaft length in the vertical direction and a pile length in the horizontal direction. They assigned absorbing boundaries both vertically and at the bottom. The numerical results were in excellent agreement with the results obtained from the field tests.

It is concluded from the discussion above that 2D axisymmetric finite element models are suitable for simulating the axial behavior of piles under static and dynamic loading. For optimized accuracy and computing efficiency, the model vertical boundary should be placed at a distance L from the model center and the bottom boundary should be placed at a depth 2L below ground surface.

4.1. Case Histories of HSDT on Helical Piles

Two case histories are considered herein for the validation of the developed finite element models. Case 1 involved HSDT on a helical pile with a single helix installed in saturated sand. The site is located at an industrial facility in Kent, Washington (CH2M HILL, 2013). The stratigraphy of the site can be divided into four distinctive layers. Layer 1 was comprised of an irregular mixture of gravel with sand and silt and extended to about 2.1 m below the ground surface. Layer 2 is a firm sandy silt 11.6 m thick. Layer 3 was 3.7 m thick and comprised saturated medium dense fine-grained sand with low to non-plastic silt.

Layer 4 4 was loosely compacted sand with silt and its thickness varied between 24 m to 30 m. The depth of the groundwater in the piezometer at the testing time was 2.1 m below the ground surface. The helical pile was 24.3 meters long, with an outer shaft diameter of 178 mm and wall thickness 11.5 mm. The helix was located at a depth of 24 m and had a diameter of 457 mm, a thickness of 19 mm, and a 133 mm pitch. The HSDT was performed using an open-end diesel hammer 3 days after completing a SLT. A series of impacts was generated by dropping a 48 kN weight form a maximum distance of 1.7 m.

In Case 2, the HSDT was carried on a helical pile with double-pitched bearing plates that was installed in cohesive soils located 12 km away from the north of Ponoka, Alberta, Canada (Sakr, 2013). The helical pile was 9 m long with a diameter of 324 mm and a wall thickness of 9.5 mm. The helix plates were 610 mm in diameter and 19 mm thick. The helices were spaced at a distance equal to 915 mm. The HSDT was performed based on a re-strike condition. A drop hammer system with a weight of 19 kN dropped for a distance of 0.9 m was used. The strike was transferred first to a pile cushion before it reached the top of the pile to minimize breakdowns and wear. Dynamic measurements in both cases were measured and recorded using a Pile Driving Analyzer (PDA). Post-processing of the recorded data with the highest energy was done by the CAPWAP. Schematic representation of the soil profile at the site is presented in Figure 4-1.

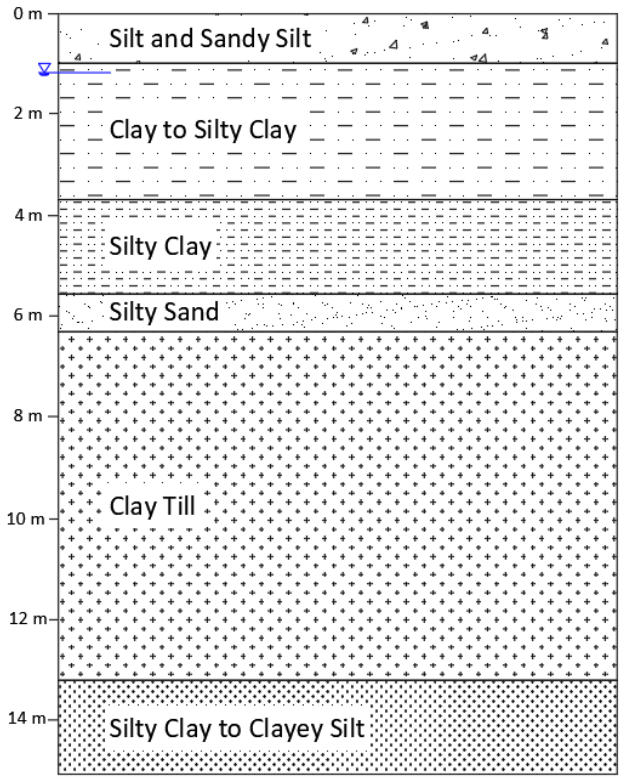

Figure 4- 1: Stratification of soil layers from the surface exploration tests and groundwater level for case 2 after Elkasabgy & El Naggar (2018).

The analysis of the HSDT conducted on helical piles in both case histories is simulated using a 2D axisymmetric finite element model employing the finite element program Plaxis 2D (Plaxis, 2018). To establish the failure mechanism, finite element models were developed and verified using two case histories of HSDT on helical piles.

Due to the symmetry along the vertical axis, only half of the model geometry is defined. A general outline of the model and its idealized axisymmetric geometry are shown in Figure 4-2. The vertical y-axis corresponds to the line of symmetry, and the x-axis denotes the radial direction. The soil medium and the helical pile are represented by 15-node triangular elements because they are suitable for the analysis of soil subjected to large deformations such as prediction deformations caused by axial dynamic loads (Bakker et al., 2010; and Fakharian et. al, 2014). Thus, the depth of the soil model is set to the greater of 2L or the reported borehole depth.

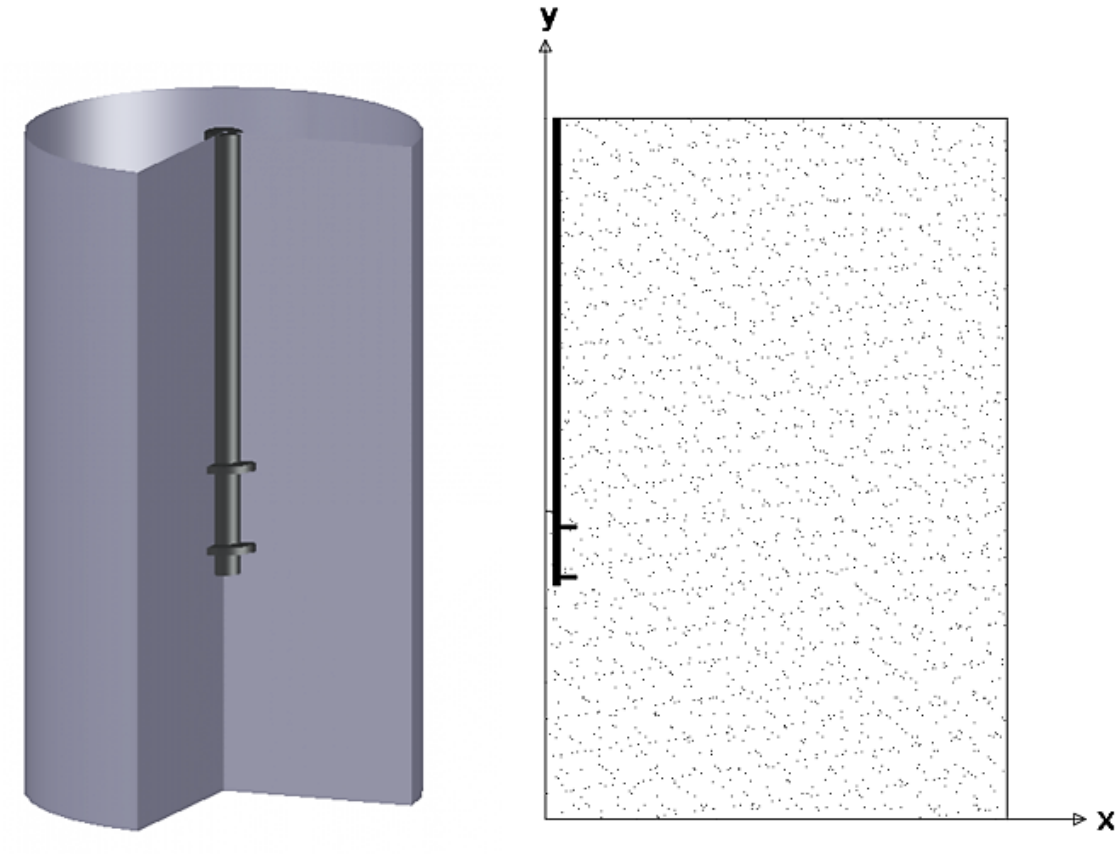

Figure 4- 2: General outline of the 3D model (left) and 2D axisymmetric (right).

Figure 4-3 shows the axisymmetric model used in this study to simulate static and dynamic load tests conducted on helical piles in sand and clay. The external boundaries for Case 1 were situated 25 m laterally from the model center and 44 m below the ground surface. For Case 2, the model boundaries were placed 18 m from the axis of symmetry and 30 m below the ground surface.

For static load simulation, the bottom boundary was restricted from movement in vertical and horizontal directions. Roller supports are assigned to the side boundaries, i.e., horizontal movement is restricted, and a free deformation boundary is assigned to the top of the model. For dynamic simulation, absorbing boundaries are assigned to the vertical and bottom model boundaries to represent the far-field behavior of the soil medium. This is accomplished by using viscous boundaries which absorb the propagated wave energy caused by the dynamic loading; hence, prohibit any wave reflection inside the soil medium. Plaxis 2D applies viscous dampers at the extreme boundaries in both x and y direction.

More information about the behavior of the viscous dampers can be found in Lysmer & Kuhlemeyer (1969).

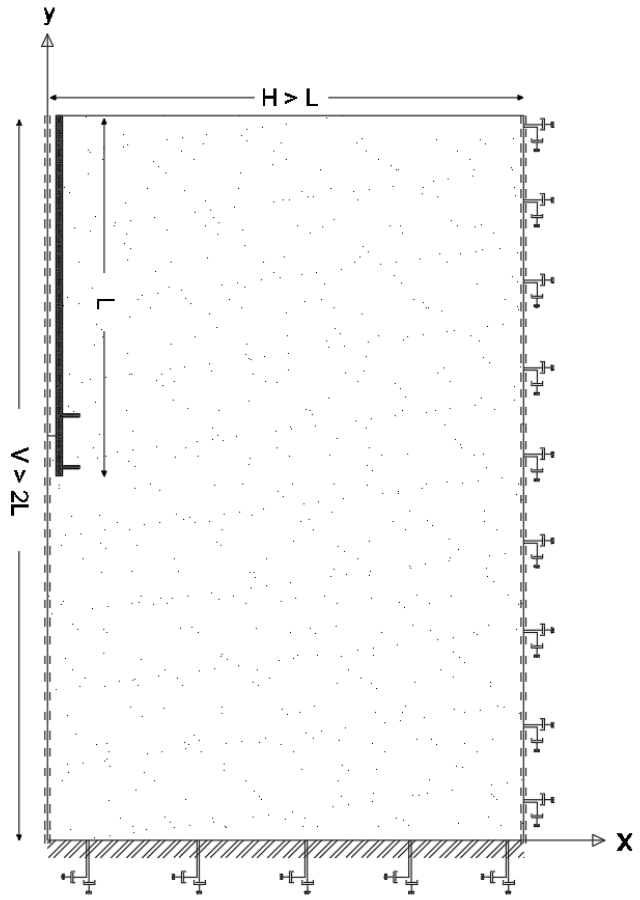

Figure 4- 3: Model geometry size and boundary conditions for FEM.

4.2. Soil Material Model

Two material models are frequently used to simulate the soil mechanical behavior under static and dynamic axial loading: the Mohr-Coulomb (MC) model, and the Hardening Soil (HS) model. The Mohr-Coulomb (MC) model considers the soil behaviour to be linear elastic perfectly plastic and is commonly used due to its simplicity. It requires basic soil parameters, including: cohesion, friction angle, dilation angle, elastic modulus and Poisson's ratio. However, the MC model is limited in terms of simulating soil non-linearity and inelasticity (Teo & Wong, 2012; Rani et al., 2014; and Plaxis, 2018), which can lead

to unrealistic simulation of the soil behavior and inaccurate results (Çelik, 2017). The Hardening Soil (HS) model can better simulate the soil non-linear behavior when subjected to changes in strain and stress, and provides more realistic results in comparison to the MC model. The required input parameters to describe the soil behavior in the HS model are presented in Table 4-1. The formulation of the HS model incorporates two hardening mechanisms; shear hardening and compression hardening, which makes it suitable for simulating both stiff and soft soils (Schanz & Vermeer, 1998; and Obrzud & Truty, 2018). This is accomplished by incorporating three input stiffness parameters corresponding to the secant triaxial loading stiffness (E_{50}^{ref}), the elastic unloading-reloading stiffness (E_u^{ref}), and the tangent oedometer loading modulus (E_{oed}^{ref}). The HS model is selected to simulate the soil behavior for both static and dynamic applications as it accounts for loading history and is suitable for both sand and clay.

Table 4- 1: Basic parameters in the HS model.

Parameter	Definition	Unit
E_{50}^{ref}	Secant stiffness in standard drained triaxial test	kPa
E_{oed}^{ref}	Tangent stiffness for primary oedometer loading	kPa
E_u^{ref}	Unloading/reloading stiffness	kPa
m	Power for stress-level dependency of stiffness	-
$(c')\ c$	(Effective) cohesion	kPa
σ_t	Tension cut-off and tensile strength	kPa
$(\varphi')\ \varphi$	(Effective) angle of internal friction	Degree
ψ	Dilatancy angle	Degree

4.3. Soil Behaviour

The high impact loading at the pile head causes transient loading in adjacent soil. The rate of loading is faster than the rate of pore water pressure dissipation, hence excess pore water pressure develops, which affects the soil resistance. Holeyman (1992) reported that rate of loading during HSDT constrains the dissipation of excess pore water pressure, even for piles embedded in sand. Hölscher and Barents (1992) found that the consolidation time of generated pore water pressure in a dense sand layer varied from 100 to 200 ms, which is

longer than the typical HSDT duration. Therefore, the soil behavior would be undrained or partially drained. Huy (2006) indicated that dynamic drainage conditions have a significant role in the analysis.

A review of the literature shows that impact loads cause a disturbance or a remolding of the cohesive soils near to the pile, in addition to the generation of excessive pore water pressure which does not have enough time to dissipate due to the rate at which the external load is applied (Airhart et al., 1967; Kequin & Jiayou, 1986; Morgano et al., 2008; and Elkasabgy & El Naggar, 2013). Several studies combined the pore water pressure effect and loading rate as a rate load effect (Charue, 2004; Huy et al., 2006; and Holscher & Van Tol, 2008). In general, the loading rate effect is stronger for cohesive soil compared to cohesionless soil (Goble et al., 1975). The rate effect on load-displacement behavior is considered in the analysis reported here.

Based on the discussion above and the short duration of loading, the behaviour of both sand and clay as simulated using the HS model under undrained conditions. For Case 1, the soil was saturated sand, with a water table near the ground surface; therefore, the soil behaviour was considered to be undrained (Undrained A). The soil profile in Case 2 comprised layers of silt and silty clay; thus, it is modelled considering undrained condition (Undrained B).

4.4. Parameter Determination of The Hardening Soil Model

4.4.1. Strength Parameters

The strength parameters in the HS model include cohesion, angle of internal friction, and angle of dilatancy. The sand model was set to be undrained and effective stress parameters were used to conduct the undrained effective stress analysis. However, it was difficult to obtain an accurate value for the friction angle, ϕ', for each layer because correlations based on SPT-N were used. The dilatancy angle, ψ, is quantified using the friction angle $\psi = \phi' - 30$ (Plaxis 2D, 2018). For Case 2, undrained shear strength, c_u, was used for each layer. The values suggested by Elkasabgy (2011) were used. The strength parameters used in the finite element models are presented in Table 4-2.

Table 4- 2: Soil strength parameters for the HS models.

Case	Soil type	Drainage type	Unit weight [kN/m³]		Peak Friction angle (φ) o	dilatancy angle (ψ) o	Undrained cohesion (c_u) [kPa]
			Wet	*Dry*			
Case 1	Site fill	Drained	20.4	20.4	37	7	-
	Firm sandy silt	Undrained (A)	16.5	14	31	1	-
	Denser sand	Undrained (A)	19.5	16	37	7	-
	Looser sand	Undrained (A)	19.2	16	33	3	-
Case 2	Silt and sandy silt	Drained	18.2	15.7	31	1	-
	Clay to silty clay	Undrained (B)	17.8	14	-	-	85
	Silty clay	Undrained (B)	17.8	14.1	-	-	137
	Silty sand	Drained	18.8	15	42	7	0
	Clay till	Undrained (B)	17.5	13.9	-	-	177
	Silty clay/clayey silt	Undrained (B)	18	14.3	-	-	150

4.4.2. Stiffness Parameters

The initial stiffness, E_i, was determined form Poisson's ratio, v, and shear modulus at small strain, G_{max}, measured from the seismic cone penetration test. Several researchers investigated the modulus degradation with the level of strain as a function of the mobilized stress level (LoPresti et al., 1993; Fahey and Carter, 1993; Mayne and Dumas, 1997; and Robertson, 2009). The modified hyperbola model is utilized here to reduce the initial stiffness, E_i, to secant modulus, E_s, at the working load level in terms of the mobilized stress relative to the ultimate stress (q/q_{ult}). The general expression of model is given by (Fahey and Carter, 1993):

$$\frac{E_s}{E_i} = 1 - f\left(\frac{q}{q_{ult}}\right)^g \qquad (4.1)$$

Where, $\frac{q}{q_{ult}}$ is the mobilized stress relative to the ultimate stress, and f and g are fitting parameters. Verbrugge & Schroeder (2018) indicated that the ratio is commonly between 0.05 and 0.3, depending on the level of strain. Based on the best match between measured and estimated pile load-displacement responses, an estimated modulus degradation ($\frac{E_s}{E_i}$) of 0.2 was used to reduce the initial stiffness, E_i, to a secant modulus, E_s. The adopted profiles for E_i and E_s in the numerical analysis for Case 2 are depicted in Figure 4-4.

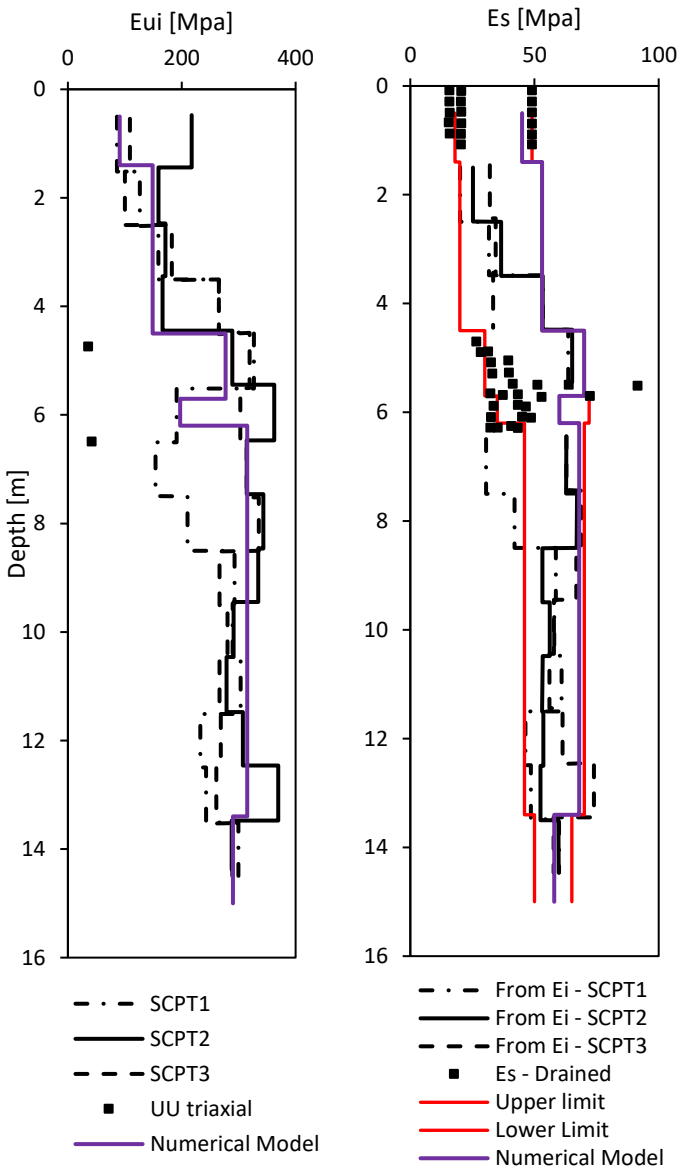

Figure 4- 4: Profile for the initial stiffness, Ei, and secant modulus, Es, for Case 2.

For Case 1, the deformation characteristics, including initial and secant modulus and shear modulus at low-strain and large-strain, were estimated from the SPT-N values along with the relationship between static and dynamic elastic modulus proposed by Alpan (1970). Considering the average static modulus of elasticity, $\frac{E_{dynamic}}{E_{static}} \approx 2$ was used. Table 4-3 presents the soil elastic modulus for Case 1.

Table 4- 3: Selected stiffness parameters for Case 1 sand model in Plaxis 2D.

Layer	E – static [kPa]	E – dynamic [kPa]
Site fill	14800	29600
Firm sandy silt	10700	21400
Denser sand	43000	86000
Looser sand	33800	60840

The relation between the secant modulus with the HS model stiffness parameters is as follows (Obrzud & Truty, 2018);

$$E_{50} < E_s < E_{ur} \tag{4.2}$$

E_{50} and E_{ur} are defined as the secant stiffness at 50% of the failure load and the stiffness obtained from the unloading-reloading curve, respectively. These values are determined from a triaxial compression test. Due to the absence of laboratory results, E_{50} and E_{ur} were approximated based on typical assumptions found in the literature. In the current analysis, $E_{50} = E_s$ was assumed, and $E_{ur} = 3E_{50} \approx 3E_s$ as recommended by Plaxis (2018). For granular soils, the stiffness E_{oed} defined as the tangent stiffness due to primary oedometer loading is approximated by $E_{oed} \cong E_{50}$ (Obrzud & Truty, 2018). For cohesive soils, $E_{oed} = 0.8\, E_{50}$ as recommended by Plaixs 2D (2018) is adopted.

4.4.3. Stress-Level Dependent Stiffness

In the hardening soil model, the exponent, m, is utilized to describe the stress-level dependency of stiffness. Typically, m varies between 0.3 to 1. In dense sand, the nonlinearity is more pronounced than in loose sand. Based on observations from oedometer tests, Van Soos (1991) proposed ranges of values of m for different sandy soils with varying grain size distribution. These ranges are presented in Table 4-4. For clayey soils,

typical m values are provided in Table 4-4. Accordingly, m = 0.5 is used for sand and silty sand soils, and m = 0.6 to 0.85 with an average of 0.7 for clay. These values resulted in good match between calculated and measured responses.

Table 4- 4: Typical values for m in cohesionless and cohesive soils.

Soil	Type	m	Reference
Sand	Fine, uniform	0.6 – 0.75	Van Soos (1991)
	Coarse, uniform	0.55 – 0.7	
	Well-graded and gravelly sand	0.55 – 0.7	
	With fines	0.65 – 0.9	
	Subround, and Subangular	0.41 - 0.51	Hoque and Tatsuoka (2004)
Silt	Low plasticity	0.6 – 0.8	Van Soos (1991)
	Medium to high plasticity	0.7 – 0.9	
Clay	Low to Medium plasticity	0.9 – 1	Van Soos (1991)
	High plasticity	1	
	London clay, and Speswhite kaolin clay	0.65 - 0.76	Viggiani and Atkinson (1995)
	Undisturbed cohesive soils	0.5	Kim and Novak (1981)

4.4.4. Groundwater Modelling

To account for the flow of pore water in the numerical analysis, the Van Genuchten model (Van Genuchten, 1980) is selected. The parameters of this model are defined according to soil type and soil grain size distribution. The United States Department of Agriculture (USDA) classification system was used in this study to classify the soil and select the flow parameters. In the analysis, the groundwater flow boundary conditions were set to Open.

4.4.5. Dynamic Properties

The soil dynamic properties, including shear modulus and damping ratio are used to describe the soil behavior during a dynamic loading event. In Plaxis, both viscous (radiation) damping and hysteretic (material) damping are accounted for. The former is considered in the analysis by means of Rayleigh damping, in which the damping matric, C, is expressed as a linear combination of mass, M, and a stiffness, K, matrices, i.e.:

$$[C] = \alpha[M] + \beta[K] \quad (4.3)$$

Where, α and β are Rayleigh coefficients. The effect of α is dominant in lower frequencies of vibration while β effect is dominant in high frequencies of vibration. The values of α and β are determined considering target frequencies. In the current analysis, a damping value of 5% was assumed and the target frequencies ($f_1 = \frac{V_S}{4H}$ and f_2 is the dynamic load predominant frequency) are obtained using the procedure suggested by Hashash and Park (2002). Where, V_s = Soil shear wave velocity and H = Soil layer thickness.

4.4.6. Interface Modeling

The interface strength between the soil medium and the pile is modelled employing the parameter R_{inter}, which is defined as the strength reduction factor. A value of 1 represents a rigid interface, i.e. a fully bonded interface. For Case 1, where the helical pile was installed in sandy soils, the β – method was used to determine the interface parameter R_{inter}. The corrected SPT blow counts, N_{60}, were used to assess β values by the following correlations (CH2M HILL, 2013);

$$\beta = \begin{cases} 1.5 - 0.075\sqrt{z}\,, & N_{60} \geq 15 \\ \left(\frac{N_{60}}{15}\right)\left(1.5 - 0.075\sqrt{z}\right), & N_{60} < 15 \end{cases} \quad (4.4)$$

Where, z is the depth below ground in meters measured at mid-depth of each layer. The interface parameter, R_{inter}, for all the soil layers were estimated form β values with the range proposed by CH2M HILL (2013), as presented in Table 4-5.

Table 4- 5: Interface parameter R_{inter} for Case 1 – Sandy soils.

Layer	R_{inter}	Proposed range, β
Site fill	0.48	0.60 – 0.35
Firm sandy silt	0.38	0.40 – 0.35
Denser sand	0.54	0.55 – 0.40
Looser sand	0.40	0.45 – 0.30

For case 2, the helical pile was installed in clayey soil; hence, the α – method (Randolph and Murphy, 1985) is used to define the parameter R_{inter}. In this method, the coefficient

α is evaluated as a function of the ratio of undrained shear strength, S_u, and effective stress, σ'_{v_o}. However, the values obtained from this model underestimated the load carrying capacity of the helical pile; therefore, an adjustment was made through an iterative process to refine α values to achieve best match between calculated and measured responses. The α values that resulted in best match are presented in Table 4-6. The β – method was used to evaluate the interface parameters of the sand and silt layers in Case soil profile.

Table 4- 6: Interface parameter R_{inter} for Case 2 – Clayey soil.

Layer	α
Silt and sandy silt	0.950
Clay to silty clay	0.688
Silty clay	0.796
Silty sand	0.952
Clay till	0.896
Silty clay to clayey silt	0.944

4.4.7. Initial Stress State

In the HS model, the coefficient of lateral earth pressure and the over-consolidation ratio are used to define the initial stresses for the numerical model. The vertical stresses are generated such that an equilibrium within the soil mass is attained. The horizontal stresses are then determined according to the specified k_o-value. The over-consolidation ratio is used to account for the stress history of the soil medium. The coefficient of lateral earth pressure and over-consolidation ratio used in the analysis are summarized in Table 4-7.

Table 4- 7: Initial stress state parameters.

Case	Soil type	Ks	OCR	Reference
Case 1	Site fill	1.388	1	CH2M HILL (2013)
	Firm sandy silt	1.096	1	
	Denser sand	1.164	1	
	Looser sand	1.330	1	
Case 2	Silt and sandy silt	1.900	10	Elkasabgy (2011)
	Clay to silty clay	1.700	10	
	Silty clay	1.950	14	
	Silty sand	1.100	6	
	Clay till	1.900	15	
	Silty clay to clayey silt	1.200	7	

4.5. Helical Pile Model

The helical pile was modeled as a volume cluster with linearly elastic non-porous material behavior. The helices are modelled as a horizontal volume cluster. The connection between the pile shaft and the helices is assumed to be fully rigid to prevent punching behavior of the shaft through the helices. The helical pile had a single helix for Case 1 and two helices for Case 2 (see Figure 4-5). The piles properties used in the analysis are: Young's modulus (210 GPa), Poisson's ratio (0.3), damping ratio (1%) and unit weight (78.46 kN/m^3).

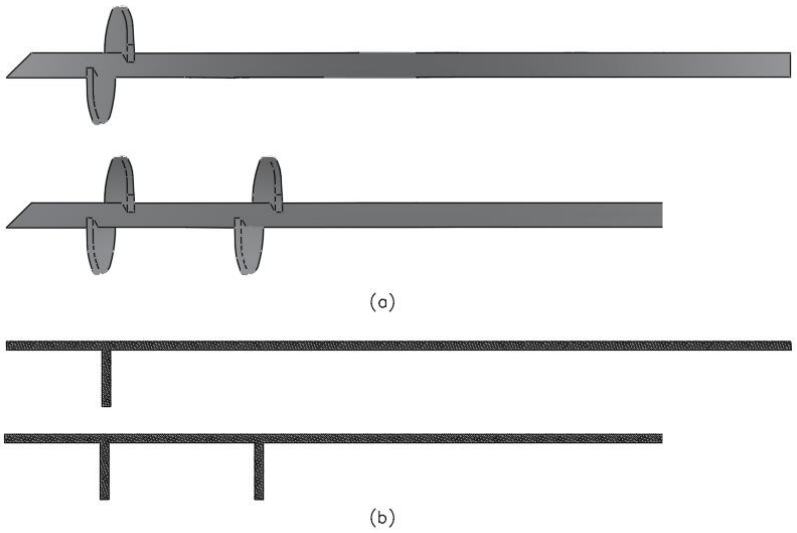

Figure 4- 5: (a) Geometry of tested helical piles; and (b) helical piles geometry in the axisymmetric numerical model.

4.6. Mesh Generation

The soil was simulated using 15-node triangular elements. The entire mesh was divided into 3 zones as shown in Figure 4-6. The mesh discretization was refined immediately adjacent to the helical pile and the refinement decreased with the distance away from the helical pile.

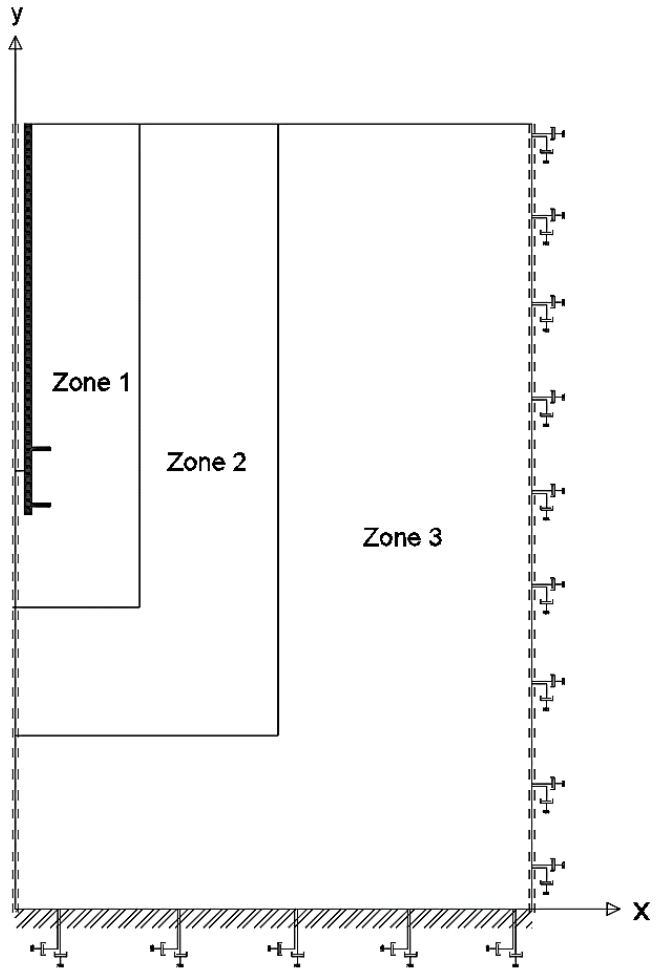

Figure 4- 6: Zones of localized mesh refinement.

To investigate the effect of mesh refinement on the accuracy of results, a sensitivity analysis was conducted, considering coarse, medium, and fine meshes. The load-displacement curve was used as the criterion for mesh convergence. Table 4-8 shows that increasing the global mesh discretization had an insignificant effect on the final deflection and the failure load for Case 1 (sandy soil); but had a minor effect the shape of the load-

displacement curve. For Case 2 (clayey soil), the final deflection and the failure load were greatly affected by the global mesh discretization of the model. Hence, for both Cases, the final mesh was used in the analysis.

Table 4- 8: Optimization of soil meshing.

Case history	Global Model Mesh	Number of Elements	Number of Nodes	Mesh quality	Mesh size	Final deflection [mm]	Failure Load [kN]	Measured deflection [mm]	Measured Failure Load [kN]
Case 1 - sandy model	Coarse	4073	34580	0.86	0.08	36	870	33.58	890
	Medium	6793	56992	0.90	0.06	36	889		
	Fine	14077	116524	0.93	0.04	36	907		
Case 2 – Clayey soil	Coarse	935	8356	0.72	0.08	19.5	2018	35.54	2500
	Medium	1267	11272	0.73	0.06	20.1	2040		
	Fine	8137	116524	0.93	0.04	35.80	2400		

4.7. Final Model Geometry and Input Parameters

The soil profile for Case 1 was discretized into 4 layers and the soil profile for Case 2 had 6 layers. Figures 4-7 and 4-8 depict the final generated model geometry for both cases. The soil material parameters used for each case are summarized in Table 4-9 and Table 4-10.

Table 4- 9: Summary of soil layers properties for Case 1 in Plaxis 2D.

Parameter	Symbol	Unit	Site fill	Firm sandy silt	Denser sand	Looser sand
Drainage Type	-	-	Drained	Undrained (A)	Undrained (A)	Undrained (A)
Unit weight above phreatic line	γ_{unsat}	[kn/m3]	20.40	14	16	16
Unit weight below phreatic line	γ_{sat}	[kn/m3]	20.40	16.50	19.50	19.20
Void ratio	e	-	0.68	0.75	0.69	0.73
Static stiffness parameters	E_{50}^{ref}	[kPa]	14800	10700	43000	33800
	E_{50}^{ref}	[kPa]	14800	10700	43000	33800
	E_{ur}^{ref}	[kPa]	44400	32100	129000	101400
Stress-level dependency	m	-	0.6	0.7	0.5	0.5
Friction angle	φ'	[o]	37	31	37	33
Dilatancy angle	ψ	[o]	7	1	7	3
Cohesion	c'	[kPa]	1	1	1	1
Dynamic stiffness	$E_{dynamic}$	[kPa]	29600	21400	86000	60840
Shear wave velocity	V_s	[m/s]	223	190	310	260
Layer thickness	H	[m]	2.1	11.6	3.7	25.9
Damping ratio	ξ	[%]	5	5	5	5
Interface strength	R_{inter}	-	0.48	0.38	0.54	0.40
Initial stress state parameters	$K_{0,x}$	-	1.388	1.096	1.164	1.330
	OCR	-	1	1	1	1

Table 4- 10: Summary of soil layers properties for Case 2 in Plaxis 2D.

Parameter	Symbol	Unit	Silt and sandy silt	Clay to silty clay	Silty clay	Silty sand	Clay till	Silty clay to clayey silt
Drainage Type	-	-	Drained	Undrained (B)	Undrained (B)	Drained	Undrained (B)	Undrained (B)
Unit weight above phreatic line	γ_{unsat}	[kn/m3]	15.70	14	14.10	15	13.90	14.30
Unit weight below phreatic line	γ_{sat}	[kn/m3]	18.20	17.80	17.80	18.80	17.50	18
Void ratio	e	-	0.83	1.03	1.03	0.83	1.15	0.93
Static stiffness parameters	E_{50}^{ref}	[kPa]	45000	60000	70000	64000	75000	58000
	E_{50}^{ref}	[kPa]	36000	48000	56000	52100	60000	46400
	E_{ur}^{ref}	[kPa]	135000	180000	210000	192000	225000	174000
Stress-level dependency	m	-	0.6	0.75	0.75	0.5	0.85	0.75
Friction angle	φ'	[o]	31	-	-	42	-	-
Dilatancy angle	ψ	[o]	1	-	-	7	-	-
Undrained shear strength	S_u	[kPa]	-	85	137	-	177	150
Dynamic stiffness	$E_{dynamic}$	[kPa]	91000	149000	277000	197000	315000	290000
Shear wave velocity	V_s	[m/s]	125	170	220	183	211	233
Layer thickness	H	[m]	1.4	3.1	1.2	0.5	7.2	16.6
Damping ratio	ξ	[%]	5	5	5	5	5	5
Interface strength	R_{inter}	-	0.950	0.688	0.796	0.952	0.896	0.944
Initial stress state parameters	$K_{0,x}$	-	1.9	1.7	1.95	1.1	1.9	1.2
	OCR	-	10	10	14	6	15	7

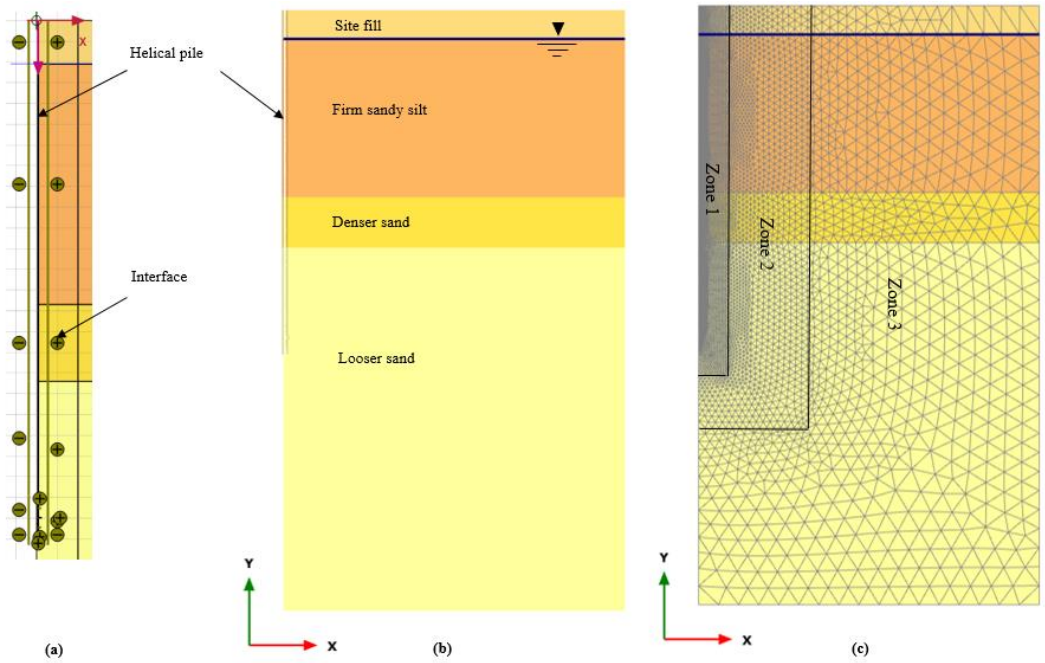

Figure 4- 7: Case 1 model (a) helical pile and soil-pile interface, (b) model geometry, and (c) Generated mesh.

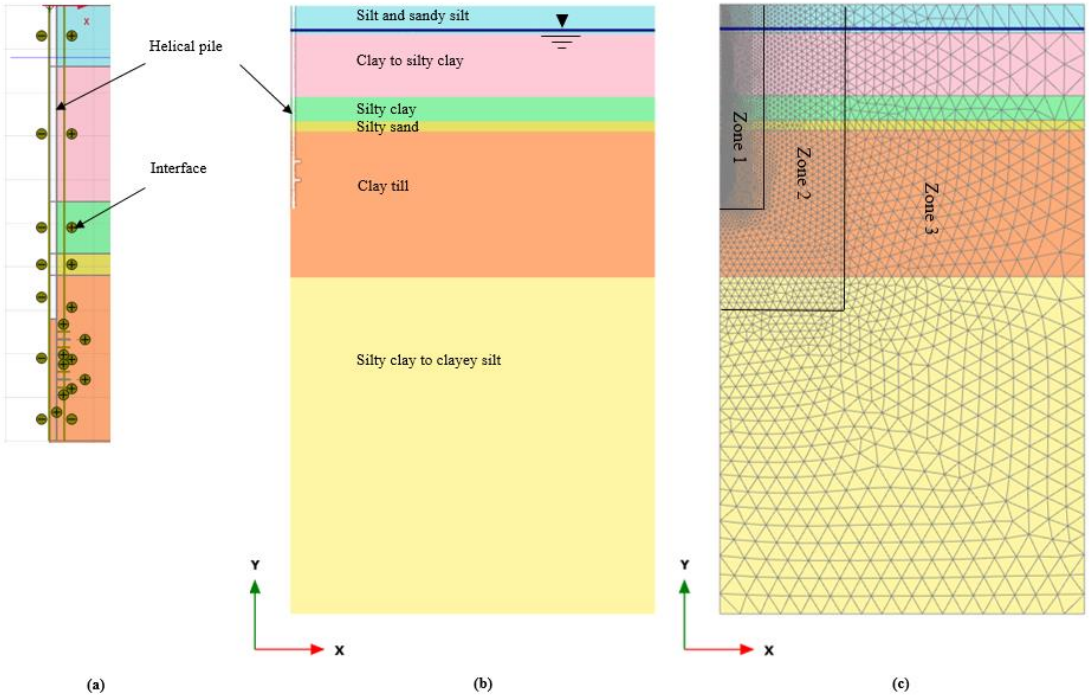

Figure 4- 8: Case 2 model: (a) helical pile and soil-pile interface, (b) model geometry, and (c) Generated mesh.

4.8. Simulation of Static Load Test

The SLT was simulated using static prescribed displacement imposed at the pile head. The assigned displacement was equal to the maximum displacement reported from the field measurements. The results of the analysis were compared with the field test results in order to validate the developed models for their static soil behavior and to evaluate the suitability of the adopted method of modelling helical piles in a 2D domain.

The analysis was performed in 3 phases: initial phase, pile activation phase, and pile load test phase. The initial phase involved activating the initial conditions, i.e., initial stress state, based on the K_o procedure calculation. The second phase involved activating the pile by assigning the helical pile properties to the pile cluster. The interfaces between the helical pile and the surrounding soil were also activated in this phase, and the boundary conditions for static loading calculation are set. In the last phase, the prescribed displacement was applied to the helical pile head to simulate the SLT. The calculated and measured load-displacement curves were used to validate the model assumptions adopted in this study.

Figure 4-9 compares the calculated and measured load-displacement curves for the Case 1 helical pile, which had a single helix installed in sandy soil. Figure 4-9 demonstrates that the load-displacement curve obtained from the numerical analysis corresponds well with field test results. The initial elastic region was captured by the numerical model before the divergence between both curves occurred. From a displacement of 5 mm to a displacement of approximately 10 mm, the predicted static curve from FEM did not match the measured static curve. This discrepancy is due to the failure of the hydraulic pump that operated the loading jack, which resulted in repeating the test more than once. As the displacement exceeded 10 mm, the calculated and measured load-displacement curves converged with less than 5% higher difference. This is because the loading was completed without interruption within this loading range. The ultimate pile capacity determined from the in-situ static load test and numerical model based on the Davisson failure criterion are in a good agreement.

Figure 4-10 compares the calculated and measured load-displacement curves for the Case 2 helical pile, which had two helices and installed in clayey soil. The two curves are almost

identical as observed in Figure 4-10. Hence, it can be concluded that the developed models are validated, and the modeling assumptions could be employed to accurately depict the behaviour of helical piles in similar soils.

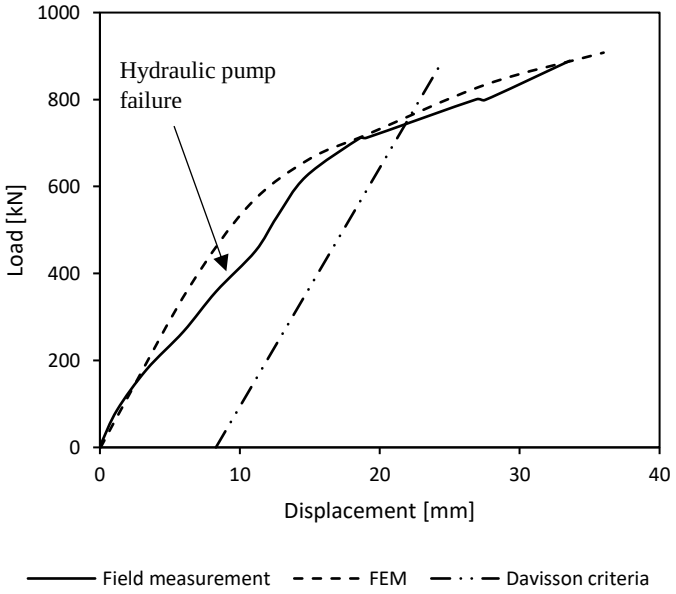

Figure 4- 10: Calculated and measured load-displacement curves for Case 1 helical pile.

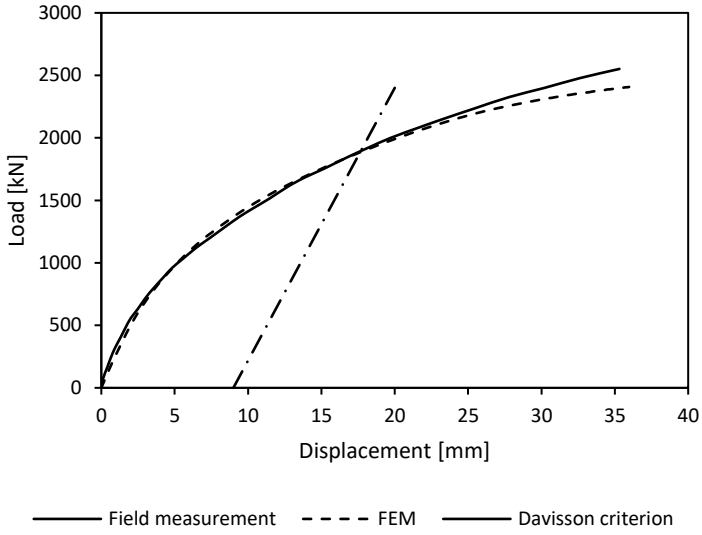

Figure 4- 9: Calculated and measured load-displacement curves for Case 2 helical pile.

4.8.1. Failure Mechanism

The obtained failure mechanisms of the modelled helical piles are compared with the typical failure mechanism reported in the literature. Figure 4-11 shows the displacement contours of the test piles in both cases. As expected, the failure mechanism of the single helix pile involves soil movement along the shaft (due to load transfer along the shaft) and large soil movement below the single helix due to the load transfer at the helix as depicted in Figure 4-11(a). For the 2-helix pile with inter-helix spacing ratio of 1.5, a cylindrical failure surface is formed between the top and the bottom helices as shown in Figure 4-11(b). Hence, the cylindrical shear method controlled the behavior of the helical pile in this case. The failure mechanisms captured by the numerical models developed herein are similar to the failure mechanisms of helical piles presented in Elsherbiny & El Naggar (2013) and Polishchuk & Maksimov (2017). Hence, the current numerical models can simulate the load-transfer mechanism at failure for helical piles.

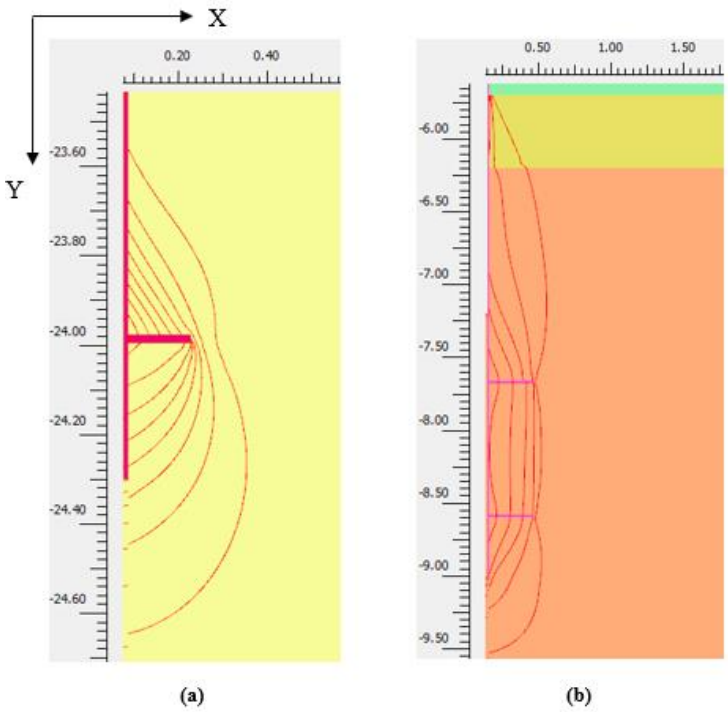

Figure 4- 11: Displacement contours for: a) single helix pile; b) 2-helix pile with cylindrical failure mechanism.

4.9. Simulation of High Stain Dynamic Test

The analysis of the impact load during HSDT is conducted in the time-domain, and simulated the dynamic measurements (i.e. force, acceleration, and velocity measurements). The shape of the impact force time history at the pile head during the HSDT is a function of the hammer-cushion-pile system impedance as discussed in chapter 3. In particular, the impedance ratio of the cushion and pile governs the behavior of the hammer-cushion-pile system during the HSDT. For systems with an impedance ratio ≥ 1, the force pulse is approximately a half-sine wave. For impedance ratio < 1, a sharp peak is developed over a short time followed by an abrupt reduction in force. The impedance ratio for the two case histories examined herein were greater than 1. Hence, the force time history at the pile head is simulated as a half-sine wave.

Figure 4-12 displays the represented force-time history and pulse duration implemented at the top of the helical pile for Case 1 – helical pile installed in sandy soils, and Case 2 – helical pile installed in clay soil. These curves are equivalent to the force measured at the top of the helical pile at the site during the HSDT.

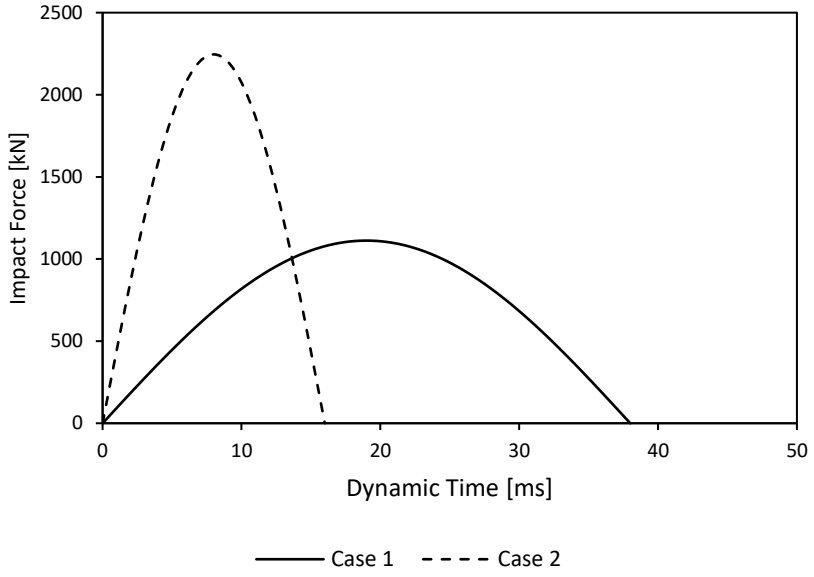

Figure 4- 12: Force functions used to simulate hammer impact in numerical models.

4.9.1. Dynamic Time Discretization

The dynamic calculations are conducted over the time interval, Δt, that is equal to the measured time of impact during the field test. This time interval is subdivided into a maximum number of steps, m, and a number of sub-steps, n. The parameters m and n are used to discretize the dynamic time interval to the most suitable number of time steps such that the dynamic loading is adequately covered. The time step can be defined as follow;

$$\delta t = \frac{\Delta t}{m\, n} \tag{4-5}$$

The time discretization was set to the *semi-automatic* option, m = 112, 144, and 192 were selected. The dynamic responses obtained from these m values were compared, and no difference was noted in the dynamic measurements. Hence, m = 112 was used in the HSDT in both case histories.

4.9.2. Dynamic Calculation Phases

The dynamic calculation comprised four phases: initial phase, pile and interface activation phase, pile hammering simulation phase, and fading phase. The k_0 procedure was used to generate the initial effective stresses and the initial groundwater condition in the model. In the second phase, the pile material was assigned to the clusters that represented the helical pile and the interface elements between the soil, and the pile were activated. The hammer impact at the top of the helical pile was simulated in the third phase using a line load with assigned dynamic multipliers having the shape of a half-sine wave as depicted in Figure 4-12. The dynamic time interval was set to 0.038 s for Case 1 and 0.0161 s for Case 2, and the viscous boundaries were specified and activated. In the last phase, the fading of the generated compression wave after the completion of the third phase was observed. The final settlement occurred in this phase since the compression wave would be still propagating downwards in the helical pile. The attenuation was simulated by continuing the dynamic analysis for 0.1 s after the impact load expired. Figures 4-13 shows the settlement of the helical pile versus time for Case 1 and Case 2, respectively.

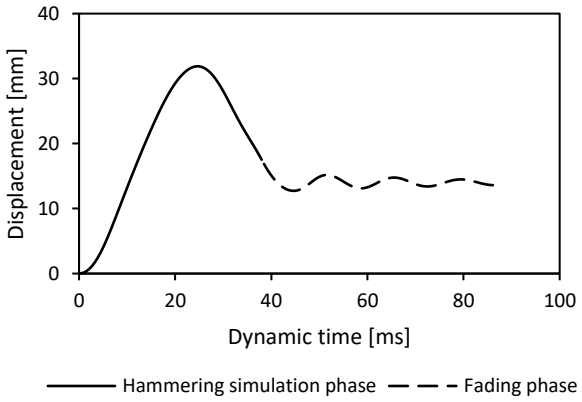

(a)

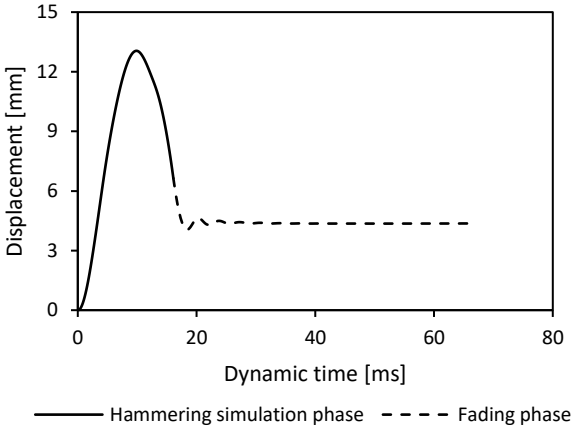

(b)

Figure 4- 13: Helical pile displacement time history, (a) Case 1 and (b) Case 2.

The results obtained from during the hammer simulation phase are shown in Figure 4-14 and 4-15, for Cases 1 and 2 respectively. Figure 4-14 shows that the velocity and acceleration at the head and toe of the pile in Case 1 differed, due to the flexibility of the long pile and associated elastic shortening of the pile shaft. There was a time lag between the movement of the pile head and toe of about 5 ms. On the other hand, for Case 2, there was no delay between the movement of the pile head and toe at the instance of impact; therefore, the pile moved almost as a rigid body. The inertia force calculated from the total pile mass must be considered.

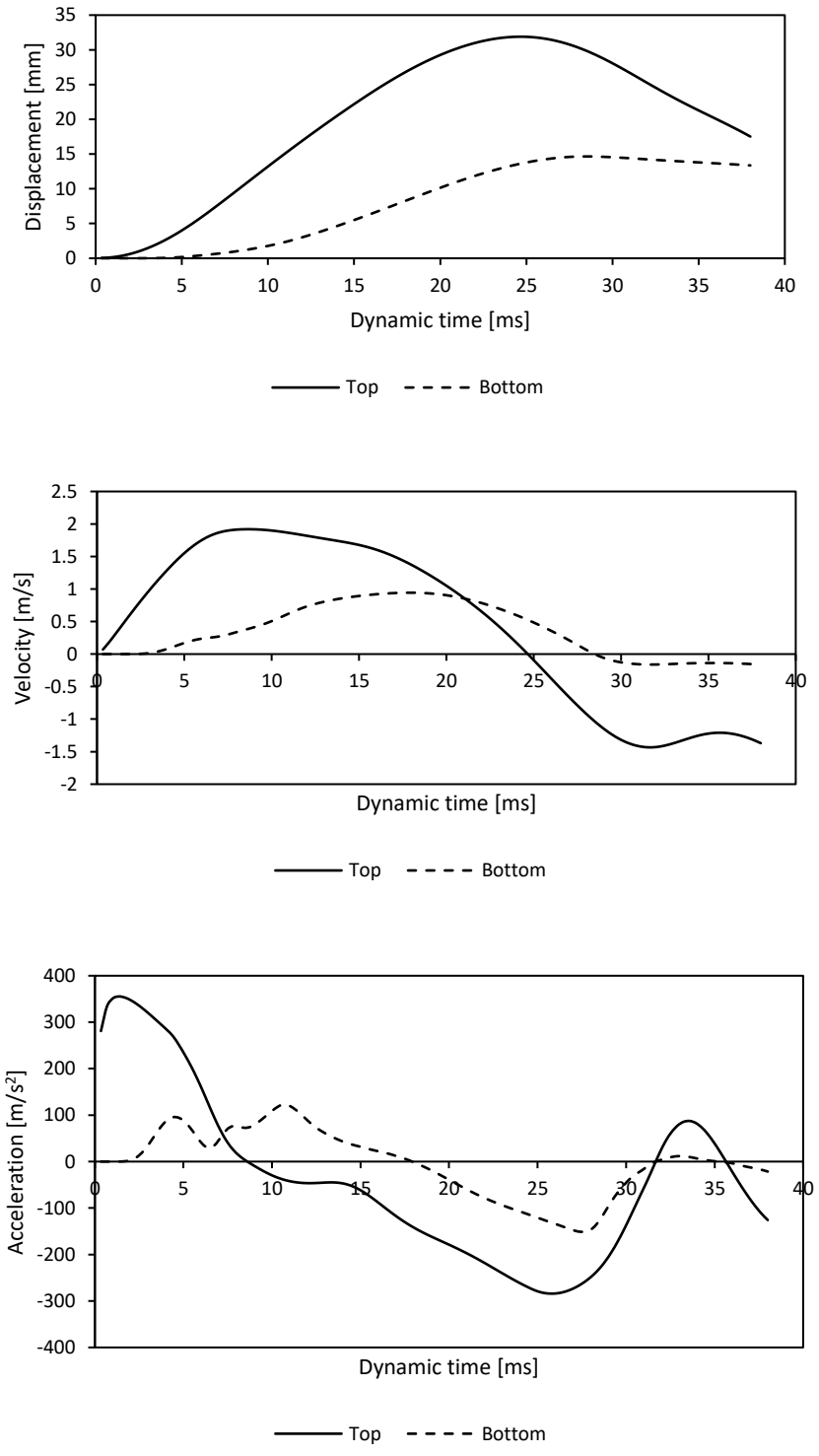

Figure 4- 14: Dynamic response of the helical pile installed in sand (Case 1).

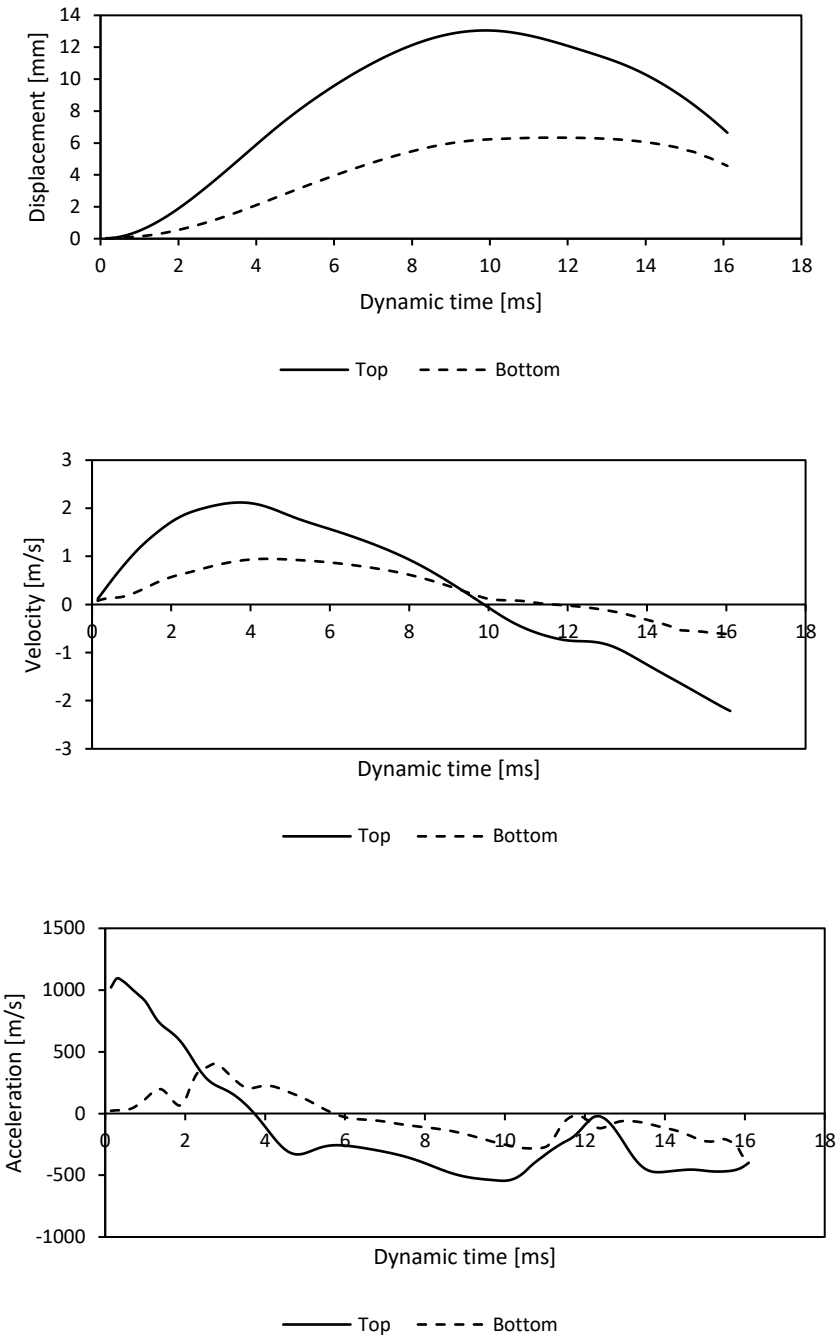

Figure 4- 15: Dynamic response of the helical pile installed in clay (Case 2).

4.9.3. Derived load-displacement curve: Case 1.

This section presents the results in terms of load-displacement curve for the helical pile installed in sandy soils obtained from different methods.

4.9.3.1 Employing CAPWAP (CAse Pile Wave Analysis Program)

The CAPWAP uses the dynamic measurements obtained by the Pile Driving Analyzer (PDA) system during the HSDT to estimate the static axial capacity of the pile. CAPWAP was used by CH2M HILL (2013) to obtain the derived static load-displacement curve, and the results are compared with the calculated static response from the numerical model in Figure 4-16. It is observed that the initial (elastic) region of both curves are similar, but the curves differ in the plastic (nonlinear) region. This discrepancy is attributed to the incorrect selection of the pile model in CAPWAP, since it considers the pile as a series of continuous uniform sections, ignoring the contribution of the helices. The ultimate load capacity obtained from the estimated load-displacement curve is approximately 1.2 times that estimated based on CAPWAP analysis.

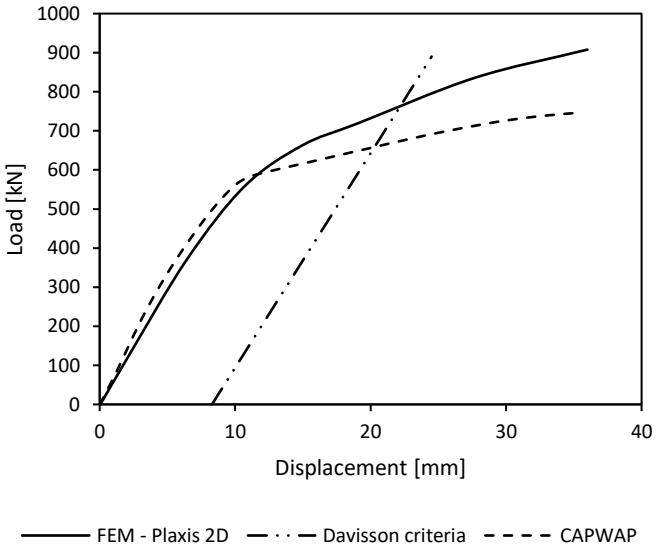

Figure 4- 16: Load-displacement curves from numerical model and CAPWAP – Case 1.

4.9.3.2 The Modified Unloading Point Method (MUP)

The helical pile did not exhibit rigid body motion during the HSDT, rather it exhibited elastic shorting behaviour (stress wave phenomenon). Consequently, the pile head response (i.e. displacement, velocity, and acceleration) varied from that of the toe as can be seen from Figure 4-14. Thus, the Modified Unloading Point Method developed by Justason (1997), described in Appendix (A), is used to interpret dynamic measurements taken from the numerical simulation to establish the derived load-displacement curve. Figure 4-17 compares the load-displacement curve obtained from the SLT (FEM – Plaxis 2D) and the derived load-displacement curve from dynamic measurements (MUP – Hyperbolic approximation). The MUP predicted reasonably well the load-displacement behavior and ultimate static capacity in comparison to the SLT results. However, the maximum measured displacement during dynamic testing was 35 mm, while the calculated value from numerical model was 31 mm.

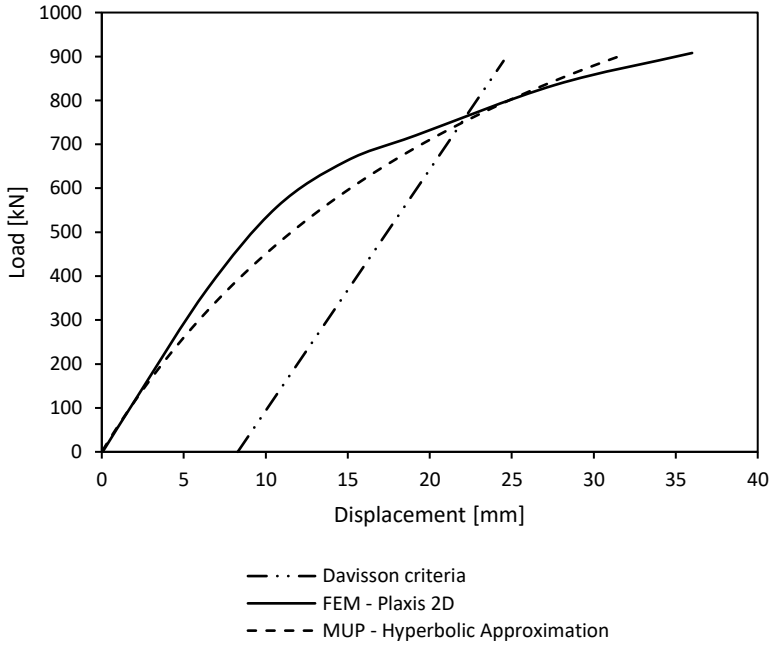

Figure 4- 17: Load-displacement curve numerical model and MUP method – Case 1.

4.9.3.3 G-C Method.

The mathematical model considered in this method, referred to as G-C method, consists of a mass representing the pile, and a spring a dashpot to represent soil stiffness and damping

(Gibson and Coyle, 1968). The derived static load-displacement curve is obtained from the dynamic responses calculated by the numerical model following the procedure described in Appendix (A). The initial stiffness of the load-displacement curve (i.e. elastic region) was derived from the dynamic measurements. The calculated load-displacement curve (G-C method) is compared with that obtained from the SLT (FEM – Plaxis 2D)) in Figure 4-18. The two curves are in good agreement.

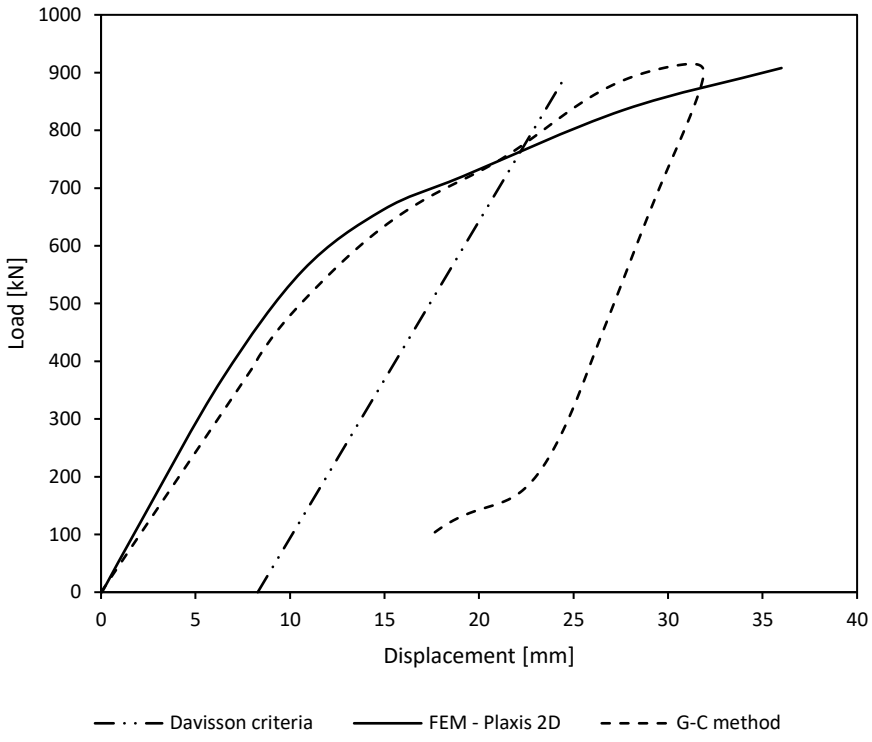

Figure 4- 18: Load-displacement curves from numerical model and G-C method – Case 1.

4.9.4. Derived Load-Displacement Curve: Case 2

This section presents the results of the methods used to determine the load-displacement curve for the helical pile installed in clayey soils (Case 2).

4.9.4.1 CAPWAP (CAse Pile Wave Analysis Program)

The signal matching procedure using CAPWAP was implemented by Sakr (2013) to extract static load response from top pile force and velocity measurements during the

hammer impact. Figure 4-19 compares the results of the CAPWAP with the results of the SLT simulated in Plaxis 2D. The predicted static capacity based on CAPWAP is significantly lower than the estimated static capacity by the Davisson criterion. This is due to the inappropriate selection of hammer weight; thus, the energy delivered to the helical pile was not sufficient to mobilize its full capacity.

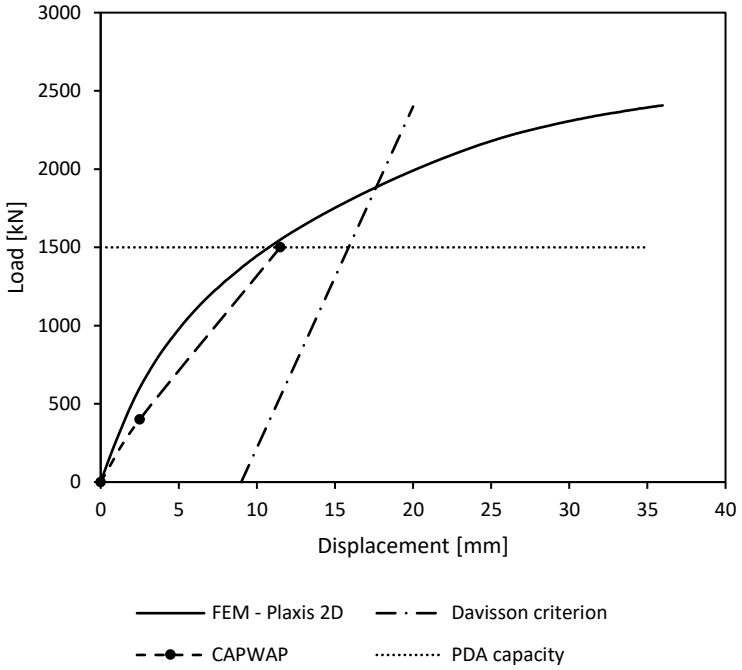

Figure 4- 19: Load-displacement curves from numerical model and CAPWAP – Case 2.

4.9.4.2 The Unloading Point Method (UP)

Since the wavenumber N_w > 10 for Case 2, the influence of stress wave phenomenon can be neglected, and the UP method can be applied. The derived load-displacement curve using the UP method and the calculated dynamic responses is compared with the results of SLT simulated in Plaxis 2D in Figure 4-20. A good agreement between both curves was found. The ultimate static capacity determined from the UP method was about 9.9% higher than that estimated from CAPWAP, but both have approximately the same final settlement.

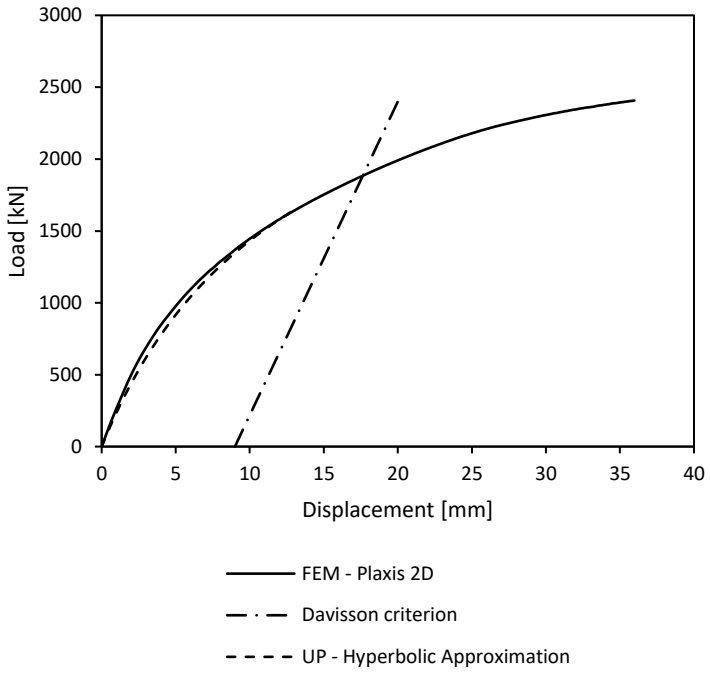

Figure 4- 20: Load-displacement curves from numerical model and the UP method - Case 2.

4.9.4.3 G-C Method

The G-C method was used to establish the derived static load-displacement curve from the calculated dynamic response and the results are compared with the measured SLT load-displacement curve in Figure 4-21 and. The figure shows good agreement between the two curves. It is observed that this method provided more accurate static response compared to the UP method. The estimated ultimate static load capacity matched the value obtained from the field data (i.e. CAPWAP) but at a slightly lower settlement.

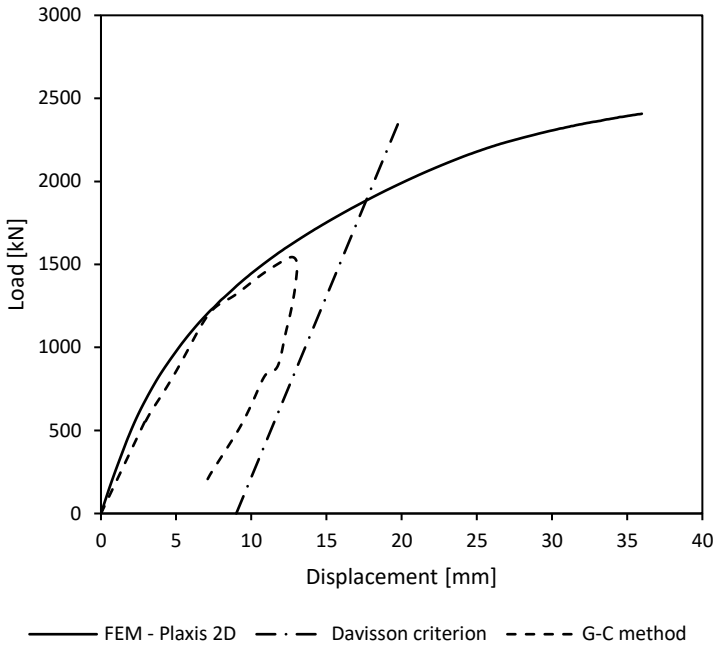

Figure 4- 21: Load-displacement curves from numerical model and G-C method – Case 2.

4.10. Validation of Dynamic Model

In summary, several methods were used to determine the mobilized soil resistance (i.e. the derived load-displacement curve) based on the developed numerical models of the HSDT conducted on helical piles. The results are compared with the measured field data to validate of the numerical models. They are also compared with results from the static simulations using the numerical models to investigate their accuracy. The results obtained from the numerical simulations agreed reasonably with the measured data from full scale helical piles load tests. Therefore, the numerical models used in the analyses, including the soil models properties, helical pile model, hammer loading model, assumptions, and boundary conditions for dynamic analysis in Plaxis 2D are validated.

4.11. Parametric Study

The model assumptions used for developing the validated numerical models (i.e. soil parameters, pile material, boundary conditions and dynamic loading) were used to develop numerical models that were employed to conduct a comprehensive parametric study to investigate the effect of different factors governing the HSDT on helical piles. The factors considered in the parametric study are: helical pile configuration, soil type, hammer weight and drop height, and cushion stiffness.

The investigated helical pile configuration included the number of helices and their spacing ratio (S/D_H). The HSDT conducted on helical piles with different configurations installed in either sand or clay profiles were analyzed to identify the failure surface and shape of failed soil mass under impact loading. In addition, the effect of the hammer impact velocity at the pile head on the effectiveness of the HSDT setup to mobilize the pile capacity fully is examined. The force-time history at the pile head during the HSDT is mainly controlled by the hammer weight and the cushion stiffness; therefore, these two parameters are also investigated. The obtained dynamic data were then interpreted following the G-C method.

4.11.1. Effect of Number of Helices

The effect of the number of helices on the response of helical pile subjected to the same axial impact loading was investigated by considering four different seniors as presented in Table 4-11. All parameters and impact load generated from the selected hammer at the actual test are kept the same as discussed in previous sections.

Table 4- 11 Helical piles configuration considered in analysis to study effect of number of helices.

Case	Soil Type	Pile configuration	No. helix	D_H	t_H	S/D_H	D_S	t_S	L
Case 1	Sand	Helical	1	457	19	N/A	178	11.5	24.3
		Helical	2	457	19	1.5			
Case 2	Clay	Helical	1	610	19	N/A	324	9.5	9
		Helical	2	610	19	1.5			

Where, D_H is helix diameter, t_H is helix thickness, S is spacing between helices, D_S is shaft diameter, t_S is shaft thickness, and L is pile length.

Figures 4-22 and 4-23 present the derived load-displacement curves for piles in sand and clay, respectively. It can be seen from Figures 4-22a and 4-23a that the static response curves of single helix piles estimated from the dynamic analyses are in good agreement with the static response obtained from the static analyses. This implies that the transferred energy by the selected hammer-cushion combination was sufficient to mobilize the axial capacity considering the Davisson's failure criterion. However, no plunging failure occurred as it is typically the case for end bearing piles installed in sand. For the double-helix piles, Figures 4-22b and 4-23b demonstrate that the derived static resistance from the dynamic analyses installed in sand and clay was significantly lower than the evaluated static resistance generated from the static test simulations. The ultimate bearing capacity at failure obtained from the dynamic analysis was about 23% lower than the value obtained from static test simulation for the helical pile installed in sand and about 60% for the helical pile installed in clay. Hence, it may be concluded that, as expected, using the same HSDT setup on helical piles with different number of helices at the same soil condition will not necessarily mobilize the full capacity and higher potential energy would be needed as the number of helices increases. Therefore, the number of helices must be considered in planning the HSDT to select a suitable hammer and cushion material that could generate enough force to fully mobilize the helical pile capacity.

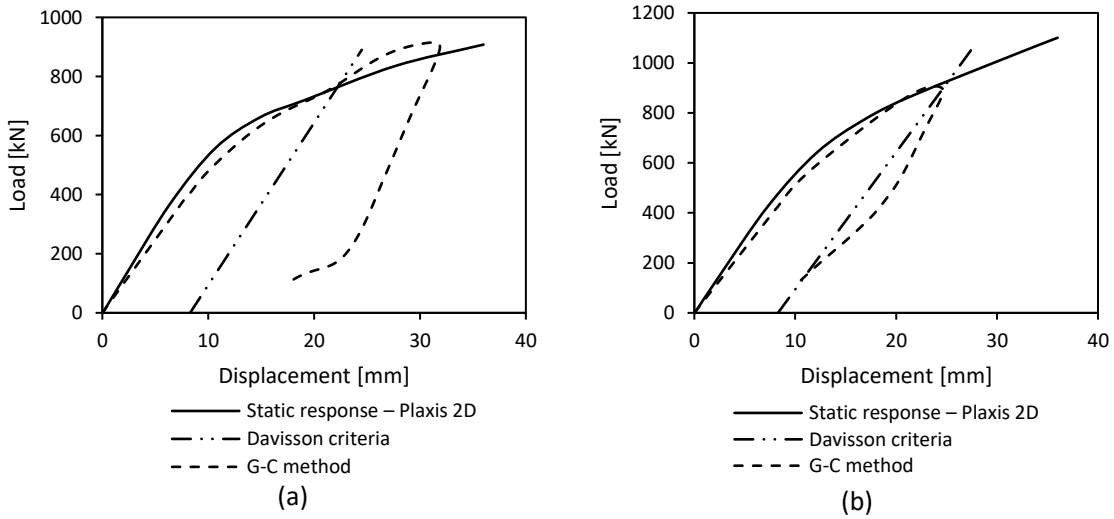

Figure 4- 22: Derived static load-displacement curves obtained from dynamic and static simulations for helical piles installed in sand: a) single helix pile; b) double-helix pile.

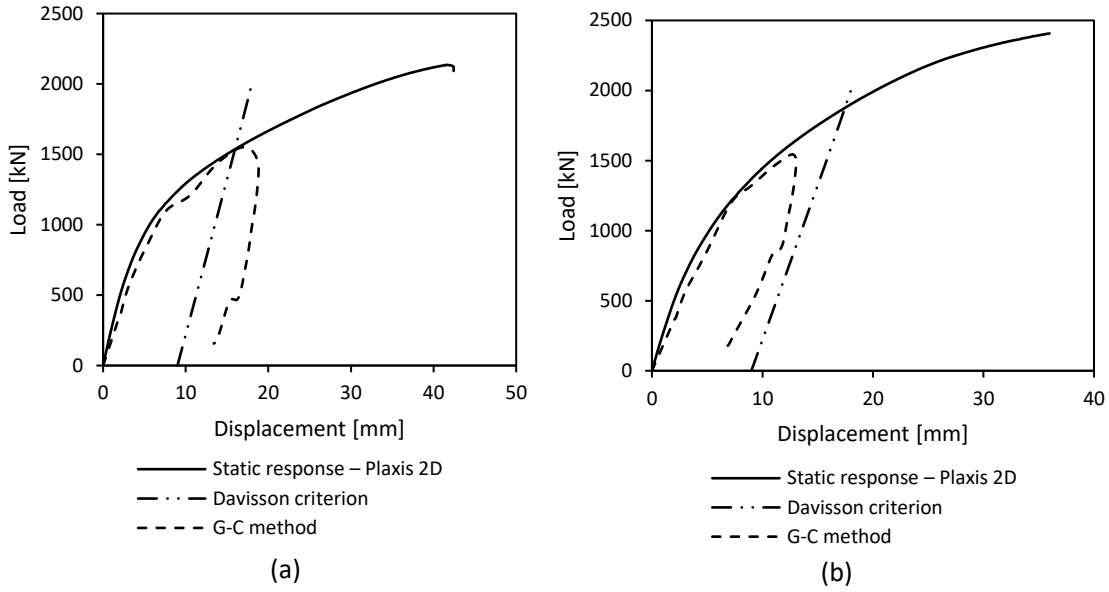

Figure 4- 23: Derived static load-displacement curves obtained from dynamic and static simulations for helical piles installed in clay: a) single helix pile; b) double-helix pile.

4.11.2. Effect of Spacing Between Helices

The effect of helix spacing ratio (S/D_H) on the mobilized soil resistance during the HSDT is investigated. Two spacing ratios are considered: 1.5, and 3. The force-time generated from the hammer impact is maintained the same in all helical piles (i.e. shown in Figure 4-12). Table 4-12 summarizes the helical pile geometries considered in this analysis.

Table 4- 12: Helical pile geometries considered to study the effect of helix spacing.

Case	Soil Type	No. helix	D_H	t_H	S/D_H	D_S	t_S	L
Case 1	Sand	2	457	19	1.5	178	11.5	24.3
		3	457	19	3			
Case 2	Clay	2	610	19	1.5	324	9.5	9
		3	610	19	3			

The calculated ultimate capacities are plotted against the helix spacing ratio (S/D_H), and the results are shown in Figure 4-25 for the helical piles in sand and Figure 4-25 for the helical piles in clay. No significant changes in the derived load-displacement curve from

the G-C method were observed with increasing spacing ratio from 1.5 to 3; however, the lower the (S/D_H) ratio, the closer the shape of the derived load-displacement to that obtained from a helical pile with a single helix. It can be concluded from this parametric study that spacing ratio is not a factor that significantly influences the results of the HSDT, unlike the number of helices.

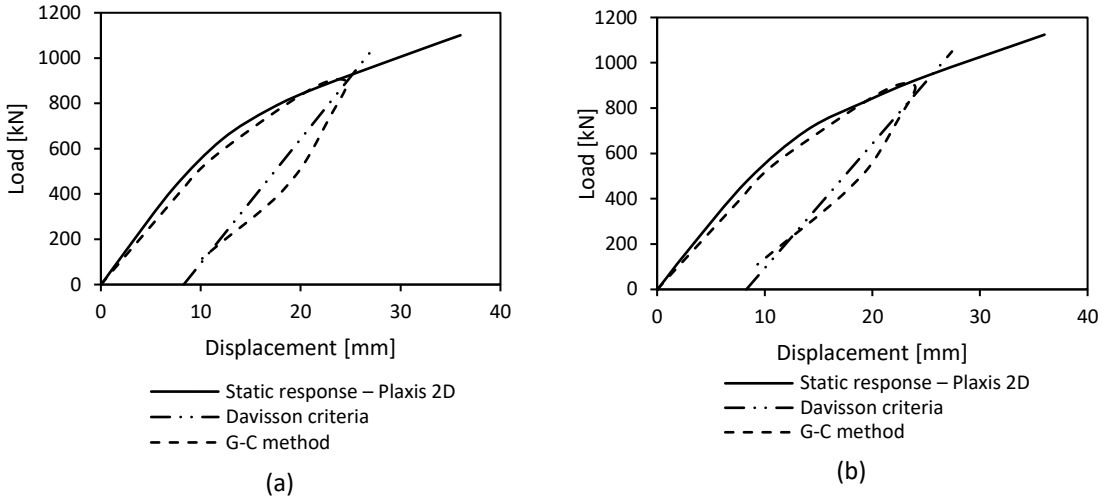

Figure 4- 24: Load-displacement curves obtained from G-C method and static simulations at different spacing ratio for the helical piles installed in sand: (a) $S/D_H = 1.5$ and (b) $S/D_H = 3$.

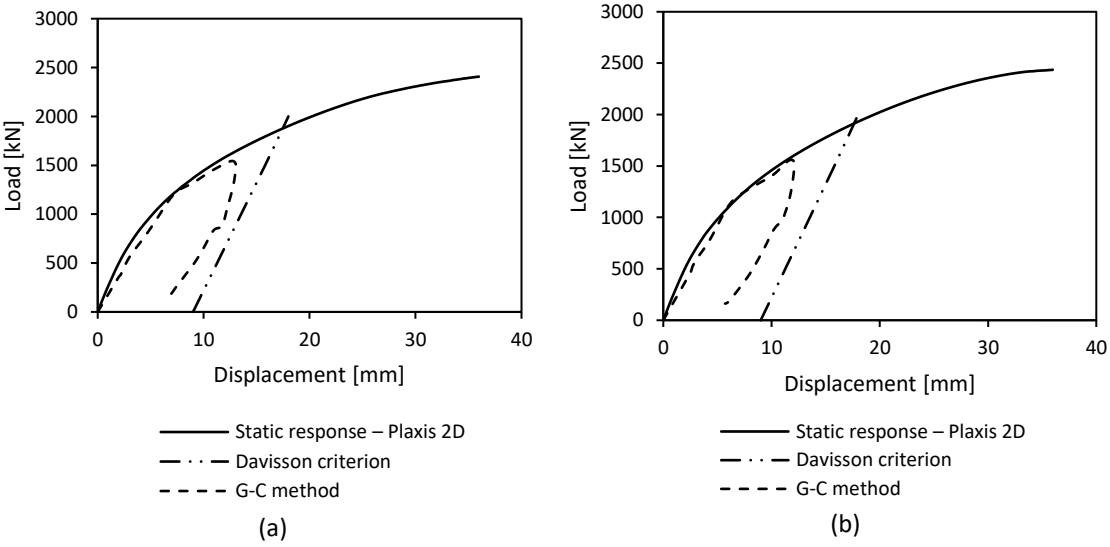

Figure 4- 25: Load-displacement curves obtained from dynamic and static simulations at different spacing ratio for the helical piles installed in clay: (a) $S/D_H = 1.5$ and (b) $S/D_H = 3$.

4.11.3. Effect of Hammer Drop Height

The response of the helical piles to varying hammer drop heights was investigated. Only the applied force-time history at the helical pile head was varied. Figure 4-26 depicts the shapes of the force-time history at the helical pile with a single helix installed in the sandy soil deposit as well as the shapes of the force-time history applied at the top of the helical pile with double helices which is torque-driven in a clayey soil deposit. In both Cases, the applied force-time history for each hammer drop height was generated in accordance to a half-sine wave with an impulse that is equivalent to that generated using the following equations (see chapter 3 for more details):

$$F(t) = \frac{k_s \dot{v}_o}{w\sqrt{1-D^2}}\, e^{-Dwt} \sin(tw\sqrt{1-D^2}) \tag{4.6}$$

$$\dot{v}_o = \sqrt{2.g.h} \tag{4.7}$$

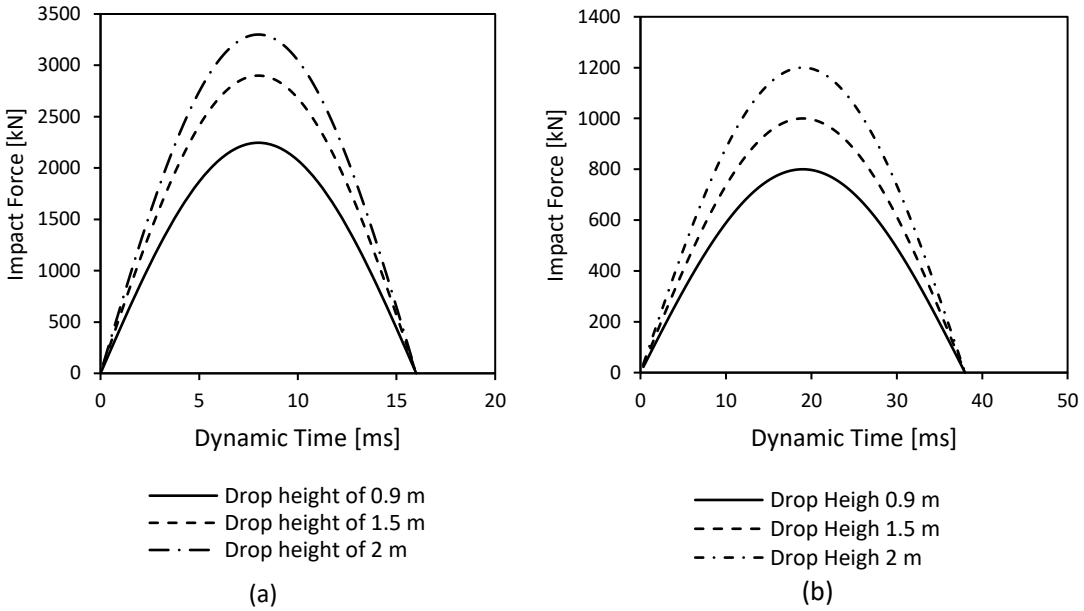

Figure 4- 26: Shape of force pulses generated at different heights: (a) for single-helix pile installed in sand, and (b) for the double-helix pile installed in clay.

Three different hammers drop heights were considered in the analysis. These drop heights were 0.9 m, 1.5 m, and 2 m. The derived load displacement curves from the dynamic analyses are presented in Figure 4-27 and 4-28. It can be seen that the hammer drop height

has a profound effect on the response of the pile when all other parameters in the hammer-cushion-pile system being relatively constant.

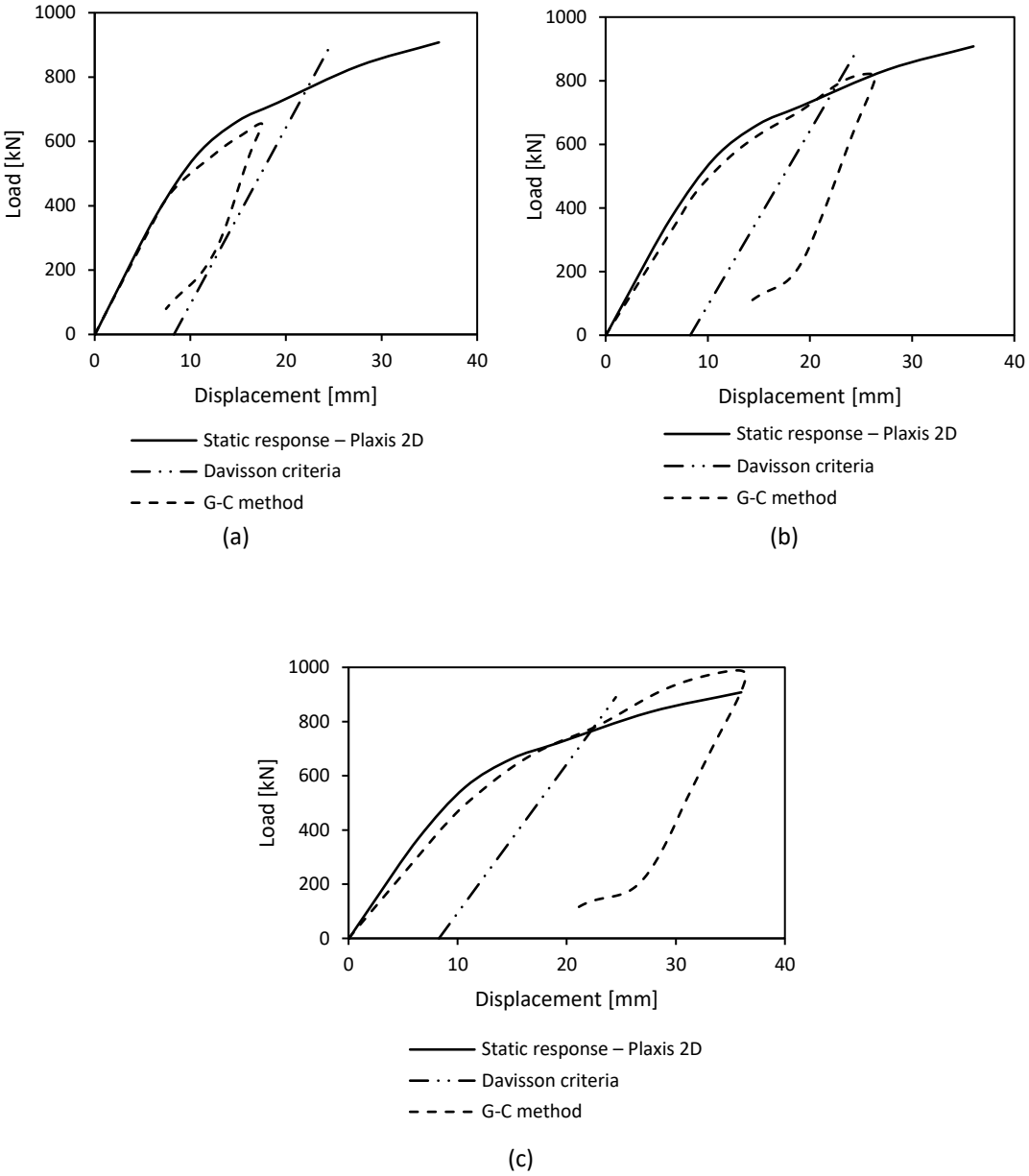

Figure 4- 27: Load-displacement curves obtained from dynamic and static simulations for different hammer drop heights for piles installed in sand: (a) 0.9 m; (b) 1.5 m; (c) 2 m.

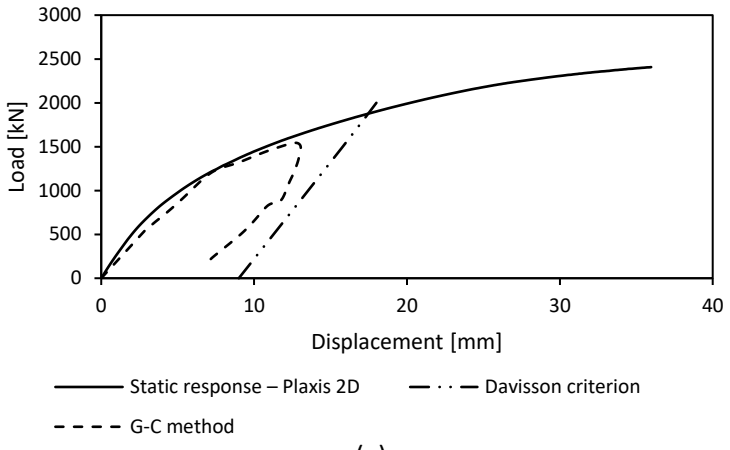

(a)

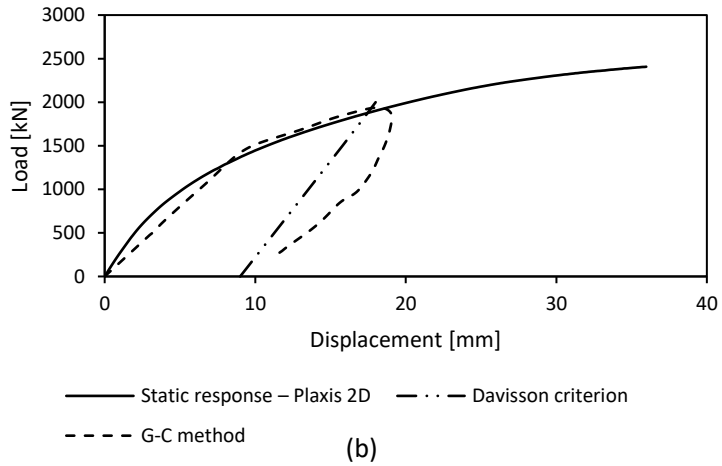

(b)

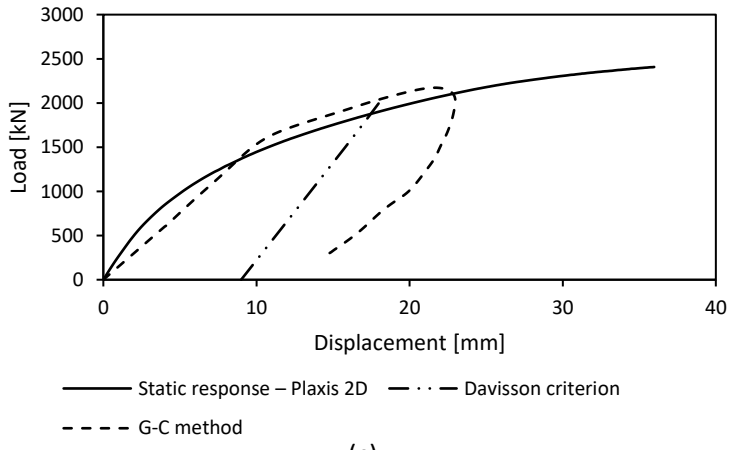

(c)

Figure 4- 28: Load-displacement curves obtained from dynamic and static simulations for different drop heights for piles in clay: (a) 0.9 m; (b) 1.5 m; (c) 2 m.

The calculated maximum pile top force and the maximum compressive stress within the helical pile are plotted against hammer drop height in Figure 4-29. The calculated results indicate that maximum compressive stress increases at a much faster rate in comparison to the maximum pile top force with increasing hammer drop height. Also, a linear relationship between the variation of the maximum force at the top of the helical pile with drop height was observed similar to the pattern reported by Hussein et al. (1992) for driven piles, as depicted in Figure 4-29a. Varying the impact height from 0.9 m to 2 m produced a force that is higher approximately by 50%, but the maximum compression stress was up to 100% higher than what has been estimated for the 0.9 m impact height for the helical pile installed in the clayey soil. For the helical pile installed in sandy soil, increasing the impact height from 0.9 m to 2 m increased the maximum pile top force by 47%. However, the maximum compressive stress calculated for a drop height of 2 m was 125% higher than that for 0.9 m drop height. The helical piles in both cases were subjected to excessive stresses (higher than steel yield strength) at a drop height greater than 1.5 m.

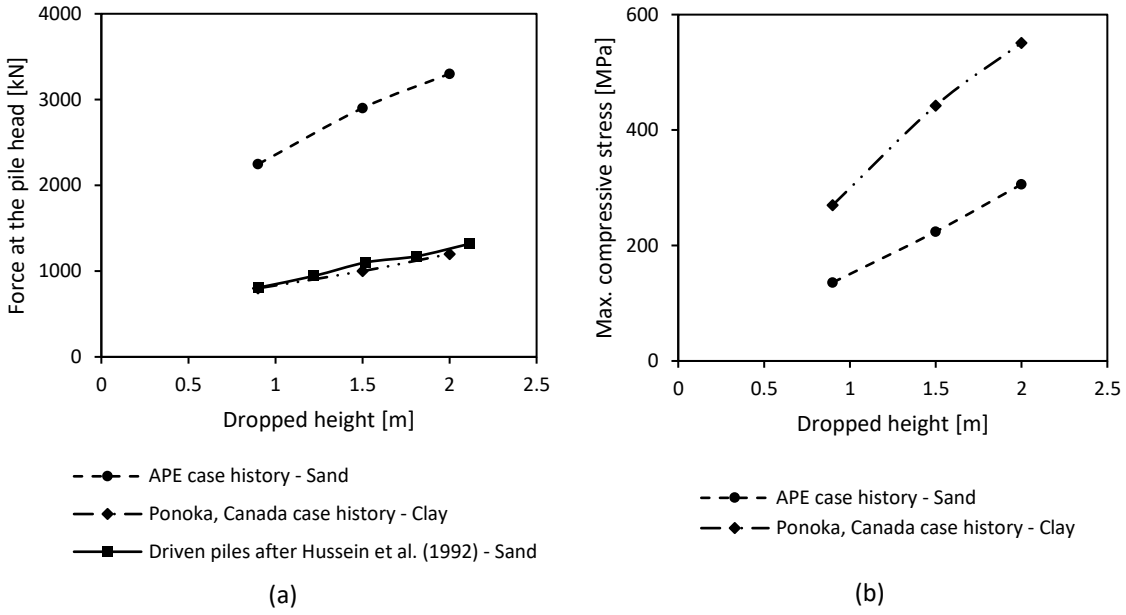

Figure 4- 29: (a) Maximum force at helical pile head; and (b) maximum compression stress generated at the helical pile due to changing in hammer drop height.

4.11.4. Effect of Hammer Weight

The hammer weight is a major factor in selecting a hammer-cushion system to effectively displace the helical pile sufficiently to ensure that the end-bearing resistance if fully mobilized. Four different values of hammer weight, W_r = 20 kN, 30 kN, 50 kN, and 80 kN, were considered in the analysis. The helical pile considered was a double-helix pile with spacing ratio (S/D_H) = 1.5. The hammer drop height was kept at 1 m for all cases. For each hammer weight, the force-time responses were generated using equations 4.8 and 4.9, then idealized as a half-sine wave with equivalent impulse energy (i.e. the product of the force and time is maintained the same in both shapes).

For D < 1,

$$F(t) = \frac{k_s \dot{v}_o}{w\sqrt{1 - D^2}}\, e^{-Dwt} \sin(tw\sqrt{1 - D^2}) \tag{4.8}$$

And; For D > 1,

$$F(t) = \frac{k_s \dot{v}_o}{w\sqrt{D^2 - 1}}\, e^{-Dwt} \sinh(tw\sqrt{D^2 - 1}) \tag{4.9}$$

The computed load-displacement curve from dynamic analyses for various hammer weights are plotted along with the static load-displacement curve in Figure 4-30 and 4-31 for helical piles in sand and clay, respectively. It is evident that the greater the hammer weight, the closer the predicted static response form dynamic analyses to the static response due to the ability of the hammer-cushion-pile system to maintain the generated loads for a long duration. In addition, the longer the duration, the lower the inertia and damping forces are.

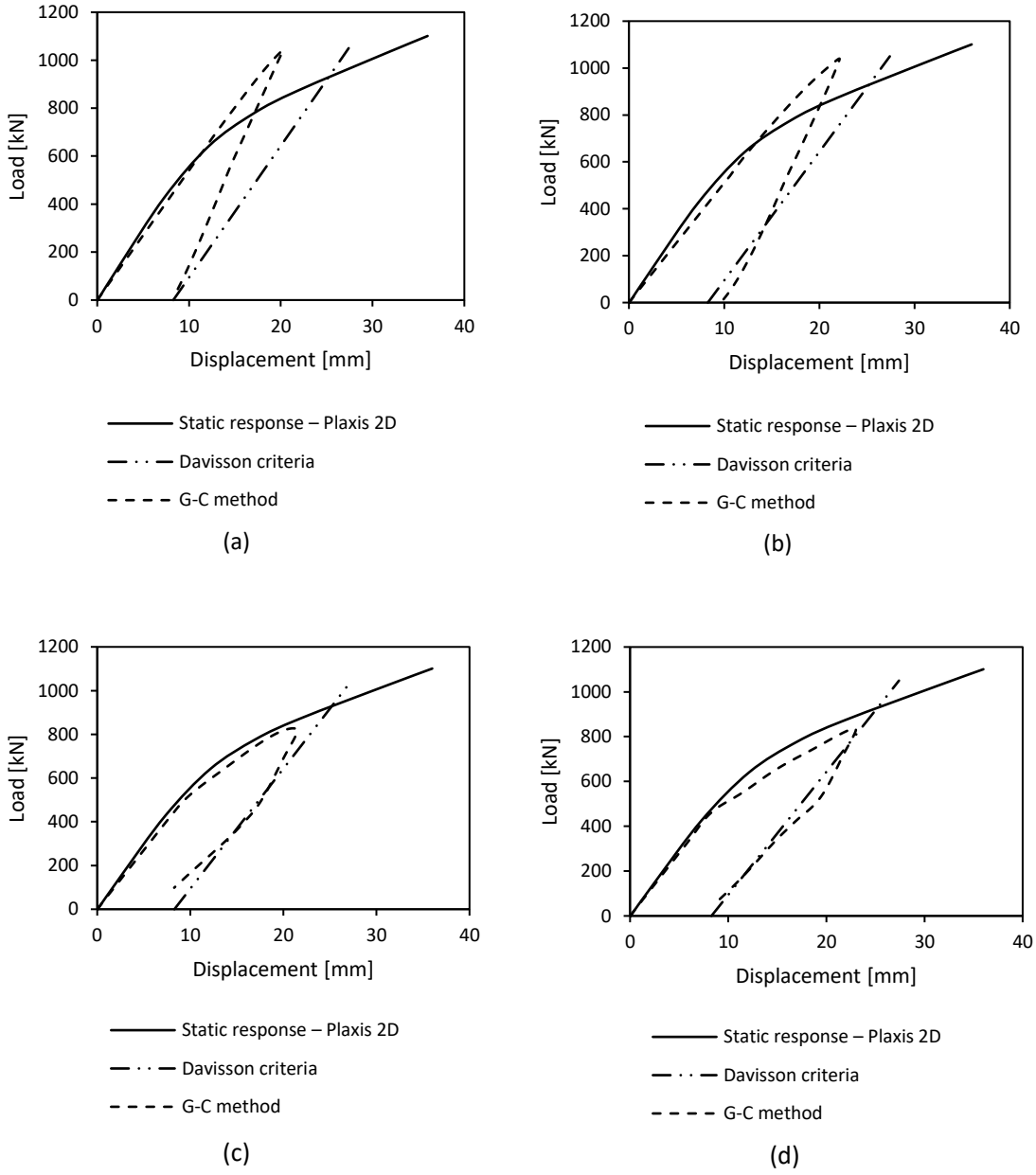

Figure 4- 30: Load-displacement curves from dynamic and static analyses for different hammer weights for helical piles installed in sand: (a) 20 kN; (b) 30 kN; (c) 50 kN; and (d) 80 kN.

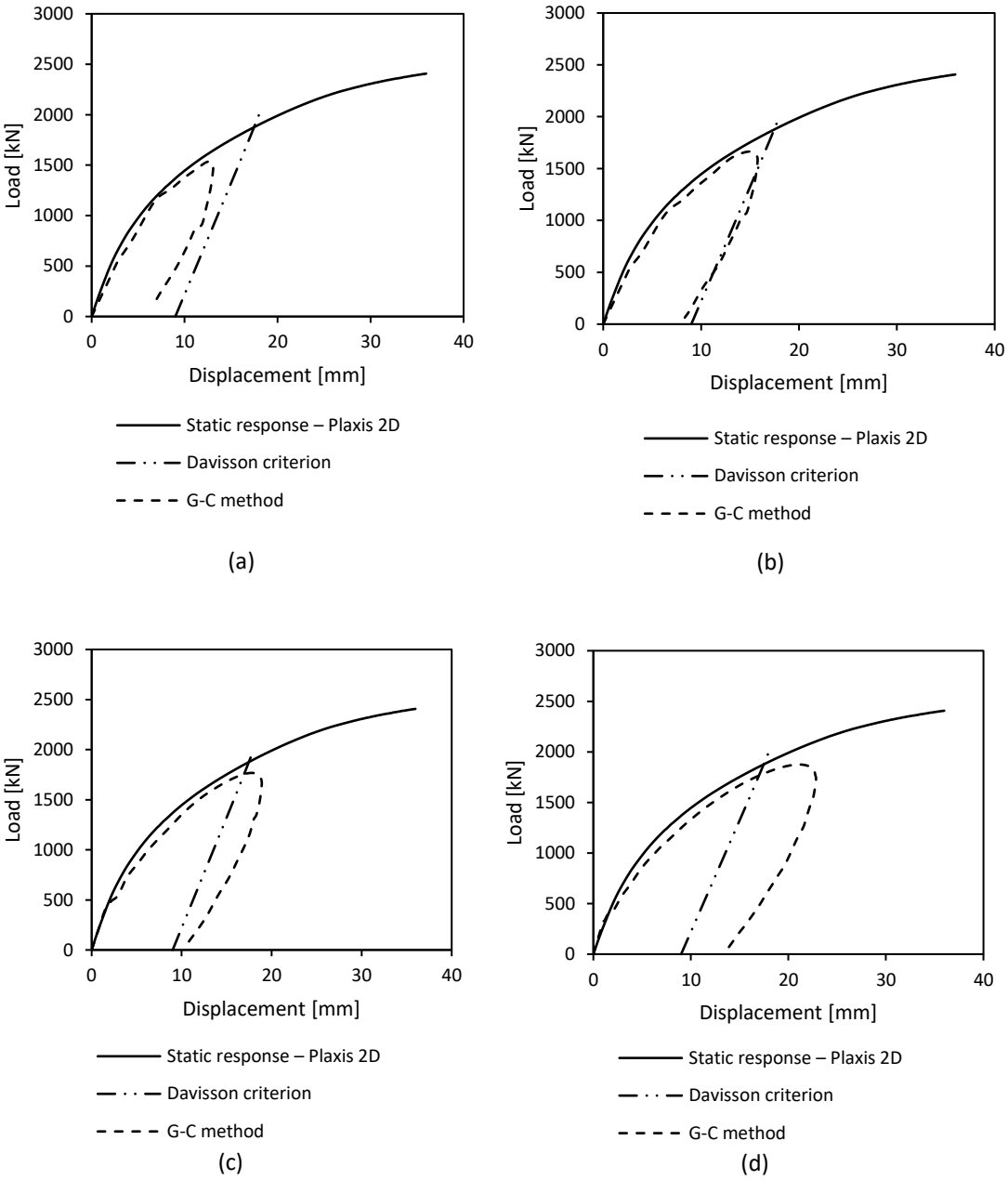

Figure 4- 31: Load-displacement curves from dynamic and static analyses at different hammer weights for helical piles installed in clay: (a) 20 kN; (b) 30 kN; (c) 50 kN; and (d) 80 kN.

For W_r = 20 kN, calculated displacement contours demonstrate that load transfer involved individual helix bearing, not a cylindrical shear failure. This indicates that the hammer weight was not enough to mobilize the ultimate pile capacity and form the expected failure mechanism for a helical pile with two closely spaced helices, as depicted in Figure 4-32(a) and Figure 4-33(a) for both soil conditions. As the hammer weight increases, the

displacement contours expand and a soil cylinder forms between the two helices with higher displacement contours, signifying the formation of the failure surface as shown in Figure 4-32 and 4-33. Nevertheless, none of the selected hammer weights was sufficient to fully mobilize the global cylindrical failure mechanism observed during the SLT. It should be noted, though, that the soil mass (cylinder) between the helices moves due to the applied dynamic forces resulting in development of shearing resistance at the interface between the soil cylinder and adjacent soil, and hence complicating the behavior of helical piles subjected to the HSDT. Thus, the mass of the inter-helix soil cylinder should be considered when evaluating the HSDT setup to determine the most suitable combination of hammer mass and drop height as well as cushion stiffness.

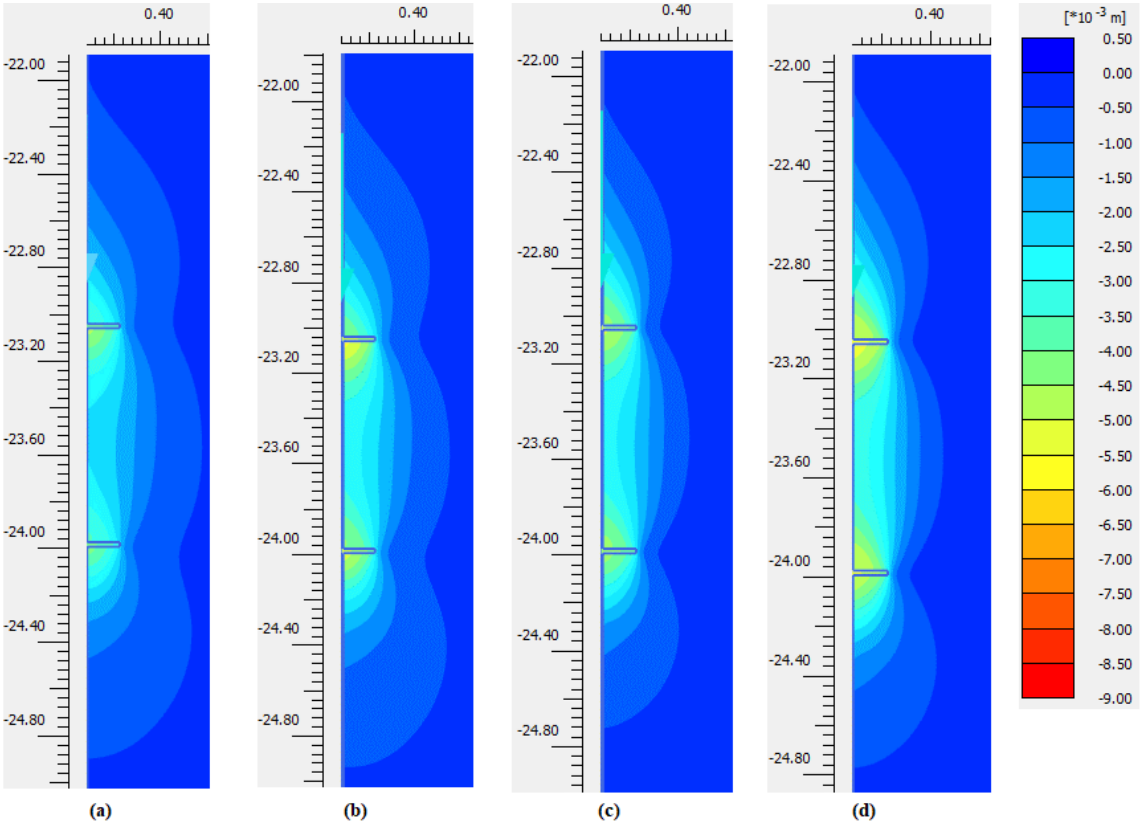

Figure 4- 32: Displacement contours obtained for the helical pile installed in sand at a different hammer weight: (a) 20 kN; (b) 30 kN; (c) 50 kN; and (d) 80 kN.

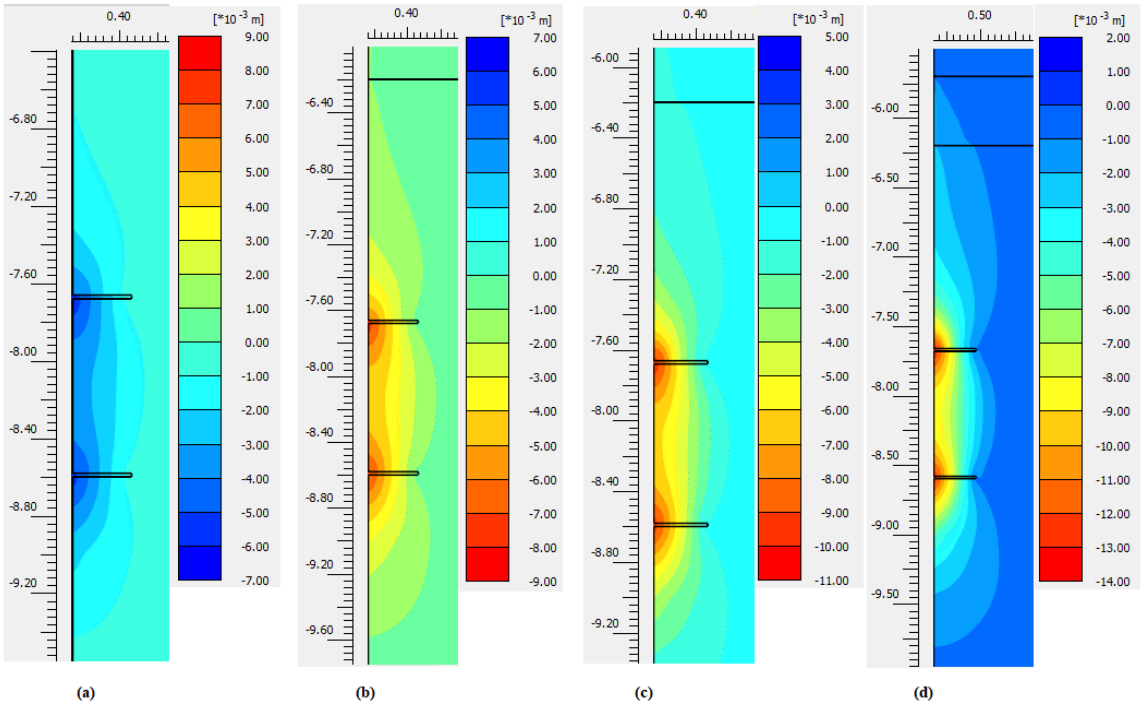

Figure 4- 33: Displacement contours obtained for helical pile installed in clay for different hammer weight: (a) 20 kN; (b) 30 kN; (c) 50 kN; and (d) 80 kN.

4.11.5. Effect of Cushion Stiffness

The cushion stiffness, k_s, controls the duration and amplitude of the impact force at the pile head. Two values of cushion stiffness were considered for each case. For Case 1, k_s = 8E06 N/m and 8E07 N/m were considered while for Case 2, k_s = 3E07 N/m and 3E08 N/m were considered. These values were selected to represent overall soft and stiff systems. The hammer weight and drop height were equal to 30 kN and 1 m, respectively. The spacing ratio (S/D_H) = 1.5 was used for all cases. Figure 4-34 shows the generated force-time history used to simulate the impact hammer considering the different cushion stiffness values.

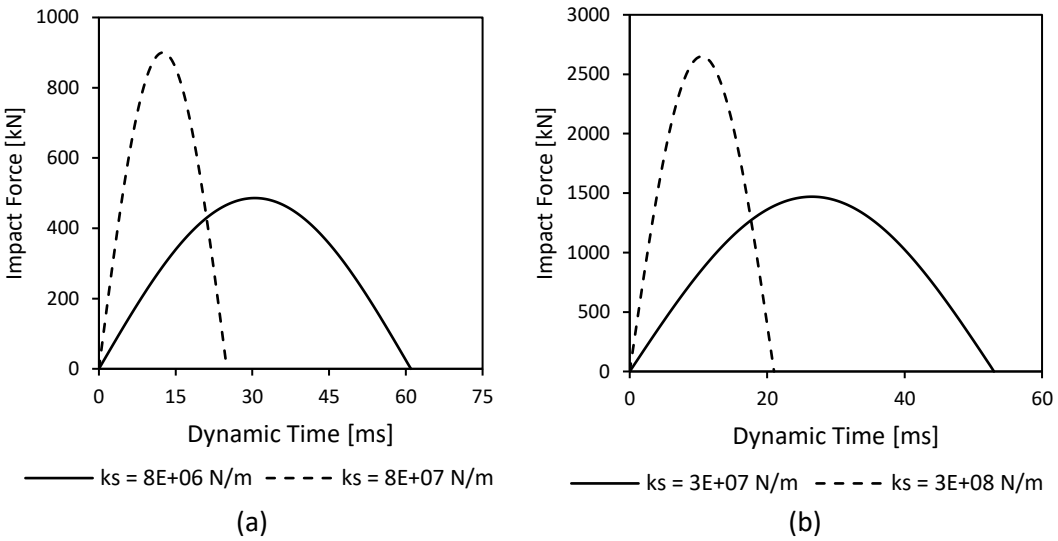

Figure 4- 34: Force pulse generated at pile head for different cushion stiffness: (a) for Case 1; and (b) Case 2.

Figures 4-35 and 4-36 present the derived static load-displacement curves obtained from G-C method compared with the static response curves for Cases 1 and 2, respectively. As can be seen from these figures, a dramatic increase in the helical pile static response with increasing cushion material stiffness. The developed displacement contours associated with an impact on a stiffer cushion at the soil region around the helices are much higher than that observed for the softer cushion as depicted in Figure 4-37 and 4-38 in both soil conditions. Hence, more soil was mobilized with the pile movement, and formed a failure surface consistent cylindrical shear failure that is anticipated for helical piles with closely spaced double helices. This clearly demonstrates the importance of proper selection of cushion stiffness for successful HSDT on helical piles.

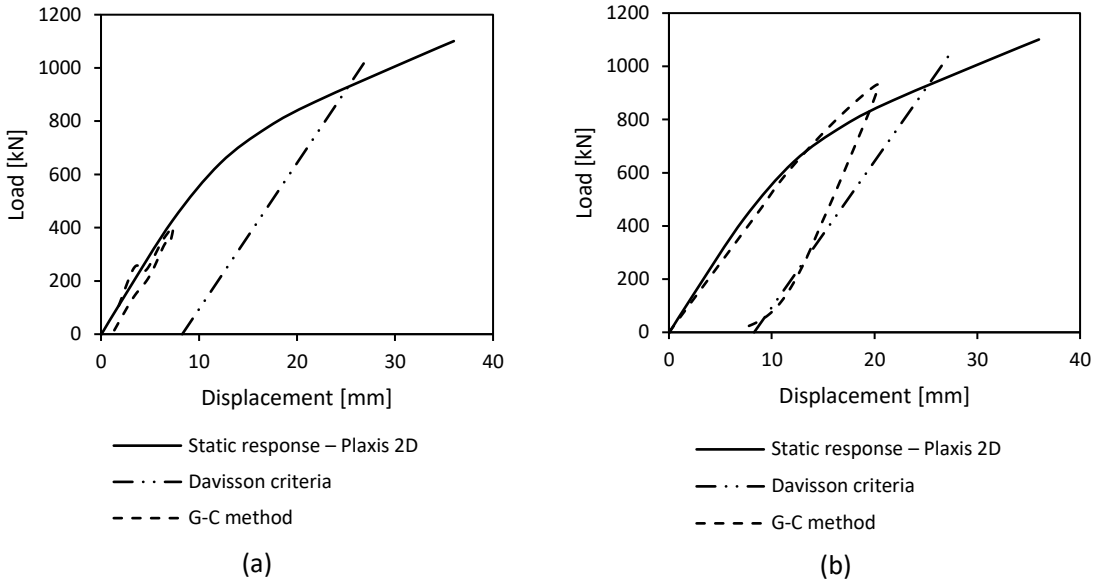

Figure 4- 35: Responses of the helical pile to different values of Ks for Case 1: (a) 8E06 N/m, (b) 8E07 N/m.

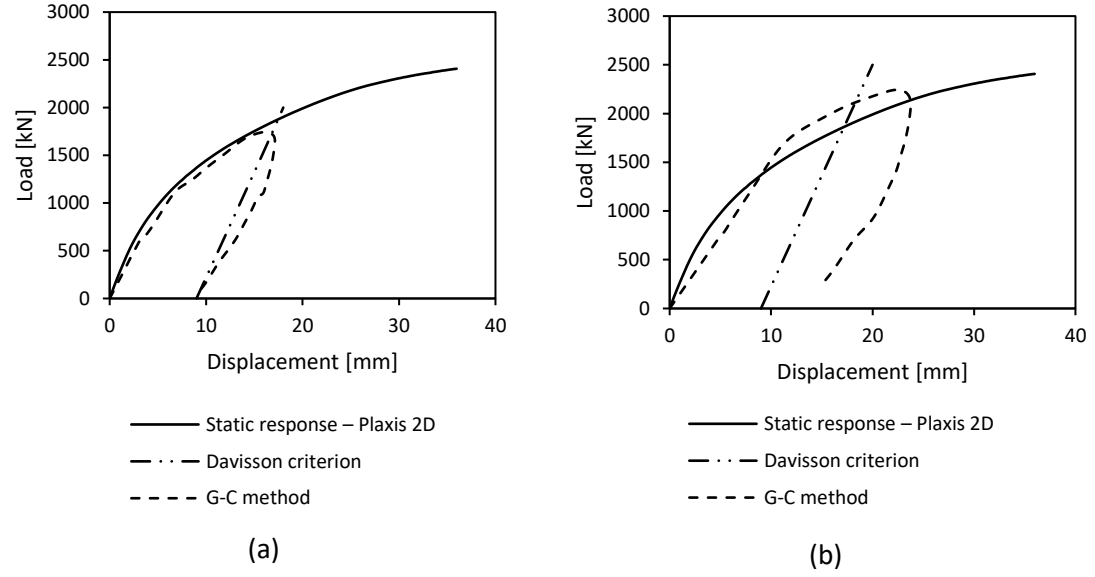

Figure 4- 36: Responses of piles at different values of Ks for Case 2: (a) 3E08 N/m, (b) 3E09 N/m.

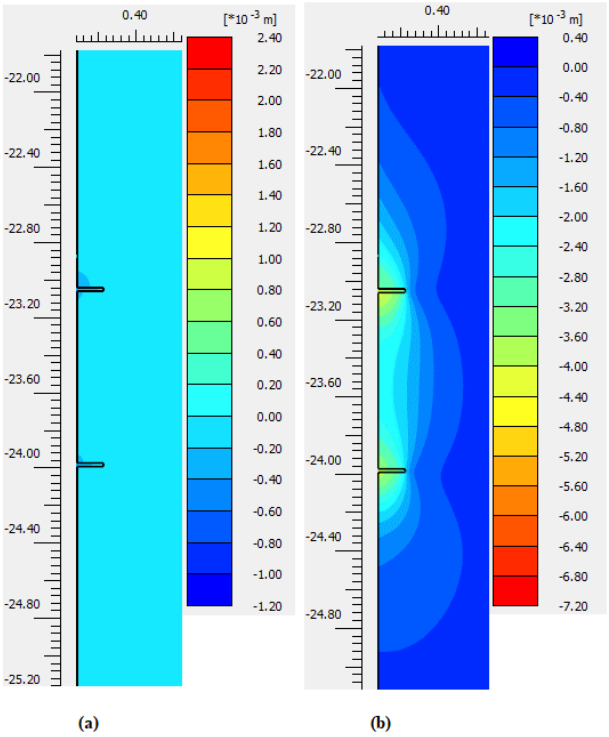

Figure 4- 37: Variations of contours of displacements with different cushion stiffness for helical pile installed in sand Case 1: (a) 8E06 N/m, (b) 8E07 N/m.

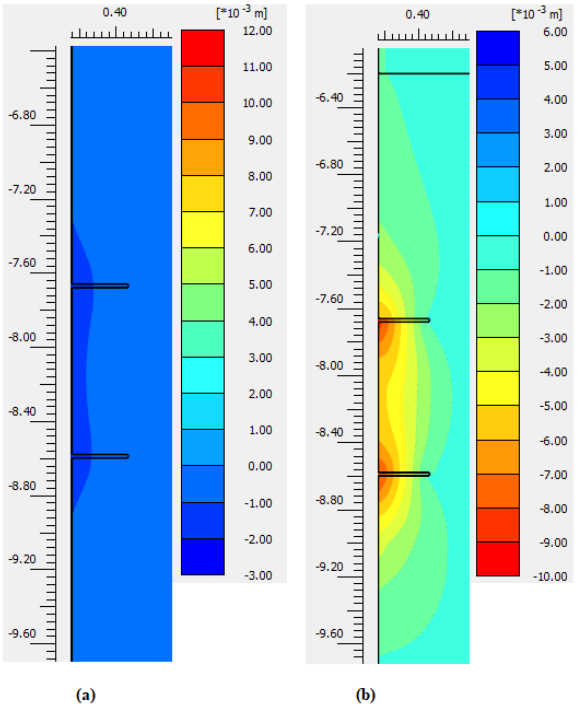

Figure 4- 38: Variations of contours of displacements with different cushion stiffness for helical pile installed in clay Case 2: (a) 3E08 N/m, (b) 3E09 N/m.

4.12. Validation of Mathematical Model

The variation of mobilized static capacity ratio (i.e. from static and dynamic tests) with impedance ratio is plotted against the results obtained from the mathematical model developed in Chapter 3 (see Figure 3-23a). A total of 28 helical pile models were considered, seven cases of single-helix pile and the rest represent double-helix piles with spacing ratio (S/D_H) = 1.5 to 3.

Figure 4-39 shows excellent agreement between the mathematical solution and the numerical analysis. This suggests that this curve can be used for estimating static capacity mobilization ratio for helical pile capacity during the HSDT, even though it was established based on collected data of HSDT conducted on driven piles. For driven piles it was proposed to utilize impedance ratio (i.e. pile impedance/hammer impedance) between 0.7 to 0.9; meanwhile, the practical range of the impedance ratio for helical piles is between 0.55 to 0.75 with most of the data concentrated around 0.6. This range resulted in a mobilized soil resistance ratio of approximately 1.

Inspecting Figure 4-39 shows three cases with mobilized soil resistance well above the upper bound. These cases represented a soft system that generated a low force-time pule at the pile head. Hence, it did not displace the helical pile sufficiently to mobilize its capacity. In fact, the helical pile in these 3 models experienced very small displacement (i.e. displacement to helix diameter = 0.021, 0.022, and 0.03).

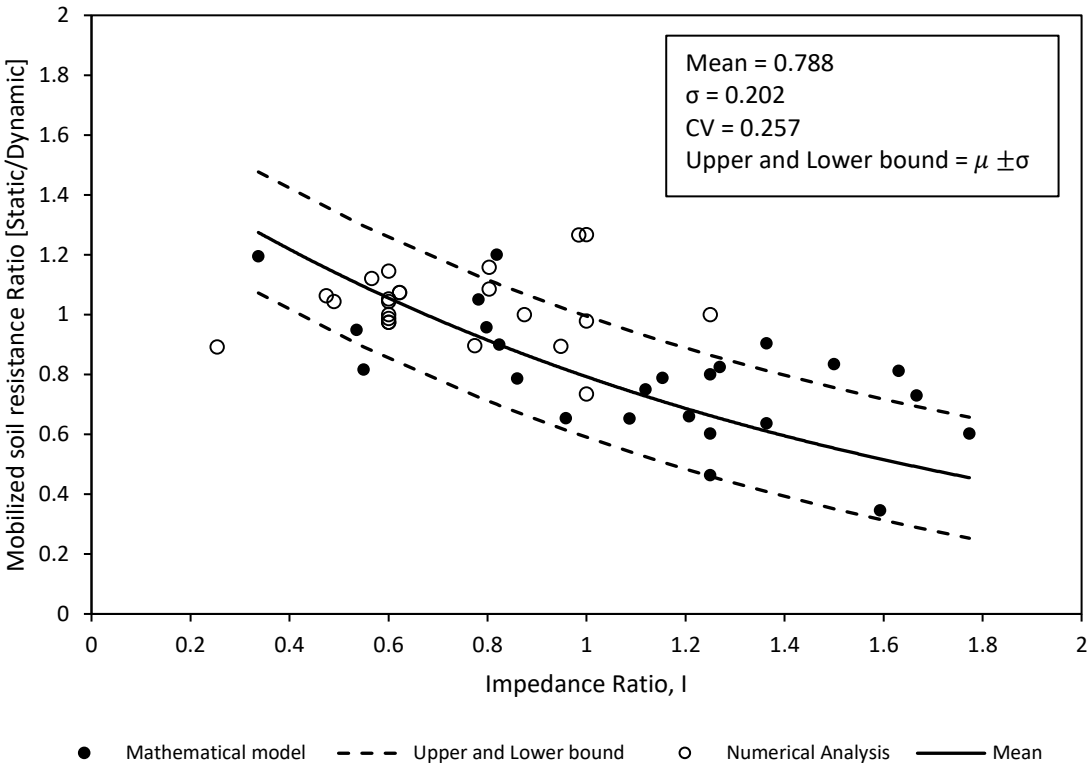

Figure 4- 39: Relationship between mobilized static soil resistance and impedance ratio obtained from numerical analysis and mathematical model results.

4.13. Relationship of Hammer Potential Energy and Mobilized Resistance at a Required Displacement

It is beneficial to develop an empirical correlation between the required impact energy to displace the pile head sufficiently to mobilize its static ultimate capacity. Such correlation can be used to select the proper hammer-cushion system for conducting the HSDT.

The pile impedance ratio can be determined by ρCA for straight shaft piles, and the modified pile impedance equations (equation 3.50 and equation 3.51) for helical piles that account for the added soil mass. The hammer and the cushion characteristic are quantified as $\sqrt{k_s m_r}$. Figure 4-39 can then be used to determine the mobilized soil resistance ratio (Static/Dynamic). This ratio will be used in the desired empirical correlation to establish the necessary displacement.

The data points obtained from actual field HSDT and from the numerical models are subjected to surface fitting procedure (Balaras and Jeter, 1990) to relate the displacement

to an impact energy value. The program MATLAB (MathWorks, 2016) was employed to accomplish the surface fitting procedure based on a Custom Fit Model. This is shown in the following for piles installed in cohesive and cohesionless soils.

4.13.1. For Clay

Thirty cases of HSDT conducted on piles installed in cohesive soil were used. Ten cases were established from the numerical models and 20 cases were collected from the literature from actual field tests as presented in chapter 3. In all cases, the pile capacity was determined using HSDT in restrike condition. The measured displacements at the pile head ranged between 5.8 mm to 23.8 mm with an average of 13.7 mm. The ratio of the mobilized capacity derived from HSDT and SLT ranged between 0.46 to 1.3 with an average value of 0.85. The pile length ranged from 4 m to 16 m. The potential energy for each case was calculated using the gravitational force formula, mgh, with an average efficiency of 60%. It should be noted that none of the cases involved excessive dynamic installation stresses or any form of damage.

The generated 3-D plot with the best fit surface is depicted in Figure 4-40. The results showed that the potential energy decreased exponentially with the decrease in the mobilized soil resistance ratio and increased as the pile head displacement increased. The most suitable empirical correlations with 70th percentile confidence interval are presented in equations 4.10 and 4.11.

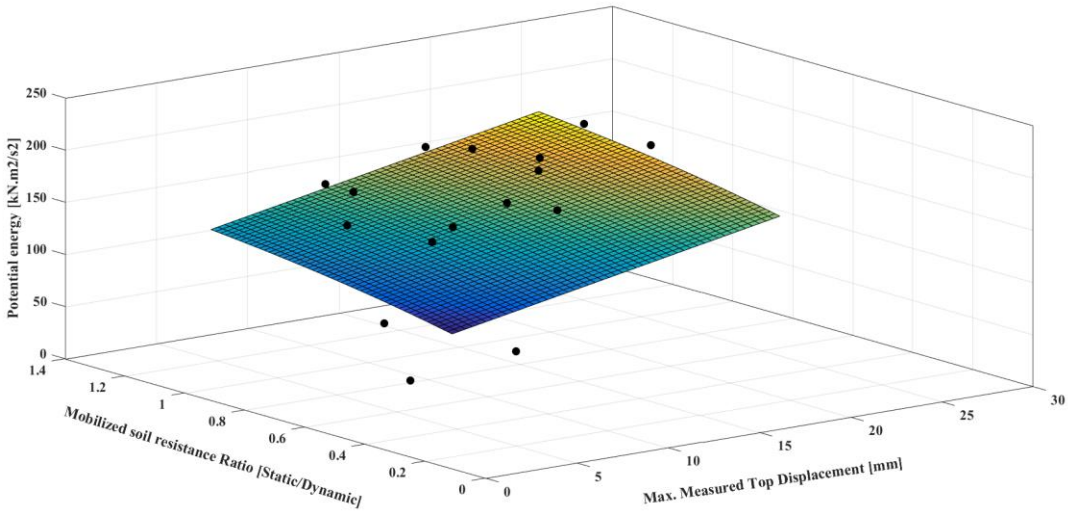

Figure 4- 40: A 3D plot of the Variation of potential energy with mobilized static resistance ratio (static / dynamic) at a maximum measured top displacement for cohesive soils.

Best fitted surface equation;

$$(E_p)_{60\%} = 3.36S_{max} - 99.03e^{-R_m} + 126.2 \quad (4.10)$$

Maximum potential energy (70th percentile);

$$(E_p)_{60\%} = 5.56S_{max} + 104e^{-R_m} + 183.26 \quad (4.11)$$

Where; $(E_p)_{60\%}$ = Potential energy in $kN.m^2/s^2$.

S_{max} = Required top pile head displacement in mm.

R_m = Mobilized static resistance ratio from Figure 4-39.

4.13.2. For Sand

The data base used for developing the empirical correlation for helical piles installed in sand comprised primarily data from numerical models and only one actual field test case. The range of the maximum measured pile top displacement varied from 7.3 mm to 36.4 mm with an average of 22 mm. The mobilized static resistance ratio varied from 0.49 to 2.31. The pile length was 24.7 m for all cases considered. The best fit surface and confidence interval were obtained, and the results are shown in Figure 4-41.

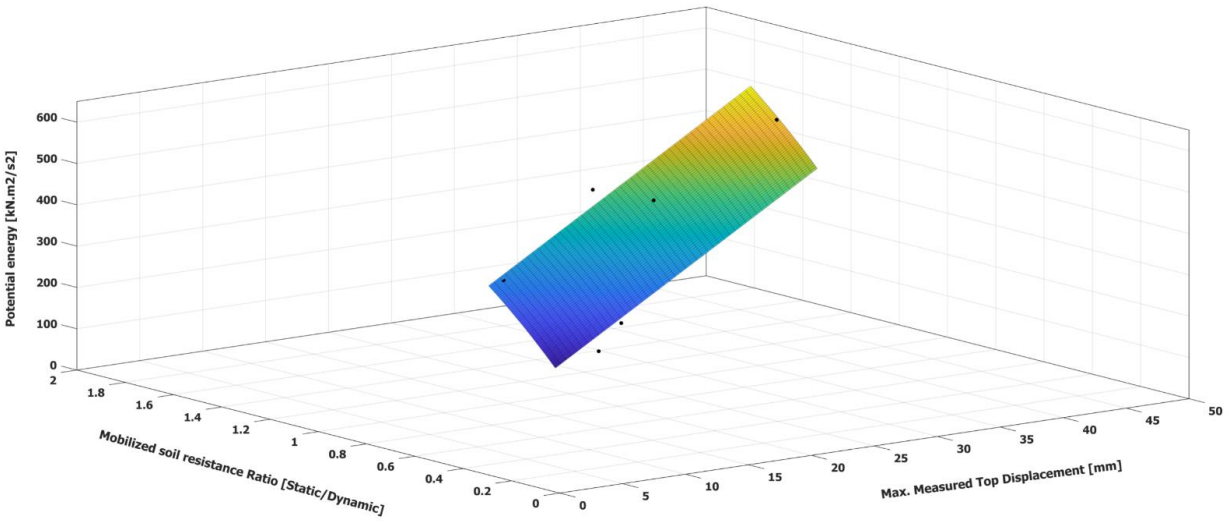

Figure 4- 41: A 3D plot of the variation of potential energy with mobilized static resistance ratio (static / dynamic) at a maximum measured top displacement for cohesionless soils.

Best fitted surface equation;

$$(E_p)_{60\%} = 11.87S_{max} - 158.4e^{-R_m} + 117.5 \quad (4.12)$$

Maximum potential energy (70th percentile);

$$(E_p)_{60\%} = 12.65S_{max} + 168.35e^{-R_m} + 217.5 \quad (4.13)$$

4.13.3. Design Procedure

(A) The procedure presented herein is for the case of known hammer mass, m_r, and equivalent cushion stiffness, k_s. The following procedure should be followed:

1. Calculate the impedance ratio, I, using equation 3.41 for driven piles and equation 3.50 and 3.51 for helical piles with single and double helices, respectively.
2. Estimate the mobilized static resistance ratio, R_m, from Figure 4-39.
3. Select the desirable top pile head displacement, S_{max}.
4. Use the most appropriate equation (eq. 4.10 to 4.13) based on the soil type at the site to calculate the potential energy $(E_p)_{60\%}$.
5. Substitute $(E_p)_{60\%}$ and m_r in equation 4.14 to estimate the drop height, h.

$$h = \frac{500\,(E_p)_{60\%}}{3gm_r} \tag{4.14}$$

6. After conducting the HSDT and obtaining the mobilized capacity of the tested pile form dynamic measurements, use equation 4.15 to correct the value. Alternately, use equation 4.15 to correct the derived load-displacement curve to reflect the one obtained from SLT.

$$Mobilized\ static\ resistance\ (SLT) = R_m\ x \text{ Mobilized static resistance (HSDT)} \tag{4.15}$$

(B) To select the hammer and equivalent cushioning stiffness, the following steps are proposed:

1. Assume a value for *I* based on the recommended ranges for the pile type to be tested (see section 4.12).
2. Determine R_m and S_{max}.
3. Calculate $(E_p)_{60\%}$ and maximum $(E_p)_{60\%}$.
4. Use equation 4.14 with assumed drop height, for example 1 m, after which estimate the range of the hammer mass using the values from step 3.
5. Select the most suitable and available hammer mass that lay within the range established from step 4.
6. From equation 3.41 for driven piles and equation 3.50 and 3.51 for helical piles, estimate the required cushion stiffness. Then, select the most approximate cushion stiffness available at the site.
7. Re-calculate *I* using the selected hammer mass and cushion stiffness and apply procedure (A).

4.13.4. Limitations of Design Procedure

Even though the proposed procedures can estimate the required energy to displace a pile to a given displacement in order to mobilize its static capacity, they have limitations as follow;

1. The equations were established based on several case histories collected from various sources, including technical and literature sources and numerical analysis. Table 4.13 shows the characteristics of the HSDT collected from these sources along with lower and upper limits, average value, standard deviation, and coefficient of variation. Most of the source performed the HSDT on piles installed in cohesive soils. Therefore, more investigations are required to provide a robust design procedure for piles installed in cohesionless soils.
2. Several methods exist in the literature for the capacity determination of piles. Herein, Davisson's criterion was used to determine the capacity of all piles in this study in order to compare it with pile capacity determined indirectly from HSDT using the methods discussed above.
3. The HSDT characteristics in most of the case histories were not sufficient to mobilize the soil resistance; therefore, a correction factor (equation 4.15) was proposed.

Table 4- 13: Limitations of Design Procedure.

Pile type	Parameter	Lower Limit	Upper Limit	Average	Standard deviation	Coefficient of variation
Driven piles	Weight of hammer (kN)	18	60	21	14	0.59
	Peak force at the pile head (kN)	800	5460	1840	600	0.80
	Time of impact (ms)	8	80	28	21	0.75
	Drop height (m)	0.8	1.4	1	0.4	0.35
	Velocity of impact (m/s)	4	8	5	1.3	0.27
	Equivalent cushion stiffness (kN/mm)	160	500	336	162	0.78
	Impedance ratio	0.55	1.3	1.02	0.30	0.36
	Diameter (mm)	230	500	300	130	0.41
Helical piles	Weight of hammer (kN)	19	49	36	12	0.33
	Peak force at the pile head (kN)	520	3410	1450	750	0.52
	Time of impact (ms)	15	60	30	12	0.40
	Drop height (m)	0.2	1.5	1	0.40	0.56
	Velocity of impact (m/s)	2	6	3.5	1	0.30
	Equivalent cushion stiffness (kN/mm)	102	800	250	130	0.77
	Impedance ratio	0.55	1.50	1.01	0.4	0.36
	Shaft diameter (mm)	178	508	260	75	0.27
	Helix diameter (mm)	356	914	610	200	0.34

4.14. Conclusion

2D Finite Element Models (FEM) were constructed by employing Plaxis 2D to investigate the behaviour of helical piles under the HSDT. The models were validated with two case histories results found in the literature. The axisymmetric model type was used to model the geometry condition of the problem in order to minimize the computational time. The size of the models was greater than L x 2L, where L is the length of the pile. No adverse effect from the boundaries was found; hence, the selected size for all models was sufficient to minimize the boundary effects. For the dynamic load simulations, the viscous boundaries were assigned for the exterior and bottom boundaries. The Hardening Soil model (HS) was selected to describe the mechanical behavior of the soils. A volume cluster with linearly elastic non-porous material behavior was selected to model the helical pile. The mesh was discretized using fifteen-nodded triangular elements. An excellent match between the measured and calculated results were achieved.

The finite element models were extended to perform a parametric study to understand better the influence of different factors that may affect the behavior of the helical pile during the HSDT. These factors included: helical effects, spacing ratio, drop height, hammer weight, and cushion stiffness. The results showed that the effect of helices should be accounted for in selecting the HSDT aspects to ensure that enough force at the helical pile is generated to fully mobilize the resistances of helical piles. The results were similar for helix spacing ratio 1.5 and 3. It was also observed that for a hammer-cushion-pile system, the dropped height has a profound effect on the response of the helical pile; however, a drop height higher than 1.5 m should be avoided due to the development of to excessive stresses greater than the allowable stresses within the helical pile.

The parametric study also showed that the predicted static response form dynamic measurements approximately matched the static response of the helical pile as the hammer weight increased, which exerted impact loads that lasted longer. It also has a significant effect on the formation of the global geometry of the failure zone in the soil mass within the inter-helical zone. Thus, a soil mass should be considered in the drivability analysis of the helical pile. Furthermore, the cushioning material plays a role in the amount of energy delivered on top of the helical piles. Softer cushions tend to minimize the mobilized

resistance, while stiff cushions create stresses that could lead to the yielding of helices and possible damage at the top of the helical pile. In addition, the finite element analysis results were in good agreement with the results obtained from the mathematical model. Finally, the results from the parametric study were used to establish a design procedure and guidelines for an effective HSDT on helical piles, as well as for uniform shaft piles.

4.15. References

Airhart, T. P., Hirsch, T. J., & Coyle, H. M. (1967). Pile-soil system response in clay as a function of excess pore water pressure and other soil properties. Texas Transportation Institute.

Alnuaim, A. M., El Naggar, M. H., & El Naggar, H. (2018). Performance of micropiled rafts in clay: numerical investigation. Computers and Geotechnics, Vol. 99; 42-54.

Alpan, I. (1970). The Geotechnical Properties of Soils. Earth Science Reviews. Elsevier, 1(6); 5-49.

API. (1987). Recommended practice for planning, designing, and constructing fixed offshore platforms, API RP2A,17th edition. American Petroleum Institute, Washington, DC, USA.

Bakker, K. J., Hoefsloot, F. J. M., & de Jong, E. (2010). Dynamic analysis of large diameter piles Statnamic load test. In Numerical Methods in Geotechnical Engineering. CRC Press. pp. 629-634

Balaras, C. & Jeter, S. (1990). Surface fitting method for three-dimensional scattered data. International Journal for Numerical Methods in Engineering. Vol. 29: 633 - 645.

Beim, J., & Luna, S. C. (2012). Results of dynamic and static load tests on helical piles in the varved clay of Massachusetts. DFI Journal, the Journal of the Deep Foundations Institute, 6(1): 58-67.

Benjamin W, P. E., & Engineers, G. R. L. (n.d.) High strain dynamic load testing on helical piles – Case Study.

Cannon, J. G. (2000). The application of high strain dynamic pile testing to screwed steel piles. In Sixth International Conference on the Application of Stress-Wave Theory to Piles. pp. 11-13.

ÇELİK, S. (2017). Comparison of mohr-coulomb and hardening soil models numerical estimation of ground surface settlement caused by tunneling. Journal of the Institute of Science and Technology, 7(4); 95-102. doi:10.21597/jist.2017.202

CH2M HILL, Inc. (2013). Geotechnical Report for the APE Yard Helical Pile Test Program. (Report No. SEA130450001). Bellevue, Washington, USA.

Charue, N. (2004). Loading rate effects on pile load-displacement behaviour derived from back-analysis of two load testing procedures [Doctoral thesis]. Université Catholique de Louvain, Belgium.

Elkasabgy, M. A. (2011). Dynamic and Static Performance of Large-Capacity Helical Piles in Cohesive Soils [Doctoral thesis]. University of Western Ontario, Canada. Electronic Thesis and Dissertation Repository. https://ir.lib.uwo.ca/etd/193

Elkasabgy, M., & El Naggar, M. H. (2013). Dynamic response of vertically loaded helical and driven steel piles. Canadian Geotechnical Journal, 50(5); 521-535.

Elkasabgy, M., & El Naggar, M. H. (2018). Lateral vibration of helical and driven steel piles installed in clayey soil. Journal of Geotechnical and Geo-Environmental Engineering, 144(9), 06018009.

Elsherbiny, Z. H., & El Naggar, M. H. (2013). Axial compressive capacity of helical piles from field tests and numerical study. Canadian Geotechnical Journal, 50(12); 1191-1203.

Fahey, M., & Carter, J. P. (1993). A finite element study of the pressuremeter test in sand using a nonlinear elastic plastic model. Canadian Geotechnical Journal, 30(2); 348-362.

Fakharian, K., Masouleh, S. F., & Mohammadlou, A. S. (2014). Comparison of end-of-drive and restrike signal matching analysis for a real case using continuum numerical modelling. Soils and Foundations, 54(2); 155-167.

Farshi Homayoun Rooz, A., & Hamidi, A. (2017). Numerical analysis of factors affecting ground vibrations due to continuous impact pile driving. International Journal of Geomechanics, 17(12); 04017107.

Gibson, G. C., & Coyle, H. M. (1968). Soil damping constants related to common soil properties in sands and clays.

Goble, G. G., Likins Jr, G., & Rausche, F. (1975). Bearing capacity of piles from dynamic measurements (No. OHIO-DOT-05-75 Final Rpt.).

Gunaratne, M. (2013). The foundation engineering handbook. CRC Press.

Holeyman, A. E. (1992). Technology of pile dynamic testing, Keynote lecture. In Proc. of the 4th Int. Conf. of Application of Stress-wave Theory to Piles. pp. 195-215.

Hölscher, P., and Barents, F. B. J. (1992). Statnamic load testing of Foundation piles. In Proceedings of the Fourth International Conference on the Application of Stress-Wave Theory to Piles, the Hague, the Netherlands. pp. 413-419.

Hoque, E., & Tatsuoka, F. (2004). Effects of stress ratio on small-strain stiffness during triaxial shearing. Géotechnique, 54(7): 429-439.

Hussein, M., Rausche, F., & Likins, G. (1992). Dynamics of pile driving as a function of ram drop height. In Proceedings of the Fourth International Conference on the Application of Stress-Wave Theory to Piles, the Hague, the Netherlands. pp. 21-24.

Huy, N. Q., Van Tol, A. F., & Hölscher, P. (2006). Laboratory investigation of the loading rate effects in sand.

Janbu, N. (1963). Soil compressibility as determined by odometer and triaxial tests. In Proceedings Europe Conference SMFE. Vol. 1: 19-25.

Kequin, G., & Jiayou, L. (1986). Influence of strain rate on undrained shear characteristics of Ko--consolidated cohesive soils. Tectonophysics, Vol., 126: 2-4.

Keshavarz, A., Malekzadeh, P., & Hosseini, A. (2016). Time domain dynamic analysis of floating piles under impact loads. International Journal of Geomechanics, 17(2); 04016051.

Khelifi, Z., Berga, A., & Terfaya, N. (2011). Modeling the behavior of axially and laterally loaded pile with a contact model. Electronic Journal of Geotechnical Engineering, Vol. 16.

Kim, T. C., & Novak, M. (1981). Dynamic properties of some cohesive soils of Ontario. Canadian Geotechnical Journal, 18(3); 371-389.

Krasiński, A. (2014). Numerical simulation of screw displacement pile interaction with non-cohesive soil. Archives of Civil and Mechanical Engineering, 14(1); 122-133.

Livneh, B., & El Naggar, M. H. (2008). Axial testing and numerical modeling of square shaft helical piles under compressive and tensile loading. Canadian Geotechnical Journal, 45(8): 1142-1155.

Lv, Y. R., Ng, C. W. W., Lam, S. Y., Liu, H. L., & Ma, L. J. (2017). Geometric effects on piles in consolidating ground: centrifuge and numerical modeling. Journal of Geotechnical and Geoenvironmental Engineering, 143(9); 04017040.

Lysmer, J., & Kuhlemeyer, R. L. (1969). Finite dynamic model for infinite media. Journal of the Engineering Mechanics Division, 95(4); 859-878.

MathWorks, I. (2016). MATLAB and Statistics Toolbox. the Mathworks, Inc., Massachusetts, United States.

Mayne, P. W., & Dumas, C. (1997). Enhanced in situ geotechnical testing for bridge foundation analysis. Transportation Research Record, 1569(1); 26-35.

Middendorp, P. (2000). Keynote lecture: Statnamic the engineering of art. In Proceedings of the Fourth International Conference on the Application of Stress-Wave Theory to Piles, the Hague, the Netherlands. pp. 570-580.

Middendorp, P., Bermingham, P. and Kuiper, B. (1992). Statnamic load testing of foundation piles. 4th International Conference on Stress Waves, The Hague, Balkema.

Morgano, C. M., White, B. A., & Allin, R. C. (2008). Dynamic testing in sensitive & difficult soil conditions. Proceedings of the 8th International Conference on the Application of Stress-Wave Theory to Piles: Lisbon, Portugal, IOS Press. pp. 8-10.

Obrzud, R., & Truty, A. (2018). The hardening soil model-a practical guidebook; Z-Soil.PC100701 Report. Zace Services Ltd, Software engineering, Switzerland.

Osula, D. O. A., Alfa, A. S., Adebisi, O., Ola, S. A., Gill, M. A., & Ola, S. A. (2016). Evaluation of bearing capacity and settlement of foundations. Leonardo Electronic Journal of Practices and Technologies, 29; 93-114.

Plaxis 2D. (2018). Reference manual. Bentley Systems: Advancing Infrastructure. Delft, Netherlands.

Polishchuk, A. I., & Maksimov, F. A. (2017). Numerical Analysis of Helical Pile-Soil Interaction under Compressive Loads. In Materials Science and Engineering Conference Series, 262(1).

Popa, C. C., Mușat, V., & Bejan, F. (2018). Numerical and analytical analysis of foundation behavior on soil reinforced with rigid inclusions. Acta Technica Napocensis: Civil Engineering and Architecture, 64(4); 41-55.

Presti, D. L., Pallara, O., Lancellotta, R., Armandi, M., & Maniscalco, R. (1993). Monotonic and cyclic loading behavior of two sands at small strains. Geotechnical Testing Journal, 16(4); 409-424.

Randolph, M. F., & Murphy, B. S. (1985). Shaft capacity of driven piles in clay. In Offshore Technology Conference. Offshore Technology Conference. Houston, Texas, USA.

Rani, R. S., Prasad, K. N., & Krishna, T. S. (2014). Applicability of Mohr-Coulomb & Drucker-Prager models for assessment of undrained shear behaviour of clayey soils. International Journal of Civil Engineering and Technology, 5(10); 104-123.

Robertson, P. K. (2009). Interpretation of cone penetration tests - a unified approach. Canadian geotechnical journal, 46(11); 1337-1355.

Sakr, M. (2013). Comparison between high strain dynamic and static load tests of helical piles in cohesive soils. Soil Dynamics and Earthquake Engineering, 54; 20-30.

Schanz, T., & Vermeer, P. A. (1998). Special issue on Pre-failure deformation behaviour of geomaterials. Geotechnique, Vol. 48; 383-387.

Teo, P. L., & Wong, K. S. (2012). Application of the hardening soil model in deep excavation analysis. The IES Journal Part A: Civil & Structural Engineering, 5(3); 152-165. doi:10.1080/19373260.2012.696445

Verbrugge, J. C., & Schroeder, C. (2018). Geotechnical Correlations for Soils and Rocks. ISTE Limited.

Viggiani, G., & Atkinson, J. H. (1995). Stiffness of fine-grained soil at very small strains. Géotechnique, 45(2); 249-265.

Van Genuchten, M. T. (1980). A closed-form equation for predicting the hydraulic conductivity of unsaturated soils 1. Soil science society of America journal, 44(5), 892-898.

CHAPTER FIVE

CONCLUSIONS AND RECOMMENDATIONS

5.1 Overview

The High Strain Dynamic Load Test (HSDT) evaluates the pile capacity using dynamic measurements generated through subjecting the pile to an axial compressive impact force by means of dropping a hammer at its head. The objective of this study is to investigate the performance and effectiveness of HSDT of helical piles using mathematical and numerical methods. Several case studies were examined to validate the mathematical model. In addition, finite element models were established and were validated using the results of two cases histories. The validated models were then used to conduct a parametric study to evaluate the effects of the HSDT parameters. The findings from the conducted studies are provided here and some recommendations are stated for future investigations.

5.2 Conclusions

Based on the mathematical analysis, the following conclusions are drawn:

1. Equations were derived to predict the force-time response for both straight shaft piles and helical piles considering their impedance. The predicted force time history from these equations matched the measured force of the pile reasonably well.
2. The force-time response at the pile head is controlled mainly by two parameters; the equivalent cushion stiffness, k_s, and pile impedance, Z. For a given system, the cushion material has a significant effect on the generated pulse shape. Softer cushion tends to elongate the time of impact and reduce the peak force while stiffer cushioning produces short time impact and increases the peak force at the head of the pile. Pile impedance influences the generated peak force for a given hammer and cushion setup. For low pile impedance, the peak force increases linearly with

the increase in pile impedance. For high pile impedance, the increase is not that significant.

3. Energy dissipation in the hammer-cushion- pile system is described by the damping ratio, D. For a system with D > 1, the force is transmitted gradually to the pile head before it returns to equilibrium with no negative force. For a system with D < 1, the force is transmitted at a high rate. Furthermore, the peak pile force is inversely related to the damping. The peak pile force decreases exponentially as D increases.
4. Maximum compressive and tensile stresses above the recommended limiting stress value or damage of the pile head may result in an overdamped system; therefore, monitoring such a system is necessary.
5. The impedance ratio, I, should be kept between 0.7 and 0.9. For impedance ratio $\geq$ 1, the hammer-cushion-pile system does not exhibit oscillatory force-time response. However, this system may experience hammer separation from the pile head, which reduces the energy transmitted to the pile head. On the other hand, for $I < 1$, the force-time response exhibits oscillatory behaviour as the force decays with time. The peak force becomes sharper and short in duration. In such cases, monitoring the dynamic data is necessary to detect any pile damage.
6. It is recommended to carry out multiple blows when conducting the HSDT with increasing drop height to simulate load-displacement curves for piles. The overall derived static load-displacement curve can be constructed by a best-fit curve that passes through the curves obtained from each height. In some cases, using one representative blow of the highest energy seems to overestimate the mobilized capacity of the pile due to the effect of dynamic forces in the determination of the pile static resistance.
7. The end-bearing resistance offered by the helices increases the pile mechanical impedance, Z. Therefore, pile impedance is modified by considering an added soil mass (equations 3.50 and 3.51) to account for the effect of helices.

Based on the two-dimensional finite element modelling and the parametric study, the following conclusions can be drawn:

1. The FE results compared well with the measured results confirming that the SLT and the HSDT could be modelled using 2D axisymmetric finite element model with reasonable accuracy.
2. The failure mechanism of the helical pile depended on the inter-helix spacing. Cylindrical shear failure was observed for helix spacing ration = 1.5, and individual plate bearing was observed for spacing ratio = 3.
3. A geometry domain size of L x 2L, where L is the pile length, is sufficient to simulate static and dynamic load tests conducted on helical piles.
4. The typical trend of load-settlement curves of helical piles were captured well by the Hardening Soil (HS) model.
5. It is appropriate to simulate the hammer impact at the top of the foundation using a half sine-wave profile provided that the system has an impedance ratio ≥ 1.
6. The load-settlement curves derived from interpreting dynamic measurements (i.e. force, acceleration, and velocity measurements) using the G-C method were compatible with field measurements and predictions from other approaches.
7. The effect of helices should be considered when determining the hammer weight and cushion material for the HSDT. Using the same HSDT setup on helical piles with different number of helices may not lead to the same mobilized load-displacement curve due to the helices resistance, which leads to increased pile impedance. Helical piles with double helices required higher force to compared to single-helix piles.
8. It is not recommended to increase the dropped height of the hammer more than 1.5 m as this may lead to excessive stresses.
9. The predicted load-displacement curves form dynamic measurements approximately match the field measurements of SLT as the weight of the hammer increases. Larger hammer weights generated a force with long duration at the pile head, and reduced inertia and damping forces.

10. The derived static response increased dramatically as the stiffness of the cushion increased; however, very stiff cushions for a given hammer and pile should be avoided since a sharper and shorter duration of the force pulse will be generated.
11. Figure 4-39 can be used for the design of HSDT for both driven and helical piles installed in cohesionless or cohesive soils. The impedance ratio, I, for helical piles should be kept between 0.55 to 0.75, with most of the data concentrated around 0.6 to obtain approximately a mobilized soil resistance ratio of 1.
12. The results from the mathematical solution and the numerical analysis were used to establish a design procedure and guidelines for an effective HSDT on driven and helical piles.

5.3 Recommendations for Future Research

To further understand the performance and load transfer mechanisms of helical piles during axial impact loading, the following recommendations are offered for future research:

1. Experimental investigations should be carried out to cover a wider range of soil types and profiles, especially in cohesionless soils. The results of such investigation can be used to further validate the findings stated in this thesis. It is recommended to record the following information during full-scale field tests; signals of force and velocity, the characteristics of the hammer and the cushion, and static and dynamic properties of the soil. These data can be used to accurately simulate the helical pile response to impact loading using finite element models, instead of using CAPWAP wave analysis.
2. The effect of non-linear cushion behavior and the amount of heat dissipated in the cushion should be investigated. The analytical solutions developed herein were sufficient to predict the generated peak force at the top of the pile for a given hammer and cushion material and the duration of the impact but approximated the real shape of the force-time response. It is believed that the real shape of the force-time response can be captured once the actual load-deformation curve for a cushion under impact loading is being accounted for if it is available.

APPENDIX A

METHOD OF ANALYZING AXIAL PILE RESPONSE UNDER DYNAMIC LOADING

Several methods are available in the literature to interpret the static behaviour of piles under dynamic axial loading. The methods that are based on one degree of freedom, commonly applied in practice, are discussed herein.

A.1. Unloading Point Method (UP)

The UP method idealizes the foundation-soil system as a single degree of freedom comprising of nonlinear spring and a linear dashpot subjected to transient forces and accelerations (Middendorp et al., 1992). The spring coefficient, k, represent static soil resistance and the dashpot coefficient, c, represent the dynamic resistance due to the rate of penetration. Two main assumptions are made in the UP method: the foundation is considered as a rigid body, and the dashpot coefficient is constant throughout the test. The unloading point is defined as the instant where the velocity (and damping) is zero, hence the derived load-displacement curve can then be obtained. A hyperbolic model can be used to describe the load-displacement curve, i.e. (Hölscher & Tol, 2009):

$$F_{static}(t) = \frac{K_o\, u(t)}{1 + B\, u(t)} \tag{A.52}$$

$$B = \frac{K_o}{\eta[F_{static}(t_{max}) - m\, a(t_{max})]} - \frac{1}{u(t_{max})} \tag{A.2}$$

Where; $F_{static}(t)$ = static soil response at time t; K_o = initial stiffness determined from dynamic measurements; $u(t)$ = pile displacement at time t; η = reduction empirical factor to account for the rate effect; t_{max} = time at zero velocity (and maximum displacement); $F(t_{max})$ = static soil response at maximum displacement; m = pile mass; and $a(t_{max})$ = acceleration at maximum displacement.

Schmuker (2005) proposed for η;

$$\eta = \left(\frac{0.33x10^{-6}}{v_{max}}\right)^{I} \quad \text{(A.3)}$$

Where; I = viscosity index, and v_{max} = maximum attained velocity during testing (m/s). For sand and silt, I ranges from 0.01 to 0.02, while for clay, it varies from 0.03 to 0.06. I = 0.017 was used for Case 1, which gave a reduction factor of 0.77. For Case 2, I = 0.03 was used which gave a reduction factor of 0.67.

The wavenumber parameter, $N_w = CL/T$ determines the applicability of the UP method in deriving the static load-displacement behavior from dynamic measurements; where, T is the impact load duration. The UP can be applied for N_w > 6 (Middendorp, 2000). Stress wave effects (i.e. stress wave phenomena) becomes large $N_w < 10$ (Gunaratne, 2013). Modified Unloading Point Method (MUP) was proposed by Justason (1997) to be applied for relatively long piles. The MUP method requires the incorporation of an additional accelerometer at the pile toe, and the pile velocity and acceleration are defined as the average of top and toe velocities and accelerations.

In this study, the calculated wave number parameters are 8.5 and 10.1 for Case 1 and Case 2, respectively. Therefore, the MUP method is adopted for Case 1, and the UP method is adopted for Case 2 to establish the derived load-displacement curve from the dynamic measurements obtained from Plaxis 2D.

A.2. Method Based on Gibson and Coyle (1968)

Gibson and Coyle (1968) conducted triaxial tests on sands and clays to investigate the influence of loading rate on the soil resistance. They proposed that the dynamic soil strength P_d can be related to the static strength P_s by considering the loading velocity, V, i.e.,

$$P_d = P_s(1 + JV^N) \quad \text{(A.4)}$$

Where, N is an exponent that control the nonlinearity of the effect, and J is damping coefficient that depends on soil type. Thus, the damping resistance, P_sJV^N, is proportional to the pile velocity and $P_d = P_s$ when the damping resistance is zero.

To include the inertia effect, which cannot be neglected in HSDT, the equilibrium equation for a single degree of freedom system representing the pile is given by

$$Impct\ force = spring\ force + damping\ force + inertial\ force$$

$$F_d(t) = Ku(t) + Cv(t) + ma(t) \quad \text{(A.5)}$$

Where, $m =$ pile mass, $K =$ stiffness, and $C =$ damping coefficient; and the external impact force $F_d(t)$ varies with time, t. The static response is determined as the resistance of the spring to deformation. Using the damping component proposed by Gibson and Coyle (1968), equation A.5 can be rewritten as:

$$F_d(t) = P_s(t) + JP_s(t)V(t)^N + ma(t) \quad \text{(A.6)}$$

The derived load-displacement curve can then be obtained from the dynamic measurement during HSDT;

$$P_s(t) = \frac{F_d(t) - ma(t)}{1 + JV(t)^N} \quad \text{(A.7)}$$

Where: $P_s(t)$ = soil static resistance; $F_d(t)$ = measured force at pile head; $a(t)$ = measured acceleration at pile head $V(t)$ = measured velocity at the pile head and N = 0.18 for clay and 0.20 for sand.

To avoid values of $1 + JV(t)^N$ smaller than one, $V(t)$ must be positive to develop the correct shape of the load-displacement curve; therefore, the velocity is defined by the following;

$$V(t) = |V(t)| \ \ for\ t < \text{ the time at max. velocity} \quad \text{(A.8)}$$

$$V(t) = V_{max}\ for\ t \geq \text{ the time at max. velocity} \quad \text{(A.9)}$$

The damping coefficient, J, can be determined from soil properties; angle of friction in sands and liquidity index in clays. For sand, J varies linearly from 1 to 0.25 for angle of friction between 30 to 45. For clay, J varies linearly from 0.65 to 1.2 for liquidity index between 0.1 to 0.55. Herein, J was estimated to be equal to 0.4 with $N = 0.2$ for the helical pile installed in sandy soils and 0.75 with $N = 0.18$ for the helical pile installed in clayey soils.

A.3. Brown and Hyde (2008)

The rate of loading effect on pile bearing capacity in clay was investigated by Brown and Hyde (2008). They proposed the following expression to derive the static resistance from the dynamic measurements during the HSDT:

$$P_s(t) = \frac{F_d(t) - ma(t)}{1 + \frac{F_d(t)}{F_{d\_max}} \alpha \left[\left(v(t) \right)^{0.2} - 0.1 \right]} \tag{A.10}$$

Where, F_{d_max} is the maximum measured force at the pile head and α depends on soil plasticity and can be estimated form the clay plasticity Index, PI, i.e. (Holscher & van Tol, 2009):

$$\alpha = 0.031PI + 0.46 \tag{A.11}$$

Equations A-8 and A-9 are used to modify the velocity to ensure it is always positive in Equation A.10.

A.4. References

Brown, M. J., & Hyde, A. F. L. (2008). Rate effects from pile shaft resistance measurements. Canadian Geotechnical Journal, 45(3); 425-431.

Gibson, G. C., & Coyle, H. M. (1968). Soil damping constants related to common soil properties in sands and clays.

Gunaratne, M. (2013). The foundation engineering handbook. CRC Press.

Hölscher, P., & Tol, F. v. (2009). Rapid load testing on piles. CRC Press.

Justason, M. D. (1997). Report of load testing at the Taipei municipal incinerator expansion project. Taipei City, Taipei.

Middendorp, P. (2000). Keynote lecture: Statnamic the engineering of art. In Proceedings of the Fourth International Conference on the Application of Stress-Wave Theory to Piles, the Hague, the Netherlands. pp. 570-580.

Middendorp, P., Bermingham, P. and Kuiper, B. (1992). Statnamic load testing of foundation piles. 4th International Conference on Stress Waves, The Hague, Balkema.

APPENDIX B

GEOTECHNICAL CORRELATIONS FOR THE DETERMINATION OF SOIL PROPERTIES

The correlations presented herein use the uncorrected Standard Penetration Test (N) values as an input and are collected from various sources found in the literature. A comprehensive review was made of the literature in order to summarize and tabulate a wide range of available existing correlations for granular and fine-grained deposits. Such correlations could be used to build a numerical model with acceptable accuracy.

B.1. Correlation Between SPT-N Value and Modulus of Elasticity

Several investigations in the literature have correlated the values of blow count, N, with the modulus of elasticity, E, for sand and sandy soils. A compiled list of these correlations is presented in Table B-1. The empirical equations in Table B-1 are plotted in Figure B-1.

Table B- 1: Correlations between E and N for granular and fine-grained soils.

Reference	Equation [kN/m^2]	Soil Type
Ferrent (1963)	$E = 718(1-v^2)N$	Sand
Webb (1969)	$E = 479(N+15)$	Sand and Silty Sand
Schmertmann (1970)	$E = 766N$	Sands
Begemann (1974)	$E = \begin{cases} 4000 + 100C(N-6) & for\ N > 15 \\ 100C(N+6) & for\ N < 15 \end{cases}$	$C = 3$ for Silt with Sand $C = 12$ for Gravel with Sand
Trofnnenkov (1974)	$E = (34300\ to\ 49000)logN$	Sand
Denver (1982)	$E = 7000N^{0.5}$	Sand
Bowles (1988)	$E = 250(N+15)$	Saturated Sand
Bowles (1988)	$E = 300(N+6)$	Silty Sand
El-Kasaby (1990)	$E = 15000 + 900N$	Sand
Kulhawy and Mayne (1990)	$\frac{E}{P_a} = 5N_{60}$	Sand with Fines
Papadopoulos (1992)	$E = 7500 + 800N$	Granular soils
Bowles (1996)	$E = 500(N+15)$	Sand

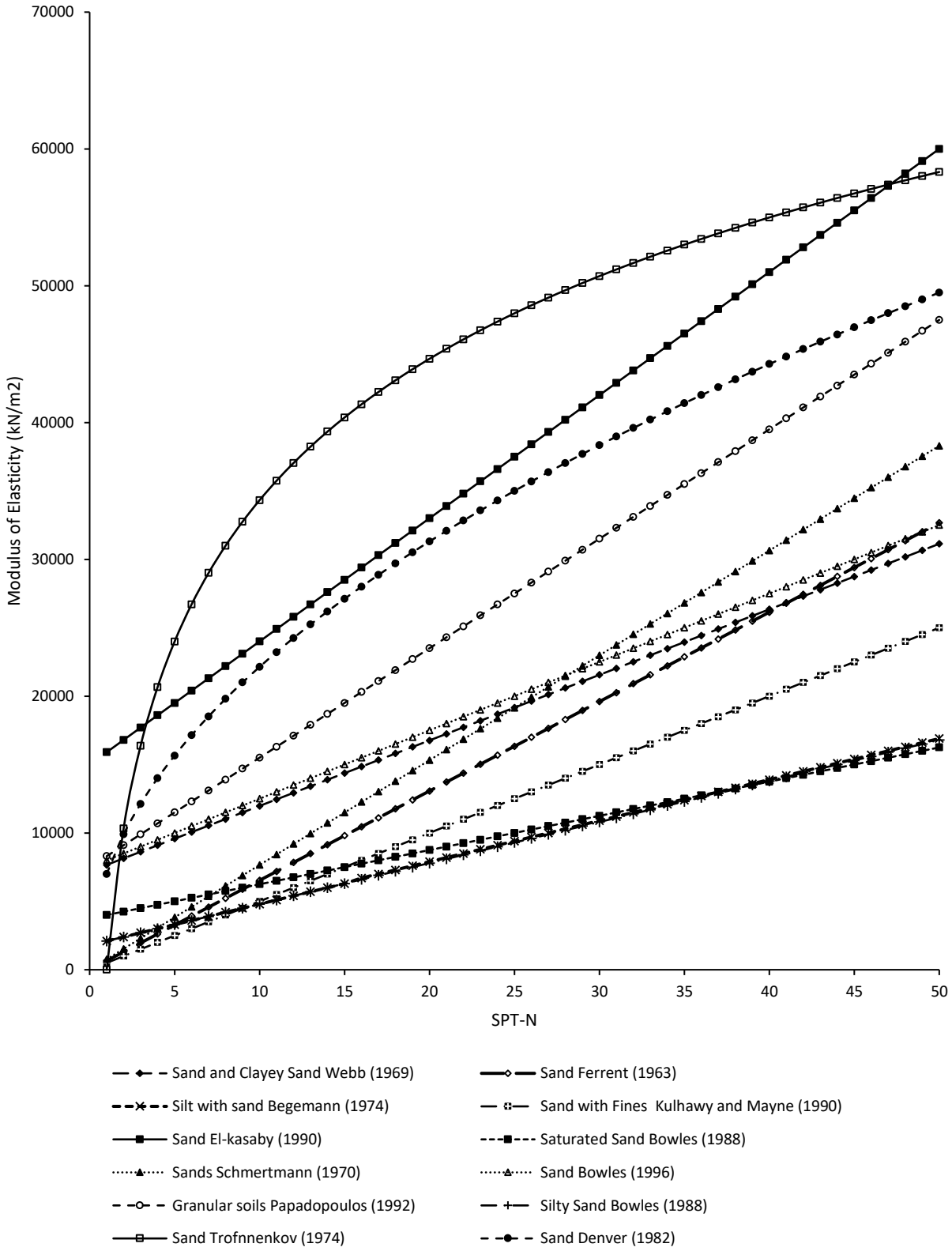

Figure B- 1: Correlations of modulus of elasticity with Standard Penetration Test for sand and silt.

B.2. Correlation Between SPT-N Value and Void Ratio

Anbazhagan et al. (2017) developed a set of empirical relations between void ratio and N value for a wide range of soil types. 293 data points of SPT-N numbers and void ratio collected from 84 boreholes were analyzed based on the least-squares method to obtain the best-fit equations that described the trend of the scattered data. The proposed correlations are as follow;

- For all soils;

$$e = 1.202N^{-0.217} \tag{B.53}$$

- For fine-grained soil;

$$e = 0.89N^{-0.12} \tag{B.54}$$

- For coarse grained soil;

$$e = 1.01N^{-0.105} \tag{B.55}$$

B.3. Correlation Between SPT-N Value and Shear Wave Velocity

A wide range of regression equations of SPT-N versus Vs is available in the literature for cohesionless soil. Most of those equations are based on a power-law relationship between Vs and uncorrected SPT-N value. Table B-2 summarizes nearly most of the empirical relationships for cohesionless soil.

Furthermore, the values of the low-strain Poisson's ratio, v, is calculated based on the theory of elasticity using equation B.4.

$$v = \frac{\left(\frac{V_p}{V_s}\right)^2 - 2}{2\left(\left(\frac{V_p}{V_s}\right)^2 - 1\right)} \tag{B.56}$$

Table B- 2: Correlations between Vs and SPT (N).

Author(s)	Type of soil	N value used	Correlation	Comment
Kanai (1966)	All	70	$V_s = 19N^{0.6}$	Most incongruous and poor prediction.
Shibata (1970)	Sandy soil	-	$V_s = 31.7N^{0.54}$	Equation based on several previous studies.
Ohba and Toriuma (1970)	All	-	$V_s = 84N^{0.31}$	Derived from Rayleigh wave velocity measurements; best for alluvial soils.
Ohta et al (1972)	Sand	100	$V_s = 87.2N^{0.36}$	Tertiary soil, and Diluvial sandy soil.
Fujiwara (1972)	All	-	$V_s = 92.1N^{0.337}$	-
Ohsaki and Iwasaki (1973)	All	220	$V_s = 81.4N^{0.39}$	Measurements done by a Downhole Borehole Test.
Imai and Yoshimura (1975)	All	26	$V_s = 76N^{0.33}$	Measurements done by a down-hole borehole test.
Imai et al (1975)	All	756	$V_s = 89.9N^{0.341}$	Includes fill soils, peats, and all other soils.
Imai (1977)	Sand	-	$V_s = 80.6N^{0.331}$	-
Ohta and Goto (1978)	All	289	$V_s = 85.35N^{0.348}$	For granular soils; overestimate Vs at shallow depths and underestimate Vs at greater depths.
Seed and Idriss (1981)	All	-	$V_s = 61.4N^{0.5}$	-
Imai and Tonouchi (1982)	All	294	$V_s = 96.9N^{0.314}$	Work well with Alluvial sands; and poor, for clay and loam soils.
Sykora and Stokoe (1983)	Sand	229	$V_s = 100.5N^{0.29}$	Based on Cross-hole Seismic Testing.
Jinan (1987)	All	-	$V_s = 116.1(N + 0.3185)^{0.202}$	-
Okamoto et al (1989)	Sand	-	$V_s = 125N^{0.3}$	Usually Overestimated Vs.
Lee (1990)	Sand	-	$V_s = 57.4N^{0.49}$	-
Athanasopoulos (1995)	All	-	$V_s = 107.6N^{0.36}$	-
Sisman (1995)	All	-	$V_s = 32.8N^{0.51}$	-
Iyisan (1996)	All	-	$V_s = 51.5N^{0.516}$	-

Jafari et al (1997)	All		$V_s = 22N^{0.85}$	-
Pitilakis et al. (1999)	Sand	300	$V_s = 145N_{60}^{0.178}$	Data obtained from Cross-Hole and Down-Hole Tests
Kiku (2001)	All		$V_s = 68.3N^{0.292}$	-
Hasancebi and Ulusay (2006)	Sand	45	$V_s = 90.82N^{0.319}$	Measurements done by Seismic refraction.
Hasancebi and Ulusay (2006)	Sand	45	$V_s = 131N_{60}^{0.205}$	Based on Seismic refractions.
Ulugergerli and Uyanık (2007)	All	-	$V_s = 23.291\ Ln(N) + 405.61$	Upper limit
	All	-	$V_s = 52.9e^{-0.011N}$	Lower limit
Dikmen (2009)	Sand	-	$V_s = 73N^{0.33}$	-

B.4. Static and Dynamic Stiffness

The initial stiffness, E_i, can be determined form the distribution of Poisson's ratio, v, and shear modulus at small strain, G_{max}, using the following expression;

$$E = 2G(1 + v) \tag{B.57}$$

The modified hyperbola model can be to reduce the initial stiffness, E_i, to a secant modulus, E_s, at the working load level. The general expression of the model is given by Fahey and Carter (1993) as follow;

$$\frac{E_s}{E_i} = 1 - f\left(\frac{q}{q_{ult}}\right)^g \tag{B.58}$$

Where, $\frac{q}{q_{ult}}$ is the mobilized stress relative to the ultimate stress, and f and g are fitting parameters. Verbrugge & Schroeder (2018) indicated that the ratio is commonly between 0.05 and 0.3, depending on the rate of the applied load. Furthermore, Alpan (1970) proposed a curve to estimate the dynamic modulus of elasticity from the elastic static modulus for different types of soils, as shown in Figure B-2.

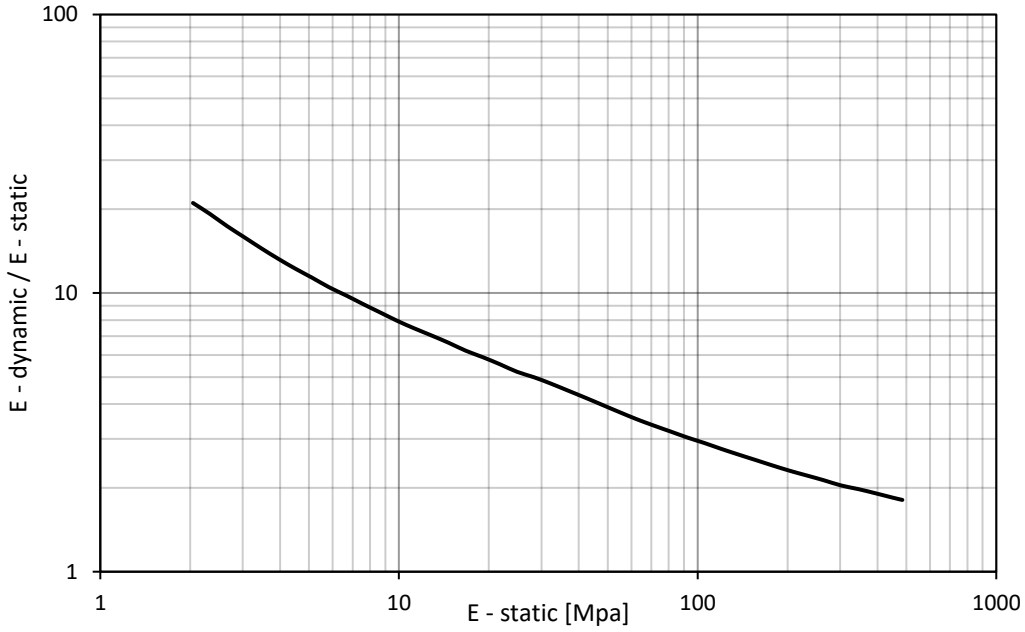

Figure B- 2: Dynamic and static modulus of elasticity after Alpan (1970).

B.5. References

Alpan, I. (1970). The geotechnical properties of soils. Earth Science Reviews. Elsevier, 1(6): 5-49.

Anbazhagan, P., Uday, A., Moustafa, S. S., & Al-Arifi, N. S. (2017). Soil void ratio correlation with shear wave velocities and SPT N values for Indo-Gangetic basin. Journal of the Geological Society of India, 89(4): 398-406.

Athanasopoulos, G. A. (1995). 1988 Armenia Earthquake. II: Damage Statistics versus Geologic and Soil Profiles. Journal of Geotechnical Engineering, 121(4): 395-398.

Begemann, H. (1974). General report for central and western Europe. In Proceedings, European Symposium on Penetration Testing, Stockholm.

Bowles, L. E. (1996). Foundation analysis and design. McGraw-hill, New York. pp. 66-190.

Burland, J. (1973). Shaft friction of piles in clay - a simple fundamental approach. Publication of: Ground Engineering, UK, 6(3): 30-42.

Denver, H. (1982). Modulus of elasticity for sand determined by SPT and CPT. In Proceedings of the 2nd European Symposium on Penetration Testing, Amsterdam. pp. 24-27.

Dikmen, Ü. (2009). Statistical correlations of shear wave velocity and penetration resistance for soils. Journal of Geophysics and Engineering, 6(1): 61-72.

El-Kasaby, E. (1991). Estimation of guide values for the modulus of elasticity of soil. Bulletin of Faculty of Engineering, Assiut University, Vol. 19: 1-7.

Farrent, T. A. (1963). The prediction and field verification of settlement in cohesionless soils. In Proceedings, 4th Australia-New Zealand Conference on Soil Mechanics and Foundation Engineering. pp. 11–17.

Fahey, M., & Carter, J. P. (1993). A finite element study of the pressuremeter test in sand using a nonlinear elastic plastic model. Canadian Geotechnical Journal, 30(2): 348-362.

Hasancebi, N., & Ulusay, R. (2006). Empirical correlations between shear wave velocity and penetration resistance for ground shaking assessments. Bulletin of Engineering Geology and the Environment, 66(2): 203-213.

Imai, T. (1982). Correlation of N-value with S-wave velocity and shear modulus. In Proceedings of the 2nd European Symposium of Penetration Testing, Amsterdam.

Imai, T., & Tonouchi, K. (1982). Correlation of N-value with S-wave velocity. In Proceedings of 2nd Europe Conference on Penetration Testing. pp. 67-72.

Imai, T., & Yoshimura, M. (1970). Elastic wave velocities and characteristics of soft soil deposits. Soil Mechanics and Foundation Engineering, The Japanese Society of Soil Mechanics and Foundation Engineering, 18(1).

Imai, T., Fumoto, H., and Yokota, K. (1975). the relation of mechanical properties of soils to P- and S-wave velocities in Japan. In Proceedings of the Fourth Japanese Earthquake Engineering Symposium (in Japanese; translated by H. Umehara). pp. 86-96.

Iyisan, R. (1996). Correlations between shear wave velocity and in-situ penetration test results. Vol. 7: 371-374.

Jafari, M. K., Shafiee, A., & Razmkhah, A. (1997). Dynamic properties of fine-grained soils in south of Tehran. Journal of Seismology and Earthquake Engineering, 4(1): 25-35.

Jinan, Z. (1987). Correlation between seismic wave velocity and the number of blows of SPT and depth. Selected Papers from the Chinese Journal of Geotechnical Engineering. pp. 92-100.

Kanai, K. (1966). Observation of microtremors, XT: Matsushiro earthquake swarm Areas. Bulletin of Earthquake Research Institute (in Japanese) University of Tokyo, Tokyo, Japan. Vol. XITV, Part 3.

Kiku, H. (2001). In-situ penetration tests and soil profiling in Adapazarı, Turkey. In Proceedings of 15th ICSMGE TC4 Satellite Conference on Lessons Learned from Recent Strong Earthquakes, Istanbul, Turkey. pp. 259-265.

Ohba, S., & Toriuma, I. (1970). Research on vibrational characteristics of soil deposits in Osaka, Part 2, on velocities of wave propagation and predominant periods of soil deposits. In technical meeting of Architectural Institute of Japan.

Ohsaki, Y., & Iwasaki, R. (1973). On dynamic shear moduli and Poisson's ratios of soil deposits. Soils and Foundations, 13(4): 61-73.

Ohta, T., Hara, A., Niwa, M., & Sakano, T. (1972). Elastic moduli of soil deposits estimated by N-values. In Proceedings of the 7th Annual Conference, The Japanese Society of Soil Mechanics and Foundation Engineering. pp. 265-268.

Okamoto, T., Kokusho, T., Yoshida, Y., & Kusuonoki, K. (1989). Comparison of surface versus subsurface wave source for P-S logging in sand layer. In Proceedings of 44th annual conference, Japan society of civil engineers. Vol. 3: 996–997.

Papadopoulos, B. P. (1992). Settlements of shallow foundations on cohesionless soils. Journal of Geotechnical Engineering, 118(3): 377-393.

Pitilakis, K., Raptakis, D., Lontzetidis, K., Tika-Vassilikou, T., & Jongmans, D. (1999). Geotechnical and geophysical description of EURO-SEISTEST, using field, laboratory tests and moderate strong motion recordings. Journal of Earthquake Engineering, 3(3): 381-409.

Schmertmann, J. H. (1970). Static cone to compute static settlement over sand. Journal of the Soil Mechanics and Foundation Division, ASCE. 3(96): pp. 1011-1043.

Seed, H. B., & Idriss, I. M. (1970). Soil moduli and damping factors for dynamic response analyses. Earthquake Engineering Research Center, University of California, Berkeley, Berkeley. Report No. UCB/EERC-70/10.

Shibata, T. (1970). The relationship between the N-value and S-wave velocity in the soil layer. Disaster Prevention Research Laboratory, Kyoto University, Kyoto, Japan.

Sisman, H. (1995). An investigation on relationships between shear wave velocity, and SPT and pressuremeter test results [Master thesis]. Ankara University, Turkey.

Sykora, D. W., & Stokoe, K. H. I. I. (1983). Correlations of in situ measurements in sands of shear wave velocity, soil characteristics, and site conditions. Civil Engineering Department, University of Texas at Austin, USA. Report GR 83-33.

Trofimenkov, Y. G. (1974). Penetration testing in Western Europe. In Proceedings, European Symposium on Penetration Testing.

Ulugergerli, E. U., & Uyanik, O. (2006). Statistical correlations between seismic wave velocities and SPT blow counts and the relative density of soils. Journal of Testing and Evaluation, 35(2): 187-191.

Webb, D. L. (1970). Settlement of structures on deep alluvial sandy sediments in Durban, South Africa. Proceedings, Conference on The In-Situ Behavior Of Soils And Rocks, Institution Of Civil Engineering, London. pp. 181-188.

Verbrugge, J. C., & Schroeder, C. (2018). Geotechnical Correlations for Soils and Rocks. ISTE Limited.

VITA

Name:	Mohammed Alwalan
Post-secondary Education and Degrees:	King Saud University, College of Engineering. Riyadh, Saudi Arabia. (2011 - 2015)
Honours and Awards:	The Award of Dean's List for Outstanding Students of the University of King Saud. (2013) Milos Novak Memorial Award (2019)
Related Work Experience:	Internship Riyadh Metro Project (2015) Teaching Assistant King Saud University (2016 - 2017) Teaching Assistant The University of Western Ontario (2018 - 2019)